Use of 3D-Printed Rock Analogues to Study Two-Phase Flow in Fractures

by

Sebastian Lopez Saavedra

A thesis submitted in partial fulfillment of the requirements for the degree of

Doctor of Philosophy
in
Geotechnical Engineering

Department of Civil and Environmental Engineering

University of Alberta

Abstract

Flow through an individual rock fracture is of fundamental importance in both experimental and numerical studies aimed at describing the hydraulic behavior of fracture networks or rock masses. A single fracture can exert dominance over fluid pathways, and the results obtained from individual fracture studies can serve as a foundation for large-scale projects. However, rock discontinuities may present complex morphologies resulting from multiple factors, including mechanical and hydraulic conditions. These conditions determine the laws and models applicable to describe flow.

Nevertheless, numerous divergent perspectives persist regarding several essential aspects of modeling single-phase flow and two-phase flow through an individual fracture. This investigation aimed to address some of these discrepancies and explore new areas, harnessing the capabilities of polyjet 3D printing technology. This technology facilitated the control of fracture roughness and mechanical conditions, visualization of flow displacements, and acquisition of local pressure measurements using fiber optic sensors. Additionally, it allowed for a preliminary experimental approximation of local fracture apertures, which were subsequently employed in numerical simulations of individual fractures.

First, this study evaluated two methodologies for removing support material from polyjet 3D-printed samples. This technology may be instrumental in investigating flow through fractures, and consequently, the removal of support material from 3D-printed prototypes represents an obstacle to using such models in laboratory experiments. This study evaluated two methodologies for the removal of support material and investigated some of the effects of improving the removal of support material from 3D-printed prototypes and some of the implications of using these enhanced models in investigations of flow-through fractures.

Second, with respect to single-phase flow, this study evaluated cubic-law-based models

to provide insights for numerical simulation projects. Additionally, this research reported on the conditions under which cubic-law-based models are most suitable for estimating the experimental hydraulic conductivity of fractures. Furthermore, this investigation provided an approximation of experimental errors associated with the various methodologies for estimating the hydraulic aperture of fractures. On the other hand, the effectiveness of the cubic law in estimating the hydraulic conductivity of fractures was assessed. Lastly, this study addressed the criteria for determining the limit of the linear flow regime for fractures. Third, concerning two-phase immiscible flow, this study investigated how surface roughness and mechanical changes, including shear motion, impact dominant flow regimes. This is an area where the experimental data is very limited. Furthermore, this research investigated the shape of the relative permeability in fractures and examined the effects of roughness and shear deformation over two-phase flow displacements.

Preface

This thesis is an original work by Sebastian Lopez Saavedra, who was funded by the National Council of Humanities Science and Technology (Conahcyt) and the Natural Sciences and Engineering Research Council of Canada (NSERC). The author of this thesis was responsible for the experimental work, data curation, conceptualization, methodology, validation, software analysis, investigation, original draft, review, and editing. Dr. Rick Chalaturnyk and Dr. Gonzalo Zambrano-Narvaez contributed to the conceptualization, methodology, supervision, project administration, funding acquisition, resources, review, and draft editing. Dr. Nathan Deismann contributed to the conceptualization and methodology, while Dr. Sergey Isutov collaborated on the conceptualization, methodology, and writing process.

Chapter 3 of this thesis has been published as a conference paper as Saavedra, S. L., Ishutov, S., Chalaturnyk, R., & Narvaez, G. Z. (2020). Importance of improving support material removal from polyjet 3d-printed porous models. *ECMOR XVII*, *2020*(1), 1–11. https://doi.org/10.3997/2214-4609.202035210

Chapter 4 will be submitted for publication as Lopez-Saaverda, S., Zambrano-Narvaez, G., Ishutov, S. and Chalaturnyk, R. Assessment on the impact of local pressure measurements on hydraulic properties of individual 3D-printed fractures.

Chapter 5 has been accepted for journal publication as Lopez-Saavedra, S., Zambrano-Narvaez, G., Ishutov, S., & Chalaturnyk, R. (2024). The influence of displacements arising from shear motion on two-phase flow through 3d-printed fractures. *Geoenergy Science and Engineering*, 212731. https://doi.org/https://doi.org/10.1016/j.geoen.2024.212731

Dedicated to my family

for their love and for being a lighthouse in my life.

In a word: experience is best. I won't tell you that experience can't be obtained by continuous contact with a library, but experience will always be above and beyond the library.

– Roberto Bolaño, *2666*.

Acknowledgements

I wish to begin by acknowledging the grace of the Almighty God, whose guidance and blessings have illuminated my path throughout this growth journey.

I extend my deepest thanks to my supervisor Dr. Rick Chalaturnyk for granting me the privilege of joining his prestigious research group. His unwavering support, financial assistance, and boundless patience have been instrumental in this project. Your concern for both my well-being and my family's, as well as your encouragement during my most challenging moments, has been a pillar.

I am immensely grateful to my co-supervisor Dr. Gonzalo Zambrano-Narvaez, for his constant advice, technical guidance, kindness, and total support. His contributions have greatly enriched my research experience. Without his help, this work would not have been possible.

To Dr. Juliana Leung, Dr. Bo Zhang, Dr. Lijun Deng, and Dr. Florian Doster, I thank them for their invaluable feedback, which has significantly improved the quality of my research.

I am also forever indebted to Nathan Deisman, Gilbert Wong, Keivan Khalegi, Dmytro Pantov, Noga Vaisblat, Mohamed Hamoud, Francy Guerrero, Sergey Ishutov, and the members of the Reservoir Geomechanics Research Group (RGRG) for their assistance with planning, designing, and completing my experimental work. In addition, I extend all my gratitude to Cecilia and Hope for their immense support throughout this endeavor.

A special thanks to Dr. Hrvoje Jasak and Dr. József Nagy for their technical assistance with OpenFOAM software. Their openness to communication and guidance with the smallest issues always raised my spirit.

I would like to acknowledge the generous support of the Conahcyt and the Secretariat of Energy (SENER), as well as the NSERC, for their financial backing throughout my PhD journey. I would also like to thank Manuel Coronado and Erick Luna from the Mexican Petroleum Institute for allowing me to participate in this amazing project.

Lastly, I want to express my profound gratitude to my wife, Glenda, for her unending love and unwavering faith in me. Her generosity and wisdom have always inspired me to be better. To my parents, Norma and Roberto, their unconditional love, unyielding hope, and example have been a constant source of teaching. To my siblings, Roberto, Emiliano, and Sofia, your love has carried me this far, and for that, I am eternally grateful.

Contents

List of Tables

List of Figures

List of Abbreviations

CL *cubic law*

NS Navier-Stokes

LCL local cubic law

CAD computer aided design

NPT National Pipe Tapered

CCD charged-couple device

COV coefficient of variation

SF smooth fracture

RF rough fracture

PN Perlin noise

PV pore volume

RMSE root mean squared error

JBN Johnson, Bossler and Neumann

JRC joint roughness coefficient

3D three-dimensional

2D two-dimensional

AM additive manufacturing

CT computer tomography

UV ultraviolet

NaOH caustic soda

Conahcyt National Council of Humanities Science and Technology

NSERC Natural Sciences and Engineering Research Council of Canada

SENER Secretariat of Energy

RGRG Reservoir Geomechanics Research Group

SIMPLE Semi Implicit Method for Pressure Linked Equations

UCS Unconfined compressive strength

LVDT linear variable displacement transducer

K-P Cretaceous-Paleocene

List of Symbols

A	area of the fracture plane
b	local aperture in the LCL model
$\bar{b}$	mean mechanical aperture
$\langle \bar{b} \rangle$	mean aperture available to flow
$b_{\parallel}$	constant aperture between two parallel plates
c	dye concentration
Ca	capillary number
d	grain size diameter
d_m	mean particle diameter
D	fractal dimension from the fractal-based variogram method
$D_{sat.}$	fractal dimension from fracture saturation binary images
e	hydraulic aperture
e_{model}	calculated hydraulic aperture from analytic models
e_{local}	hydraulic aperture calculated with local pressures
$e_{ext.}$	hydraulic aperture calculated with external pressures
f_o	oil fractional flow
$\bar{g}$	gravity
h	lag distance
H	Hurst exponent from the fractal-based variogram method
I	light intensity
I_0	transmitted intensity at zero concentration
$1/I_r$	reciprocal of the relative injectivity
k	absolute permeability
$\bar{\bar{k}}$	absolute permeability tensor
k_f	fracture permeability

k_r relative permeability

k_{ro} relative permeability of oil

k_{rw} relative permeability of water

$\bar{\bar{k}}_\alpha$ effective permeability tensor of phase α

$k_{r\alpha}$ relative permeability of phase α

L length of medium, fracture length

L_e fracture length used to estimate hydraulic aperture

m slope

N_{pD} oil production in pore volume units

N_{pD}^{bt} oil production in pore volume units at water breakthrough

$N(h)$ number of pairs separated by a lag distance

n total number of measurements

P total pressure

p pressure in NS equations

p_{10}, p_9 and p_8 inlet local pressure sensors

p_7, p_6, p_5 and p_4 middle local pressure sensors

p_3, p_2 and p_1 outlet local pressure sensors

p_{11} and p_{12} external pressure sensors

$\bar{p}_{in}$ averaged inlet local pressure

$\bar{p}_{mid}$ averaged middle local pressure

$\bar{p}_{out}$ averaged outlet local pressure

Q water flow rate

q flow rate

Q_o oil flow rate

q_α source or sink of phase α

Re Reynolds number

Re_c critical Reynolds number

R_a average asperity height

R_{ku} kurtosis (sharpness)

RMS root mean square

R_L linear roughness coefficient, ratio between the actual 2D profile lengh to the nominal

S_{sk} skewness

S_w water saturation

S_w^{bt} water saturation at water breakthrough

S_{O_2} oil saturation at the fracture outlet

S_{wavg} average water saturation

S_{w2} water saturation at the fracture outlet

S_α saturation of phase α

T thickness of the gap filled with the dyed solution

$\bar{u}$ velocity vector in NS equations

$\bar{u}_\alpha$ Darcy velocity of phase α

w fracture width

W_i water injection as a fraction of pore volume

x_{norm} normalized x coordinates

y_{norm} normalized y coordinates

z surface elevations

z_{max} maximum elevation

z_{min} minimum elevation

z_i ith elevation

z_j jth elevation

z_k mean of z_i elevation values

Z peak asperity height

Z_2 root mean square of the profile's first derivative

Z_3 root mean square of the profile's second derivative

β aperture correction parameter

γ_0 amplitude from fractal-based variogram method

δ_y shear displacement in the y-direction

Δp pressure drop between the inlet and the outlet of a fracture

ΔP pressure drop

$\Delta \bar{p}_{ext.}$ external differential pressure

$\Delta x = x_{i+1,j} - x_{i,j}$ $x-$coordinates spacing

θ_p mean angle of inclination

κ_c Kozeny constant

κ absorptivity of the material

μ_α phase viscosity of phase α

μ_w water viscosity

μ mean value

μ_s mean of the surface elevations

ρ density

ρ_w water density

ρ_α phase density of phase α

σ standard deviation

σ_{p_i} standard deviation of local pressure measurement i, $i = 1, ..., 10$

σ_s standard deviation of the surface elevations

σ_{slope} standard deviation of the local surface slope

σ_{wo} interfacial tension between oil and water

ϕ porosity

Chapter 1

Introduction

1.1 Background

The physics involved in flow through fractured media have been the subject of extensive study for various purposes, including underground storage of contaminant waste, carbon dioxide, and, more recently, hydrogen storage, as well as fluid flow through aquifers and hydrocarbon production. However, given the complexity of hydro-mechanical processes in a rock mass, understanding their behavior at a single-fracture scale may be fundamental prior to examining reservoir-scale rock volumes.

A single fracture or rock discontinuity is frequently conceptualized by two plates with a constant separation between them (L. Zhang, 2016). However, real rock fractures possess complex morphologies with rough topographic characteristics resulting from stress effects or mechanical displacements. Such mechanical properties, as well as the varied hydraulic conditions, will determine the governing laws and applicable models that can express the flow through a single fracture. Furthermore, the nature of reservoir fractures can be highly heterogeneous. They may serve as high-permeability pathways but can also exhibit anisotropic characteristics or form through the deformation of low-permeability rock (R. A. Nelson, 2001). Fractures can be classified into three categories according to stress conditions (Stearns & Friedman, 1972). The main characteristics of each fracture type are as follows (R. A. Nelson, 2001; Shen et al., 2020): Shear fractures occur when their walls slide in parallel to each other along the fracture plane. Extension fractures, on the other hand, are characterized by the displacement of fracture surfaces perpendicular to the fracture plane, often forming in alignment with the minimum stress direction. Finally, tension fractures involve the displacement of fracture walls perpendicular to the fracture plane, but their formation typically requires at least one of the principal stresses to be tensile.

Flow through a single fracture is fundamental to better understanding the physics that control transport phenomena in many disciplines (R. W. Zimmerman & Bodvarsson, 1996), and studying individual rock fractures is crucial not only for theoretical purposes but also because experimental and numerical applications can benefit from it. For example, in the area of single-phase flow, cubic-law-based models have been developed to provide a more accurate description of the hydraulic behavior of fractures. These models are formulated based on the so-called *cubic law* (*CL*), which describes the flow between two parallel plates (Indraratna et al., 1999). Such models are regularly employed in experimental studies (e.g., Konzuk and Kueper (2004)) and in numerical modeling of flow through a fracture network (e.g., Ishibashi et al. (2019) and Suzuki et al. (2019)). However, there could be cubic-law-based models that are potentially better suited for specific mechanical or topographic conditions. Consequently, examining these models could indicate which models can more accurately estimate the hydraulic conductivity of fractures, which could prove advantageous for both experimental and numerical studies.

On the other hand, the hydraulic aperture is used to express the permeability or hydraulic conductivity of a single fracture (L. Zhang, 2016). This parameter is typically obtained from experimental studies on individual fractures using the *CL* expression (Hakami & Larsson, 1996; H. Lee & Cho, 2002). However, there may be experimental conditions under which this parameter offers a better approximation.

In the realm of immiscible flow through fractures, a topic of practical importance is the relative permeability in fractures. There is a continuous scientific discussion on the appropriate model to describe the displacement of immiscible phases. On the other hand, the influence of mechanical displacements on two-phase flow experiments remains relatively unexplored. In particular, the impact of shear motion on two-phase flow has yet to be described.

Due to their nature, characterizing the roughness of individual fractures has been the focus of numerous studies (e.g., Y. Zhang and Chai (2020)). However, there is an ongoing debate regarding the adequate approach to quantify the roughness of rock fractures. Some suggest that fractal-based methods provide a better approximation (Y. Ge et al., 2014); however, there are numerous methodologies and although standards exist (e.g., International Organization for Standardization (2021)), they are not free from shortcomings. Consequently, more discussion is needed on the most suitable approach to describe surface roughness. Hypothetically, incorporating scale-independent roughness properties into numerical and experimental models may lead to improved accuracy.

The introduction of three-dimensional (3D) printing technology in research projects has opened many possibilities in the study of individual fractures; however, it is essential to develop workflows to digitize, 3D print, and conduct experiments on these 3D-printed fractures. This will facilitate more complex numerical and experimental studies in the future.

1.2 Problem Statement

While there is general consensus with respect to the relevance of fractures, there are contrasting postures with respect to specific fundamental aspects. Concerning the single-phase flow across a rough-wall fracture, although it continues to be broadly used, the effectiveness of the cubic law to estimate the hydraulic conductivity of fractures is still questioned (Kishida et al., 2013; V. V. Mourzenko et al., 2018; Nicholl et al., 1999; Pyrak-Nolte et al., 1987). Additionally, it is necessary to clarify the conditions under which cubic-law-based models are most suitable for estimating this parameter. Hydraulic aperture is often determined by measuring the pressure drop externally from fracture specimens, and the impact of using local pressure measurements versus external measurements on hydraulic aperture estimates remains unknown. Therefore, obtaining an approximation of the experimental error might be useful for laboratory studies.

On the other hand, the criteria for determining the limit of the linear flow regime for a fracture under shear deformation have been the subject of prevalent controversy in the literature (Y. Zhang & Chai, 2020), and this controversy also extends to static fractures. Given these challenges, an evaluation of cubic-law-based models can provide valuable insights for numerical simulation projects.

With respect to two-phahse flow, there are conflicting data concerning the appropriate model for relative permeability in fractures (Huo & Benson, 2016). Additionally, the impact of shear on relative permeability and flow regimes in fractures remains unknown. Therefore, more scientific data is needed to understand the effects of fracture topography and mechanical changes during immiscible flow through an individual fracture.

The technology of 3D printing has gained momentum in different scientific areas, and for the study of flow through fractures, PolyJet 3D printing has become very important because of its capability to print with high detail. However, there are challenges, such as improving the removal of support material from samples, as well as evaluating its potential in flow visualization, that should be addressed to fully utilize the potential of this technology.

1.3 Knowledge Gaps

- Limited literature on the effect of shear on multi-phase flow through fractures
- Limited studies on the shape of relative permeability in fractures and the effect of roughness
- Methodological considerations for the experimental application of the cubic law are missing.
- There is debate on the adequate approach for characterizing rock fracture roughness.
- There is a need for a standard workflow to digitalize, 3D print, and model flow through rock fractures.

1.4 Hypothesis

Fluid recovery from fractured porous media not only involves fluid displacement in fractures but also involves mechanical changes. Phase mobility in porous media has traditionally been analyzed through studies of relative permeability, and relative permeability in fractures is often assumed to be a linear function of saturations. However, this premise may be invalid for real fractures that undergo significant mechanical changes as the reservoir is depleted.

The relative permeability of fluids in fractures is not a linear function of saturations. Roughness and shear displacements can introduce phase interference and affect flow regimes.

Furthermore, in the context of single-phase conditions, among the existing cubic-law-based models, there may be a universal model that offers a more accurate description of the hydraulic behavior of individual fractures.

PolyJet 3D printing may be instrumental in analyzing these research areas, and testing its potential may serve to develop methodologies that can fully utilize its capabilities in flow through fractures studies.

1.5 Research Objectives

The main objective of this investigation is to improve the understanding of fluid flow through an individual fracture while assessing the influence of mechanical changes and fracture morphological properties on single-phase and multi-phase flow through fractures. This study involved experimental and numerical modeling. The specific objectives are detailed as follows:

- To evaluate methodologies for characterizing fractures topography.
- To develop methodologies for 3D printing and post-processing PolyJet fractured samples.
- To establish a benchmark for the mathematical models used in describing single-phase flow through individual fractures.
- To experimentally verify the linearity of the relative permeability curves in fractures.
- To examine the effect of aperture changes and shear displacements on two-phase flow through 3D-printed features.
- To investigate the relationship between shear displacements and flow regime.
- To assess the accuracy of single-phase flow experiments through individual fractures using the Navier-Stokes (NS) equations and modifications to the local cubic law.

1.6 Research Scope

1.6.1 Experimental

In this study, the term *fractures* referred to laboratory-scale cracks, fissures, or joints, which may encompass porosity. As a result, the mechanics and flow dynamics were examined at a macroscopic level.

The experimental scope of this research centered on investigating single-phase and multiphase flow through an individual 3D-printed rock under static conditions. Each experiment was conducted at specific fracture aperture conditions and at a particular *shear displacement*. This term was adopted to denote the relative lateral displacement of one fracture face with respect to the other. However, in fracture mechanics, the term *shear displacement* frequently refers to a process where shear stress not only induces displacement of one fracture face relative to the other but simultaneously leads to degradation of asperities through contact between the fracture surfaces. However, this mechanical phenomenon was beyond the scope of this investigation.

Laboratory work aimed to establish correlations between fracture topography and flow measurements, while also monitoring fluid displacements and saturation changes in a single fracture under different mechanical conditions.

The flow experiments were conducted using a 3D-printed horizontal fracture formed with two 3D-printed textured surfaces facing each other. The fracture topography was digitally generated using a texture generation method. Synthetic surfaces were preferred over scans from natural rock surfaces due to the practical challenges observed when attempting to scan and stitch large domains, such as 150 mm $\times$ 150 mm.

Fracture roughness was characterized using fractal and statistical approaches. The fracture samples were 3D printed with a PolyJet Stratasys Eden 260 VS in VeroClear resin (a translucid material to allow visualization of flow).

Mechanical and wettability characterization of VeroClear material was performed. Investigating the wettability of the 3D printing material was carried out for the purpose of experiment design and was not intended to replicate the wettability of real rock. The absorption of fluids into 3D printed surfaces was beyond the scope of this study. Similarly, physical processes occurring in the rock matrix, such as diffusion, and those at the matrix-fracture interface, such as capillary imbibition/drainage, were not included in this investigation. All experiments were carried out at room temperature (25 °C). Flow conditions were characterized by low Reyonlds number (Re), where inertial advective forces were significantly smaller than viscous forces, resulting in minimal non-linear flow. Consequently, it was anticipated that fluid displacement would be primarily influenced by fracture aperture, surface topography, mechanical displacements, pressure gradient, and viscous forces.

In the case of non-conforming fractures, it was anticipated that surface disparities would lead to increased flow tortuosity. The fluids utilized in the experiments were dyed water and silicone oil. In the context of monophasic experiments, these fluids were injected to observe their behavior under steady-state conditions while maintaining a Re of less than 10 and a low-pressure gradient, as expected in real subsurface flow (see examples Camacho-V. et al. (2014), Streltsova (1983), and Tiab and Donaldson (2015)).

In the context of multi-phase flow, fluids were injected to monitor fluid displacements under unsteady-state conditions. This approach was adopted to attempt estimating relative permeability through an unsteady-state method, utilizing a high flow rate of 40 cm^3/min, resulting in a convex low-pressure drop. These laboratory experiments were conducted under low capillary numbers (that is, $Ca \leq 10^{-4}$). This choice ensured that the experiments operated near porous media values, but were sufficiently high to disregard capillary effects. The mean fracture aperture was determined by closing the flow cell and was approximately in the order of millimeters.

Digital CAD modeling and 3D printing allowed the estimation of local apertures per fracture using an image processing technique based on the Beer-Lambert. Pressure sensors positioned throughout the fracture were instrumental in collecting local pressure measurements during the test and were used to estimate the actual pressure throughout the fracture. Shear displacements were introduced to one of the textured surfaces on a millimeter-scale basis before flow experiments. This was achieved by 3D printing samples with varying shear displacements. The advantage of using mechanical displacements, rather than applying normal or shear loads, was that they caused minimal damage to the displaced surfaces, allowing them to retain their original morphology to a significant extent. Changes in fluid saturation in the fractures were monitored using a Basler camera.

1.6.2 Numerical Simulation

The numerical simulation centered on modeling steady-state single-phase flow through an individual fracture. Each fracture was modeled in a static mechanical condition. The aim of the numerical simulations was to replicate the experimental results. Consequently, numerical simulations did not include chemical reactions, contaminant transport phenomena, or thermal effects.

The numerical modeling was conducted with the OpenFOAM Finite-Volume Software. This process involved solving the *NS* equations using the Semi Implicit Method for Pressure Linked Equations (SIMPLE) algorithm, alongside solving versions of the local cubic law. Furthermore, simulation meshes were generated on the basis of the fracture geometry obtained from experimental local aperture maps. These maps were processed to obtain 3D and two-dimensional (2D) numerical simulation meshes.

1.7 Dissertation Structure

This thesis comprises six chapters. Chapter 1 presents the research background, problem statement, and research objectives. Chapter 2 presents a framework and literature review on flow through a single fracture, as well as pertinent information on 3D printing and the description of fracture roughness. Chapter 3, which has already been published, evaluates post-treatment methods for PolyJet 3D-printed fractured samples. Chapter 4, which will be submitted for publication, provides an assessment of the impact of local pressure measurements on the hydraulic properties of individual 3D-printed fractures. Chapter 5, which has already been published, addresses the influence of displacements arising from shear motion on two-phase flow through 3D-printed fractures. Chapter 6 presents conclusions, contributions and recommendations for future research projects, four appendices are included to provide further details on the experimental and practical aspects of this investigation.

Chapter 2

Literature Review

2.1 Flow through an Individual Fracture

2.1.1 Single-phase Flow

Conceptual Fracture A well-known model to represent a rock discontinuity or a single fracture is by using two parallel plates (Berkowitz, 2002). This classic approach considers a single fracture as a set of plates with a constant small space between them. For such configuration and under certain conditions (i.e., Newtonian fluid and weak inertial regimes), single-phase flow rate can be calculated analytically employing the so-called *CL* (R. Olsson & Barton, 2001). This scalar equation takes into account that the pressure drop is linearly proportional to the volumetric flow rate in a fracture aperture (Tsang & Witherspoon, 1981) and can be expressed as follows (Bear, 1988; Huitt, 1956; Snow, 1965):

$$Q = -\frac{b_{\parallel}^3 w \Delta p}{12 \mu_w L} \tag{2.1}$$

Where Q is the water flow rate, Δp is the pressure loss, $b_{\parallel}$ is the distance between the plates, L is the fracture's length, w is the fracture's width, and μ_w is the water viscosity. Equation 2.1 has been verified experimentally flowing at laminar regimes through two glass plates with constant aperture (Lomize, 1951; Romm, 1966). This equation is a solution of the *NS* equations for the parallel plates geometry and its use is valid for *Re* <1150 (R. W. Zimmerman & Bodvarsson, 1996).

Equation 2.1 has been combined with Darcy equation (Bear & Cheng, 2010) to derive an analytical method that estimates the overall permeability of fractured porous media (Parsons, 1966).

Rough Fracture A rough fracture is separated by two rough surfaces. This implies that the aperture field can be constant across the domain if the fracture is composed of mirror surfaces; however, if there is a mismatch in the surfaces, the aperture map will vary spatially which may involve complex fracture morphologies with asperities and potential contact points.

For such configurations, single-phase flow studies through fractures have progressively moved from the parallel-plates model towards more complex fracture morphologies avoiding the simplifications of the *CL* and analyzing the incompressible *NS* equations. These expressions represent the governing laws of single-phase flow across an individual rough fracture and are expressed as follows (R. Zimmerman & Main, 2004):

$$\rho \frac{\partial \bar{u}}{\partial t} + \rho \left(\bar{u} \cdot \nabla \right) \bar{u} = -\nabla P + \mu \nabla^2 \bar{u} \tag{2.2}$$

Where $\bar{u}$ is the water velocity, ρ is the density, P is $P = p - \rho \bar{g}$ where p is pressure, $\bar{g}$ is the gravity vector and μ is viscosity. The 3D form of this nonlinear partial differential equation has been solved numerically for the geometry of an individual rough fracture (Brush & Thomson, 2003). However, due to the complicated morphology of these fractures, numerically solving the 3D form of equation 2.2 is frequently avoided, and instead, the so-called local cubic law (*LCL*) is solved numerically by integrating Stokes equation and coupling it with the mass continuity equation as follows (Brown, 1987):

$$\nabla \cdot \left[\frac{b^3}{12\mu} \nabla p \right] = 0 \tag{2.3}$$

This expression has been formulated under the assumption that the cubic law holds locally and the mechanical aperture varies spatially $b = b(x, y)$. The *LCL* is typically used to numerically approximate the hydraulic behavior of a single fracture.

A fracture with high variation in local apertures or under stress could have a mean aperture $\bar{b}$ considerably different from the local aperture values due to roughness or contact points (Figure 2.1). Therefore, using $\bar{b}$ in equation 2.1 may overestimate the flow rates (Brush & Thomson, 2003; R. W. Zimmerman & Bodvarsson, 1996). Thus, several models exist that calculate an effective parameter referred to as the hydraulic aperture e based on the mechanical aperture $\bar{b}$ (N. Barton et al., 1985; R. Olsson & Barton, 2001; Renshaw, 1995).

On the other hand, for the numerical *LCL*, different criteria have been developed to define b locally (e.g., S. Ge (1997), V. Mourzenko et al. (1995), and Oron and Berkowitz

(1998)), which has derived in modified formulations of the LCL based on local geometrical characteristics. This version is referred to as the *modified local cubic law* (e.g. Mofakham et al. (2018), L. Wang and Cardenas (2016), and Z. Wang et al. (2018)).

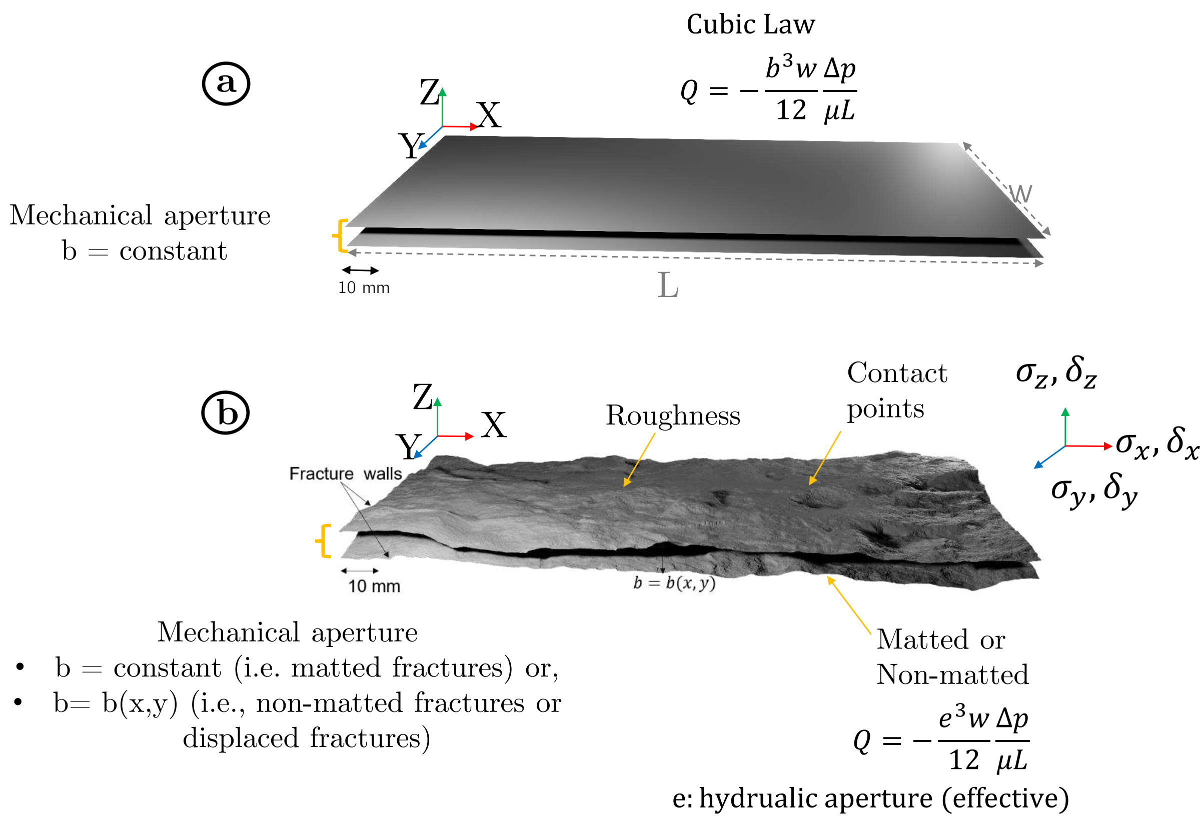

Figure 2.1: Fracture representations. (a) Conceptual and (b) real.

The validity of equation 2.1 to express the hydraulic behavior of a single rough fracture has been a matter of debate from various perspectives (Rutqvist & Stephansson, 2003). On the one hand, its validity has been verified experimentally on different configurations (radial and prismatic) under high normal stress and up to micrometer apertures (Witherspoon et al., 1980) and for different contact ratios (B. Li et al., 2008). On the other hand, other studies have established that such expression does not hold for a rough fracture (Kishida et al., 2013; V. Mourzenko et al., 1995; Nicholl et al., 1999; Pyrak-Nolte et al., 1987), and is invalid for $Re \geq$1-6.8 (Brush & Thomson, 2003; S. H. Lee et al., 2014; Nicholl et al., 1999; R. W. Zimmerman & Yeo, 2000). However, the study of this threshold is a subject of active research, and different criteria have been proposed (see J.-Q. Zhou et al. (2015)). Analogously, the conditions for which equation 2.3 is applicable have been studied (Brush & Thomson, 2003; Oron & Berkowitz, 1998).

To describe potential strong inertia flow regimes in a rough fracture, the empirical Forchheimer equation has been utilized (Y.-F. Chen et al., 2015; Javadi et al., 2014; C. Zhu et al., 2019). In scalar form, this expression is (Nowamooz et al., 2009):

$$|\nabla p| = \frac{\mu_w}{k_f} |\bar{u}| + \rho\beta \left|\bar{u}^2\right| \tag{2.4}$$

Where k_f is fracture permeability and β is the non-Darcy coefficient.

Rough Fracture under Mechanical Displacements In engineering projects, rock deformation may be more frequent than desired. Such deformation may be due to different geomechanical circumstances and could potentially modify the geometrical characteristics of existent fractures. Because of its importance, the hydraulic behavior of a single fracture under mechanical displacement is a broad subject of study.

Experimental studies have employed modifications of equation 2.1 for individual rough fractures under normal stress (Y. Chen et al., 2019; Vogler et al., 2018) and under shear conditions (Cao et al., 2019; Esaki et al., 1991; Koyama et al., 2008; Yeo et al., 1998). In this regard, some researchers have found reasonable estimates employing equation 2.1 without modifications (B. Li et al., 2008).

With respect to numerical modeling, some studies have employed equation 2.3 to investigate scale effects of a sheared single fracture (Koyama et al., 2006; Laura J. & David D., 2016). Meanwhile, some studies have reported good results simulating equation 2.4 for shear displacements up to 4 mm (Javadi et al., 2014; Q. Yin et al., 2017; J. Zhou et al., 2018). Recently, the 3D form of equation 2.2 has been solved for different shear displacements (Mofakham et al., 2018).

2.1.2 Two-phase Immiscible Flow

Parallel-Plates Fracture Whereas single-phase flow behavior in a single fracture is majorly controlled by fracture morphology, hydraulic gradient, and monophasic viscous and inertia forces, two-phase immiscible flow may be additionally driven by phase saturation and capillary pressure (National Research Council, 1996). Fluid wettability may also play a role in both processes but might be more critical for biphasic flow.

Movement of phases across porous media has traditionally been described by coupling Darcy equation (Bear & Cheng, 2010) with the empirical model of relative permeability as follows (Bear, 1988):

$$\begin{cases} \bar{u}_\alpha = -\frac{\bar{\bar{k}}_\alpha}{\mu_\alpha} \left(\nabla p_\alpha - \rho_\alpha \bar{g} \right) \quad \alpha = 1, 2 \\ \bar{\bar{k}}_\alpha = k_{r\alpha} \bar{\bar{k}} \end{cases} \tag{2.5}$$

Where $\bar{u}_\alpha$ is Darcy velocity of a phase α, $\bar{\bar{k}}$ is the absolute permeability tensor, $\bar{\bar{k}}_\alpha$ is the effective permeability tensor and $k_{r\alpha}$ is the relative permeability, which is normally considered an isotropic function of the saturation and does not incorporate pore-scale effects. Popular expressions are the Corey-type models (Corey, 1954; Laliberte et al., 1966) in which relative permeability behaves as a non-linear monotonic function of saturation (Figure 2.2).

Experimental studies on two-phase flow in a single parallel-plates fracture have reported that relative permeability behaves as a linear function of phase saturations (Pan et al., 1996; Romm, 1966). While this linear relationship has traditionally been used in *dual-porosity* reservoirs simulators (Babadagli & Ershaghi, 1992; Saboorian-Jooybari, Hadi, 2016), it might be inadequate (Schiozer & O. Mun̈oz Mazo, 2013). This is not a trivial consideration, as flow in some hydrocarbon reservoirs may be governed by fractures. An investigation has visualized flow structures and observed the cited linear tendency (Alturki et al., 2013). However, others have found deviations from the linear tendency, and strong phase interference has been documented in experiments on transparent parallel plates (C.-Y. Chen et al., 2004; Fourar et al., 1993). These studies visualized flow structures at different non-Darcian regimes. Phase interference can be qualitatively analyzed by comparing results to the expression, $k_{r1} + k_{r2} = 1$ (Pruess & Tsang, 1990).

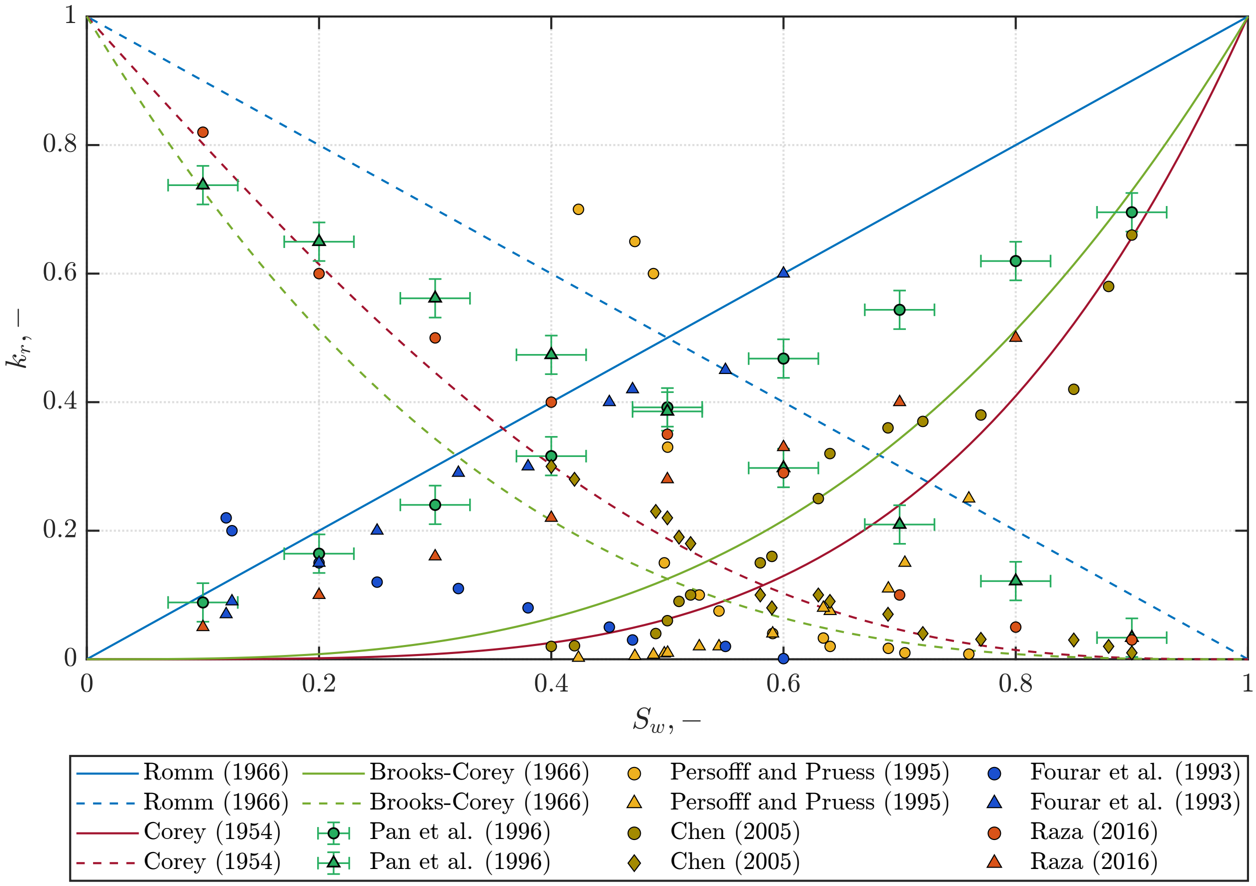

Figure 2.2: Relative permeability models (indicated with lines) and liquid-liquid relative permeability experimental data in fractures (indicated with markers).

Rough Fracture Similarly, as in the single-phase flow section, the ideal parallel-plates approach has been a precursor of more complex morphologies for studies of immiscible two-phase flow studies through rock fractures. The following governing equations could be formulated based on the mass balance equations in a single fracture (Bear et al., 1993) and the porous media equations for immiscible two-phase flow (Z. Chen, 2007):

$$\begin{cases} \frac{\partial(bS_\alpha)}{\partial t} + \nabla \cdot (b\bar{u}_\alpha) = q_\alpha \quad \alpha = 1, 2 \\ \bar{u}_\alpha = \frac{\bar{\bar{k}} k_{r\alpha}}{\mu_\alpha} \nabla (p_\alpha - \rho_\alpha \bar{g}) \end{cases} \tag{2.6}$$

Where S_α is the phase saturation, q_α is a source or sink, and b is the aperture as a scalar field.

Two-phase flow studies on rough transparent replicas have reported a non-linear behavior between relative permeability and saturation and phase interference (Fourar et al., 1993; Persoff & Pruess, 1995). While it has been suggested that relative permeability in fractures behaves similarly as in porous media (Ambusso et al., 1996; Pieters & Graves, 1994), contrary postures exist (C.-Y. Chen & Horne, 2006; Persoff & Pruess, 1995). On the other hand, recent results supported the linear relationship between relative permeability and saturation (Watanabe et al., 2015) while a different experimental study indicated that relative permeability is related to flow regime (Radilla et al., 2013).

On the other hand, it has been documented that local variations in fracture aperture can modify capillary effects and phase distribution in the direction of flow along a rough fracture (Pruess & Tsang, 1990). Surface roughness effects can induce preferential flow paths for a single phase (C.-Y. Chen & Horne, 2006). Fractals analysis has been implemented to investigate flow regimes dominance and assess capillary or viscous fingering (Y.-F. Chen et al., 2017, 2018; L. Cheng et al., 2019).

Rough Fracture with Mechanical Displacements Experimental results on parallel-plates fractures evidenced the need for more data with respect to the link between fracture aperture and relative permeability (Alturki et al., 2013). Fractal methods have been used to estimate topographic parameters and correlate them to, fluid displacement results, and shear displacements (Raimbay et al., 2017). Other studies have focused on investigating the effect of stress on fracture relative permeability (Huo & Benson, 2016; Lian & Cheng, 2012; A. E. McDonald et al., 1991).

2.2 3D Printing to Study Flow in Porous Media

A technology that is transforming industrial manufacturing and medical sciences is additive manufacturing (AM) or 3D printing. It is a process that consists of creating an object by adding material layer by layer. 3D printers can now produce complex geometries from a computer aided design (CAD) (Taufik & Jain, 2013). In geosciences, this method is opening new alternatives to characterize porous media and their properties (Head & Vanorio, 2016; Kong et al., 2018). In the area of rock mechanics, research has shown that comparing the properties of 3D-printed rocks to natural rocks can help better understand the effects of the sample size on elasticity and failure mode (Kong. et al., 2017). In addition, a comparison of mechanical properties of 3D-printed and natural rocks suggested that attaining rock-like material and achieving heterogeneity contributes to synthetic rocks replicating the behavior of natural rocks (C. Jiang & Zhao, 2015).

In the area of fluids flow across porous media, recent work has been conducted to investigate single-phase flow in a 3D-printed microfluidic chip (Watson et al., 2019). Furthermore, 3D-printed models have been used to create fracture networks and study flow through them with promising results on validating experimental measurements (Suzuki et al., 2019). Meanwhile, the advantages of 3D printing are been tested to study the effects of shear during single-phase flow on a single fracture (Fang et al., 2019; Ishibashi et al., 2020; J. Xie et al., 2020; P. Yin et al., 2020).

The technologies of 3D printing have been cataloged in seven different categories (American Society for Testing and Materials, 2022). The polymerization of ink-jetted material (PolyJet) has gained attention from scientists due to its promising potential in multiple research areas (Gibson et al., 2021). This technology has been tested to represent cement (Ju, Wang, Xie, Ma, Mao, et al., 2017), visualize stress fields (L. Wang et al., 2017), and reproduce the geomorphology of sandstone pore networks (Ishutov et al., 2015). On the other hand, the limitations of ink-jet 3D printing towards replicating natural rock have also been documented (Ishutov et al., 2018). One of the identified challenges is the post-treatment of porous samples with complex networks of minuscule pores (Hasiuk et al., 2018). In practical terms, this issue refers to removing a wax-type material —whose function is to provide support and stability to prototypes while being 3D printed— from internal micron-scale interconnected cavities. To overcome this issue, research targeting to represent rock features through ink-jet AM is using chemical methods to remove such material (Suzuki et al., 2017).

2.3 Description of Rock Fracture Roughness

Fracture roughness is usually decomposed into two conceptual scales: primary (large-scale waviness) and secondary (small-scale unevenness) roughness (Zou et al., 2015). However, due to its intricate nature, various methodologies are available for quantifying the properties of fracture walls. Some authors have employed empirical expressions (N. Barton, 1973; Witherspoon et al., 1980), statistical parameters (Auradou, 2009; Y.-F. Chen et al., 2015; V. V. Mourzenko et al., 2018; Tsang & Witherspoon, 1981) and fractals methods (Babadagli, 2020; Brown, 1987; Crandall et al., 2010; J. Li et al., 2018; Oron & Berkowitz, 1998; Zheng et al., 2020). The characteristics of any surface can be classified into the following groups: roughness (amplitude and frequency or slope variability), statistical distribution, and fractal properties (Bhushan, 2000). Statistical parameters typically describe the first two categories, while fractal approaches represent the complexity (Zelinka et al., 2013).

Frequently, studies characterize fracture walls through only one of these approaches, which could lead to an incomplete description of all facets of fracture roughness, thereby hindering a comprehensive analysis of results. Additionally, a partial description of fracture roughness may not allow for the reconstruction of fracture topography through fracture generation methods, which provide control over various texture properties and could be instrumental in studying scale effects.

Each method to characterize fracture roughness has its advantages and shortcomings. For instance, statistical parameters are relatively easy to implement; however, they frequently show a scale effect (P. Kulatilake et al., 1995) which is a feature that could prevent upscaling of results. These characteristics are also shared by the empirical joint roughness coefficient (JRC) parameter (N. Barton & Choubey, 1977). This coefficient is regularly estimated through experimental models based on a single statistical property (Y. Li & Zhang, 2015; Z. Y. Yang et al., 2001). However, the application of these models is limited to a short range, and the estimated JRC values might be biased by the selected model, reflecting the statistical property behavior rather than the overall fracture roughness.

Fractal techniques, despite being widely used in the scientific community, are not considered standardized surface measurements. For instance, they are not included in recognized standards (International Organization for Standardization, 2021), and some suggest that methodological differences between fractal-based approaches make them inadequate for roughness description (Charkaluk et al., 1998). On the other hand, some indicate that they are quantitatively unreliable (Wen & Sinding-Larsen, 1997) and the values obtained from different fractal methods are not comparable (H. Xie & Wang, 1999) or they are comparable within a narrow range (Gallant et al., 1994). Additionally, implementing them requires several considerations to be resolved beforehand (Magsipoc et al., 2020; Tate, 1998).

A fractal dimension is a scale-independent parameter that describes how a component of a smaller size fills a higher dimension object (Mandelbrot & Blumen, 1989). Fractal geometry enables inferring the characteristics of an unobserved scale based on properties identified at a different scale (Kwafniewski & Wang, 1997). There are self-similar and self-affine fractals. The former are patterns that are equal at different scales, and the latter are similar when scaled anisotropically (Dershowitz et al., 1992). Thus, geologic features such as fault surfaces and fracture topography can be considered to have a self-affine character (C. C. Barton & La Pointe, 1995).

Fractal-based methods have been suggested to be superior (Y. Ge et al., 2014) because they can provide scale independence if a certain distance threshold is surpassed (Fardin et al., 2001), employing them in conjunction with other methods is a convenient approach to correctly characterize fracture topography (Piggott, 1990). This is because the fractal dimension can be considered a measure of complexity, while other statistical parameters describe attributes such as amplitude and spatial variation (Zelinka et al., 2013), or a combination of these parameters (Y. Ge et al., 2014). In accordance with this approach, some studies have investigated the relationship between fractal dimension and other descriptors (e.g., Ishibashi et al. (2020), Odling (1994), and Vogler et al. (2017)). Consequently, in this study, besides the fractal dimension obtained from the variogram method, multiple statistical parameters were calculated to provide a complete description of the fracture roughness.

Chapter 3

Importance of Improving Support Material Removal from PolyJet 3D-Printed Porous Models

S. Lopez-Saavedra, G. Zambrano-Narvaez, S. Ishutov and R. Chalaturnyk (manuscript published in the proceedings of the European Conference on the Mathematics of Geological Reservoirs, ECMOR XVII, 2020; https://doi.org/10.3997/2214-4609.202035210).

3.1 Overview

The use of 3D printing technology to study physical processes that occur in subsurface porous media is rapidly gaining ground. However, the removal of support material from 3D-printed prototypes represents an obstacle to using such models in laboratory experiments. This study addresses some of the effects of improving the removal of support material from 3D-printed prototypes and some of the implications of using these enhanced models in investigations of flow through fractures. Two groups of porous models were manufactured using a PolyJet 3D printer: 1) cylindrical pore throat samples and 2) porous models with fractures. Two types of post-processing methods were also tested: 1) a chemical method and 2) a chemical-mechanical method. A Darcy flow experiment was used to measure absolute permeability in the second group. The experimental results helped correlate the test time with the amount of support material removed and revealed the need to better estimate the injection pressure required to remove support material from 3D-printed porous models. The permeability measurement was compared with analytical calculations. The results of the post-treatment methods highlight the importance of using flushed 3D printed samples when studying physical processes occurring in porous media.

3.2 Introduction

A technology that is transforming industrial manufacturing and medical sciences is AM or 3D printing. It is a process that consists of creating an object by layering the material. 3D printers can now produce complex geometries from a CAD (Taufik & Jain, 2013).

In geosciences, this method is opening up new alternatives to characterize porous media and their properties (Head & Vanorio, 2016; Kong et al., 2018). In the area of rock mechanics, research has shown that comparing the properties of 3D-printed rocks to natural rocks can help better understand the effects of the sample size on elasticity and failure mode (Kong. et al., 2017). Furthermore, comparison of the mechanical properties of 3D-printed and natural rocks suggests that attaining rock-like material and the achievement of heterogeneity contribute to synthetic rocks replicating the behavior of natural rocks (C. Jiang & Zhao, 2015).

In the area of fluid flow across porous media, recent work has been conducted to investigate single-phase flow on a 3D-printed microfluidic chip (Watson et al., 2019). Furthermore, 3D-printed models have been used to create fracture networks, and study flow through them with promising results on validating experimental measurements (Suzuki et al., 2019).

The technologies of 3D printing have been cataloged in seven different categories (American Society for Testing and Materials, 2022). Polymerization of ink-jetted material (PolyJet) has gained attention from scientists due to its promising potential in multiple research areas (Gibson et al., 2021). This technology has been tested to represent cement (Ju, Wang, Xie, Ma, Mao, et al., 2017), visualize stress fields (L. Wang et al., 2017), and reproduce the geomorphology of the sandstone pore networks (Ishutov et al., 2015). On the other hand, the limitations of ink-jet 3D printing to replicate natural rock have also been documented (Ishutov et al., 2018). One of the identified challenges is the post-treatment of porous samples with complex networks of minuscule pores (Hasiuk et al., 2018). In practical terms, this issue refers to the removal of wax–type material, whose function is to provide support and stability to prototypes while being 3D-printed, from interconnected internal micron–scale cavities. To overcome this problem, research targeting the representation of rock features using inkjet AM is using chemical methods to remove such material (Suzuki et al., 2017).

Therefore, in order to use 3D-printed porous models to characterize rock structures and understand the flow processes of porous media, removal of support material should be further examined. Therefore, the objective of this study was to evaluate methodologies for better removal of support material from porous samples 3D-printed in polymer, quantify their effectiveness and time efficiency, and assess the results of using these post-treated models in investigations of flow through fractures.

3.3 Experimental Methodology

3.3.1 Samples Design

3D geometric shapes such as spheres, cylinders, and parallel plates, have been used routinely to represent rock pore systems (Graton & Fraser, 1935; Sutera & Skalak, 1993). Consequently, they have recently been used to 3D print porous models (Hasiuk et al., 2018). The digital models of porous samples in this study were created using Inventor CAD and Meshmixer mesh generation software. Two groups of samples were chosen to investigate the removal of support material from 3D-printed rock analogs (Figure 3.1). Both geometries were embedded in cylindrical shapes of 26.4 mm in diameter and 25.4 mm in height as follows:

- Group 1 (G1): Cylindrical pore throats, 1 mm in diameter, aligned along the vertical axis of the model.
- Group 2 (G2): Cylindrical sample with spherical grains, 2 mm in diameter, packed cubically with a partial overlap of 0.2 mm. Random fractures of 0.3 mm in width and one vug of $\sim$2.3 mm in width were created with the computer graphics software Blender utilizing the Voronoi algorithm. A 1-mm porous cladding was placed around the perimeter of the samples to keep the unity of the sample.

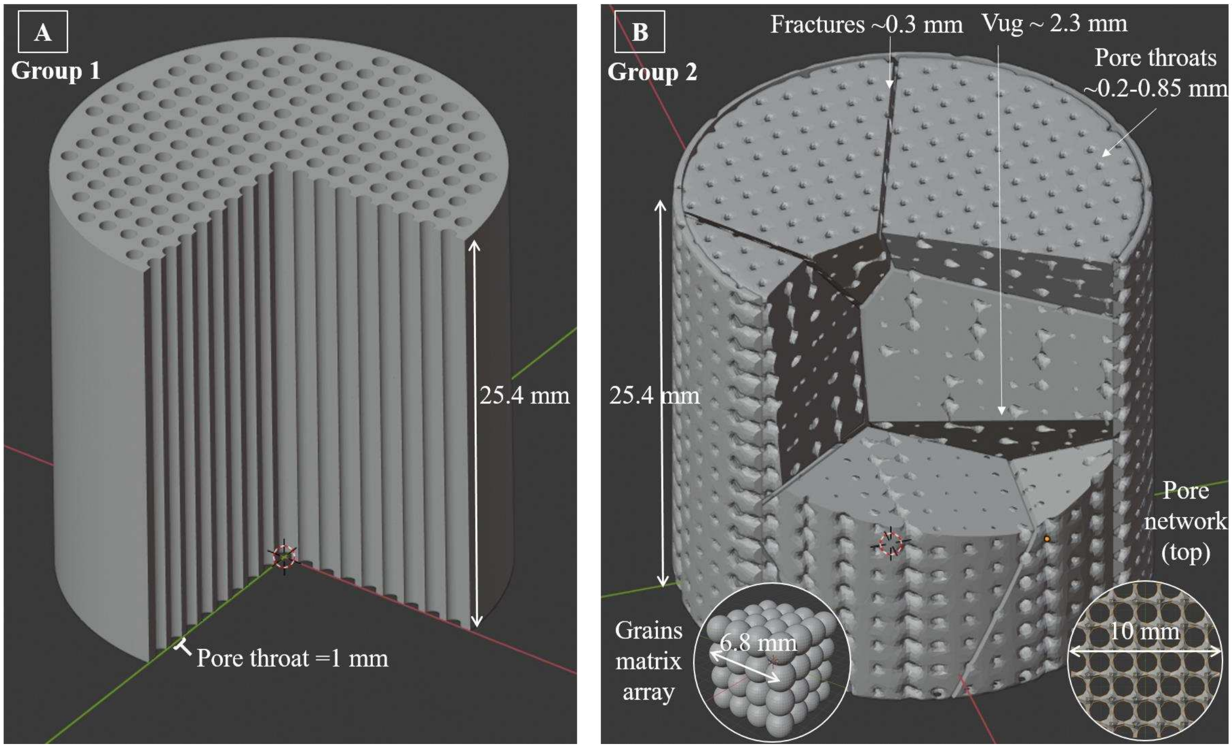

Figure 3.1: CAD Design of digital models. (a) G1 cylindrical pore throats. (b) G2 porous model with fractures.

To investigate the removal of support material, six samples were 3D-printed per group in order to have twelve samples. For each group, three samples were post-processed with Method 1 (M1) and the remaining three with Method 2 (M2). This was done to verify the repeatability of the experiment. A description of these methods is presented later in this document. Subsequently, an absolute permeability test was performed on a G2 sample (Table 3.1).

Group	No. Samples	Labels	Post-treatment method	Permeability measurement
1	3	1T, 2T, 3T	1	-
	3	1E, 2E, 3E	2	-
2	3	F1, F2, F3	1	-
	3	F1E, F2E, F3E	2	F3E
	12			

Table 3.1: Laboratory experiments conducted on samples.

During the design process, each group of models was digitally characterized to obtain geometric and petrophysical properties (Table 3.2).

Group	Diameter, mm	Matrix volume, mm	Pore volume, mm	Porosity, %	Fracture/ Vugular porosity, %	Pore-throats sizes, mm
1	26.4	9.67	4.23	30.43	-	1
2	26.4	11.48	2.42	17.41	3.93	∼0.3 –2.3

Table 3.2: Digital model characteristics. The specimen height was 25.4 mm.

3.3.2 3D Printing

The samples were produced using a Stratasys Eden 260 VS 3D printer at the Reservoir Geomechanics Research Group at the University of Alberta. The principle of this machine is to use nozzles to jet layers of two types of liquid photo-polymers on a build platform, which are solidified layer by layer, through ultraviolet (UV) light (Gibson et al., 2021). Each photo-polymer has a different purpose: the one referred to as *model material* solidifies to a rigid material, which is the 3D-printed physical model. Meanwhile, the *support material* cures into a wax-like material to provide support in spaces or fragile geometries within the model. Hence, the support material must be removed after the printing process is complete. The manufacturer's specifications indicate that the 3D printer has an XY resolution of 42 μm per dot and a minimum layer thickness of 16 μm per layer. The manufacturer reports a polymerized density of 1.18 – 1.19 g/cm^3 at ambient temperature and a water absorption of 1.1-1.5%.

For this study, we used VeroClear model material with a matte finish (a coating layer that covers the samples after 3D printing) and a water-soluble SUP707 support material. The advantages of this combination are that it allows high-quality printing (theoretical 16 μm resolution), visual inspection of porous translucid samples, dissolution of support material in tortuous samples, and, avoiding clogging of the nozzles by adhering to the manufacturer's best printing practices. The printing orientation was vertical (Figure 3.2).

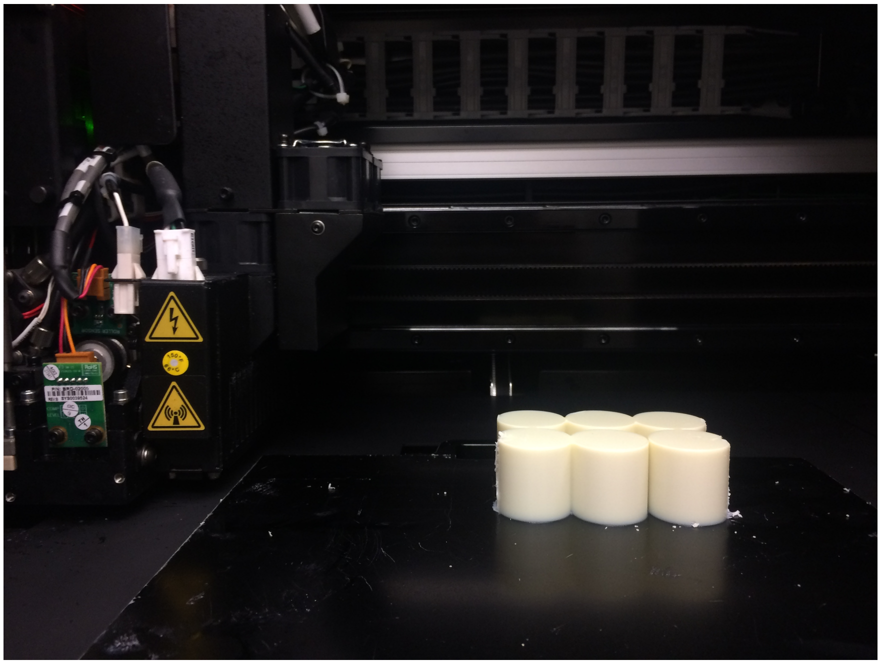

Figure 3.2: G1 specimens on the metallic build platform after 3D printing.

3.3.3 Post-processing

The samples were removed from the tray, ensuring that most of the support material remained in each sample except for a bottom layer of $\sim$ 2 mm that was cleaned from all samples. Subsequently, the samples were weighed and measured. These measurements facilitated mass balance calculations to estimate the mass of cured model material and support material within samples.

The samples were submerged in water for four hours to dissolve the support material from the external surfaces and some internal pores (Figure 3.3). Subsequently, two cleaning methodologies were applied to each group of samples. The motivation to test different post-treatment methods was to assess which could better remove the support material from 3D-printed porous samples in a time-efficient manner while preserving the integrity of the samples. This workflow could be used for future flow experiments in porous media on 3D-printed models. The methods were as follows:

- M1: immersion of the samples in agitated water baths with caustic soda (NaOH), mass concentration of $\sim$1% in a clean station DT3 for cycles of 4 and 8 at a temperature of 32-47°C. Models were weighed after drying with fluorescent light for 12-16 hours.

- M2: Submerge the samples in water with NaOH, the mass concentration of $\sim$2%, placed on a hot plate magnetic stirrer for a cycle of 8 hours at a temperature of 60-

65°C and agitated at 220-300 RPM. As a final cleaning stage, pressurized water was axially jetted to unplug the pore throats and thus reduce the clean-up time to remove the support material inside the samples. G1 samples were flushed with a Balco high-pressure water cleaner (7 MPa) for ∼13 minutes. G2 samples were flushed into a cylindrical cell (50-350 kPa) designed for this purpose for ∼20 minutes. Models were weighed after drying with fluorescent light for 12-16 hours.

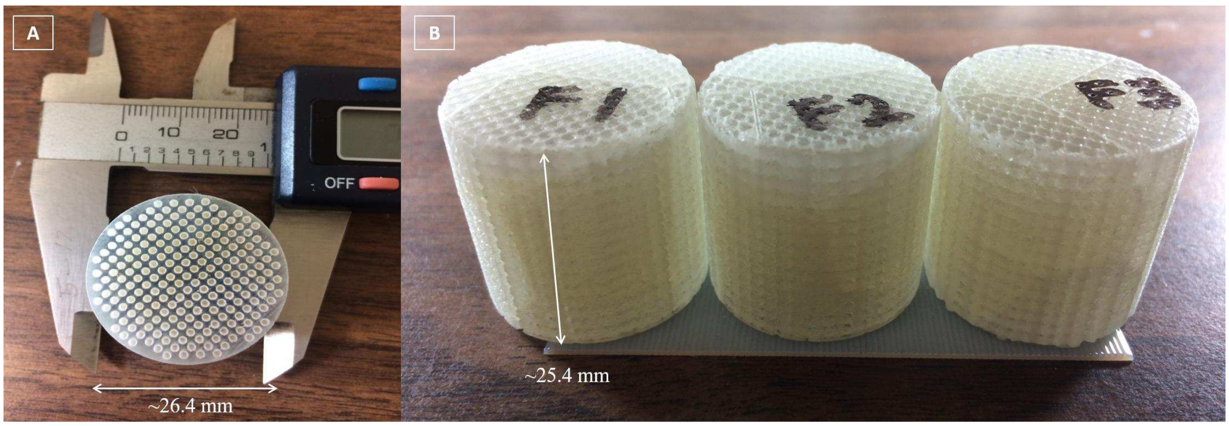

Figure 3.3: 3D-printed models during M1 post-processing. (a) G1 sample. (b) G2 samples.

3.3.4 Darcy flow experiment

A cell was designed for M2 to remove the support material from the cylindrical samples and was subsequently used to perform an absolute permeability test on the F3E sample (Figure 3.4). A core holder (sleeve) was 3D-printed in VeroClear material to adjust the experiment to the dimensions of the sample. The specimens were sealed to the core holder through an o-ring seated in a groove inside the sleeve. In addition, the seal with the core holder was tested with a solid, non-porous sample. After flushing, steady-state permeability tests at constant pressure differences of 40, 26, 17 kPa were conducted. A porous stone and diffuser arrangement was used at the inlet and outlet to achieve homogeneous injection. The sample was saturated in water for approximately an hour prior to the experiment. The discharged water volume was used to estimate the flow rate. Re was estimated using the following expression (Dwivedi & Upadhyay, 1977):

$$Re = \frac{q\rho d}{A\mu\,(1-\phi)} \tag{3.1}$$

Where q is the flow rate, ρ is the fluid density, d is the grain size diameter ($\sim$ 1.6 mm for the sample F3E), A is the cross-sectional area, μ is the dynamic viscosity of the water and ϕ is porosity. The values obtained with Equation 3.1 were Re<10.

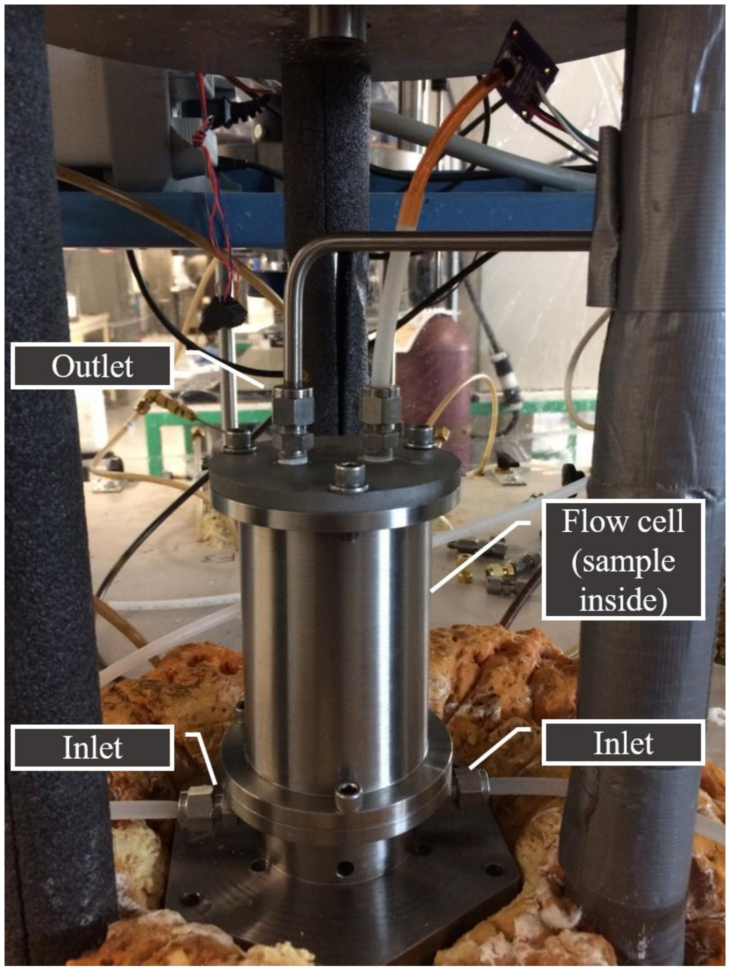

Figure 3.4: Designed cell for flushing samples and measuring absolute permeability.

In addition, a linear relationship between pressure differences and flow rates indicated steady-state laminar flow. Consequently, the Darcy equation expressed as follows (Bear & Cheng, 2010) was used to estimate permeability:

$$q = -\frac{kA}{\mu L}(\Delta P) \tag{3.2}$$

Where k is the absolute permeability, L is the length of the medium and ΔP is the pressure drop. The slope m of a plot Δ P vs. q was used to estimate the permeability as follows: $k = \frac{\mu L}{mA}$.

3.3.5 Analytical permeability calculation

The Kozeny-Carman equation (Kaviany, 1995) was used in this calculation:

$$k = \frac{\phi^3}{36\kappa_c\left(1-\phi\right)^2 d_m^2} \tag{3.3}$$

Here d_m is the mean particle diameter and κ_c is the Kozeny constant.

3.4 Results

3.4.1 Properties of samples and visual inspection

After post-processing, the dimensions and weights of all samples were recorded (Table 3.3 and Table 3.4). Samples F1E and F2E from G2 broke when flushed.

Sample	Height, mm	Diameter, mm	Sample Weight, g
1T	25.34	26.34	13.89
2T	25.33	26.32	13.89
3T	25.34	26.32	13.99
Average	25.34	26.33	13.92
SD	0.005	0.009	0.047
1E	25.31	26.16	11.31
2E	25.36	26.25	11.02
3E	25.46	26.33	11.28
Average	25.38	26.25	11.2
SD	0.062	0.069	0.13

Table 3.3: Measurements of 3D-printed samples G1 and weights after post-processing.

Sample	Height, mm	Diameter, mm	Sample Weight, g
F1	25.43	26.34	14.55
F2	25.43	26.35	14.55
F3	25.42	26.36	14.56
Average	25.43	26.35	14.55
SD	0.005	0.008	0.005
F1E	25.24	26.26	13.3
F2E	25.25	26.23	13.43
F3E	25.41	26.25	13.57
Average	25.3	26.25	13.43
SD	0.078	0.012	0.11

Table 3.4: Measurements of 3D-printed samples G2 and weights after post-processing.

3.4.2 Post-processing results

The support material removed with respect to post-processing time for both methods was estimated on the basis of mass balance calculations. For G1, samples post-processed with M1 showed an average 48% support material mass after 32 hours of clean-up. The samples post-processed with M2 indicated no internal support material after 20.2 hours (Figure 3.5).

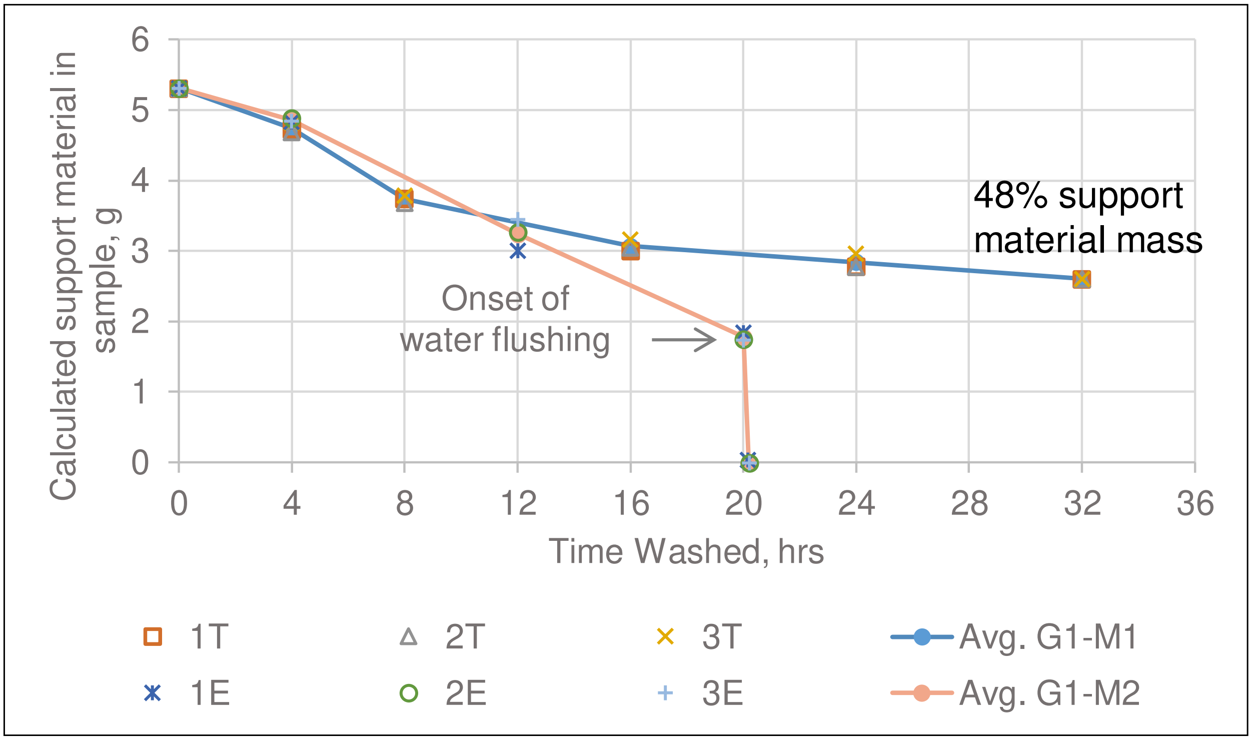

Figure 3.5: Removal of support material — G1.

For G2, the samples post-processed with M1 showed an average of 33% of the mass of the support material after 32 hours of clean-up. Meanwhile, the weights of the G2 samples indicated that there was no internal support material after 20.33 hours (Figure 3.6).

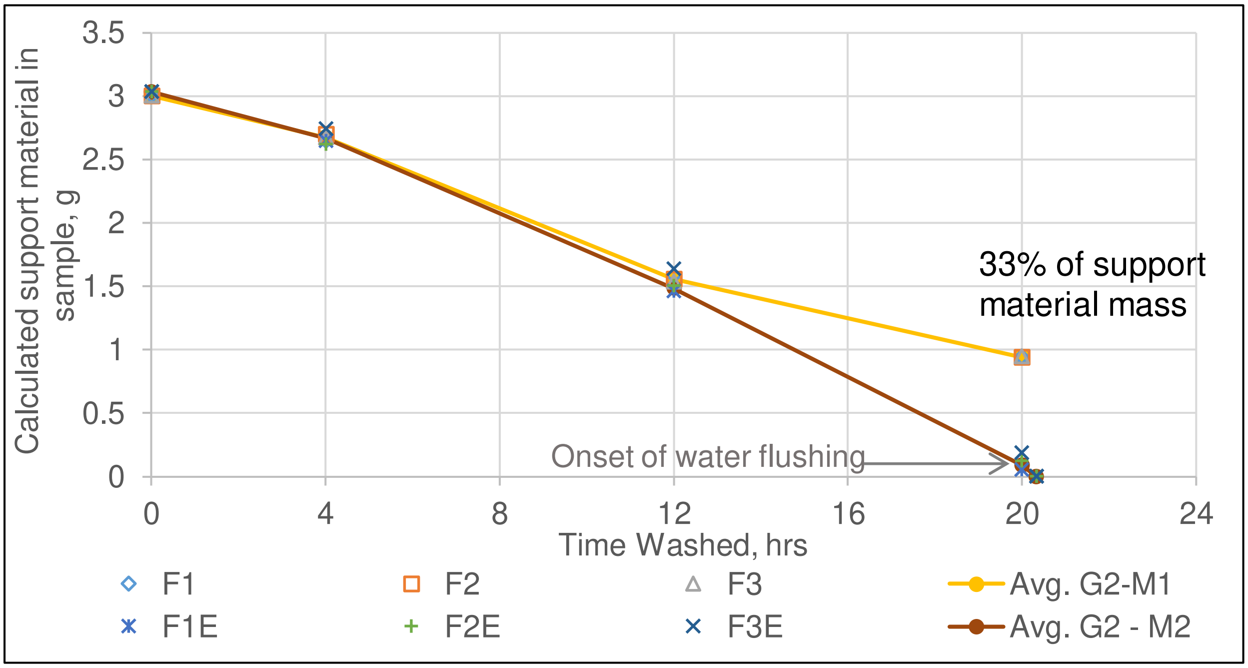

Figure 3.6: Removal of support material — G2.

3.4.3 Experimental and analytical permeability

The absolute permeability measured for sample F3E was estimated using the equation 3.2, and a value of 7.70·10-13 m2 was obtained.

The design parameters of grain size - d_m ≈1.6 mm and porosity - ϕ = 0.1741 were used for analytical calculations. Then the Kozeny constant κ_c=5 was considered as it was in agreement with the experimental data of the packed beds (Bear, 1972): Consequently, the calculated permeability using equation 3.3 was $k = 1.10 \times 10^{-10}\ m^2$.

On the other hand, a second analytical calculation was conducted with equation 3.3 to estimate the Kozeny constant from the experimental permeability measurement. The obtained value was κ_c=714.

3.5 Discussion

3.5.1 Dimensions and samples geometry

G1 and G2 samples showed height and diameter values below the designed properties. For G1 samples cleaned with M2, the average differences in height and diameter were 20 μm and 150 μm, respectively. For G2 samples cleaned with M2, these differences were 100 μm and 150 μm, respectively. However, these values are consistent with the manufacturer's accuracy specifications.

The estimated theoretical model masses at room temperature after 3D printing were between 11.41 g and 11.51 g for G1 and between 13.55 g and 13.67 g for G2. G1 samples cleaned with M2 showed an average weight of 11.2 g after post-processing, and G2 samples 13.43 g. The mass measurements for the first group might be lower than the theoretical calculations due to post-processing effects (Verhaagen et al., 2016). Regarding G2, two samples (that is, F1E and F2E) detached during post-treatment. Consequently, the average weight was below theoretical as a result of post-treatment and mechanical alteration of two samples.

3.5.2 Post-processing

G1 samples cleaned with M2 showed a non-uniform clean-up front. The peripheral pore throats showed better chemical dissolution than the centered pore throats. This was qualitatively assessed when water was jetted through the samples with Balco unit; due to the amount of support material, the centered pores required water jetting for longer periods. On the other hand, G2 samples had shorter clean-up times. This phenomenon was attributed to the better connectivity of the pore throats, as these samples had non-zero horizontal permeability.

In general, M2 showed better results in removing the support material. The combination of higher caustic soda concentration, higher water temperature, and agitation improved the chemical dissolution of the support material and resulted in shorter post-processing times (Figure 3.5 and Figure 3.6). Additionally, applying water flushing when samples had internal flow paths opened accelerated the clean-up rate. However, the G2 samples that detached might have become more brittle due to submersion in a caustic soda solution (Safka et al., 2016). In addition, the samples' weights from both methods showed low statistical variation but both group samples weighed lower than theoretical measurements. Weight and size reduction has been reported when post-processing samples with NaOH (Verhaagen et al., 2016). For G2 samples, weight loss could have masked the removal of residual support material.

3.5.3 Experimental permeability and analytical calculation

For sample F3E, the experimental estimate was discrepant with the computed value. One potential explanation for this is that due to its morphological characteristics, specimen F3E might have considerable deviations from the designed model. On the other hand, residual support material could be present in the sample pores. Therefore, future studies will include computer tomography (CT) scanning to obtain petrophysical measurements and will evaluate the removal of support material. However, the presence of fractures could be better incorporated into the analytical computation. Nonetheless, 3D printing has significant potential for investigation of fractured media.

3.6 Conclusions

This study investigated two post-treatment methods to improve the removal of support material from 3D-printed porous samples and some of the implications of using enhanced models in flow experiments.

The post-treatment methods suggested that the combination of chemical dissolution and water-jetting can accelerate the removal of support material from porous prototypes with different morphologies. However, the internal geometry plays an important role in selecting the appropriate pressure for mechanical removal. Therefore, challenges in this approach include developing ways to estimate the appropriate pressure of the water jet per sample. Before conducting flow experiments on 3D-printed samples, tracking the removal of support material can help minimize cleaning time and preserve the integrity of the samples. However, post-treatment NaOH weight loss can mask the removal of residual support material. In addition, flow experiments on 3D-printed porous samples can help minimize the redundancy of experimental tests. The experimental permeability showed a discrepancy with the analytical calculation. This calculation was reconciled by calculating the Kozeny constant from the experimental permeability measurement.

In future studies, CT scanning and helium porosity will be incorporated to better measure the effectiveness of post-treatment methodologies on the petrophysical properties of the samples. They will be coupled with numerical simulation for validation of flow experiments.

3.7 Acknowledgments

The authors are grateful for the financial support of the CONACyT-SENER -Hidrocarburos Sector Fund and the University of Alberta.

Chapter 4

Assessment on the Impact of Local Pressure Measurements on Hydraulic Properties of Individual 3D-Printed Fractures

S. Lopez-Saavedra, G. Zambrano-Narvaez, S. Ishutov and R. Chalaturnyk (a version of this manuscript will be submitted for publication).

4.1 Overview

The hydraulic aperture is a property used to express the hydraulic conductivity of individual fractures. Numerous single-phase flow experimental studies tend to estimate this parameter using the fluid pressure drop measured externally to the fracture specimens. The impact of this fundamental methodological consideration on the estimation of the hydraulic aperture is not clear. Using PolyJet 3D printing and fiber optic pressure sensors, this study examines the impact of this consideration using an experimental and computational investigation of the effects of local pressures on the estimation of the hydraulic aperture.

Experiments were conducted on synthetic fractures of different roughness at different shear displacements perpendicular to flow. Local aperture maps were compared with digital fractures, and variation in experimental maps was assessed through basic statistical coefficients. The hydraulic apertures were calculated using both local pressure measurements and external measurements. Using local pressures reduced the deviation from the mechanical apertures, while employing external pressure values underestimated the hydraulic apertures. The theoretical hydraulic aperture values, estimated from analytic cubic law models, closely matched the hydraulic apertures calculated from local pressure measurements.

OpenFOAM software was used to numerically estimate the average pressure profiles from local cubic law models and the 3D incompressible *NS* equations. These results were compared to the experimental local pressure data. Average local pressure drops at different shear displacements were more consistent with all types of numerical simulations, indicating that local pressure measurements provided a more accurate representation of the actual pressure in the fractures studied compared to external pressure measurements.

4.2 Introduction

Rock fractures can play a preponderant role in recovering fluids from a reservoir. Given the complexity of flow behavior in a fracture network, understanding flow on a single fracture scale is a stepping stone to larger-scale projects (J. Xie et al., 2020; R. W. Zimmerman & Yeo, 2000). The classic approach to modeling flow through a rock discontinuity is using the equation known as the *CL* (R. Olsson & Barton, 2001), which is defined as (Bear, 1988; Huitt, 1956; Snow, 1965):

$$Q = -\frac{b_{||}^3 w \Delta p}{12 \mu_w L} \tag{4.1}$$

This expression constitutes an analytic solution to the incompressible *NS* equations for a system of one-dimensional parallel plates. The plates have a constant separation denoted as $b_{||}$ between them, and the fluid flows at a steady state, dominated by pressure and viscous forces. In this equation, Q is the volumetric rate of water, w is the width of the fracture, μ_w is the viscosity of the water, L is the length of the fracture, and Δp is the pressure drop between the inlet and the outlet. The *CL* considers that the change in pressure is linearly proportional to the volumetric flow rate (Tsang & Witherspoon, 1981). Hence, it is analogous to Darcy's equation for flow in porous media (Witherspoon et al., 1980; R. Zimmerman & Main, 2004).

The validity of the *CL* for an individual rock fracture has been a matter of discussion due to hydraulic and geomechanical factors. Fractures roughness (Brown, 1987), contact areas due to normal and shear stresses (Esaki et al., 1999; B. Li et al., 2008), normal and shear displacements (Auradou et al., 2005; Javadi et al., 2014; Koyama et al., 2008), hydraulic gradient (B. Li et al., 2016), and flow regime conditions (Xiong et al., 2011) have been identified to alter the accuracy or applicability of the *CL* model.

In laboratory experiments conducted under low inertia flow regimes, an approach is to input the flow and pressure data into the *CL* expression to calculate an effective coefficient referred to as the hydraulic aperture e (Rutqvist & Stephansson, 2003). This parameter is commonly used to express the hydraulic conductivity of a fracture. Experimental observations (Durham & Bonner, 1994; Hakami & Larsson, 1996) have shown that it deviates from the parallel-plates aperture.

A methodological consideration in laboratory measurements that is often overlooked when utilizing the CL is the approximation of the overall pressure drop across a single fracture. Due to experimental difficulties, a major number of laboratory configurations measure the pressure across a single fracture externally, rather than across the specimen. Some articles examining fluid flow through a fracture under normal stresses have employed an external upstream pressure reading and no outlet measurement (Develi & Babadagli, 2015; Vogler et al., 2018; Witherspoon et al., 1980).

The implication of this configuration is that the outflow pressure might be larger than the atmospheric pressure, which can lead to an overestimation of the differential pressure. Investigations using confinement stress conditions have used external upstream and downstream pressure sensors (Y.-F. Chen et al., 2015; Y. Chen et al., 2019; Phillips et al., 2021; Ranjith & Darlington, 2007). Studies including normal and shear stress have used a constant head pressure reservoir reading and no downstream sensor (Cao et al., 2019; Esaki et al., 1991; H. Lee & Cho, 2002), external differential transducers (Javadi et al., 2014; Koyama et al., 2008; B. Li et al., 2008; Xiong et al., 2011), external upstream and downstream sensors (Ahola et al., 1996; Z. Chen et al., 2000; Giger et al., 2011; Sharifzadeh et al., 2017), an external inflow sensor and no outlet reading (Crandall et al., 2017; Esaki et al., 1999; Hans & Boulon, 2003; Ishibashi et al., 2020; Mofakham et al., 2018; R. Olsson & Barton, 2001; Q. Yin et al., 2017). Only a few studies included local pressure sensors (Gale et al., 2001; Ji et al., 2020). However, the hydraulic conductivity of the fractures used was not reported. To the authors' knowledge, only Yeo et al. (1998) and Cunningham et al. (2020) have used local pressure measurements to estimate the hydraulic aperture. In the former study, the samples underwent normal stress and shear displacements; however, no measurement of the deviation magnitude was provided concerning the upstream and downstream values. Other analyzes have not been explicit about the location of their pressure transducers, and it is speculated that these were collected externally (Boulon et al., 2002; Boulon et al., 1993; Durham & Bonner, 1994; Hakami & Larsson, 1996; W. Olsson & Brown, 1993; W. A. Olsson, 1992; Ranjith & Viete, 2011; J.-Q. Zhou et al., 2015).

Investigations on single- and multiphase flow in fixed aperture fractures have measured pressure drop outside the sample (Persoff & Pruess, 1995), and some have incorporated single local measurements (Radilla et al., 2013) or in-line local measurements (C.-Y. Chen & Horne, 2006; C.-Y. Chen et al., 2004; Diomampo et al., 2001; Fourar et al., 1993; Nowamooz et al., 2009; Pan et al., 1996; Speyer et al., 2007). However, if the pressure values change directionally, in-line local measurements might not capture such variation.

Clearly, local pressure measurements are not commonly used in experimental studies on single-phase flow through individual joints. However, this study reports on their relevance to better estimate the hydraulic conductivity of fractures.

Local pressure measurements are important because, at the scale of a single fracture, heterogeneous local pressure values may appear (Yeo et al., 1998). This implies that even under low inertia conditions, the geomechanical state of a fracture can induce pressure fluctuations that lead to sectorial pressure values deviating from a linear pressure gradient (Cunningham et al., 2020), or to a non-uniform pressure distribution and zonal variations in flow velocity. Nevertheless, local pressure measurements should reflect the actual pressure drop across a fracture specimen, providing a better representation of its hydraulic behavior.

The use of 3D printing in experimental scientific projects has become more frequent due to its versatility in various areas. For example, this technology has been used to investigate the petrophysical properties of porous media (Head & Vanorio, 2016; Ishutov et al., 2015; Kong et al., 2018), as well as to analyze the mechanical properties of intact and fractured samples (Ju, Wang, Xie, Ma, Mao, et al., 2017; Ju, Wang, Xie, Ma, Zheng, & Mao, 2017; Liu et al., 2020; L. Wang et al., 2017; J. Zhu et al., 2018).

PolyJet 3D printing has shown potential in studies related to flow through fractures, offering several distinct advantages compared to other sample generation methods or materials. For example, it can be used to obtain control over fracture morphology (Suzuki et al., 2017), reproduce digital models with high precision (Fang et al., 2018), attain sample repeatability (Ishibashi et al., 2020), and visualize experiments (W. Yang et al., 2020). Due to these advantages, this type of 3D printing has been used to experimentally evaluate fracture network permeability (Suzuki et al., 2019), investigate flow anisotropy (J. Xie et al., 2020) and non-linear flow effects (P. Yin et al., 2020; Y. Zhang et al., 2022). However, no investigations have been conducted to analyze the impact of local pressures in more accurately predicting the hydraulic behavior of fractures, and due to its capabilities, PolyJet 3D printing could be very useful for this purpose.

Based on the above, the objective of this investigation has been to evaluate the impact of local pressure measurements on the calculation of the hydraulic aperture of fractures employing an approach that, through the benefits of PolyJet 3D printing, allowed experimentally, analytically, and numerically benchmark results. Two types of fracture surfaces were generated digitally. Roughness characteristics were obtained for such topographies. The surfaces were digitally inserted into 3D solids and reproduced through 3D printing. These models were used to form 3D-printed fractures and conduct experiments to estimate local apertures through an imaging technique and local pressures with fiber optic sensors. The experimental data was used to calculate hydraulic apertures, which were compared to cubic-law analytic models. In turn, the local aperture maps were used in numerical simulations and compared with the experimental local pressure drops. This work focuses on providing a reference of the expected experimental error when local pressure measurements are not available. In conjunction with other sources, this study could be used to find an adequate generic model to better estimate fractures in hydraulic aperture.

4.3 Methodology

4.3.1 Experimental Procedure and Materials

Preparation of 3D-Printed Fractures

Digital Synthetic Rock Surfaces Fracture topographies with distinct levels of roughness were created using Blender, a computer graphics software, applying the Perlin noise (PN) method (Perlin, 1985). The dimensions of the surfaces created were 155 mm $\times$ 155 mm, with a XY resolution of 151 μm, which was equivalent to 1,050,625 data points.

By applying a *clouds* texture to a 155 mm $\times$ 155 mm flat plane and varying the parameters of the PN algorithm, two different types of fracture surfaces were generated computationally. A fracture composed of type 1 surfaces (Figure 4.1a & 4.1b), the sample was labeled as a smooth fracture (SF). Conversely, if it was formed from type 2 surfaces (Figure 4.1c & 4.1d), the fracture sample was designated as a rough fracture (RF).

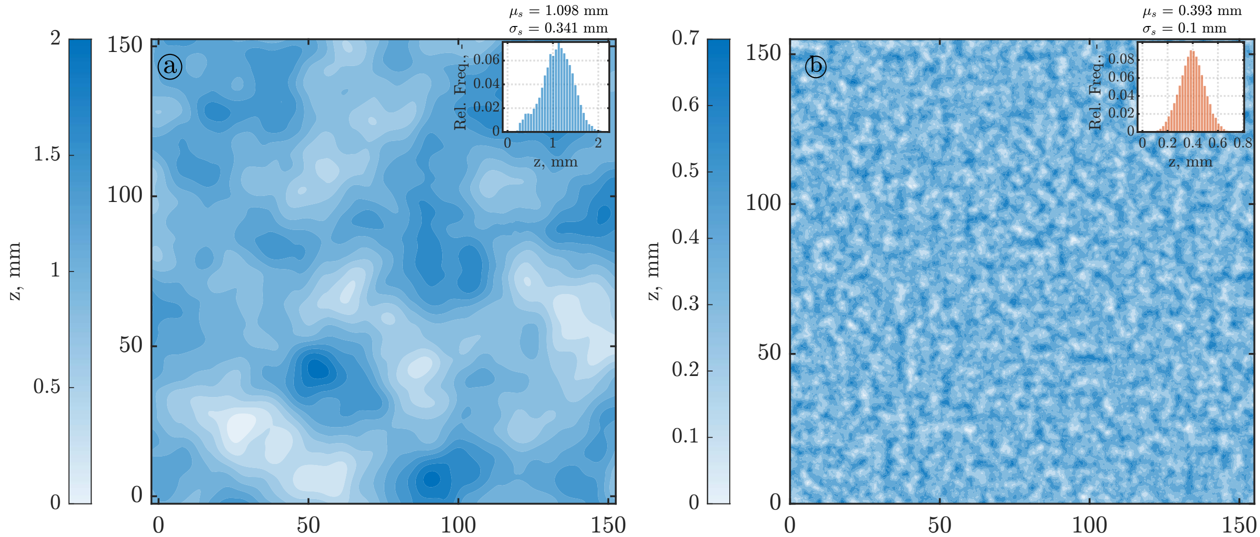

Figure 4.1: Synthetic fracture surfaces. (a) Type 1 surface and its relative frequency histogram of the elevation values with mean $\mu_s = 1.098$ mm and standard deviation $\sigma_s = 0.341$ mm. (b) Type 2 surface and its relative frequency histogram of the elevation values with mean $\mu_s = 0.393$ mm and standard deviation $\sigma_s = 0.1$ mm.

Design of 3D-Printed Fracture Parts and Experimental Cell A hybrid CAD modeling approach was used to take advantage of the capabilities of different CAD software. This process first involved creating upper and lower solid models in Autodesk Inventor; the upper half solid model was designed with eight peripheral orifices for 1/4-in screws to face-seal against a rectangular gasket. The lower-half solid model included ten pressure ports (1/16 in National Pipe Tapered (NPT) ports) distributed in three columns with a cylindrical cavity of 1 mm diameter, designed to connect the fracture topography to the ports. The next step was to embed extracted sections of the digital synthetic rock topographies into solid models using the software Blender, which concluded the digital design of the fracture samples.

The sections were 150 mm × 150 mm and were extracted from the digital fracture surfaces at different $y-$direction displacements (Figure 4.2a & 4.2b) from 0 mm ($\delta_y = 0$ mm) to 5 mm ($\delta_y = 5$ mm). The $\delta_y = 0$ mm sections of each surface type were uniquely integrated into the top solid models (Figure 4.2c). The surfaces $\delta_y = 0, 2.5$ and 5 mm were embedded in the lower SF solid models while the RF incorporated the sections $\delta_y = 0, 1.25, 2.5, 3.75$ and 5 mm. Shear displacement values of up to 2.5 mm fall within the range of seismic events of magnitude 1-2 (Marchand et al., 2019), and events of this nature can be encountered during various stages of engineering projects.

The mentioned computational approach permitted the production of digital fracture samples with the lower fracture walls displaced perpendicular to the flow direction. This allowed for examining fracture flow properties under these conditions, thereby addressing the lack of experimental data in this area. Most of the experimental literature regarding flow through a single fracture under shear has focused on parallel-to-flow shear effects. This has occurred in part because conventional laboratory experiments have been limited to unidirectional flow in the direction parallel to shear because of sealing issues (Vilarrasa et al., 2011).

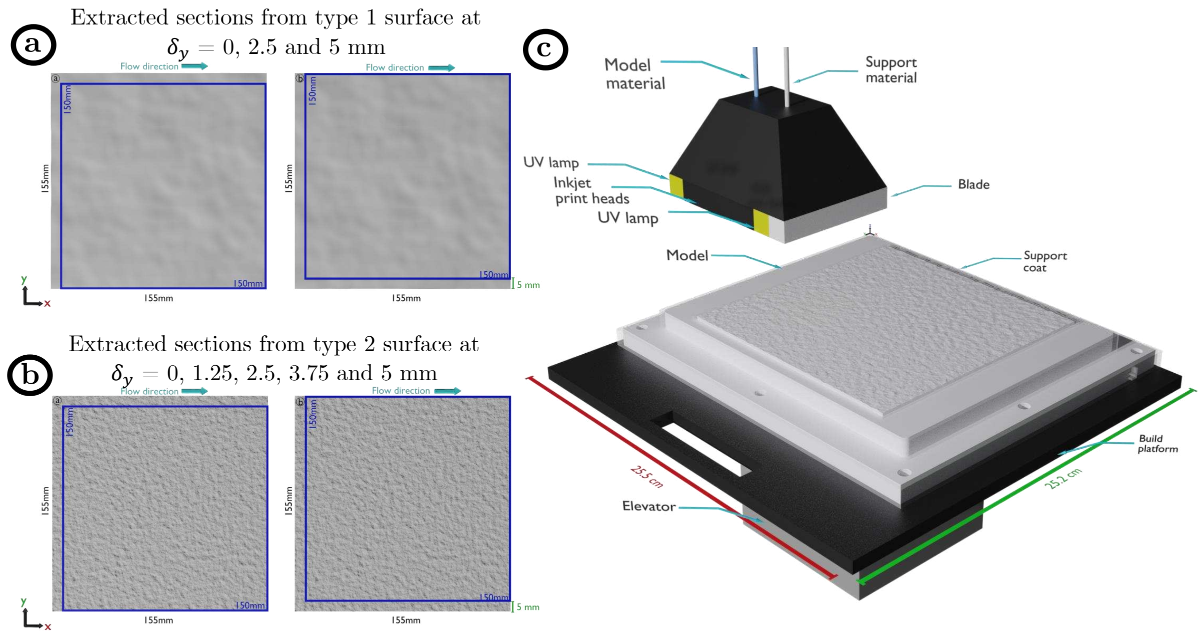

Figure 4.2: (a) Type 1 surface extracted sections at $\delta_y = 0$ mm and $\delta_y = 5$ mm. (b) Type 2 surface extracted sections at $\delta_y = 0$ mm and $\delta_y = 5$ mm. (c) Top solid model with embedded fracture topography.

An aluminum cell was designed to assemble the 3D-printed fractures and to facilitate the execution of the experimental procedure. The cell included four 1/4-in NPT inlet and outlet ports and internal conduits to guide the flow vertically (Figure 4.3a). A cross-section of the assembled experimental cell has been included to display the seal treatment, the cell area in contact with the lower sections, and the location of the local pressure measurements (Figure 4.3b). The testing process for a single surface type involved replacing the bottom parts and reusing the top part in different experiments (see Figure 4.4). Consequently, only one top part was 3D printed per surface type, and many bottom parts were printed according to the shear displacement used.

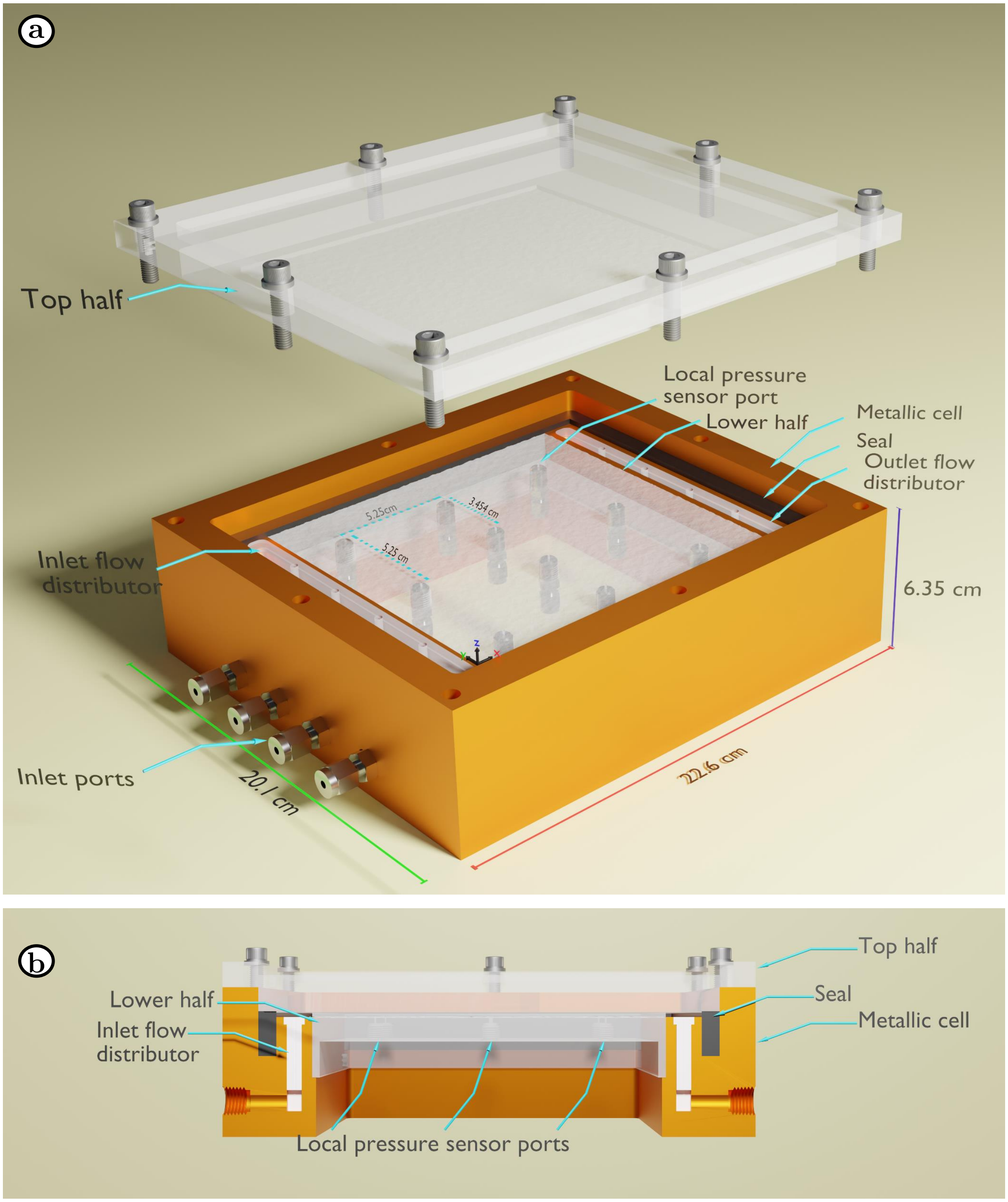

Figure 4.3: (a) Experimental flow cell with a transparent 3D-printed fracture and local fiber optic pressure ports. (b) Cross section of the experimental flow cell.

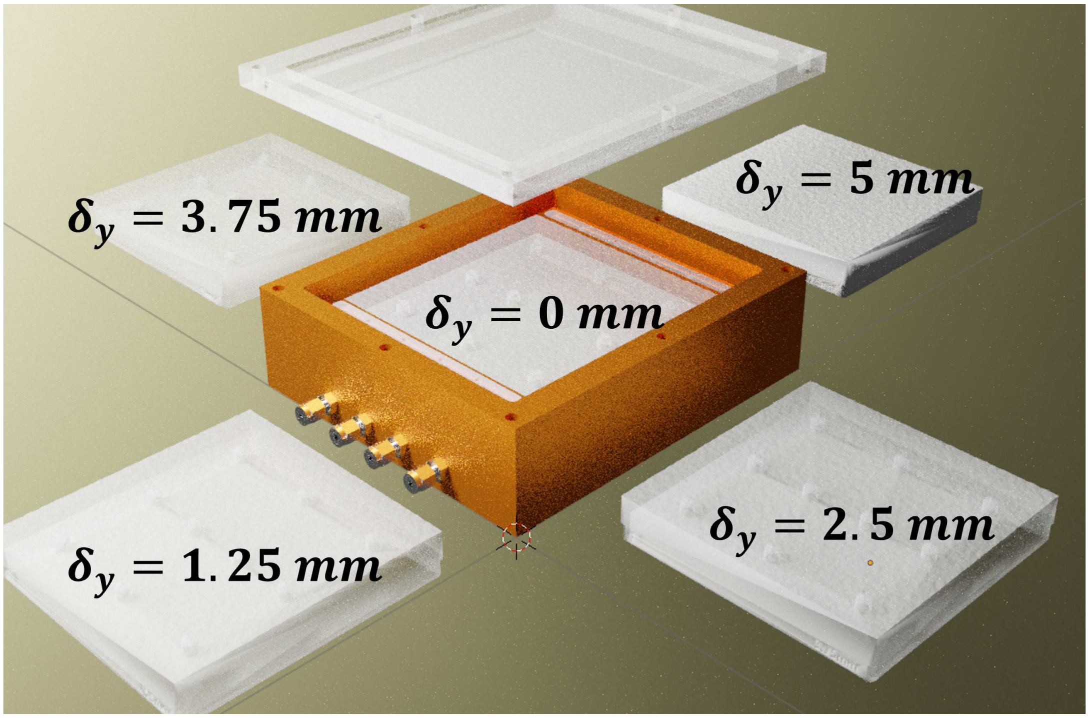

Figure 4.4: Schematics displaying how the 3D-printed lower sections were interchanged for experimental testing, while the top sections were printed only once at $\delta_y = 0$ mm and then reused for subsequent tests.

3D printing Fracture Replicas The samples were 3D-printed with a Stratasys Eden 260 VS using VeroClear model material and a matte finish of SUP707 support material. PolyJet technology enables high resolution, and in addition, the selected combination of materials and surface finish allows the production of clear samples (Stratasys, 2016, 2017). The samples were placed on the printer platform with the fracture walls facing upward (Figure 4.5a); this helped minimize the residual support material left on the textured surfaces after the first post-treatment stage (Figure 4.5b).

Post-Treatment of 3D-Printed Samples To remove the support material, each sample was first washed in a DT3 clean station for four hours at a temperature of 32-47° C (Figure 4.5c). Then the water at the station was replaced with water with a caustic soda (NaOH) concentration of 0.02 g/mL, and the samples were washed separately for four hours at a temperature of 32-47° C. Subsequently, each specimen was cleaned with water and the pressure sensor ports were scraped. Subsequently, the samples were dried with fluorescent light for 12 hours, and the non-rough side of the models was wet-sanded with progressively finer sandpaper (#800, #1000, and #2000). Finally, a polishing compound was applied to the area not exposed to flow (Figure 4.5d). Additionally, to evaluate the fidelity of the 3D printing technique, a 45 mm × 45 mm section from one lower half of a 3D-printed RF was scanned (Figure 4.6a) with a chromatic confocal Nanovea JR 50 profilometer to compare it with the digital model (Figure 4.6b). The $x-y$ resolution used was 10 μm, and the sampling frequency was 100 Hz. The elevations on both surfaces showed a normal distribution with very similar mean values (Figure 4.6c). This suggested that 3D-printed samples reproduced the digital model with good accuracy.

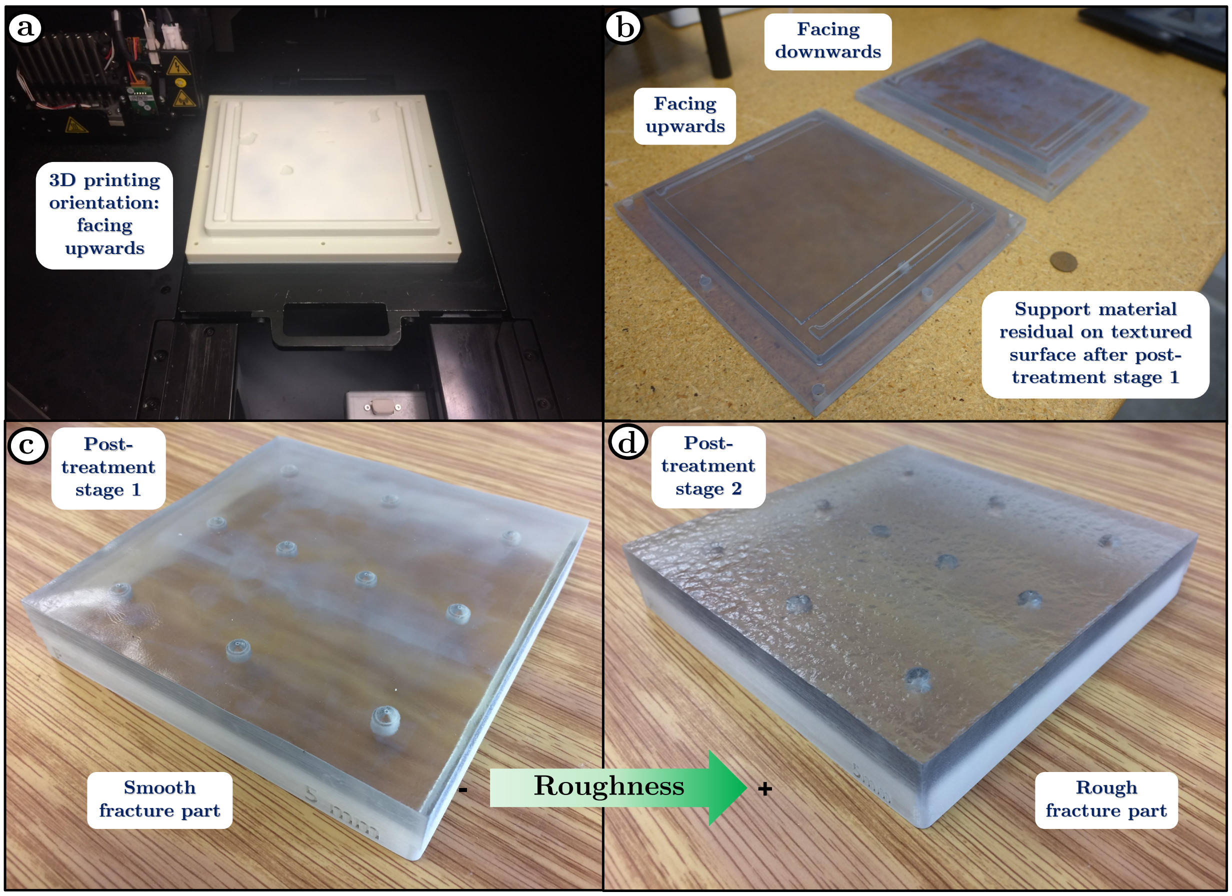

Figure 4.5: (a) 3D printing orientation on the build platform. (b) Support material residue after the first post-treatment stage with respect to 3D printing orientation. (c) 3D-printed model after post-treatment stage 1. (d) 3D-printed model after post-treatment stage 2.

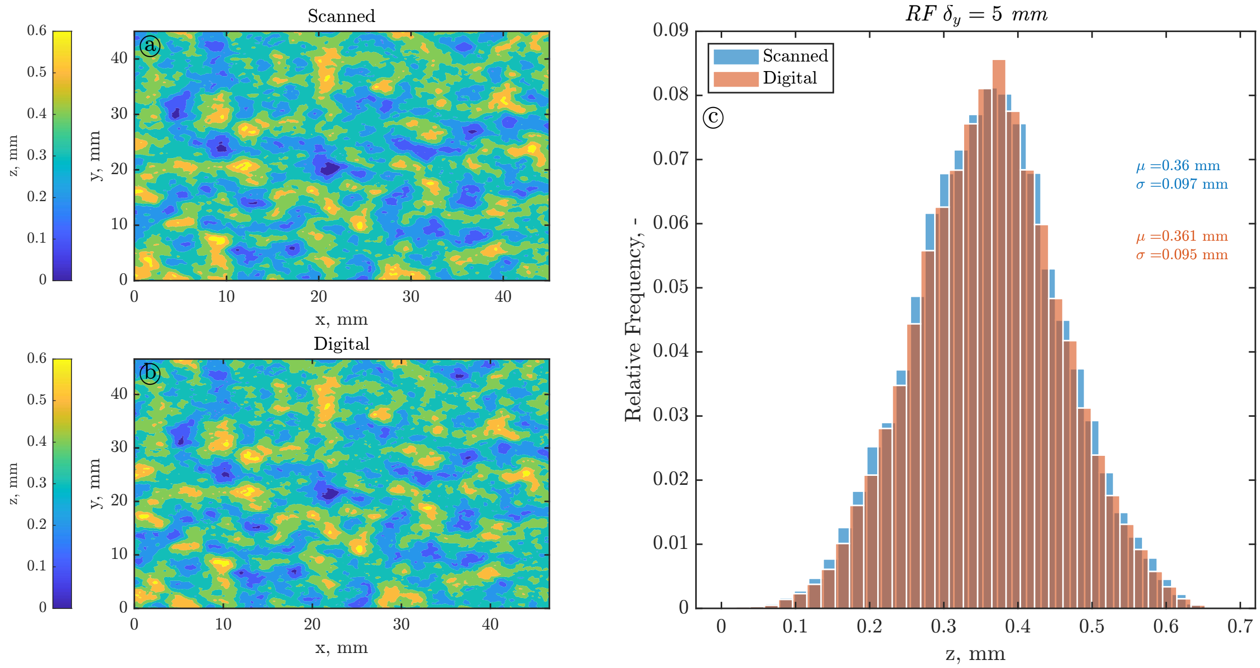

Figure 4.6: $RF\ \delta_y = 5$ mm — comparison between a scanned 3D-printed section (a) and a digital section (b). Histograms of surface elevation values (c).

Characterization of Synthetic Fracture Topography

There are three main methods to describe the roughness of rock surfaces (Fardin et al., 2001): statistical (Auradou, 2009; Y.-F. Chen et al., 2015; V. V. Mourzenko et al., 2018; Tsang & Witherspoon, 1981), empirical (N. Barton, 1973; Witherspoon et al., 1980) and fractal (Brown, 1987; Crandall et al., 2010; J. Li et al., 2018; Oron & Berkowitz, 1998; Zheng et al., 2020).

Although fractal-based methods have been proposed as superior (Y. Ge et al., 2014), as they can provide scale independence beyond a certain distance threshold (Fardin et al., 2001), employing them in conjunction with other methods is a convenient approach to correctly characterize fracture topography (Piggott, 1990). This is because the fractal dimension can be considered a measure of complexity, while other statistical parameters describe attributes such as amplitude and spatial variation (Zelinka et al., 2013), or a combination of these parameters (Y. Ge et al., 2014). In accordance with this approach, some studies have investigated the relationship between fractal dimension and other descriptors (e.g., Ishibashi et al. (2020), Odling (1994), and Vogler et al. (2017)). Consequently, in this study, besides the fractal dimension obtained from the variogram method, multiple statistical parameters (Table 4.1) were calculated to provide a complete description of the fracture roughness.

The variogram method provides estimates of the amplitude parameter (γ_0) and the fractal dimension (D) of a fracture surface profile (P. H. S. W. Kulatilake et al., 2006). This approach has been considered the most accurate among fractal-based procedures for quantifying roughness (Y. Ge et al., 2014) and has been applied based on the considerations outlined in previous works (Babadagli & Develi, 2003; Klinkenberg, 1994; P. Kulatilake et al., 1998; P. H. S. W. Kulatilake et al., 2021; Murata & Saito, 1999).

For each synthetic surface, it was considered that the one-dimensional profiles complied with the self-affine behavior (Méheust & Schmittbuhl, 2001). Subsequently, the fractal parameters γ_0 and D were determined for each profile from variograms calculated with the *variogram* Matlab function (Schwanghart, 2023). A fractal dimension was obtained for each profile in the $x-$ direction and in the $y-$ direction. Then, an average value was obtained for each direction and these two values were averaged for an overall parameter. This calculation process is illustrated in Figure 4.7 and Figure 4.8.

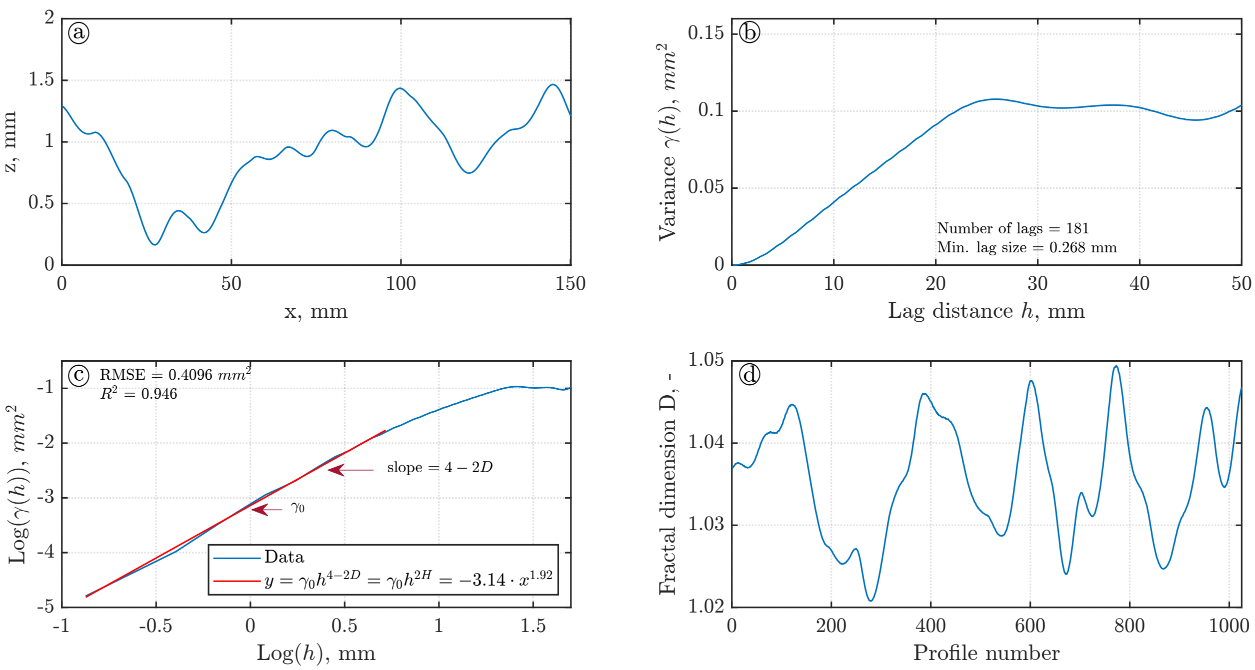

Figure 4.7: Variogram method workflow for type 1 surface. (a) Plot of a one-dimension profile in the $x-$direction, (b) variogram plot of the entire profile, (c) log-log plot of the variogram with a power law fit of the initial section, (d) fractal dimension of all the surface profiles in the $x-$direction.

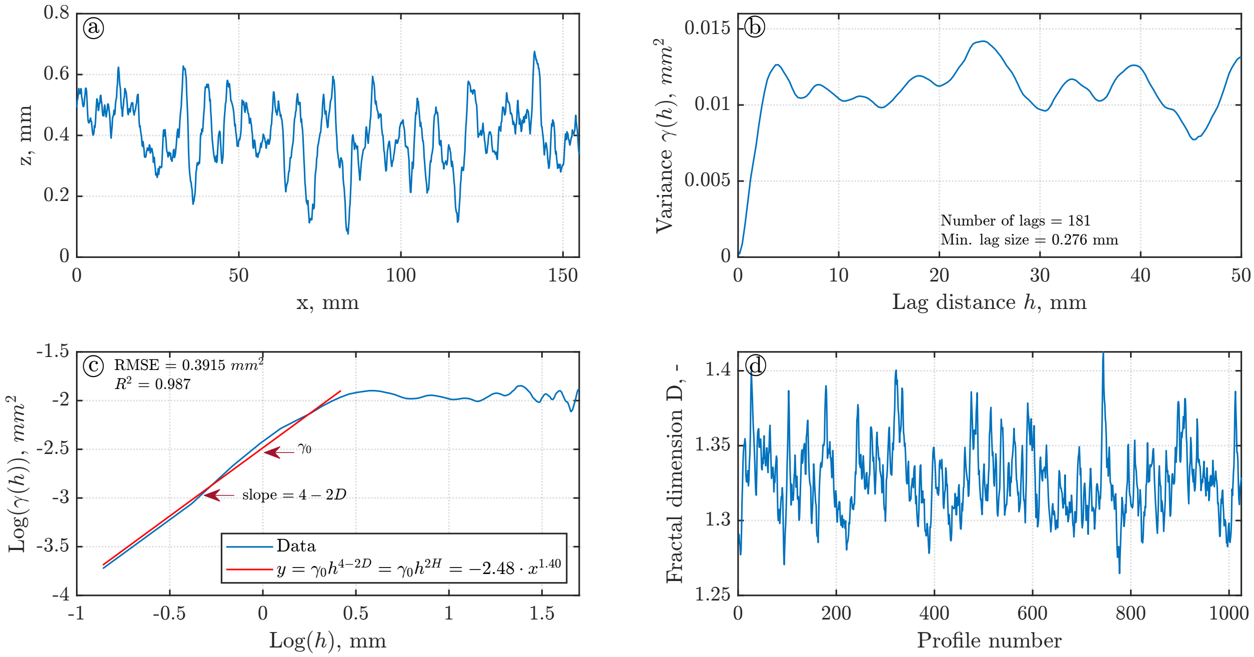

Figure 4.8: Variogram method workflow for type 2 surface. (a) Plot of a one-dimension profile in the $x-$direction, (b) variogram plot of the entire profile, (c) log-log plot of the variogram with a power law fit of the initial section, (d) fractal dimension of all the surface profiles in the $x-$direction.

Parameter	Definition & Numerical Form	Reference
Z	Peak asperity height $z_{max} - z_{min}$	Y.-F. Chen et al. (2015)
R_a	Average asperity height $\frac{1}{n}\sum_{i=1}^{n}\lvert z_i - z_k\rvert$	Thomas (1981)
RMS	Root mean square $\sqrt{\frac{1}{n\times\Delta x}\left[\sum_{i=1}^{n}\Delta x((z_i - z_k)^2)\right]}$ $= \sqrt{\frac{1}{n}\sum_{i=1}^{n}(z_i - z_k)^2}$	Tse and Cruden (1979)
S_{sk}	Skewness $\frac{1}{n\times RMS^3}\sum_{i=1}^{n}(z_i - z_k)^3$	Thomas (1981)
R_{ku}	Kurtosis (sharpness) $\frac{1}{n\times RMS^4}\sum_{i=1}^{n}(z_i - z_k)^4$	Thomas (1981)
Z_2	Root mean square of the profile's first derivative $\sqrt{\frac{1}{n-1}\sum_{i=1}^{n-1}\left(\frac{z_{i+1}-z_i}{\Delta x}\right)^2}$	Belem et al. (2000)
Z_3	Root mean square of the profile's second derivative $\sqrt{\frac{1}{n-2}\sum_{i=1}^{n-2}\left(\frac{\left(\frac{z_{i+2,j}-z_{i+1,j}}{x_{i+2,j}-x_{i+1,j}}\right)-\left(\frac{z_{i+1,j}-z_{i,j}}{x_{i+1,j}-x_{i,j}}\right)}{\frac{x_{i+2,j}-x_{i,j}}{2}}\right)^2}$	Myers (1962)
θ_p	Mean angle of inclination $\tan^{-1}\left(\frac{1}{n-1}\sum_{i=1}^{n-1}\frac{z_{i+1}-z_i}{\Delta x}\right)$	Modified after Belem et al. (2000)
R_L	Linear roughness coefficient ratio of the actual 2D profile length to the nominal profile length $\frac{1}{n-1}\sum_{i=1}^{n-1}\sqrt{1+\left(\frac{z_{i+1}-z_i}{\Delta x}\right)^2}$	Belem et al. (2000)

[a] z_{max}: maximum elevation, z_{min}: minimum elevation, z_i *ith* elevation, z_k: mean of z_i values, n: total number of measurements and $\Delta x = x_{i+1,j} - x_{i,j}$: $x-$coordinates spacing.

Table 4.1: Statistical roughness parameters[a].

Experimental Configuration and Laboratory Testing

The laboratory setup included a positive displacement pump (Vindum maximum injection rate of 30 mL/min with an accuracy of ± 0.1%), and a rectangular aluminum cell where 3D-printed fracture halves were assembled for experimental testing (Figure 4.9 and Figure 4.10a). The experiment was sealed with a 3D-printed rectangular face seal (TangoBlack FLX973 material).

A charged-couple device (CCD) camera (Basler acA1300-30 gc with a C125-1218-5M lens) was used to capture the local aperture map (Figure 4.10b). A CCD camera was used because such devices can obtain images that are linear representations of light intensity (Russ, 2016;

Villamor et al., 2019) and can be useful in estimating the aperture between transparent rough surfaces (Kishida et al., 2013). The camera resolution was 1294 $\times$ 964 pixels, which yielded a spatial resolution of the captured images of $\sim$151 μm in the $x-$direction and a $\sim$157 μm $y-$direction. A light source from LED (The Big Orchard, A4) was used below the experimental cell. Ten miniature fiber optic sensors (Opsens Solutions OPP-MT 0.3 mm diameter) with a resolution of less than $\sim$103 Pa were distributed across the lower models of the fracture specimens to measure the local pressures (Figure 4.10c). A data acquisition system (KeySight 34970A) in conjunction with a demodulator (Validyne CD15) was used to operate a differential pressure sensor (Validyne DP15) and record upstream differential pressure. An electronic balance was used to measure the mass of the outflow fluid.

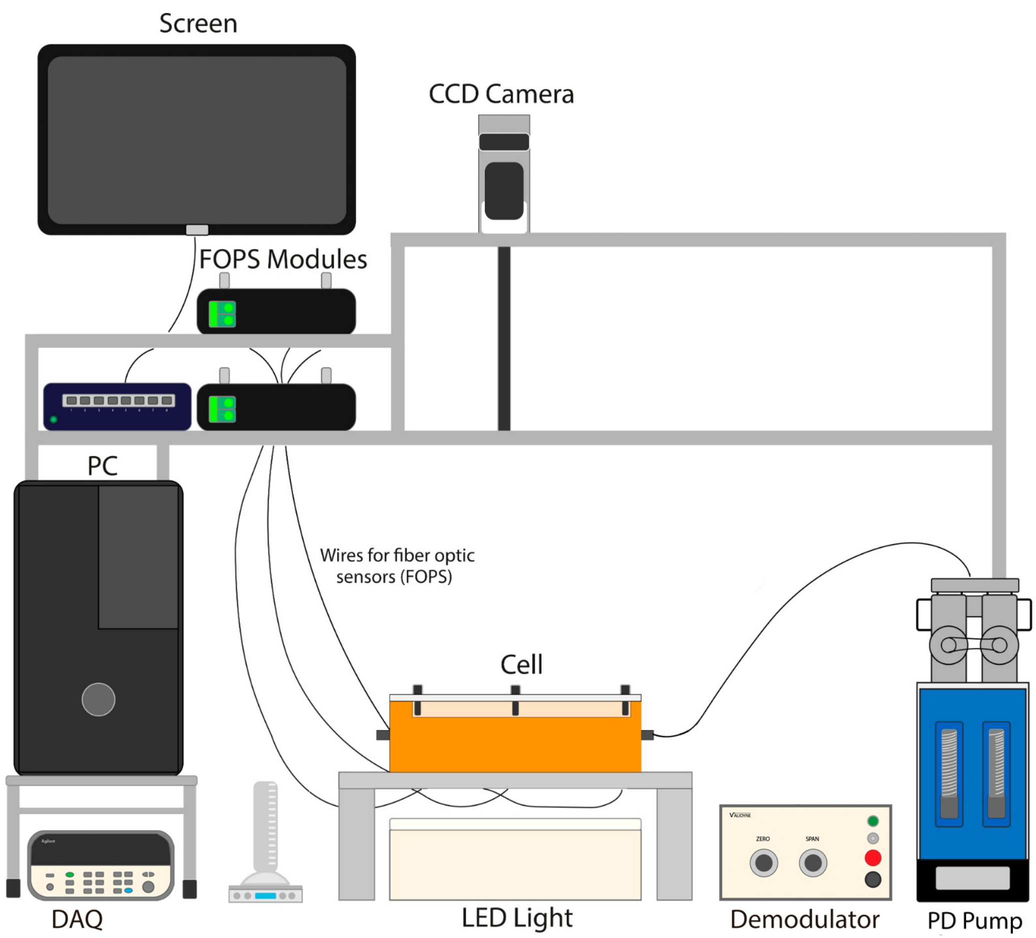

Figure 4.9: Experimental configuration.

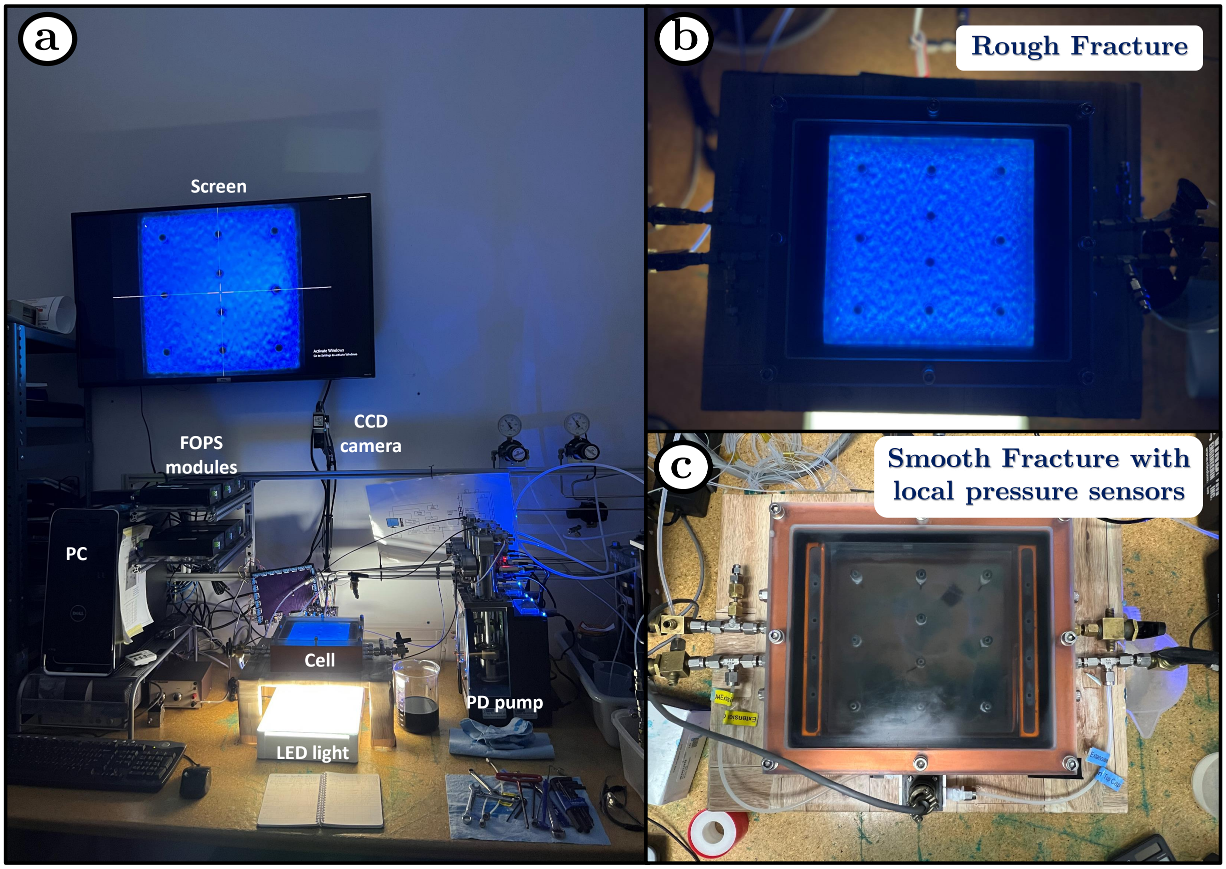

Figure 4.10: Laboratory setup. (a) Laboratory experiment with a 3D-printed fracture. (b) Fracture saturated with dyed fluid. (c) Fracture with local pressure sensors.

Testing Preparations To initiate a test, the lower half of a fractured specimen was placed in the aluminum cell, and its area was sealed with silicone for at least 24 hours (Figure 4.11). Subsequently, the rectangular seal was introduced within the metallic cell. For samples at non-zero shear displacement, a 3D-printed flat shim was placed below the seal to increase the vertical separation between surfaces. For *SF* samples, its thickness was 0.3 mm, and 0.2 mm for *RF* specimens. Other experimental configurations have used this approach (Z. Chen et al., 2000; Cunningham et al., 2020; Nicholl et al., 1999).

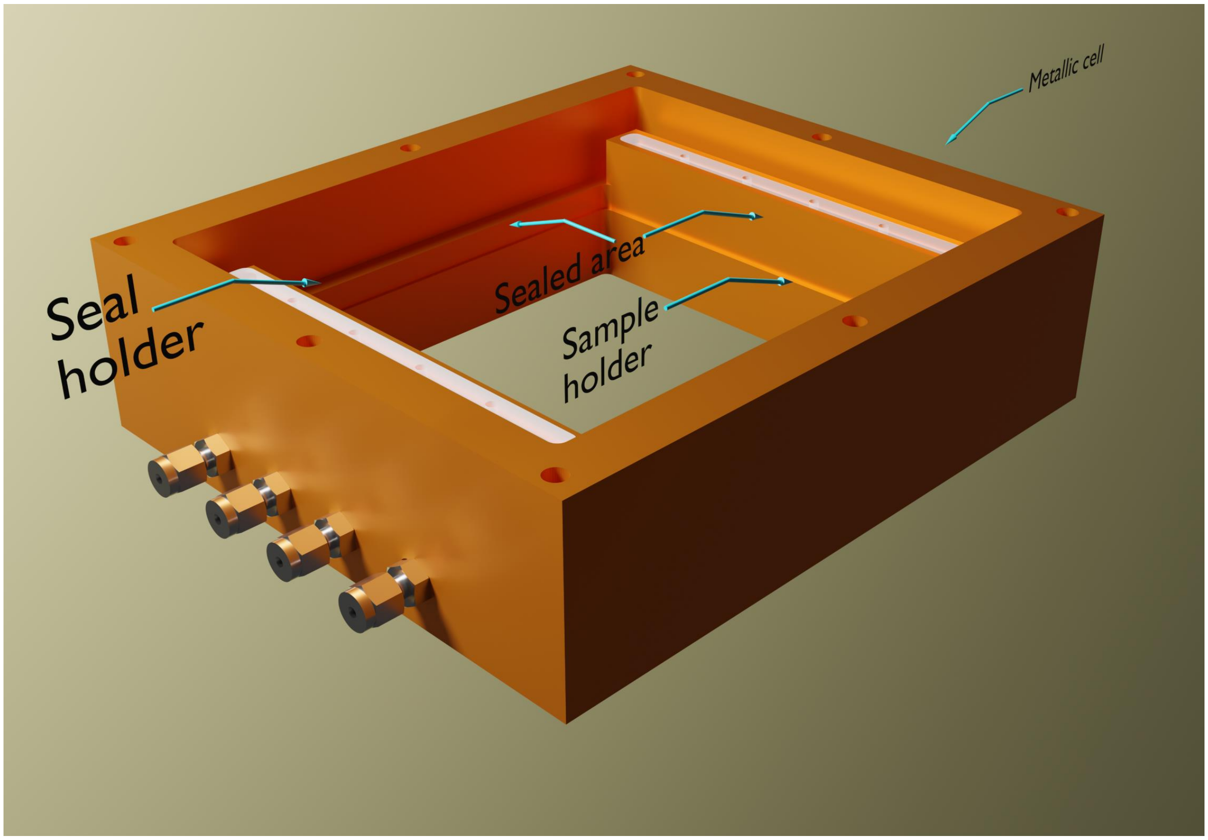

Figure 4.11: Testing preparations: sealing process and sampling placement.

The computational design of the lower half models facilitated the production of 3D-printed fracture samples with integrated surface displacements. Upon assembly, each fracture sample statically replicated a discrete shear displacement position perpendicular to the flow direction. Fracture samples at $\delta_y = 0$ mm consisted of two mirror surfaces without contact. Thus, theoretically, the local apertures should have been more homogeneous. The aperture in the subsequent samples varied according to the surface displacement imposed on the lower side of the fracture walls.

Mean Mechanical Aperture The mean mechanical aperture ($\bar{b}$) of the fracture specimens was measured using a volumetric method (Pan, 1999). The fracture cell was placed upright on its injection side, and a positive displacement pump was used to inject distilled water to fill the fracture cell until just before the outlet manifold. The volume of pumped water was used to calculate the mean mechanical aperture by dividing the injected volume by the area (A) of the fracture plane calculated as $A = L \times w$ (where L is the length and w is the width of the fracture). First, the cell volume associated with the inlet connections and the inlet manifold was estimated by metering the injected volume just before the water entered the fracture. This involved filling the cell at a rate of 10 mL/min and once the observed water level approached the entrance of the fracture, the precision pump was set to inject small water volumes, ensuring that the level reached the entrance of the fracture. The subsequent injection covered the fracture until just before the outlet manifold. Subsequently, a mass balance between the total injected water and the liquid in the cell cavities yielded the water in the fracture sample. After the measurement, the cell was drained, and the unsaturated cell and the collected water were weighed with an electronic scale.

Local and External Pressure Measurements Ten fiber optic pressure sensors distributed in three columns in each fracture were used to obtain local pressure measurements. Three sensors at the inlet column (i.e., p_{10}, p_9 and p_8), four sensors in the middle (that is, p_7, p_6, p_5 and p_4) and three sensors in the outlet column (that is, p_3, p_2 and p_1). Additionally, a differential pressure sensor was connected to the aluminum cell through a single injection port at approximately 8 cm of linear tubing distance. The fiber optic sensors were enclosed in a 12 mm long stainless steel tubing with 0.635 mm outside diameter. The local sensors were placed inside 1/16-in NPT fittings and internally sealed with silicone segment when closed (Figure 4.12). These fittings were then connected to the local ports (Figure 4.3a & 4.3b). The sensors operated at a frequency of 20 Hz and were calibrated to zero when the cell reached full saturation. This ensured that the measured pressure changes were solely associated with the flow experiments.

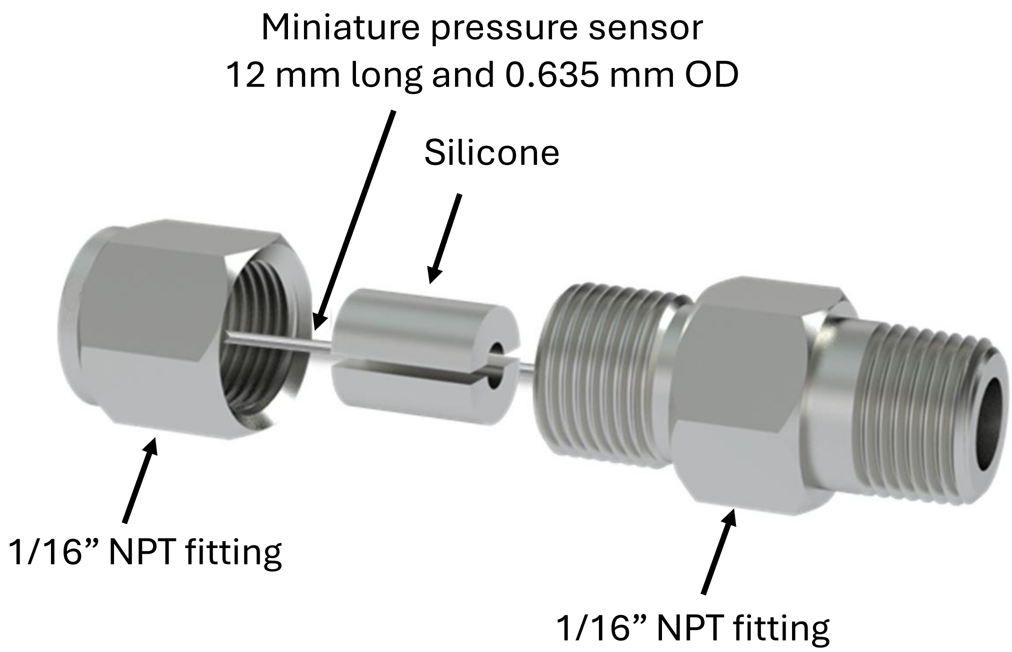

Figure 4.12: Seal concept for fiber optic pressure sensors. Modified from Connax technologies.

Hydraulic Aperture The volume flow rate and pressure drop were used to calculate the hydraulic aperture (e), which corresponds to the effective conductivity of a fracture with rough topography estimated from the experimental parameters and is defined as follows (Mofakham et al., 2018):

$$e = \left(\frac{12\mu_w L_e Q}{w\Delta p}\right)^{1/3} \tag{4.2}$$

Two types of hydraulic apertures were calculated and are referred to in the text as, local e_{local} and external $e_{ext.}$. For the first, the pressure drop (Δp) was calculated from the difference between the average inlet local sensors (.i.e. p_{10}, p_9 and p_8) and the average local sensors at the outlet (i.e. p_3, p_2 and p_1). For e_{local}, the distance in the flow direction ($x-$direction) L_e was equivalent to 105 mm, the distance between the first and third columns of the local sensors. For $e_{ext.}$, the distance was equal to the length of the fracture of 150 mm. The hydraulic aperture measurement was repeated at least six times to calculate the mean and standard deviation of the estimated values. A constant flow rate of 27 mL/min was used to inject distilled water through a single inlet and outlet ports of the aluminum cell.

For four tests, before calculating the hydraulic aperture, steady-state flow tests were conducted to obtain the behavior between pressure drop and flow rate (Figure 4.13a-d). For such tests, the Reynolds number (Re) was calculated from $Re = \rho Q/\mu_w w$ (Koyama et al., 2008) and the linearity between the pressure drop and the flow rate was maintained from 5.4 to 27 mL/min (i.e., $Re = 0.67$ to 3.4). The pressure drop was obtained through an external differential pressure sensor. The linear fit deteriorated slightly as a result of shear displacements or higher roughness, which, in turn, made the linear fit steeper. Overall, the relationship between these variables appeared linear for the flow rates studied. Consequently, the data obtained indicated that $Re < 3.4$ complied with the linearity behavior between pressure and flow rate and was in the range of what has been reported elsewhere (Durham, 1997; Nicholl et al., 1999; Oron & Berkowitz, 1998; Ranjith & Darlington, 2007; Skjetne et al., 1999; R. W. Zimmerman & Yeo, 2000). However, there is debate in the literature about this topic, and some studies suggest that this threshold should be $Re < 1$ (Bear, 1988) while others indicate that the limit depends on the fracture aperture (Quinn et al., 2020; J.-Q. Zhou et al., 2015) or that roughness and hydraulic aperture in conjunction impact this threshold (Cunningham et al., 2020).

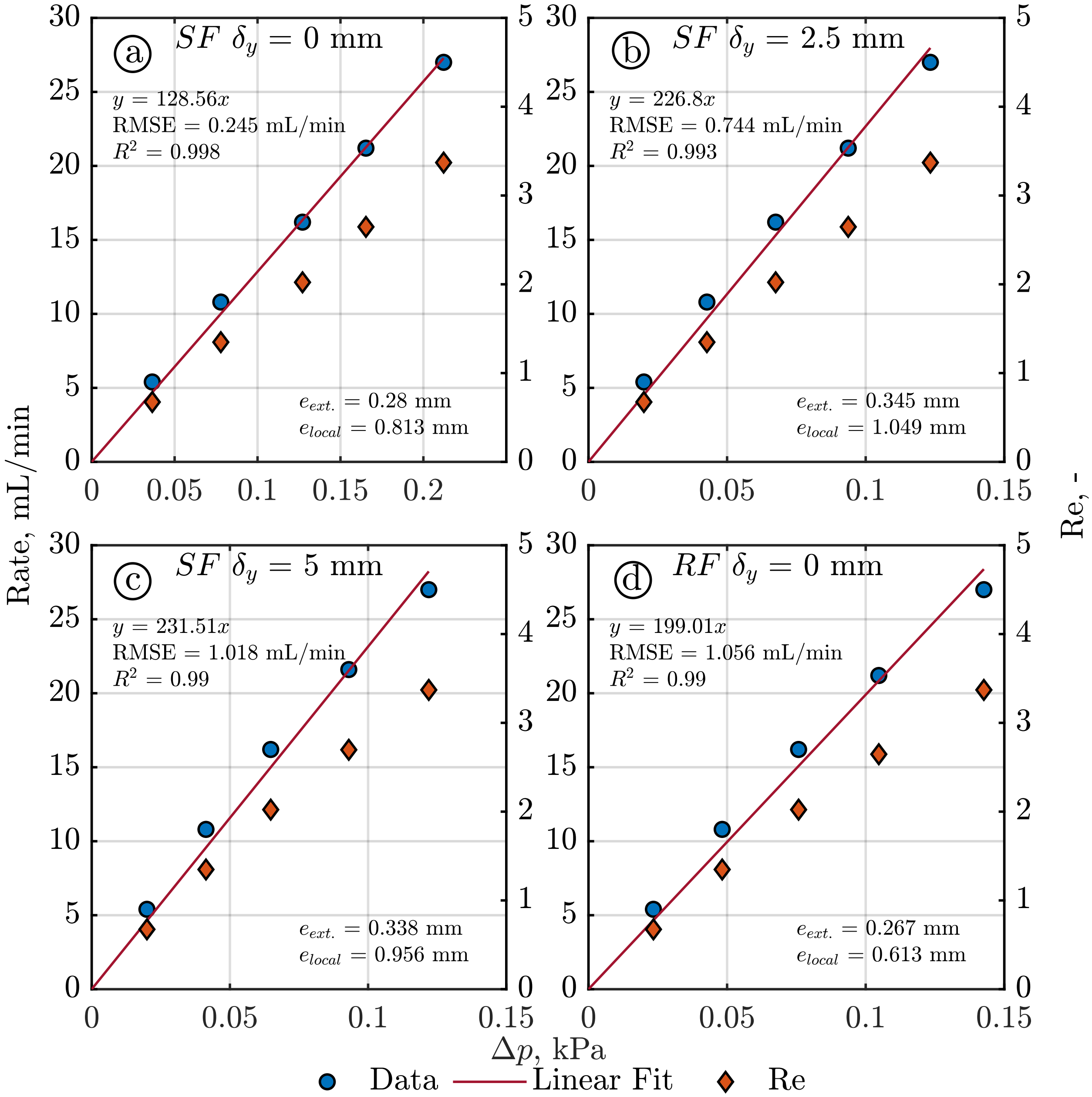

Figure 4.13: Experimental flow rate and pressure drop behavior for four fracture samples.

For comparison, experimental models used to approximate the critical Reynolds number Re_c based on the aperture and roughness of the fracture were examined (Figure 4.14). These models indicate that Re_c increases non-linearly as the hydraulic aperture increases. Based on this data, it is reasonable to infer that inertia effects were minimal in this investigation, given the range of hydraulic values studied.

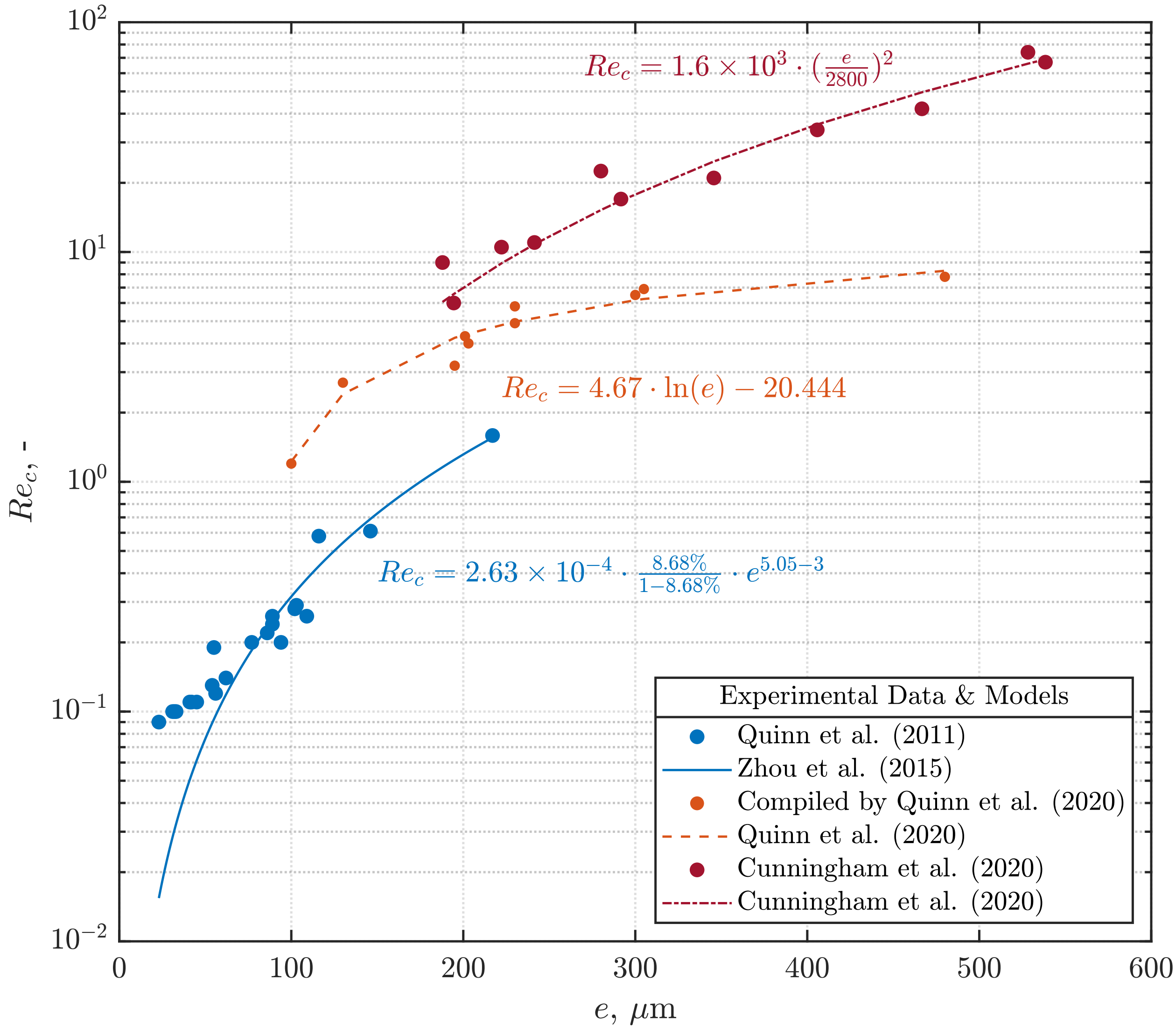

Figure 4.14: Approximating the critical Reynolds number Re_c of fractures based on the hydraulic aperture e through empirical models.

Cubic Law Models Modifications to the *CL* have been proposed to better estimate the hydraulic aperture of a single fracture. Such models are based on the mean mechanical aperture and the statistical parameters of the wall's topography or aperture (Konzuk & Kueper, 2004). In this study, several of these models (Table 4.2) have been used to compare the experimentally obtained hydraulic aperture with the value calculated from these models. The comparison provides a reference for the magnitude of the error in the experimental estimates. Other investigations have examined these models experimentally (C. Cheng et al., 2020; Konzuk & Kueper, 2004; Phillips et al., 2021) and numerically (He et al., 2021; Matsuki et al., 1999; L. Z. Xie et al., 2015; Xiong et al., 2011). Benchmarking these models might yield an adequate generic model for different types of fractures.

Model	Expression	Reference
1	$e=\bar{b}\left[0.94-5(\bar{b}/\sigma_{\bar{b}})^{-2}\right]^{1/3}$	L. Z. Xie et al. (2015)
2	$e=\bar{b}\left[\frac{1}{1+20.5(2\bar{b}/\sigma_{\bar{b}})^{-1.5}}\right]^{1/3}$	Quadros and Cruz (1982) as per C. Cheng et al. (2020)
3	$e=\bar{b}\left[\left(1-\frac{\sigma_{\bar{b}}}{\bar{b}}\right)\left(1-\frac{\sigma_{\bar{b}}}{\bar{b}}\frac{\sqrt{\sigma_{slope}}}{10}\sqrt{Re}\right)\right]^{1/3}$	Xiong et al. (2011)
4	$e=\langle\bar{b}\rangle\left[\frac{1}{1+17(2\bar{b}/\sigma_{s})^{-1.5}}\right]^{1/3}$	Lomize (1951) as per Brown (1987)
5	$e=\bar{b}\left[1-1.5\left(\frac{\sigma_{\bar{b}}}{\bar{b}}\right)^{2}(1-2c)\right]^{1/3}$	R. W. Zimmerman and Bodvarsson (1996)
6	$e=\langle\bar{b}\rangle\left[\frac{1}{1+8.8(2\bar{b}/\sigma_{s})^{-1.5}}\right]^{1/3}$	Louis (1969) as per Brown (1987)
7	$e=\bar{b}\left[1-\frac{1.13}{1+0.191(\sigma_{\bar{b}}/2\bar{b})^{-1.93}}\right]^{1/3}$	Matsuki et al. (1999)
8	$e=\bar{b}\left[\frac{1}{1+0.6(\bar{b}/\sigma_{\bar{b}})^{-1.2}}\right]^{1/3}$	Amadei and Illangasekare (1994)
9	$e=\bar{b}\left[1-0.9e^{-0.56\bar{b}/\sigma_{s}}\right]^{1/3}$	Patir and Cheng (1978)

[a] e: hydraulic aperture, $\bar{b}$: mechanical aperture, $\sigma_{\bar{b}}$: standard deviation of the aperture, σ_s: standard deviation of the surface elevations, $\langle\bar{b}\rangle$: mean aperture available to flow (see Brown (1987)) was considered $\langle\bar{b}\rangle=\bar{b}$, σ_{slope}: standard deviation of the surface slope and Re: Reynolds number, and c: contact ratio.

Table 4.2: Cubic law models[a].

Local Apertures Maps To estimate the local apertures in the fracture samples, the cell was saturated with distilled water dyed with commercial food coloring Blue No. 1 at a concentration of 0.2% wt, and the CCD camera was used to collect an image of the fracture. The dye concentration used was equal to other studies (Y.-F. Chen et al., 2017, 2018). The Beer-Lambert equation was employed to estimate the local apertures by processing a binary image of the saturated fractures. This expression indicates that the light intensity transmitted through a dyed solution varies exponentially depending on the thickness of the solution (Detwiler et al., 1999; Isakov et al., 2001):

$$I=I_0e^{-\kappa cT} \tag{4.3}$$

Where T is the thickness of the gap filled with the dyed solution, κ is the absorptivity of the material, I is the intensity of light at a dye concentration c, and I_0 is the intensity transmitted at zero concentration. First, the mean mechanical aperture was measured and then an iterative procedure was implemented in Matlab to obtain the local aperture map (see

Y.-F. Chen et al. (2017)). The resolution of the obtained maps was approximately 151-156 μm $\times$ 151-156 μm.

Some limitations encountered were that the port geometry caused light interference at the port locations; hence, these areas were not included in the image processing. Similar image processing artifacts have been documented previously (Radilla et al., 2013). Additionally, parts of the outer perimeter of the fracture were excluded from image processing due to light interference. Therefore, the effective areas analyzed were quadratic sections (~75%) of the total flow area used in the laboratory. Including these areas resulted in an overestimation of the aperture map values approximated from the image processing data. Consequently, the removal of these areas was necessary and implied that the mechanical aperture experimentally obtained was identical to that of the extracted section.

The aperture maps obtained were compared to digital fracture models, which were produced in Blender software by perpendicularly displacing the synthetic surfaces by the experimental mean mechanical aperture $\bar{b}$. As a result, the apertures in these digital models approximated the distribution of the aperture maps, theoretically reflecting the actual local aperture values.

4.3.2 Numerical Modeling

Governing Equations

The equations that describe the single-phase steady-state incompressible flow of Newtonian fluid across an individual rock fracture are the incompressible mass conservation and the *NS* equations (see Bear (1988) for a detailed discussion) expressed as (R. Zimmerman & Main, 2004):

$$\nabla \cdot \bar{u} = 0 \tag{4.4}$$

$$\rho \left(\bar{u} \cdot \nabla\right) \bar{u} = -\nabla P + \mu_w \nabla^2 \bar{u} \tag{4.5}$$

Where ρ is density, $\bar{u}$ is velocity, P is $P = p - \rho\bar{g}$ where p is pressure, $\bar{g}$ is the gravity vector and μ_w is water viscosity.

A simplification of the coupling between equation 4.4 and equation 4.5, can be derived by considering steady-state, dominant pressure, and viscous forces, assuming a two-dimensional component velocity, and the fracture walls as non-slip boundaries. The derived expression is known as the *LCL* (Berkowitz, 2002; Brush & Thomson, 2003):

$$\nabla \cdot \left[\frac{b^3}{12\mu_w}\nabla p\right] = 0 \tag{4.6}$$

In this equation, the mechanical aperture varies locally $b = b(x, y)$. Several modifications to the *LCL* exist (e.g.,Nicholl et al. (1999), L. Wang and Cardenas (2016), and Z. Wang et al. (2018)) and are formulated by discretely calculating the local apertures differently in order to incorporate fracture geometry (Konzuk & Kueper, 2004; V. Mourzenko et al., 1995).

In this study, the 3D *NS* and 2D *LCL* were solved numerically using OpenFOAM finite-volume software. *NS* simulations were used to assess if the inertia forces were large compared to the viscous forces. This was analyzed from the difference in the average pressure drop profile between the simulations of the *NS* and the *LCL*.

Mesh Generation

The visualization of the aperture field yielded local aperture values on a structured squared grid where the local aperture was known at each cell corner. This grid was processed to obtain 2D and 3D meshes for numerical modeling. However, the obtained local aperture maps were quadratic portions ($\sim 75\%$) of the fractures. Consequently, the dimensions of the inlet and outlet boundaries were less than in the experiments.

For each fracture, a 3D mesh was generated from the experimental local aperture map. To generate a top and lower surface, a mid-plane was calculated from the aperture map data. Then, the top surface and lower surface were exported in *stl* binary format using the *surf2stl* Matlab function (B. McDonald, 2023). Afterward, these files were imported to Blender, where the lacking boundaries (i.e., inlet, outlet, front, and back) were generated manually by adding a closing planar face. The watertight fracture model was converted to a 3D numerical mesh by using the *SnappyHexMesh* application. The zones where the pressure ports were located were filled with interpolated values from the local perimeter apertures (Figure 4.15). Consequently, the simulation implicitly assessed the impact of the *noise* introduced by these artifacts, along with the reduced area analyzed, during the meshing of the experimental local apertures. The majority of the cells were hexahedral, and the number of cells for case zero was consididred adequate after conducting a mesh sensitivity evaluation for a single fracture (Table 4.3) to ensure a negligible difference in pressure drop and optimize computational efficiency. The internal boundaries connected to the pressure ports were not considered in the simulations. This occurred because these areas were filled with interpolated values.

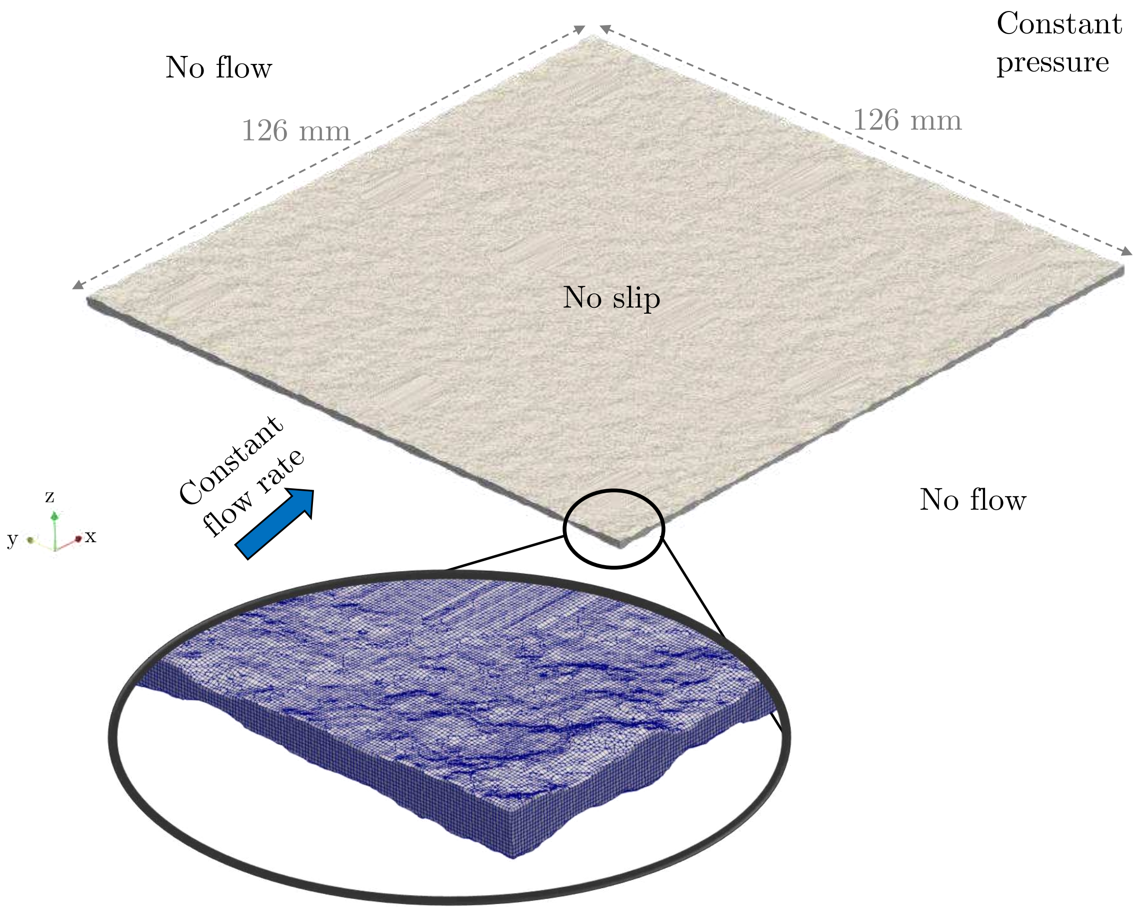

Figure 4.15: *RF* $\delta_y = 5$ mm mesh generation and boundary conditions for *NS* simulations.

Case	Number of cells	Avg. Pressure drop, Pa	Avg. pressure drop difference from the resolution used, %
0	7,711,565	3.53	-
1	11,490,638	3.55	0.57
2	15,676,729	3.59	1.70

Table 4.3: *RF* $\delta_y = 5$ mm — Mesh sensitivity.

		SF			*RF*				
	δ_y, mm	0	2.5	5	0	1.25	2.5	3.75	5
Aperture Map	Size, mm	127×127	122×122	128×128	129×129	126×126	129×129	126×126	126×126
Aperture Map	3D Mesh Cells, $\times 10^6$	7.56	7.70	7.00	6.48	7.10	7.07	7.06	6.18
Aperture Map	2D Mesh Grid Size	801×801	779×779	811×811	814×814	799×799	816×816	807×807	803×803
Water	Viscosity, Pa s	8.90×10^{-4}							
Water	Density, kg/m3	1000							
Water	Flow rate, mL/min	27							

Table 4.4: Numerical simulation parameters for 2D and 3D cases.

Navier-Stokes Simulations

The *simpleFoam* solver based on the SIMPLE algorithm was used to solve the *NS* equations in 3D by coupling equations 4.4 and 4.5 and specifying a constant inflow rate equal to the one used experimentally and a zero pressure value at the outlet boundary (Table 4.4). The top and bottom of the fracture were considered no-slip boundaries, while the sides were considered no-flow boundaries (Figure 4.15). The average pressure profile per fracture was obtained from the modeling results (for example, Figure 4.16a-b and Figure 4.17a-b).

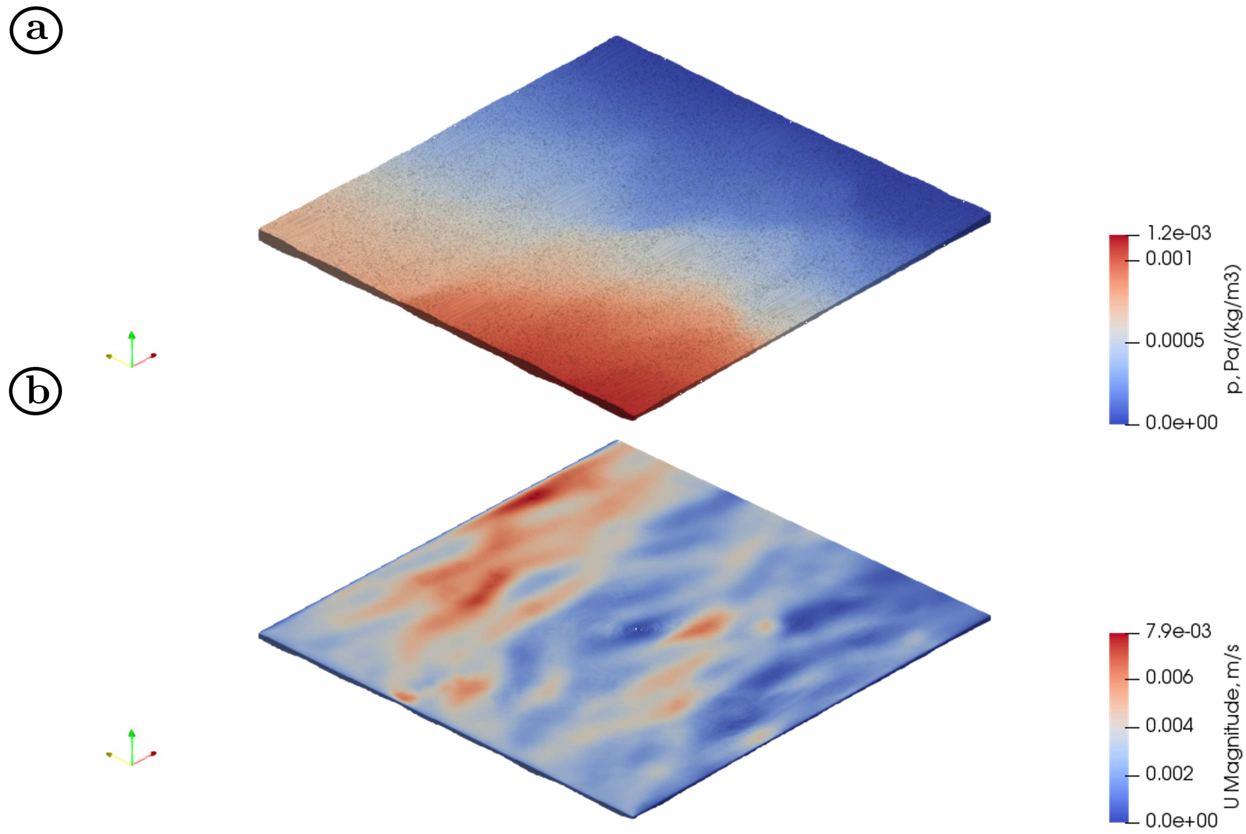

Figure 4.16: *NS* simulations results for *SF* $\delta_y = 5$ mm: (a) pressure field and (b) mid-plane velocity magnitude.

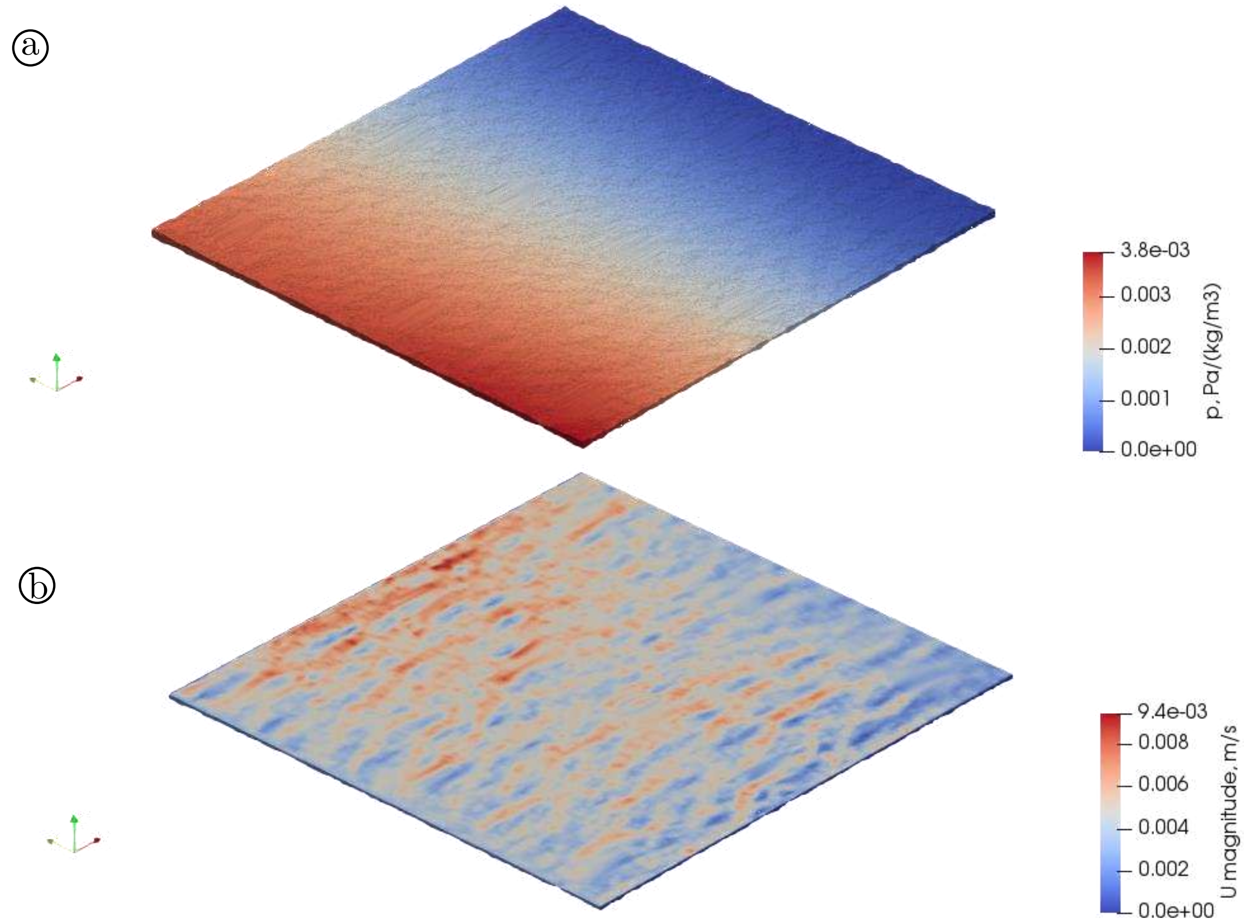

Figure 4.17: *NS* simulations results for *RF* $\delta_y = 5$ mm: (a) pressure field and (b) mid-plane velocity magnitude.

Local Cubic Law Modeling

For 2D simulations, the aperture map data format made it natural to subdivide the fracture into a single layer of prisms and calculate 2D face transmissibility values per control volume.

Two *LCL* models based on the finite-volume method (Figure 4.18) were implemented in Matlab to calculate the transmissibility values at the interface between the control volumes. The first approach involved calculating the cube of the arithmetic mean aperture over the half-control volume (Nicholl et al., 1999), and the second involved calculating the cube of the harmonic mean aperture over the half-control volume (Iwai, 1976).

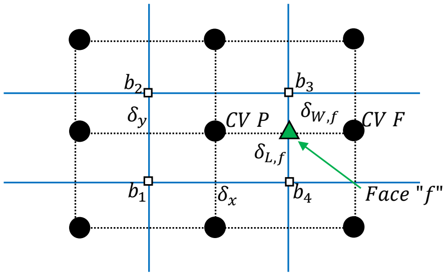

Surface integral of local cubic law over a CV,

$$\int_s \rho \left[\frac{b^3 \nabla p}{12\mu}\right] \cdot \bar{n}\, dS = 0$$

Discrete approximation of the equation above,

$$\sum_f \dot{m}_f = 0$$

One-dimensional mass flux normal to face f,

$$\dot{m}_f = \frac{\overline{b_f^3}\,\delta_{W,f}}{12\mu}\left[\frac{\Delta p}{\delta_{L,f}}\right]$$

$\overline{b_f^3}$ is a characteristic average of b^3 defined over the CV centered around f,

Weighted harmonic mean,

$$\frac{\overline{b_f^3}}{\delta_{L,f}} = \left[\frac{\delta_{L,fP}}{\beta_{fP}\bar{b}_{fP}^3} + \frac{\delta_{L,fF}}{\beta_{fF}\bar{b}_{fF}^3}\right]^{-1}$$

1 $\bar{b}_{fP}^3 = \left[\frac{1}{2}\left(b_f + b_P\right)\right]^3$ Nicholl, 1999

2 $\bar{b}_{fP}^3 = \dfrac{2b_f^2 b_P^2}{b_f + b_P}$ Iwai, 1976

$\bar{b}_{fF}^3$ is treated analogously.

The average aperture for CV P,

$$b_P = \frac{1}{4}\sum_{i=1}^{4} b_i = b_1 + b_2 + b_3 + b_4$$

The aperture at face "f",

$$b_f = \frac{1}{2}(b_3 + b_4)$$

$\delta_{W,j}$ and $\delta_{L,f}$ are the width and length of the interface CV,

$\delta_{L,f} = \delta_x = \delta_{W,j} = \delta_y$ because it is a homogenous grid of quadratic elements.

Figure 4.18: 2D Finite volume discretization and definitions from Brush and Thomson (2003). β is a parameter that corrects the aperture.

The solver used was a custom solver developed by modifying the *Darcyfoam* open-source solver (Horgue et al., 2015) version PMFv1912 to read the transmissibilities at the interface of each control volume. The inlet boundary condition was a constant inflow rate equal to that used experimentally (Table 4.4). The outlet pressure was set to zero. A no-slip condition was applied to the remaining boundaries. The average pressure profile per fracture was obtained from the modeling results (for example, Figure 4.19a-b, Figure 4.20a-b, Figure 4.21a-b & Figure 4.22a-b).

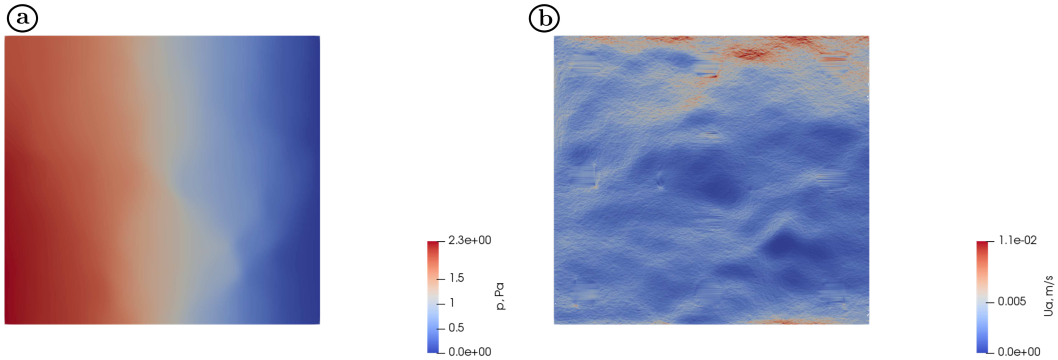

Figure 4.19: 2D *LCL* 1 simulations results for *SF* $\delta_y = 5$ mm: (a) pressure field and (b) mid-plane velocity magnitude.

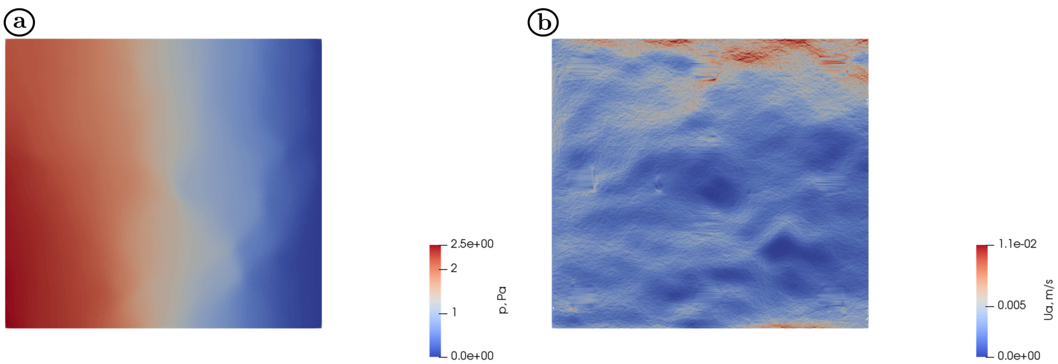

Figure 4.20: 2D *LCL* 2 simulations results for *SF* $\delta_y = 5$ mm: (a) pressure field and (b) mid-plane velocity magnitude.

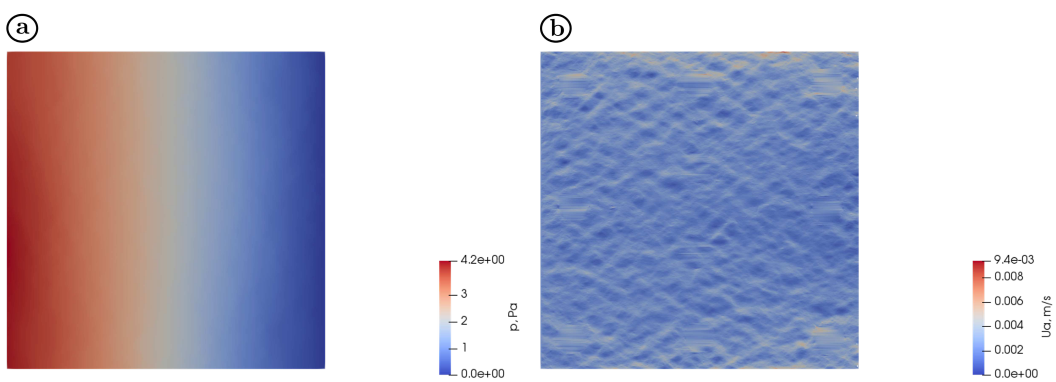

Figure 4.21: 2D *LCL* 1 simulations results for *RF* $\delta_y = 5$ mm: (a) pressure field and (b) mid-plane velocity magnitude.

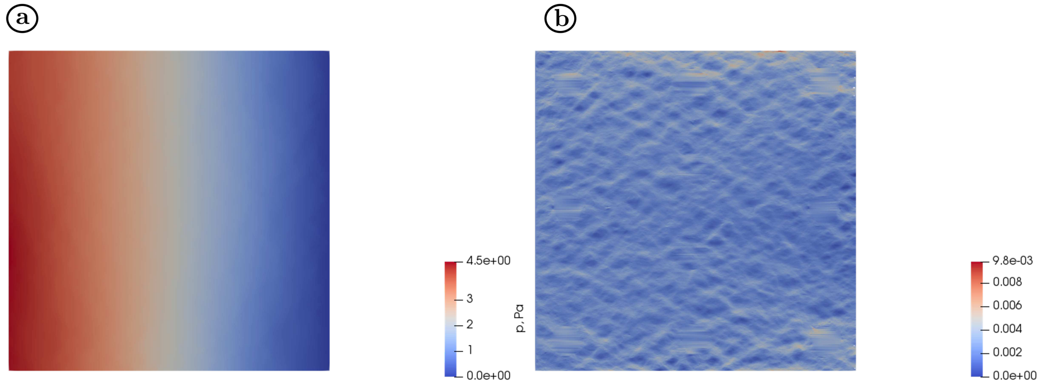

Figure 4.22: 2D *LCL* 2 simulations results for *RF* $\delta_y = 5$ mm: (a) pressure field and (b) mid-plane velocity magnitude.

4.4 Results and Discussion

4.4.1 Roughness of Synthetic Surfaces

The roughness parameters were determined for each profile in both directions x and y, and an overall mean value was calculated (Table 4.5). Type 1 synthetic profiles, exhibited higher surface elevation values, resulting in higher values of the amplitude parameters (that is, Z, R_a, and RMS). However, this surface displayed lower values of the slope or spatial variation parameters (that is, Z_2, Z_3, and σ_{slope}). Consequently, type 2 surface displayed higher values of R_L, which is a measure of amplitude and spatial variation (Y. Ge et al., 2014). On the other hand, the two surfaces exhibited slightly negative profile skewness (S_{sk}), implying that the profiles had relatively fewer peaks or less pronounced valleys (Thomas, 1981). The height distribution of the synthetic profiles showed a kurtosis (R_{ku}) slightly lower than 3, suggesting a scarcity of high peaks and pronounced valleys (Thomas, 1981). Additionally, the profiles of the two surfaces exhibited a low mean angle of inclination (θ_p), indicating that the profiles were stationary (P. H. S. W. Kulatilake et al., 2021). The absolute value was excluded in the calculation to estimate a global trend angle. Overall, the statistical parameters revealed significant variations in both amplitude and spatial distribution between the profiles of the two surfaces.

The Hurst exponent (H) and the fractal dimension (D) suggested that the two surfaces had different levels of roughness. The dissimilar values of the fractal-based amplitude (γ_0), which should reflect the slope of the surface (Fardin et al., 2001; H. Xie et al., 1997), coincided with the high contrast observed in the values of the spatial variation indicators between both surfaces.

Besides the fractal-based parameters, amplitude indicators were included to ensure the characterization of this behavior.

	Parameter	Type 1 surface	Type 2 surface
Profiles Average	Z, mm	1.221	0.539
	R_a, mm	0.255	0.079
	RMS, mm	0.313	0.098
	Z_2, -	0.037	0.13
	Z_3, mm^{-1}	0.035	0.789
	σ_{slope}, -	0.037	0.13
	R_L, -	1.001	1.008
	S_{sk}, -	-0.12	-0.018
	R_{ku}, -	2.472	2.86
	θ_p,°	-0.012	-1.61×10^{-5}
	H, -	0.966	0.671
	D, -	1.034	1.329
	γ_0, -	0.001	0.003

Table 4.5: Average roughness parameters for profiles in surfaces type 1 and 2.

4.4.2 Analysis of Local Aperture Maps

Visual inspection of the digital fractures (Figure 4.23a and Figure 4.24a) and the experimental local aperture maps (Figure 4.23c and Figure 4.24c) for *SF* δ_y = 5 mm and *RF* δ_y = 5 mm suggested that the experimental maps tended to reflect aperture shapes similar to the digital models. However, the experimental maps showed a wider range of aperture values than the digital fracture maps. Consequently, to qualitatively assess the properties of the experimental maps obtained, the difference between these map types was examined by comparing basic statistical parameters.

The mean aperture imaged was identical or very similar in both directions (e.g. Figure 4.23b). When comparing between map types (that is, Figure 4.23b with Figure 4.23d and Figure 4.24b with Figure 4.24d), the directional mean values tended to be higher in the experimental maps. On the other hand, for the digital fractures, the standard deviation of the mean $x-$direction profile was at least two times higher than the respective value in the $y-$direction (Figure 4.23b and Figure 4.24b). This suggested that the local apertures varied in different directions. This magnitude difference was similar (that is, 1.5) for the experimental map of *SF* $\delta = 5$ mm (Figure 4.23 d). However, this magnitude difference was smaller (i.e., 0.8) for the experimental map *RF* $\delta = 5$ mm (Figure 4.24 d).

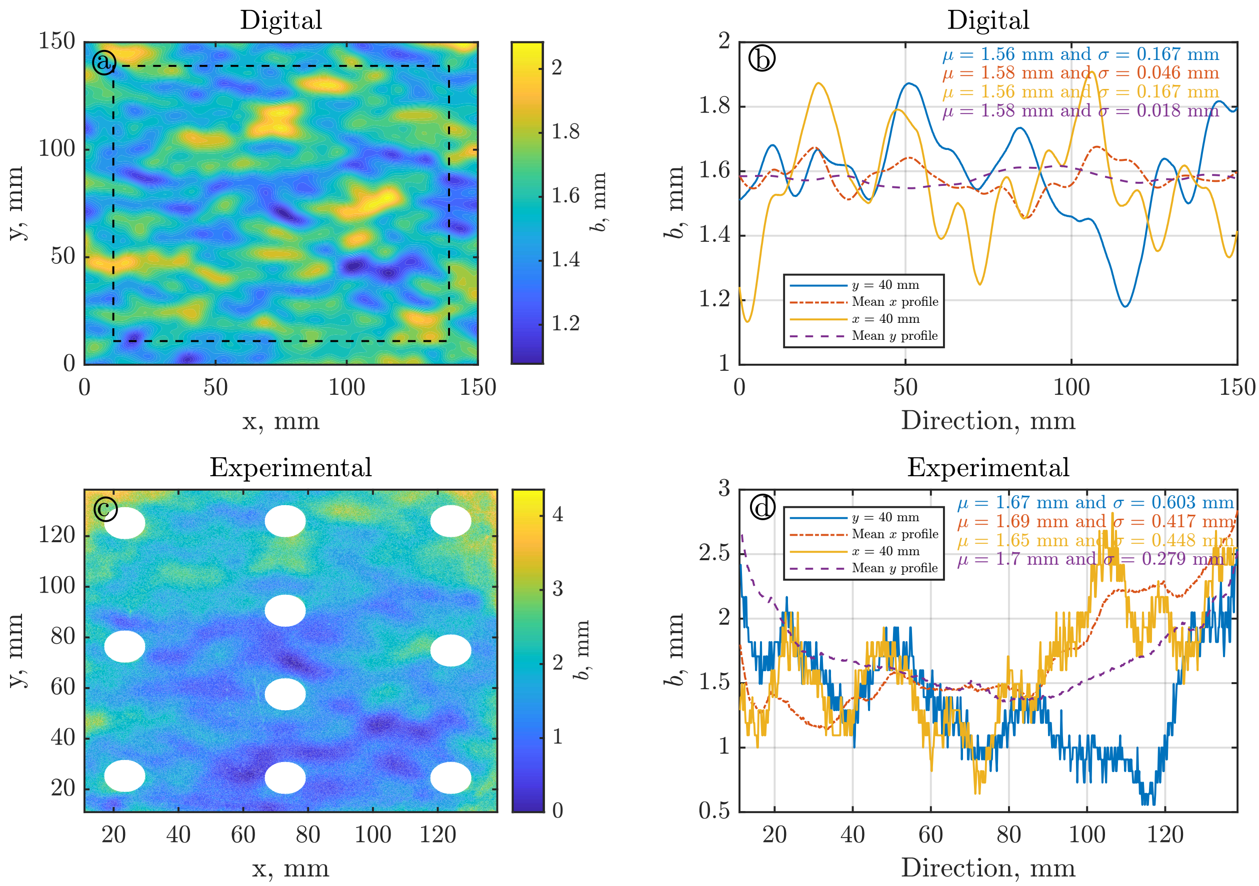

Figure 4.23: Experimental and digital aperture maps for *SF*. (a) Digital map indicating the section analyzed experimentally. (b) Digital mean apertures in both directions. (c) Experimental map. (d) Experimental mean apertures in both directions.

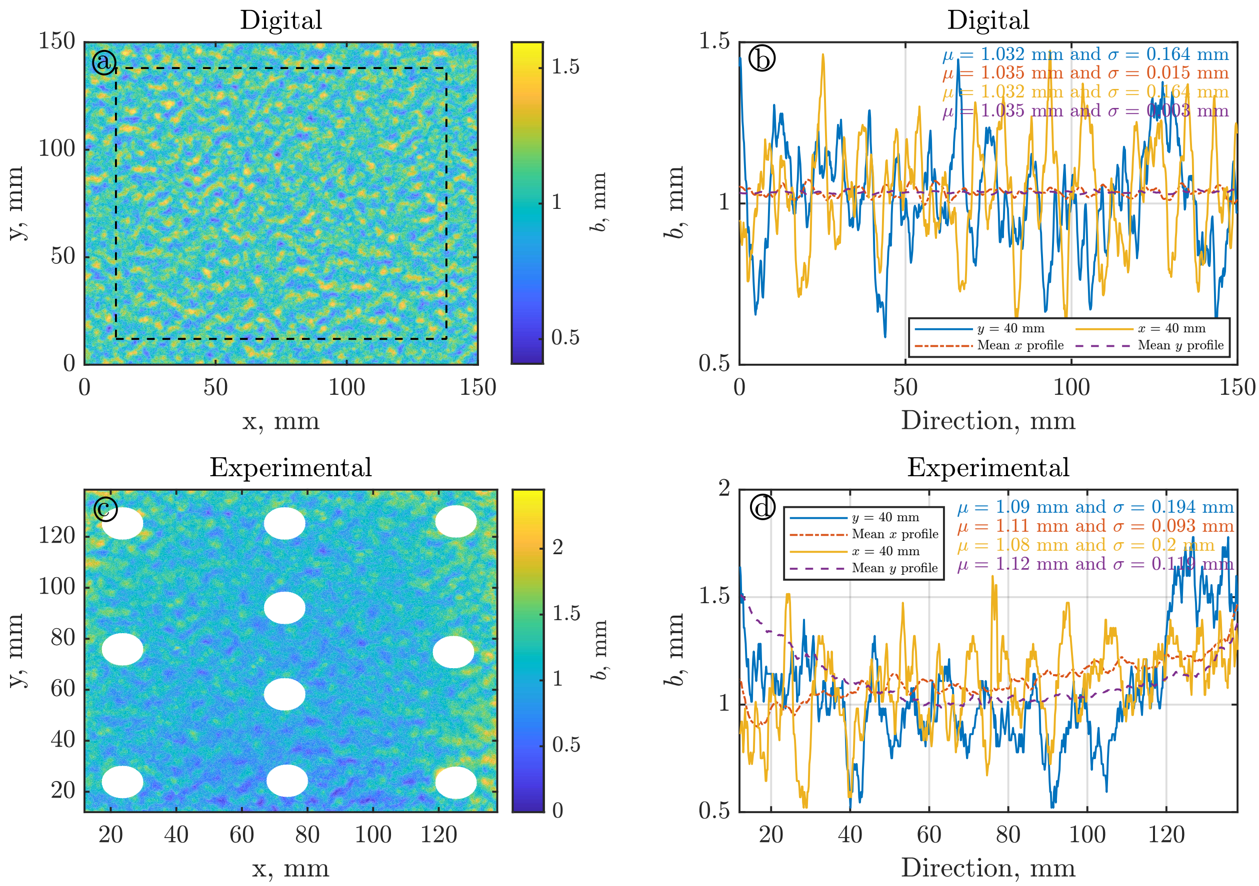

Figure 4.24: Experimental and digital aperture maps for *RF*. (a) Digital map indicating the section analyzed experimentally. (b) Digital mean apertures in both directions. (c) Experimental local apertures map. (d) Experimental mean apertures in both directions.

The coefficient of variation (COV) is defined as the standard deviation over the mean and expresses the degree of variability with respect to the mean. In this study, this parameter was used to analyze the experimentally obtained local aperture maps. The mean aperture and the aperture standard deviation were calculated for each individual profile in the $x-$ and $y-$ directions. Then, a value of COV was calculated for each profile in each direction.

The COV values for aperture profiles in the $y-$direction (perpendicular to flow) were plotted versus the $x-$direction (Figure 4.25a) and the COV values for aperture profiles in the $x-$direction (parallel to flow) were plotted against the $y-$ direction (Figure 4.25b).

The shear displacements increased the heterogeneity of the COV values regardless of the roughness or orientation analyzed (Figure 4.25a & 4.25b). On the other hand, the COV values for the samples of $\delta_y = 0$ mm tended to be more homogeneous in both directions, indicating less aperture variability in these fractures. However, the fact that these were not zero contradicted the theoretical value of the $\delta_y = 0$ mm digital fractures. This difference could be associated with light interference in the experimental aperture maps. Hence, COV was considered a rough indicator of local variability.

The values of COV in sheared-displaced fractures exhibited an oscillating pattern that suggested greater variability in the local apertures in both directions (Figure 4.25a-b). This was examined by estimating a mean spatial frequency f_{mean} of the experimental COV values for these samples. This frequency was calculated by counting the number of peaks and dividing that count by the distance between the positions of the maximum and minimum peaks.

In comparison with their respective non-shear samples, a lower variation in the local apertures along the y-direction (Figure 4.25a) was characterized by a lower-frequency behavior and a tendency towards lower amplitude in the COV values.

In comparison with their respective zero-shear displacement samples, the COV values of $SF\ \delta_y = 5$ mm and $RF\ \delta_y = 5$ mm exhibited a pattern that suggested greater variability in the local apertures in both directions for these samples (Figure 4.25a-b). This was examined by estimating a mean spatial frequency f_{mean} of the experimental COV values for the 5-mm shear displacement samples. It was calculated by counting the number of peaks and dividing that count by the distance between the positions of the maximum and minimum peaks. The lower values of the mean spatial frequency suggested less variation in the local apertures along the y-direction (Figure 4.25a) compared to the slightly higher frequency values in the x-direciton (Figure 4.25b). The local aperture contrast in the smooth fracture ($\delta_y = 5$ mm) was higher because it was formed of surfaces with greater variation in amplitude parameters. Consequently, the estimated mean frequency of COV values was higher for this sample compared to the rough sample ($\delta_y = 5$ mm).

Previous observations on the effect of shear displacements on local aperture variations have indicated the development of preferential flow paths (Archambault et al., 1997; Marchand et al., 2019; Matsuki et al., 2010; National Research Council, 1996), and sheared fractures have been reported to have a higher conductivity in the direction perpendicular to shear displacement than to parallel displacement (Esaki et al., 1999; Koyama et al., 2006; H. Lee & Cho, 2002; Nemoto et al., 2009; Vilarrasa et al., 2011; Yeo et al., 1998). The comparison between the experimental and digital results obtained here pointed to directional aperture variations that could lead to the development of flow channels, however, improving the image processing method previously described as well as minimizing the error during the laboratory imaging process (see Isakov et al. (2001) and Arshadi et al. (2015) for details) can help better visualize this effect. Nevertheless, the workflow used here could be useful for error analysis or correction of visualized local aperture maps.

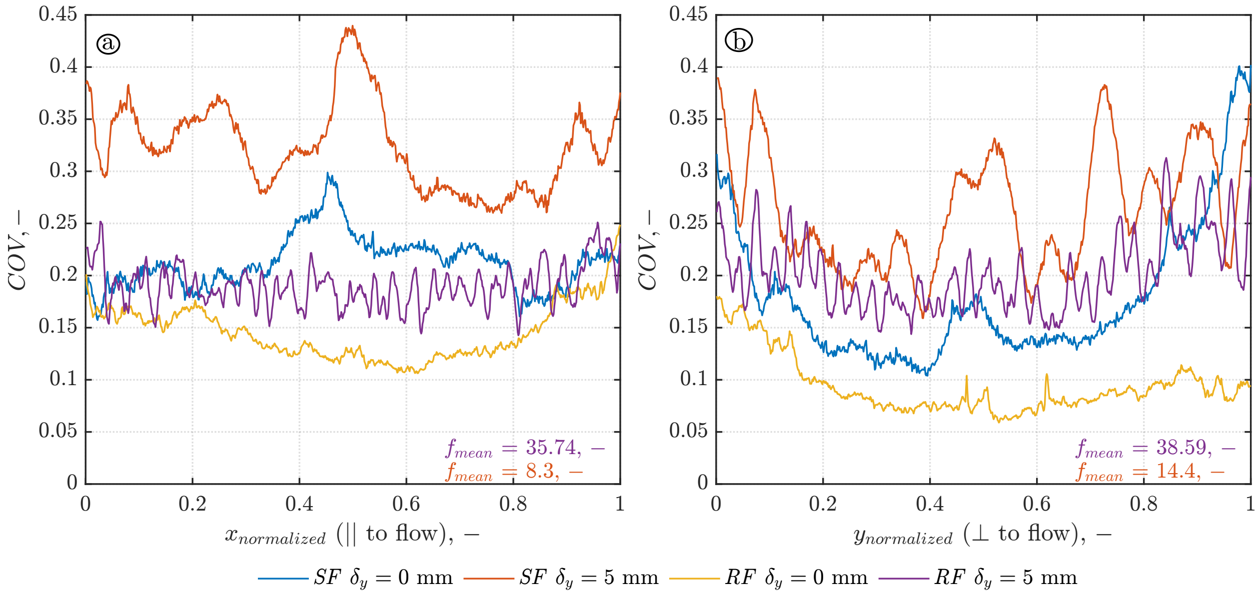

Figure 4.25: COV values of aperture (a) profiles in the $y-$direction and (b) profiles in the $x-$direction.

Statistical parameters for surface topography and fracture aperture were obtained for each fracture sample and subsequently applied in analytical CL models (Table 4.6).

	SF			*RF*				
δ_y, mm	0	2.5	5	0	1.25	2.5	3.75	5
$\sigma_{\bar{b}}$, mm	0.347	0.558	0.610	0.132	0.391	0.280	0.324	0.257
σ_s,mm	0.341	0.341	0.341	0.100	0.100	0.100	0.100	0.100
Re, −	3.500	3.500	3.500	3.500	3.500	3.500	3.500	3.500
σ_{slope}, −	0.037	0.037	0.037	0.130	0.130	0.130	0.130	0.130

Table 4.6: Geometrical parameters of fracture samples.

4.4.3 Local and External Pressure Measurements

The individual local measurements approached the resolution limit of the sensors (Figure 4.26a-b). Therefore, consecutive tests were conducted for each fracture to approximate the true local pressures. Hence, pressure values were estimated based on at least six individual flow tests (Figure 4.27). Variation was assessed using two methods: first, by calculating the standard deviation of individual pressures (Figure 4.27), and then estimating the ratio of the standard deviation to mean values per sensor (i.e., the COV coefficient), ranging from 0.217 to 0.736 for the smooth fractures and 0.239 and 0.462 for the rough fractures. The sample *SF* $\delta_y = 5$ mm showed the largest variation, possibly due to a combined effect of lower roughness and increased aperture. Moreover, these ranges suggested that while there is variation, the local measurements could be useful but more than one realization was required. In line with this, the second approach consisted in calculating the standard deviation of the estimated hydraulic apertures (Figure 4.28a and 4.28b), providing both an uncertainty measurement and a range of possible realizations (see the following section for details).

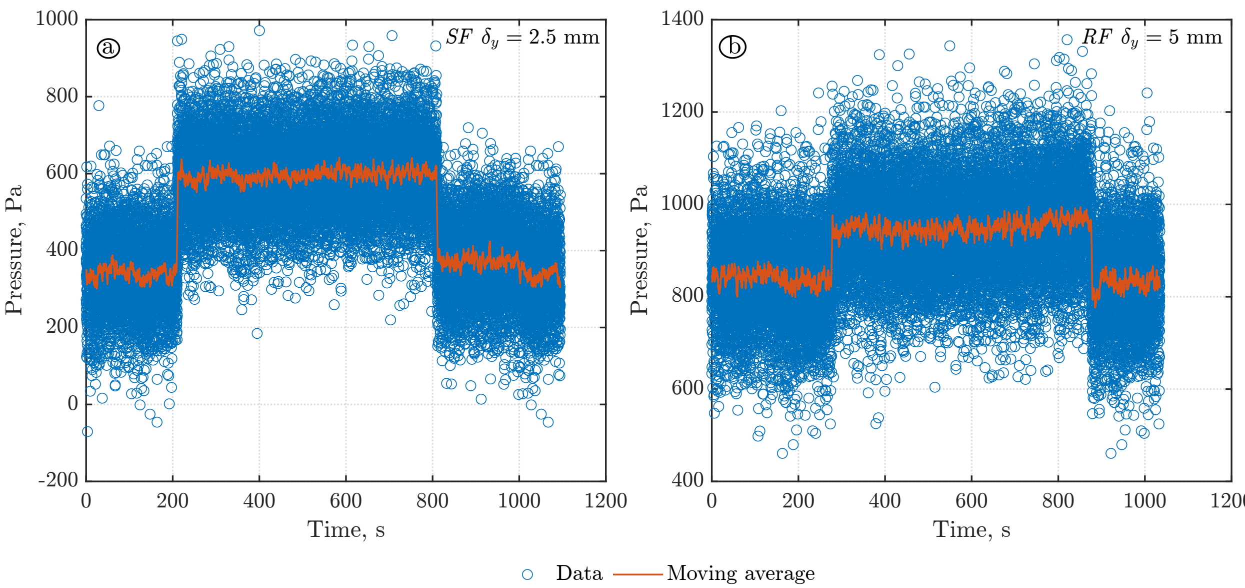

Figure 4.26: Examples of local pressure readings for hydraulic aperture calculation. (a) Smooth fracture sample $\delta_y = 2.5$ mm. (b) Rough fracture sample $\delta_y = 5$ mm.

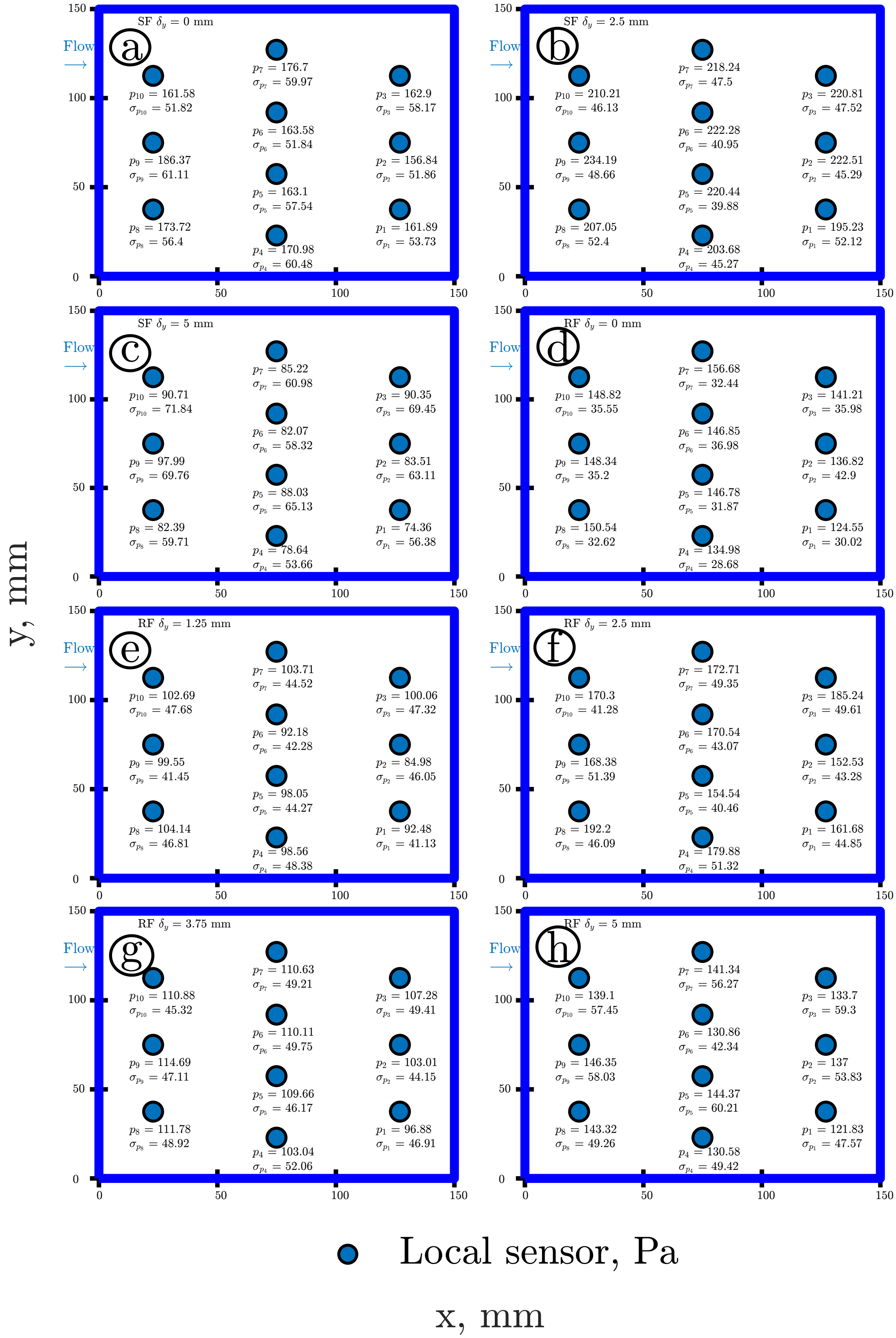

Figure 4.27: Local pressure measurements for all fracture specimens. Each square represents a fracture sample with three columns of fiber optic sensors displaying the average pressure reading and the standard deviation of subsequent measurements.

The pressure values of the first column of local sensors (that is, p_{10}, p_9 and p_8) was averaged to obtain a mean local inlet pressure $\bar{p}_{in}$. Analogously, the pressures in the middle $\bar{p}_{mid}$ and in the outlet $\bar{p}_{out}$ were calculated using the second and third column of the local sensors, respectively. Then, $\bar{p}_{in}$ and $\bar{p}_{out}$ mean pressure values were used to obtain the experimental local pressure drops (Table 4.7). Surface roughness showed a clear effect on the pressure difference $\bar{p}_{in} - \bar{p}_{out}$, which tended to be higher for RF samples regardless of the fracture specimen. Meanwhile, $\bar{p}_{mid} - \bar{p}_{out}$ did not show a clear trend, possibly because these pressure drops were too small. Furthermore, the comparison of pressure values indicated that the use of external sensors to estimate the pressure drop across the fractures overestimated the pressure drop, and the pressure distribution across the fractures was not observed (Table 4.7). The higher pressure difference between the external pressure sensors was associated with friction in the tubing connections and manifolds and not with elevation because the sensors were set to zero when the cell was fully saturated, so the pressure drop was only associated with the flow of water.

Specimen	δ_y, mm	$\Delta\bar{p}_{ext.}$, Pa	$\bar{p}_{in} - \bar{p}_{out}$, Pa
SF	0	217.43	13.35
	2.5	122.69	4.3
	5	118	7.62
RF	0	249.9	15.37
	1.25	136.07	9.62
	2.5	269.74	10.48
	3.75	126.3	10.06
	5	123.33	12.08

Table 4.7: Experimental average local and external pressure drops.

4.4.4 Aperture Estimations and Cubic Law Models

Hydraulic apertures were calculated using local differences and external measurements (Figure 4.28a & 4.28b). The hydraulic aperture values closer to the mean mechanical apertures were those estimated with the local pressure values. The cubic ratio of the local hydraulic aperture and the mean mechanical aperture tended to decrease for samples with a higher shear displacement (Figure 4.28c & 4.28d). Comparatively, this ratio did not exhibit a trend for the external hydraulic apertures.

The deviation between the hydraulic apertures and the mean mechanical apertures was calculated for the local and external measurements (Figure 4.29). This calculated deviation was limited to the open fractures studied and the specific experimental configuration used in this study; consequently, it can be considered a rough approximation. Estimating the hydraulic aperture using local pressure values resulted in an error difference of -28 % compared to the mean mechanical aperture (Figure 4.29a). On the other hand, using external pressures to estimate the hydraulic aperture exacerbated the deviation to -70.18% from the mechanical aperture (Figure 4.29b) and, consequently, underestimated the flow capacity of the fractures studied. Hydraulic apertures are expected to have lower values compared to the mean mechanical aperture due to tortuous flow caused by the variation in the fracture aperture (Hakami & Larsson, 1996). However, external pressure measurements may not accurately capture this effect.

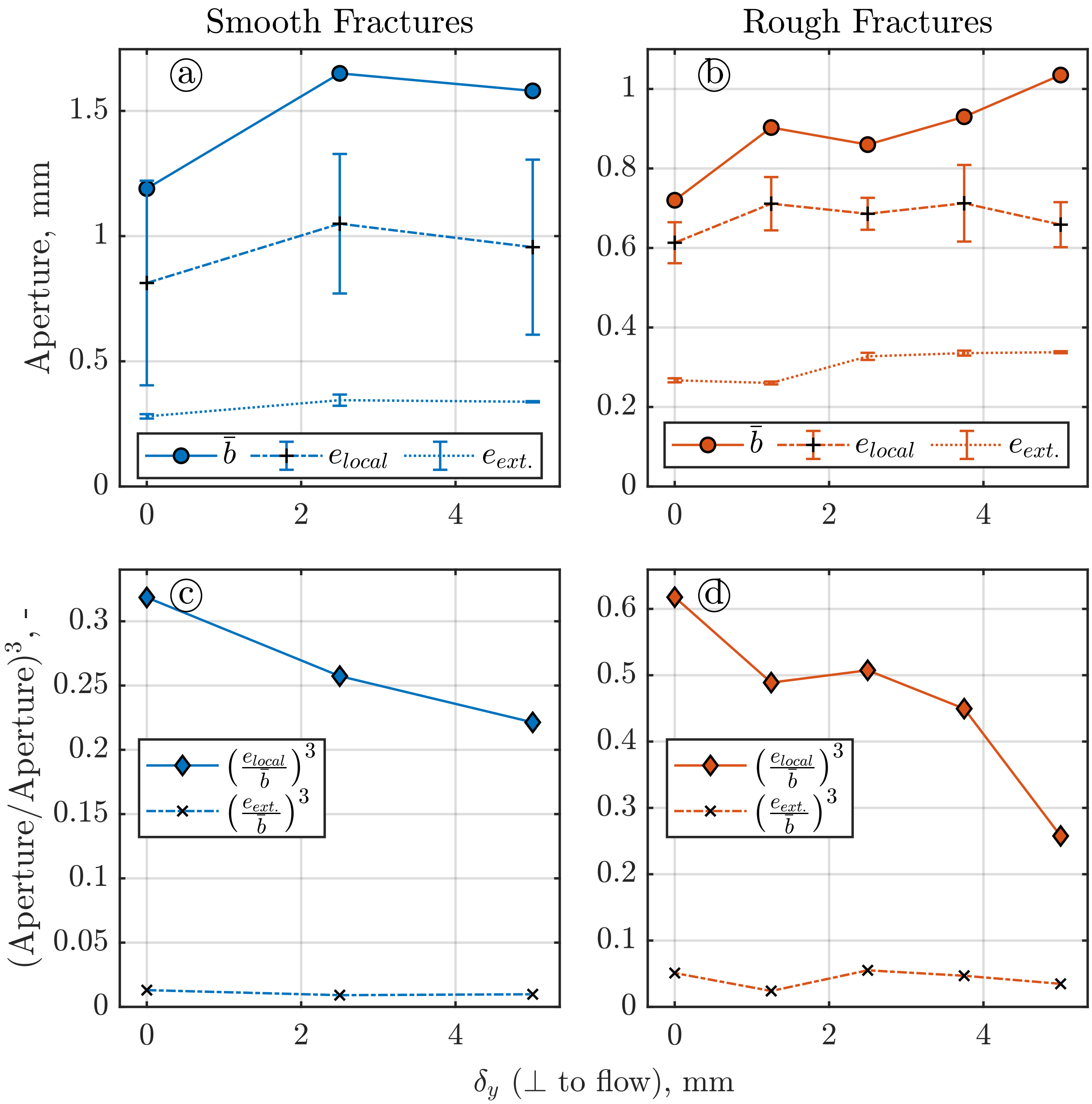

Figure 4.28: Fractures apertures. (a) *SF* samples mean mechanical aperture and hydraulic apertures. (b) *RF* samples mean mechanical aperture and hydraulic apertures. (c) Apertures ratio for*SF* specimens. (d) Apertures ratio for *RF* specimens.

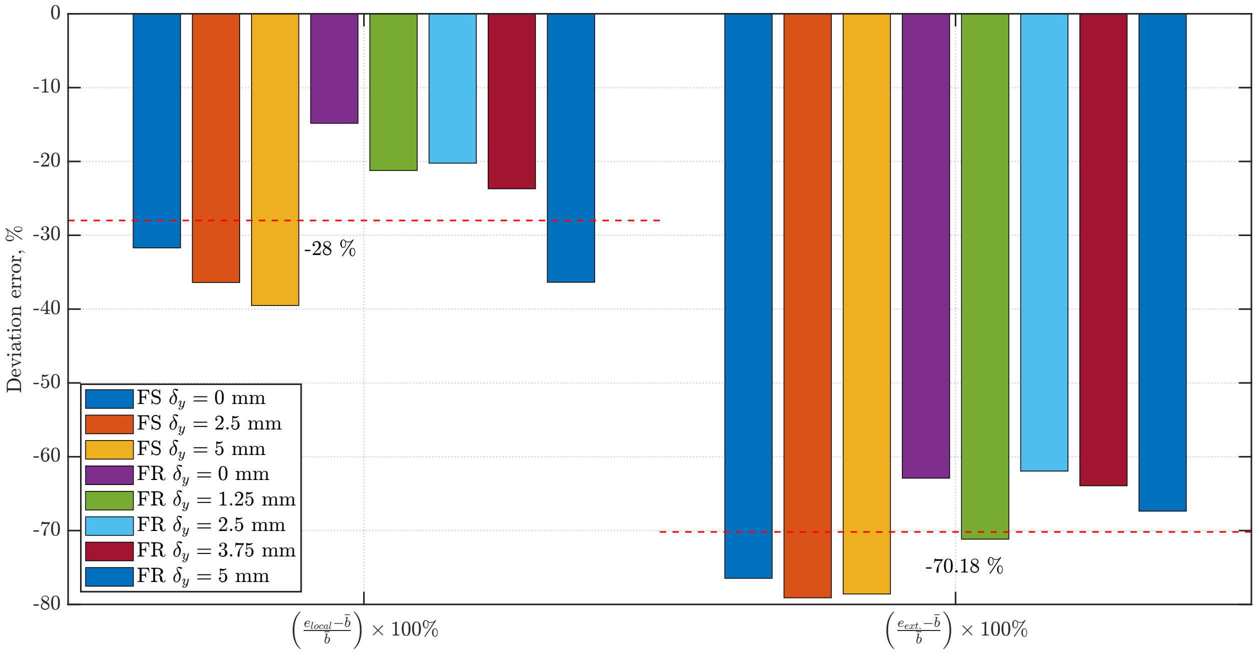

Figure 4.29: Deviation error between hydraulic aperture and mechanical aperture (a) using local pressure measurements and (b) external measurements.

Figure 4.30 shows the relative error calculated between the hydraulic apertures obtained experimentally (i.e., e_{local} and $e_{ext.}$) and several cubic-law-based approaches e_{model}. On each box, the bottom and top edges of the box indicate the 25th and 75th percentiles, respectively. The red line shows the median, the green diamonds the mean, and the whiskers extend to the most extreme data points; the red cross is an outlier. For e_{local}, the error was computed as follows $\frac{(e_{model}-e_{local})}{e_{local}} \times 100\%$. Similarly for $e_{ext.}$, the error was estimated from $\frac{(e_{model}-e_{ext.})}{e_{ext.}} \times 100\%$. Overall, the local hydraulic aperture demonstrated less deviation from the estimates provided by the cubic-law models, ranging from -3.71% to 37.26%. Similarly to other studies (C. Cheng et al., 2020; He et al., 2021), models 1, 2, and 3 are among the models that produce the best results.

Despite a broad variation in local pressures and a wide range of hydraulic apertures, using local pressures provided greater accuracy compared to external differential sensors, as corroborated by the analytic cubic law models (Figure 4.30a and 4.30b). Local differential pressure measurements may reduce uncertainty in estimated pressure drops, but additional research is needed to enhance this methodology.

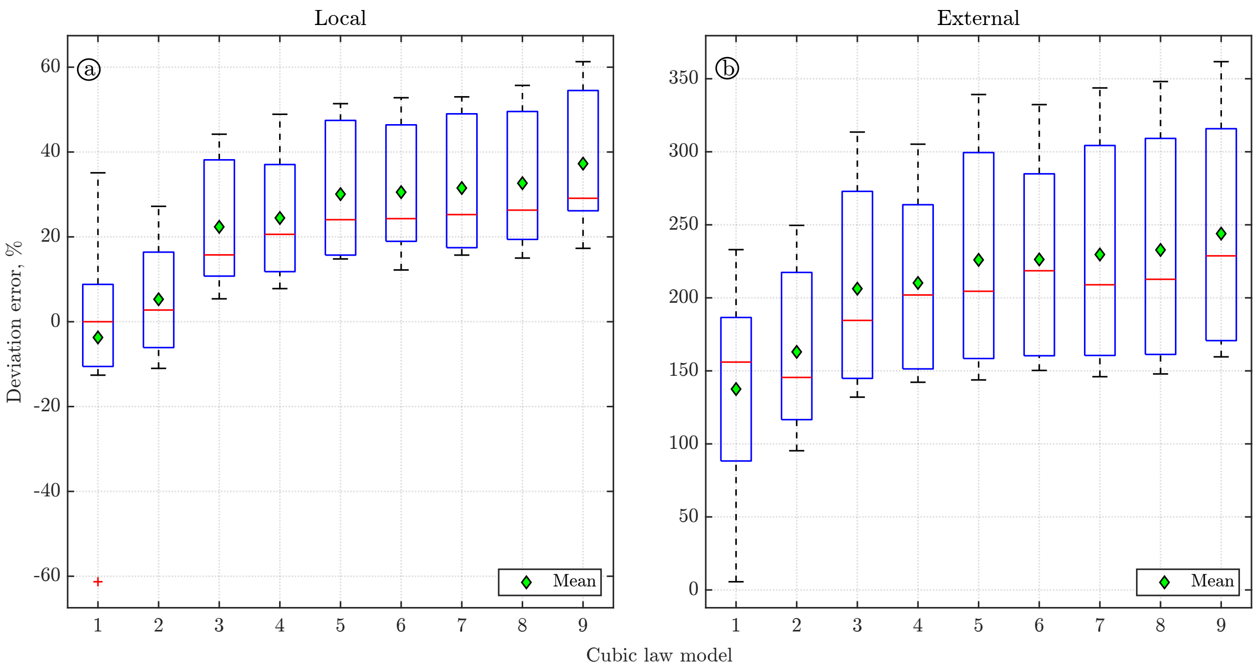

Figure 4.30: Deviation error between experimental hydraulic aperture and estimates from cubic law models using (a) local hydraulic apertures and (b) external hydraulic apertures.

4.4.5 Comparison to Numerical Modeling

The calculated average local pressures were compared with 3D *NS* and 2D *LCL* numerical simulations to have an approximation of the accuracy of the experimental pressure drop (Figure 4.31). For this, the average outlet pressure ($\bar{p}_{out}$) was subtracted from the experimental values ($\bar{p}_{in}$, $\bar{p}_{mid}$ and $\bar{p}_{out}$) to estimate a pressure drop between the sections of the fractures.

The difference between the average local pressure drops and the average simulated pressure profiles tended to be greater for the *SF* samples (Figure 4.31a-c), which was probably due to the greater variation of the local pressure measurements in these samples. On the contrary, the difference between these data sets was smaller for the *RF* samples (Figure 4.31d-h). In any case, these results indicated that the local pressure drops calculated using the measured data were closer to all types of numerical simulation. This suggested that local pressure measurements provided a better approximation of the actual pressure across the fractures studied compared to external pressure measurements. The fact that the average pressure profiles of the 3D *NS* numerical simulations were close to the 2D *LCL* profiles suggested that the flow inertia effects were low. The model *LCL* 1 seemed to perform better than *LCL* 2 because its average pressure drop was closer to *NS* simulations.

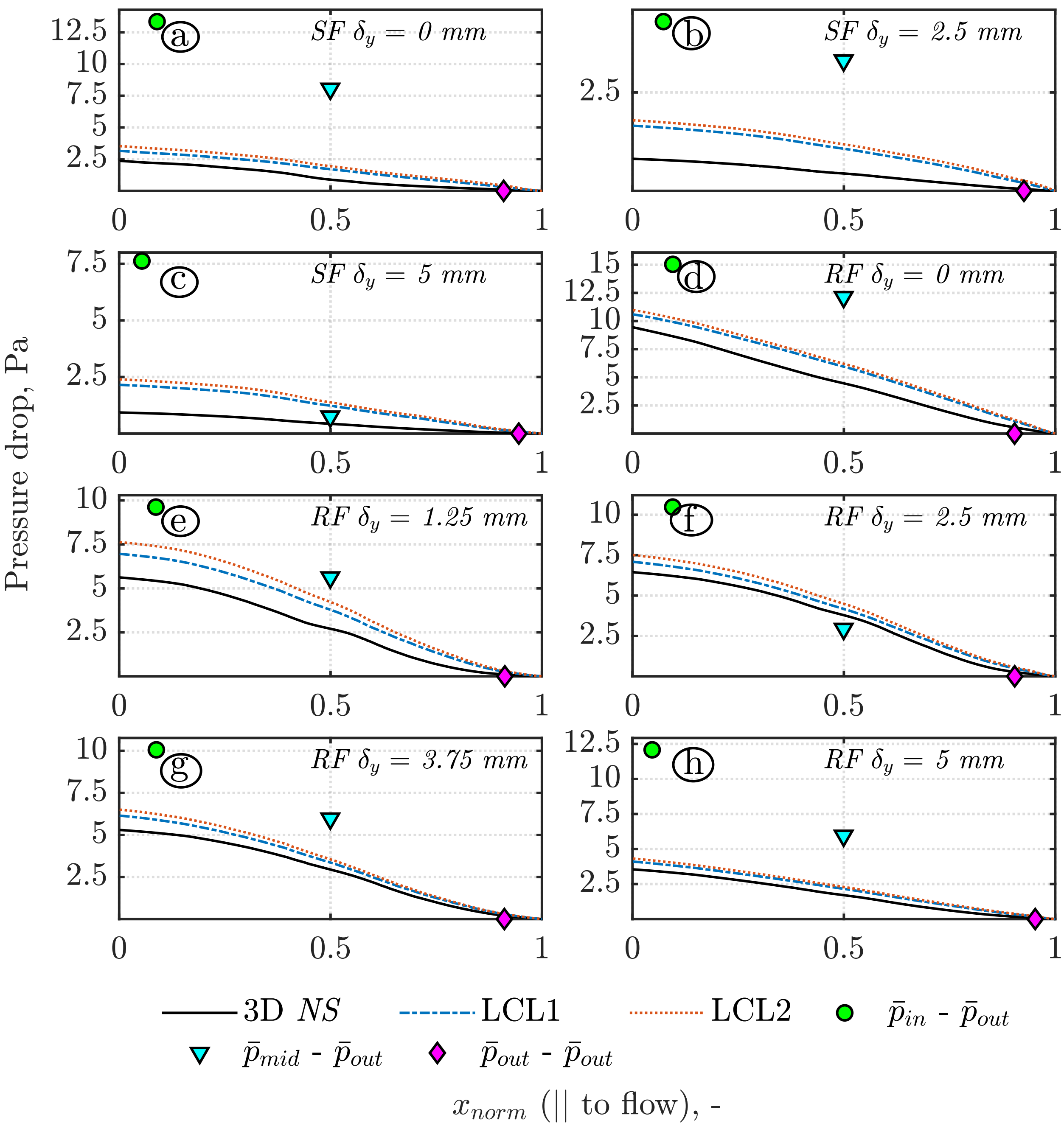

Figure 4.31: Comparison of numerical modeling of incompressible 3D *NS* equations and 2D *LCL* approaches to experimental local pressure measurements — q = 27 mL/min (a) - (c) *SF* samples and (d)-(h) *RF* samples.

4.5 Conclusions

This study reported on the relevance of local pressure measurements for estimating the hydraulic aperture of individual joints in laboratory experiments. PolyJet 3D-printed fractures of two types of roughness and at different shear displacements were used to experimentally and computationally investigate flow through single fractures.

Two fracture surfaces were produced digitally and their roughness properties were obtained. These topographies were embedded in 3D solids and 3D-printed to create fracture specimens. For each fracture, the aperture map was experimentally obtained, local pressure values were measured at a constant flow rate, and the hydraulic aperture was estimated using external pressure measurements and fiber-optic local pressure readings. The experimental hydraulic apertures were compared to a set of analytic cubic law models. The comparison served as a reference for the magnitude of error in the experimental estimates. In turn, the local aperture maps were used in numerical simulations, which were compared with the experimental local pressure drops.

The analysis of surface roughness through different methods indicated that the fractal-based variogram method correlated with parameters of spatial variation. However, additional statistical parameters were required to characterize the amplitude behavior of the fracture surfaces. Analysis of the experimental aperture maps indicated that shear displacement increased the variability of the aperture values. Based on the data analysis, it was estimated that shear displacements perpendicular to the flow predominantly contribute to higher aperture variability in the direction parallel to the flow. However, improving imaging processing and laboratory visualization processes could help to better observe this phenomenon in experimental aperture maps. Additionally, PolyJet 3D-printing technology demonstrated potential in fracture visualization studies.

Regardless of the fracture properties, surface roughness increased the average local pressure drops in the samples. Using external pressure measurements to estimate the pressure drop across the fracture specimens increased the difference between the mean mechanical apertures and consequently underestimated the hydraulic apertures. Comparatively, using locally averaged pressure measurements reduced the deviation error to -28 %. However, using the external pressure values resulted in an error of -70.18 %. Furthermore, the experimental local hydraulic aperture exhibited less deviation from the estimates provided by the cubic-law models, ranging from -3.71% to 37.26%. Thus, these findings indicated that the hydraulic apertures estimated from local apertures were closer to the mean mechanical apertures and that cubic law models could be more accurate in predicting hydraulic apertures than using external pressure measurements.

The average pressure profiles of the numerical simulations were closer in range to the average local pressure drops, which in turn showed that the local pressure measurements provided a better approximation of the actual pressure in the fractures studied than the external pressure measurements. This research highlights the importance of employing local pressure measurements in experimental studies of flow through fractures and demonstrates the advantages of 3D printing and fiber optic sensors in such investigations.

4.6 Data Availability Statement

Experimental data is available online at the following address https://zenodo.org/records/7384370. Diagrams were created in open-source computer graphics software Blender version 3.2. Data processing and figures were made with Matlab version R2021a license number 1088131.

Chapter 5

The Influence of Displacements Arising From Shear Motion on Two-Phase Flow through 3D-Printed Fractures

S. Lopez-Saavedra, G. Zambrano-Narvaez, S. Ishutov and R. Chalaturnyk (a version of this manuscript has been accepted for publication in the Geoenergy Science and Engineering Journal). Experimental data, alongside high-resolution figures, can be accessed from https://doi.org/10.1016/j.geoen.2024.212731.

5.1 Overview

Fractures can constitute a large portion of the pore volume in a hydrocarbon reservoir and, consequently, undertake substantial deformation during production activities. However, numerous experimental studies on immiscible two-phase flow through fractures have relegated deformation. While the impact of surface roughness and aperture changes has been addressed, data are absent concerning the effect of shear deformation in these types of studies. Therefore, this investigation examined this subject by utilizing 3D printing to visualize experiments, control fracture roughness, and incorporate shear displacements. Drainage experiments where water displaces silicone oil at a constant injection rate were conducted on synthetic fractures of a smooth and a rough surface type. These experiments involved increasing shear displacements perpendicular to flow and increasing mean fracture aperture values. Surface roughness was measured using the fractal dimension obtained from the variogram method. Fluid saturations were estimated through image processing, and the displacement patterns were analyzed through the fractal-based box-counting method. The image analysis of the two-phase flow displacements at water breakthrough indicated that surface roughness and displacements arising from shear motion could lead to a flow regime where capillary effects are more prevalent. Surface roughness was observed to affect the efficiency of the oil swept. Smooth fracture samples facilitated oil recovery before water breakthrough, but afterward, water channeling predominated over oil sweeping. Additionally, oil recovery exhibited a concave behavior with respect to shear displacements, with an increase in oil recovery from zero to mid-shear displacements, followed by a decrease in oil recovery at higher shear displacements. On the other hand, pressure measurements from two-phase flow displacements exhibited features that suggest the degree of surface roughness and the displacements resulting from shear motion altered their response. This research demonstrates the potential of 3D printing in the study of fluids flow through fractures and represents pioneering results on the effects of shear deformation in fractures on two-phase flow.

5.2 Introduction

Understanding the flow of fluids in permeable faults and fractures is essential for comprehending the production behavior of hydrocarbon reservoirs. These geologic features may experience significant geomechanical changes throughout a reservoir's lifecycle. Nowadays, many experimental studies focus on investigating the flow of non-reactive fluids through rock fractures as a coupled process between geomechanics and fluids. However, initial studies characterized the hydraulic and mechanical behavior of individual fractures separately. Some of the earliest experiments examined flow through a fracture by conceptualizing it as flow through parallel plates. These experiments revealed that surface roughness and fracture aperture influenced the onset of turbulence (Huitt, 1956; Lomize, 1951; Louis, 1967; Parrish, 1963; Romm, 1966). Meanwhile, studies in fracture mechanics developed models to describe fracture behavior under normal (Bandis et al., 1983) and shear loading conditions (N. Barton, 1972), as well as to describe the relationship between normal stress and roughness towards peak fracture shear-strength (N. Barton & Choubey, 1977).

Later, some investigations have created synthetic fractures with different mean apertures and developed methodologies to obtain local apertures (Detwiler et al., 1999; Isakov et al., 2001; Kishida et al., 2013; Konzuk & Kueper, 2004; Nicholl et al., 1999). On the other hand, many have investigated different aspects of the effect of normal stress on monophasic flow through a single fracture. For example, some studies have described its effect on the hydraulic behavior of a fracture (Phillips et al., 2021; Pyrak-Nolte et al., 1987; Witherspoon et al., 1980). In this field, some researchers have investigated the conditions for the emergence of non-linear flow (Y.-F. Chen et al., 2015; Y. Chen et al., 2019; Ranjith & Darlington, 2007; Ranjith & Viete, 2011).

Numerous hydro-mechanical investigations have demonstrated that shear motion induces displacements that alter the hydraulic properties of a fracture (Crandall et al., 2017; Esaki et al., 1991; Gentier et al., 1997; Giger et al., 2011; Ishibashi et al., 2020; H. Lee & Cho, 2002; W. Olsson & Brown, 1993; W. A. Olsson, 1992). In addition, a significant number of monophasic studies has described the role of surface roughness for a sheared fracture (Archambault et al., 1997; Boulon et al., 1993; Z. Chen et al., 2000; Fang et al., 2019; Hans & Boulon, 2003; Kwafniewski & Wang, 1997; Sharifzadeh et al., 2017). Some publications have evaluated cubic law-based models on single fractures under shear stress (Esaki et al., 1991, 1999; B. Li et al., 2008; Mofakham et al., 2018; R. Olsson & Barton, 2001; Xiong et al., 2011). Other researchers have detailed how shear displacements influence directional permeability (Auradou, 2009; Auradou et al., 2005; Auradou et al., 2001; Yeo et al., 1998), while others have examined the influence of shear stress on non-linear flow (Cao et al., 2019; Javadi et al., 2014; Koyama et al., 2008; Q. Yin et al., 2017).

With respect to two-phase flow through fractures, researchers have examined the subject under static mechanical conditions attempting to establish an adequate model to describe the relative permeability in fractures (C.-Y. Chen et al., 2004; Fourar et al., 1993; Pan et al., 1996; Pieters & Graves, 1994; Speyer et al., 2007). In turn, some studies have analyzed the effect of surface roughness on two-phase flow through fractures (Babadagli et al., 2015; C.-Y. Chen & Horne, 2006; Diomampo et al., 2001), models to describe non-Darcian flow (Nowamooz et al., 2009; Radilla et al., 2013), and capillary pressure in fractures (Bertels et al., 2001; Persoff & Pruess, 1995). On the other hand, others have investigated the effect of normal stress on relative permeability (Huo & Benson, 2016) and capillary pressure (Reitsma & Kueper, 1994). The review of the aforementioned literature indicates that historically, non-reactive flow through fractures has been mainly studied under monophasic conditions (Figure 5.1a). Moreover, there is a clear absence of experimental data regarding the effect of shear on two-phase flow through fractures (Figure 5.1b), as evidenced by the gap in the available data in the categories 7 to 9 of this figure. Shear stress on fractures is essential because it can considerably modify the fracture aperture under different mechanical boundary conditions (Y. Jiang et al., 2004). However, its effects on two-phase flow through fractures have not been studied. The use of 3D printing in experimental scientific projects has become more frequent because of its applicability in different areas. Polyjet 3D printing has demonstrated potential in studies of flow through fractures because it has unique advantages compared to other sample generation methods or materials. For example, it can be used to obtain control on fractures morphology (Cunningham et al., 2020; Suzuki et al., 2017), reproduce digital models with high precision (Fang et al., 2018), attain sample repeatability (Ishibashi et al., 2020) and visualize experiments (W. Yang et al., 2020). Because of these advantages, this type of 3D-printing has been used to experimentally evaluate fracture network permeability (Suzuki et al., 2019), investigate flow anisotropy (J. Xie et al., 2020) and non-linear flow effects (P. Yin et al., 2020; Y. Zhang et al., 2022). Based on the above, the objective of this investigation is to study the influence of displacements resulting from shear motion on two-phase flow through fractures. This study employs an approach that thoroughly explores the potential of polyjet 3D printing. This technology allows for the visualization of experiments, control of fracture roughness, use of local pressure measurements and the incorporation of shear displacements— capabilities that are difficult to simultaneously attain with natural rock samples. The experimental process first involved digitally generating two types of fracture surfaces and estimating their roughness degree. These surfaces were digitally integrated into 3D solids and were reproduced through 3D printing. These models were used to form 3D-printed fractures and conduct two-phase flow experiments at different shear displacements, which were visualized to estimate fluid saturations and recovery. These data were analyzed to assess the effect of surface roughness and shear displacements on two-phase flow through fractures.

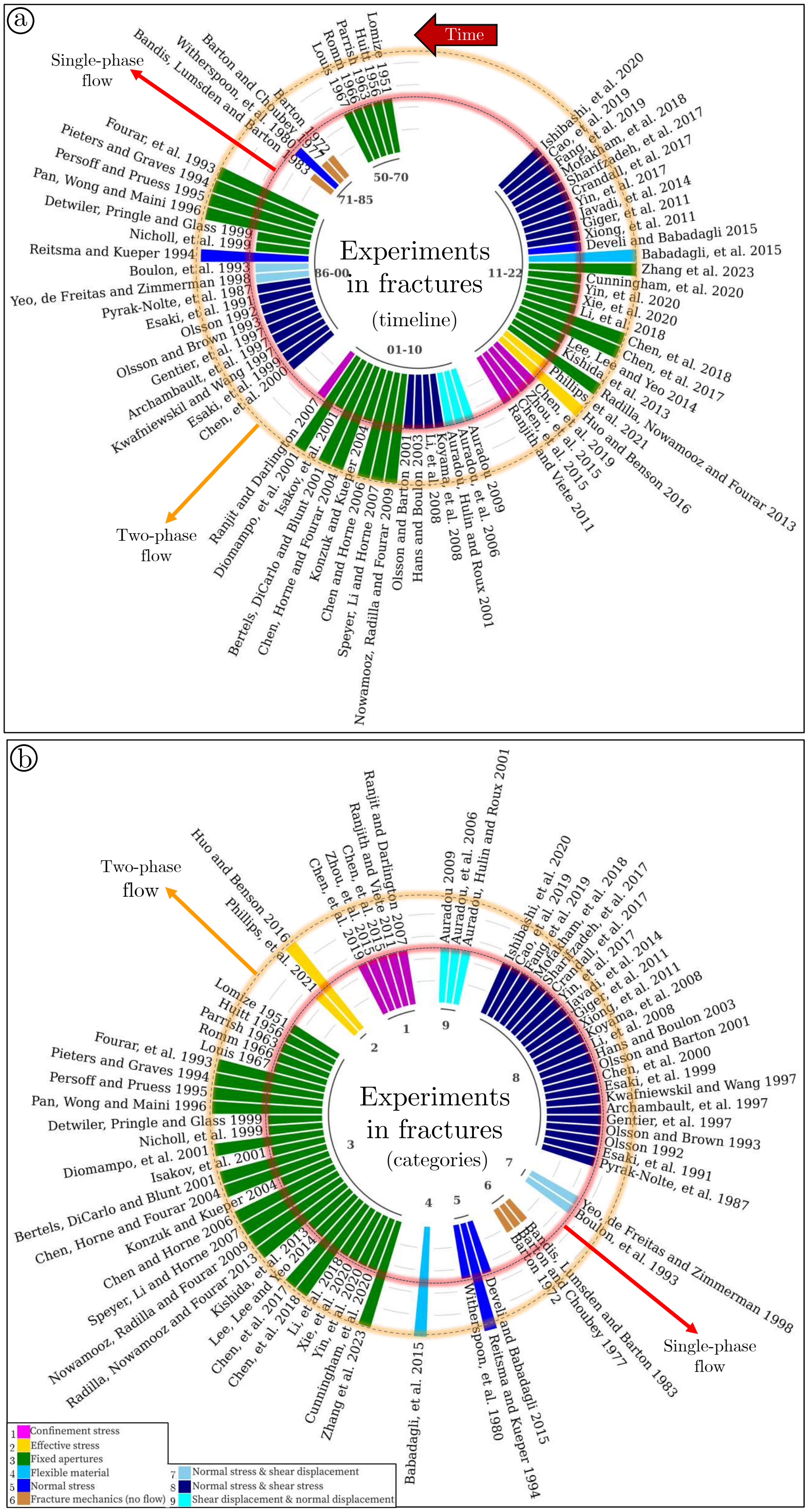

Figure 5.1: Literature review on experiments in fractures. Bars within the inner circle correspond to single-phase experiments, while bars in the external circle correspond to two-phase flow studies: (a) Literature in a timeline; (b) Literature organized per applied mechanical conditions.

5.3 Materials and Experimental Methodology

5.3.1 Preparation of 3D-Printed Fractures

Digital Synthetic Rock Surfaces

The Perlin noise algorithm (Perlin, 1985), implemented through the software Blender, was used to create fracture topographies with different roughness degrees. This method involved creating a grid of randomly generated normalized gradient vectors, calculating the dot product of these vectors with their respective neighbors, and then performing interpolation between the resulting values (Gustavson, 2005).

The methodology employed in this study may not be strictly identical to typical approaches used to model fracture roughness. Fracture models generally fall into two categories, some generate fracture aperture based on measurements (Tsang, 1984) or analytical functions (Tsang & Tsang, 1987), while others create fracture geometry using fractal models (Brown, 1987). The parameters distinguishing between these model types have been addressed elsewhere (Di Federico & Neuman, 1997).

Two types of fracture topographies were produced by applying a *clouds* texture to a 155×155 mm grid and varying the software parameters (Table 5.1) to create synthetic surfaces of 155×155 mm with 1,025 profiles in each direction, with a resolution of ~151 μm for both directions. This resolution permits high-detail surfaces while accounting for the polyjet 3D printer capability and the size of the generated binary and ASCII stl files.

In this study, rough surfaces had a resolution of ~151 μm in the $x-$ and $y-$ directions. This resolution was selected so that the surfaces had sufficient detail, and simultaneously the binary *stl* file could be handled by the 3D printer software, and the resolution was practical for the CAD modeling software. Additionally, the resolution of the ASCII *stl* file had to be practical for roughness characterization in Matlab software. The resultant *stl* file sizes were ~100 MB for the binary and ~367 MB for ASCII.

Parameter character	Parameters	Type 1 surface	Type 2 surface
Texture	Size	0.5	0.05
	Depth	2	5
Displace Modifier	Nabla	0.03	0.03
	Strength	0.003	0.001
	Midlevel	0.5	0.5

Table 5.1: Parameters for fracture surface generation in Blender.

A fracture composed of the type 1 surfaces (Figure 5.2a and 5.2b) was referred as a SF, and one formed from the type 2 surfaces (Figure 5.2c and 5.2d) was referred as a RF.

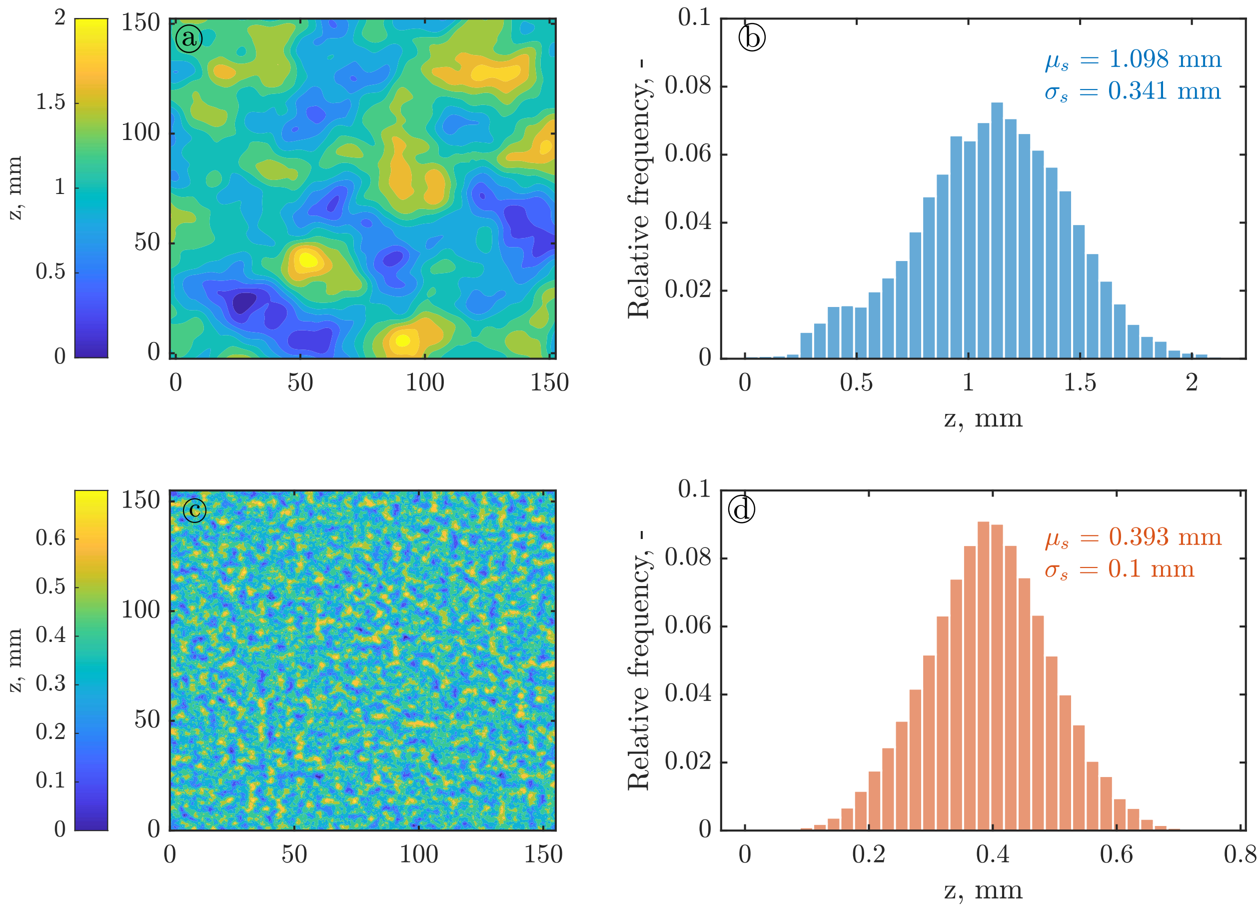

Figure 5.2: Synthetic fracture surfaces: (a) Type 1 surface; (b) its relative frequency histogram of the elevation values with $\mu_s = 1.098$ mm and $\sigma_s = 0.341$ mm; (c) type 2 surface; (d) its relative frequency histogram of the elevation values with $\mu_s = 0.393$ mm and $\sigma_s = 0.1$ mm.

Design of Fracture Parts and Experimental Cell

To produce upper and lower fracture parts, sections of 150 $\times$ 150 mm were extracted from the synthetic rock topographies at different y-direction displacements (Figure 5.3a and 5.3b), and these sections were embedded into upper and lower solid models. The upper half-solid model was designed with eight peripheral orifices for 1/4-in screws (Figure 5.3c). The lower half-solid model included ten pressure ports distributed in three columns with a 1-mm diameter cylindrical cavity designed to connect the fracture topography with the ports. Integrating the fracture topographies with the solid models completes the digital design of the fracture parts. For both fracture types, the top parts were 3D-printed once, embedding surfaces with zero displacement. The *SF* lower parts were printed integrating surfaces at y-direction displacements of 0, 2.5, and 5 mm, while the *RF* lower parts were printed incorporating surfaces at y-direction displacements of 0, 1.25, 3.75, and 5 mm. Producing 3D-printed parts in this manner enabled the manufacturing of 3D-printed fractures with shear displacements perpendicular to flow, ranging from 0 mm (δ_y = 0 mm) to 5 mm (δ_y= 5 mm). Shearing deformation of 2.5 mm could be associated with seismic movements of magnitude 1-2 (Marchand et al., 2019), and such magnitudes have been reported in hydrocarbon production fields (Ottemöller et al., 2005).

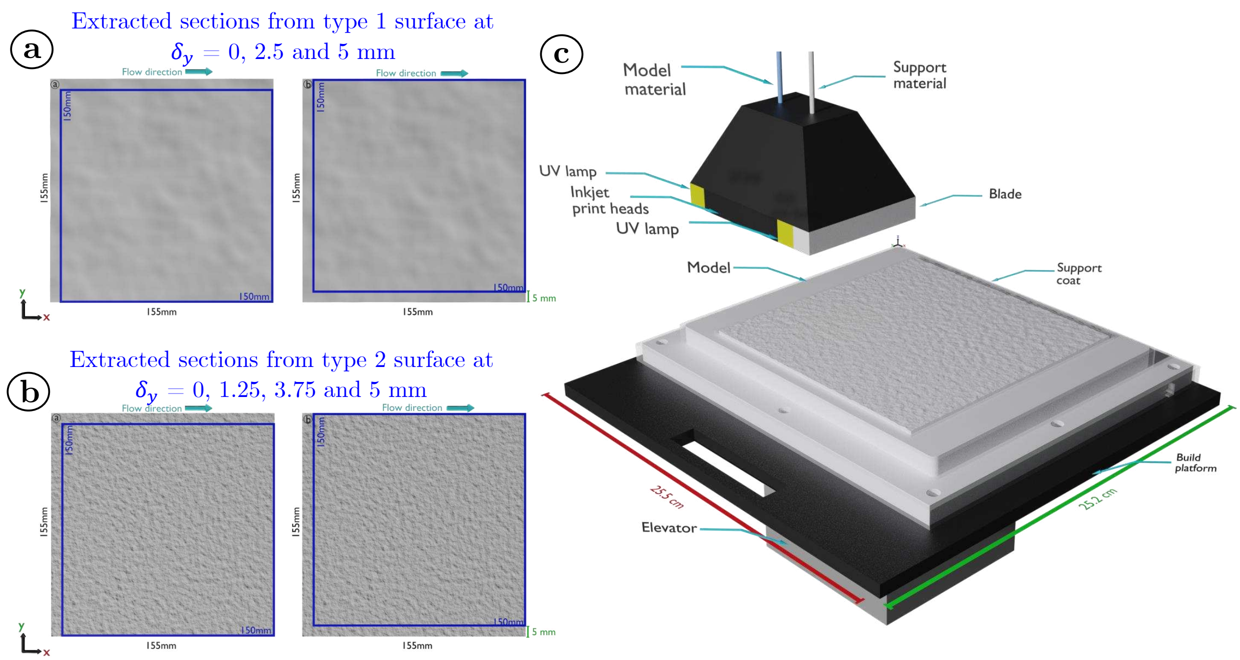

Figure 5.3: Placement of fracture topography into solid models: (a) Type 1 surface extracted sections at δ_y = 0 mm and δ_y = 5 mm; (b) type 2 surface extracted sections at δ_y = 0 mm and δ_y = 5 mm; (c) top solid model with embedded fracture topography.

3D Printing Fracture Replicas

The fracture samples were 3D-printed with a Stratasys Eden 260 VS operated by the Reservoir Geomechanics Research Group at the University of Alberta. This equipment jets layers of two types of photo-polymers, which are solidified with ultraviolet light (Gibson et al., 2021). The *model* photo-polymer solidifies into a rigid plastic-like material, the *support* photo-polymer cures into a wax that supports the voids in the part and must be removed after finalizing the printing process. The specifications of the 3D printer are available elsewhere (Saavedra et al., 2020). The model material used is VeroClear printed with a matte finish and the support material is SUP707. The advantages of using these materials together are high-quality printing (Stratasys, 2015) and maximum clarity (Stratasys, 2016). On the other hand, the average contact angle for VeroClear and water was 78° (Figure 5.4), measured on a flat surface using VCA Optima equipment. Silicone oil was completely spread on VeroClear, indicating an oil-wet behavior. Additional properties of VeroClear can be consulted externally (Macdonald et al., 2017; L. Wang et al., 2017).

The average contact angle for VeroClear and water was 78° (Figure 5.4) taken with VCA Optima equipment. Silicone oil was completely spread on VeroClear, indicating an oil-wet behavior.

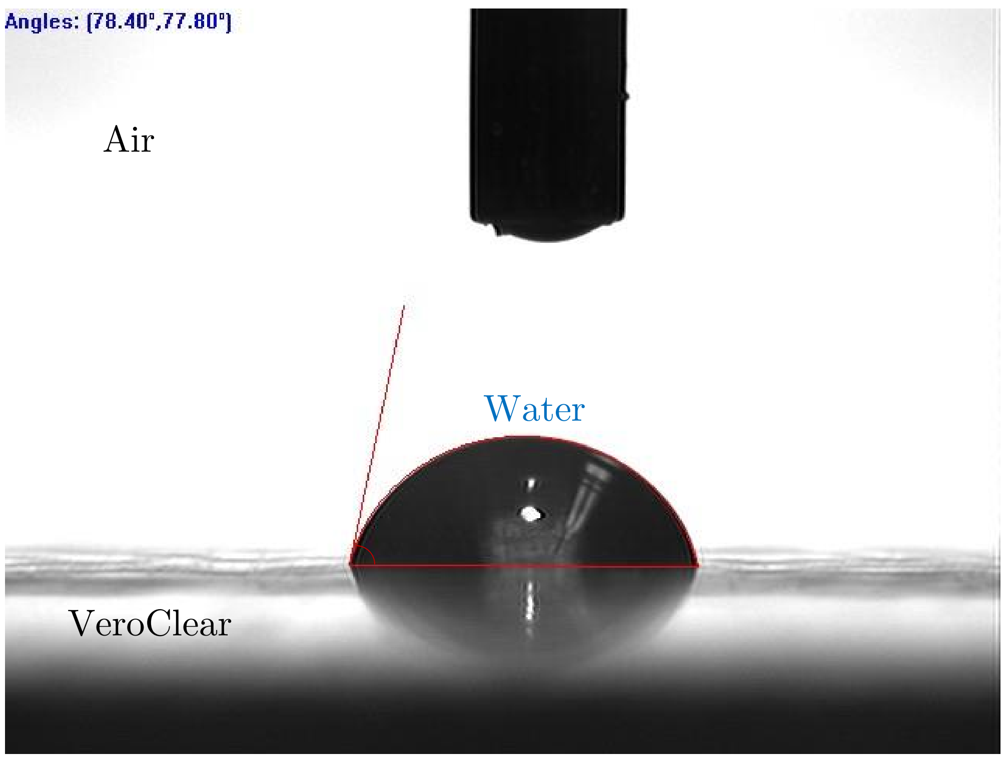

Figure 5.4: Wettability of VeroClear and water.

Post-Treatment of 3D-Printed Samples

After completing the 3D printing process, the samples were submerged and washed individually in a DT3 clean station for four hours at a temperature of 32 to 47°C to dissolve the external support material. Subsequently, the samples were washed individually in the DT3 station in a caustic soda (NaOH) 0.02 g/cm^3 solution for four hours at a temperature of 32 to 47°C. Afterward, the models were rinsed with water, and the pressure sensor ports on the lower models were scraped with a spatula and water-jetted. Each specimen was dried with fluorescent light for 12 hours. To improve clarity, the non-textured side of the models was wet-sanded with sandpaper (#800, #1000, and #2000), and finally, a polishing compound was applied to the surface not exposed to flow.

5.3.2 Roughness of Fracture Topography

This study quantified the stationary roughness through the fractal-based variogram technique, which yielded three parameters for each one-dimensional profile, i.e., the amplitude γ_0 the Hurst exponent H and the fractal dimension D (P. H. S. W. Kulatilake et al., 2006). A fractal dimension is a scale-independent parameter that describes how a component of a smaller size fills a higher dimension object (Mandelbrot & Blumen, 1989). Fractal geometry enables inferring the characteristics of an unobserved scale based on properties identified at a different scale (Kwafniewski & Wang, 1997). There are self-similar and self-affine fractals. The former are patterns that are equal at different scales, and the latter are similar when scaled anisotropically (Dershowitz et al., 1992). Thus, geologic features such as fault surfaces and fracture topography can be considered to have a self-affine character (C. C. Barton & La Pointe, 1995).

A premise of this study was that the one-dimensional profiles complied with the self-affinity condition (Méheust & Schmittbuhl, 2001). The mentioned fractal parameters were determined from a variogram for each profile in the x- and y-direction. Then, an average value was obtained for each direction and these two values were averaged for an overall parameter.

The variogram $\gamma(h)$, is defined as half the average squared difference between the paired data points (Isaaks & Srivastava, 1989):

$$\gamma\left(h\right)=\frac{1}{|2N(h)|}\sum_{(i,j)|h_{i,j}=h}^{2}\left(z_i-z_j\right)^2 \tag{5.1}$$

Where h is the lag distance between measurements, $N(h)$ is the number of pairs separated by h, $z_i - z_j$ is the height difference between the data values i and j. Additionally, a portion of the variogram of a self-affine profile behaves like a power law model such that $\gamma(h) = \gamma_0 h^{4-2D} = \gamma_0 h^{2H}$, where, H is the Hurst exponent, γ_0 is the amplitude, where for a profile $D = 2-H$ where D is the fractal dimension (Murata & Saito, 1999). The parameters H and γ_0 can be obtained from the slope (i.e., $4 - 2D$) of the linear portion of the plot $\log(\gamma(h))$ vs $\log(h)$ (Klinkenberg, 1992; P. H. S. W. Kulatilake et al., 2006; H. Xie et al., 1997).

The minimum suitable lag distance was calculated using a well-known model (P. Kulatilake et al., 1998). Then, the variogram was computed for a maximum lag distance smaller than half the entire profile length, as suggested (Dowd, 1984; Klinkenberg, 1994). The subsequent step involved estimating the slope of the linear portion of the log-log variogram plot. Typically, 10% of the profile length is adequate (Babadagli & Develi, 2003) however, in this study, this linear section was shorter ~3-5% and was defined considering a threshold value for the correlation coefficient (R^2) and root mean squared error (RMSE) of the fitted data. The threshold values were $R^2 \geq 0.94$ and $\frac{RMSE}{\log(\gamma(h))_{max} - \log(\gamma(h))_{min}} \leq 22\%$.

The second-order stationary requirement (P. H. S. W. Kulatilake et al., 2021), namely the absence of a global trend in the surface profiles, was verified by calculating the mean angle of inclination expressed as (Belem et al., 2000):

$$\theta_p = \tan^{-1}\left(\frac{1}{n-1}\sum_{i=1}^{n-1}\left|\frac{z_{i+1} - z_i}{\Delta x}\right|\right) \tag{5.2}$$

Where $\Delta x = x_{i+1,j} - x_{i,j}$: x-coordinate spacing and n is the total number of measurements. This parameter was calculated per profile in the x- and y-direction and subsequently a single average value is calculated per direction. However, to obtain global trend angles, the absolute value was not applied to the local slopes (i.e., $\Delta z/\Delta x$). For surface type 1, the θ_p in the x- and y-direction were equal to $-9.04 \times 10^{-3\circ}$ and $7.00 \times 10^{-4\circ}$, respectively. For surface type 2, this value was $2.22 \times 10^{-4\circ}$ and $-2.54 \times 10^{-4\circ}$ for each direction.

5.3.3 Experimental Configuration

The experimental configuration used in this study consisted of two positive displacement pumps (Vindum maximum injection rate 30 cm^3/min with a ± 0.1% accuracy), an aluminum cell with two inlet/outlet manifolds on the flanks for better fluids distribution, and inlet/outlet connection ports. Transparent 3D-printed upper and lower parts were placed in the cell to form fracture replicas for flow testing (Figure 5.5). A 3D-printed (TangoBlack FLX973 material) rectangular rubber-like face seal was employed to seal the upper half with the aluminum cell and confine the fluid in the fracture. The setup included a CCD camera (Basler acA1300-30 gc with a C125-1218-5M lens) placed above the cell to capture the two-phase flow experiments. A LED light source (The Big Orchard, A4) with brightness control was placed below the fracture. Ten miniature fiber optic sensors of 0.3 mm diameter (Opsens Solutions OPP-MT) with a resolution of less than ~103 Pa and a scalable sampling rate of 20 to 1000 Hz (utilized with optical modules CoreSens 2-channel) were distributed to measure local pressure in the fractures. A data acquisition system (KeySight 34970A) was connected to a demodulator (Validyne CD15), which was used with a differential pressure sensor (Validyne DP15) to obtain the pressure difference between cell's inlet and the outlet.

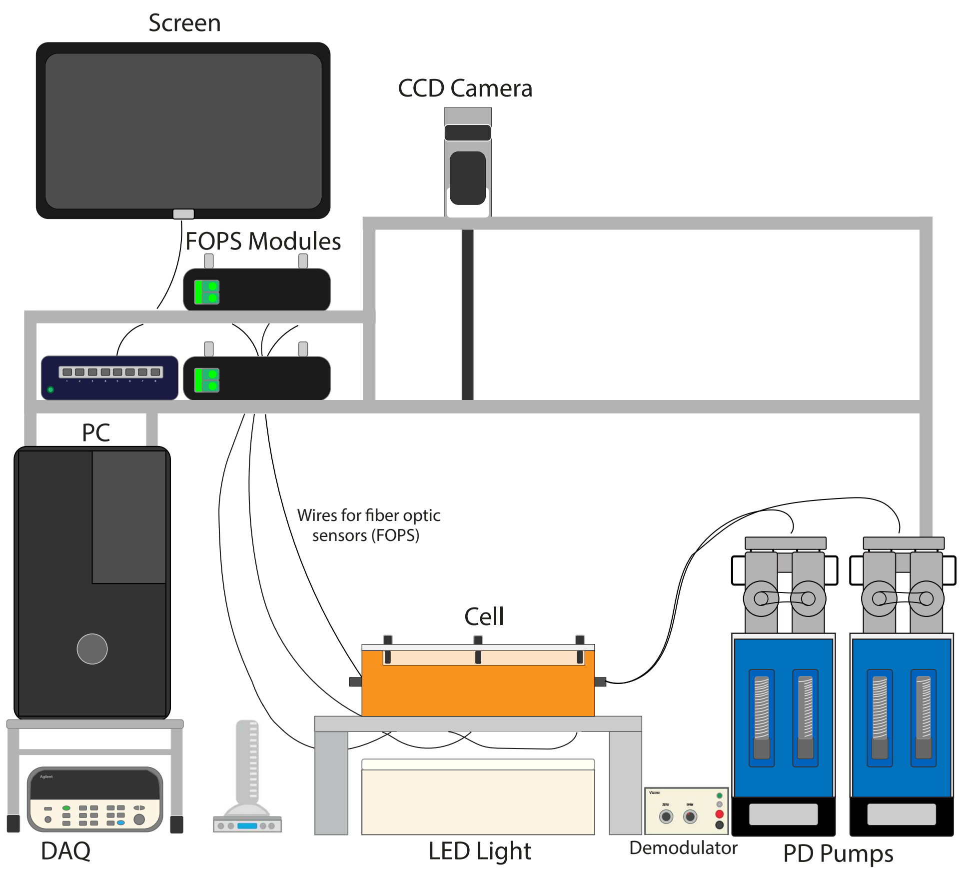

Figure 5.5: Experimental configuration.

5.3.4 Laboratory Testing

Testing Preparations

First, the lower half of the fracture was placed in the center of the aluminum cell on a 11/16-inch thick (1.5875 mm) border, and the entire cell's internal perimeter was sealed with silicone. This fixed the lower half of the fracture and prevented lateral and downward displacements. Then, the face seal was inserted into the designated gap in the aluminum cell. Additional silicone was applied to seal the front and back tiny gap between the lower half of the fracture and the rectangular seal for at least 24 hours. The tests were conducted at perpendicular-to-flow shear displacements by interchanging the lower half of the fracture. Fractures at $\delta_y = 0$ mm, were open and formed by two complimentary surfaces with no contact points. At this state, the fracture aperture should had been more uniform. For subsequent shear displacements, a mismatch of the surfaces occurred and induced spatial variations in the fracture aperture but without contact points; for SF samples at non-zero shear displacements, a 3D-printed flat shim of thickness 0.3 mm was placed below the seal to increase the vertical separation between surfaces. Analogously, a 0.2-mm flat shim was used for RF specimens.

In direct shear laboratory test conditions and under a constant normal stress, the typical behavior of fracture aperture is to increase after a short closure period (Javadi et al., 2014). Subsequently, as shear displacement increases, the aperture behavior ideally tends to be larger than the initial aperture, regardless of shear stress (e.g. Esaki et al. (1991)). In this study, this coupled mechanical behavior was replicated using 3D-printed fractures to control shear displacement and shims to increase the fracture aperture at different static mechanical conditions. This approach allowed to study the effects of shear displacement and surface roughness on two-phase flow through fractures without considering the effects of asperities degradation associated with shear stress.

Two-phase Flow Tests

First, the fracture cell was placed upright on its injection side, and a positive displacement pump was used to inject dyed distilled water at a rate of 10 cm^3/min to displace the air in the fracture cell. The injected volume was used to estimate the mean mechanical aperture $\bar{b}$ of the fracture specimen through a volumetric approach (Pan, 1999). The water was dyed with commercial food coloring Blue No. 1 at a concentration of 0.2% wt, equal to other studies (Y.-F. Chen et al., 2017, 2018). Afterward, an imbibition process was conducted to displace the water and saturate the fracture with silicone oil. Then, a drainage process was conducted to displace the silicone oil with distilled water at a constant flow rate of 40 cm^3/min such rate was selected to avoid capillary end effects and to attain a capillary number $Ca = \frac{\mu_w Q}{\sigma_{wo} A}$ (Dullien, 1979) in the $10^{-5} < Ca < 10^{-4}$ range. Where μ_w is the water viscosity, Q is the water flow rate, σ_{wo} is the interfacial tension, and A is the cross-sectional area of the fracture plane. Fluid properties considered are presented below (Table 5.2). A subsequent drainage process was conducted for the RF samples to examine hysteresis effects. Namely, after finalizing displacing silicone oil with dyed water, the fracture cell was re-saturated with silicone oil, and dyed distilled water was injected at 40 cm^3/min.

Parameter	Value
Water density $\rho_w, kg/m^3$	0.997[a]
Water viscosity $\mu_w, Pa-s$	0.0089[a]
Temperature, °C	25
Silicone oil specific gravity $\gamma_o, -$	0.818[b]
Silicone oil viscosity $\mu_o, Pa-s$	0.01[b]
Interfacial tension $\sigma_{wo}, N/m$	0.0359[c]

[a]The water properties were obtained from the National Institute of Standards and Technology (NIST) [b]The silicone oil properties were obtained from the supplier's datasheet https://parkesscientific.com/. [c]The interfacial tension was obtained from (Peters & Arabali, 2013).

Table 5.2: Summary of fluid properties.

Pressure Measurements

For each fracture, local pressure measurements were collected using three fiber optic sensors at the inlet, four at the middle and three at the outlet. Each sensor was carefully inserted into a 1/16-inch NPT fitting, which was subsequently connected to a local port in the lower section of a 3D-printed fracture. Data collection operated at a frequency of 20 Hz; however, local measurements were processed as an average per second. Externally, the differential pressure sensor captured readings between the cell's inlet and outlet.

Calculation of Fluids Saturation

The CCD camera was used to capture images of the 3D-printed fractures during the fluid displacements. The color contrast between the dyed distilled water and the silicone oil allowed for image processing using Matlab to estimate the fluid saturations. The square central section of the images of approximately 140×140 mm was processed utilizing a color threshold because it was found that, for these sections, color thresholding, rather than segmentation based on intensity values, minimized the artifacts when calculating the saturations at the local pressure ports (Figure 5.6a-5.6f). The four smaller perimeter images of ∼10 ×140 mm were processed by converting them to grayscale and applying an intensity threshold.

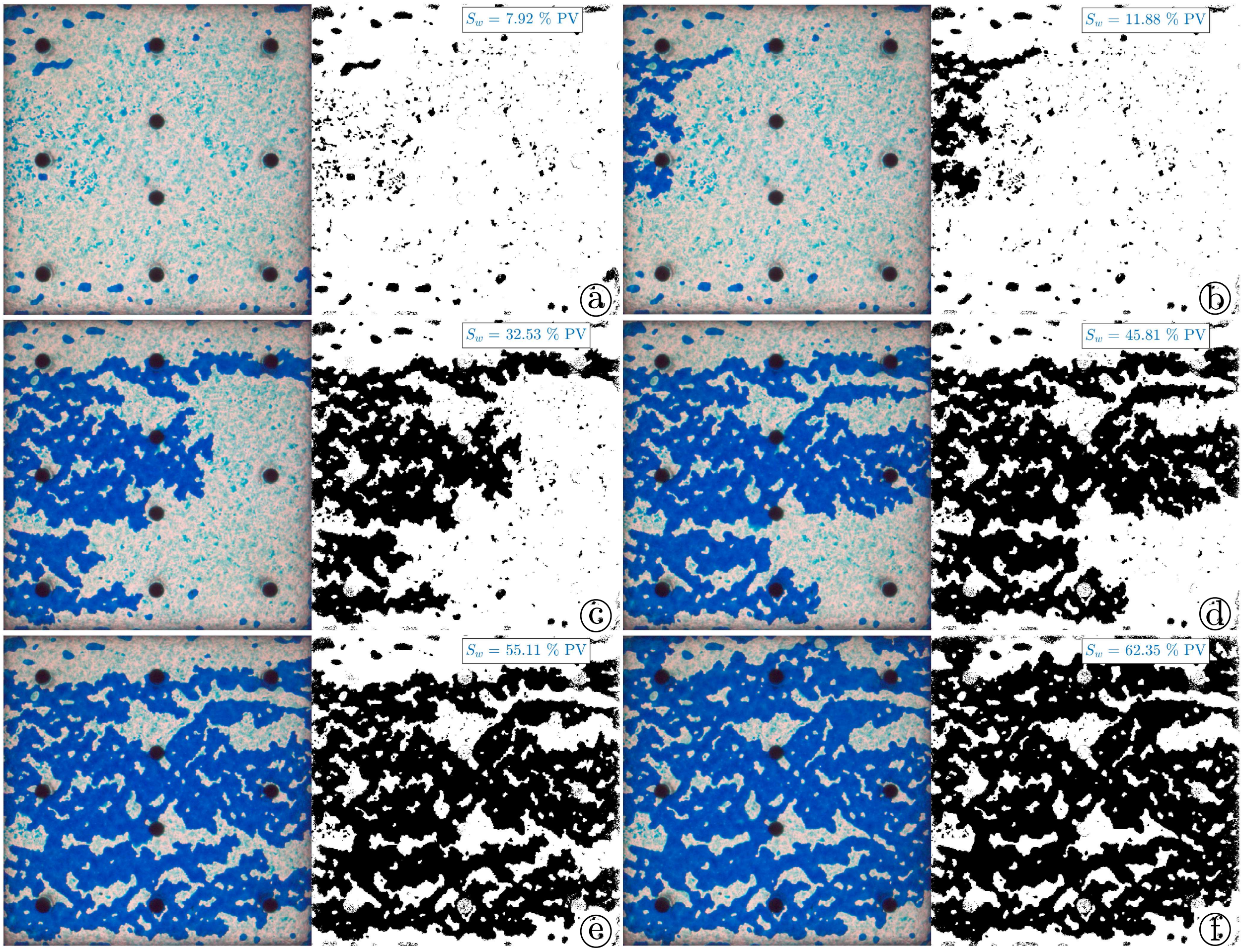

Figure 5.6: Calculation of fluid saturations through image processing: (a-f) original central sections on the left and binary images on the right.

Relative Permeability from Unsteady State Data

There are two main approaches to conducting relative permeability measurements: the steady-state and unsteady-state method (Tiab & Donaldson, 2015). Each methodology has its specifc advantages and disadvantages as enumerated elsewhere (Choi et al., 2020; Dullien, 1979). In this study, the so-called Johnson, Bossler and Neumann (JBN) method (Johnson et al., 1959), variant of the unsteady approach, was used as it is relatively straight-forward and quick to implement (Loomis & Crowell, 1962; Tiab & Donaldson, 2015). This technique is formulated based on the Buckley-Leverett displacement model and can only be used to calculate relative permeability after the breakthrough of the displacing fluid (Peters & Arabali, 2013).

5.4 Results and Discussion

5.4.1 Roughness of Fracture Walls

Fractal parameters were obtained for each profile (Figure 5.7a and Figure 5.8a) in the x-direction (parallel to the flow direction of the experiments) and each profile in the y-direction by calculating the variogram per profile (Figure 5.7b-5.7c and Figure 5.8b-5.8c) using the variogram Matlab function (Schwanghart, 2023). Then, average values were obtained for each direction (Figure 5.7d and Figure 5.8d), and these two values were averaged for an overall parameter. The Hurst exponent H and fractal dimension D reflect a roughness difference between the two surfaces (Table 5.3). Higher values of H should indicate lower local surface slopes, and vice versa for lower H values (Seybold et al., 2020). While the Hurst exponent (fractal dimension) of the type 1 surface indicated a near-ideally smooth surface, the type 2 surface exhibited a rougher H, similar to 0.5 and 0.63 values found in surfaces used by other studies on two-phase flow in fractures (Babadagli et al., 2015; L. Zhang et al., 2023). These values were within the range of the reported roughness of rock profiles, which typically exhibit Hurst exponents ranging from 0.46 to 0.8 (Odling, 1994; Schmittbuhl et al., 1995). On the other hand, the fractal-based amplitude γ_0 (back-transformed to linear scale), which should indicate the surface slope at the scale used (Fardin et al., 2001), was slightly larger for type 2 surface. It appeared that the fractal parameters only express local spatial variation but do not provide a surface amplitude indicator. Consequently, this study also presented the standard deviation of the surface elevations (Figure 5.2).

Parameter	Type 1 surface	Type 2 surface
$H, -$	0.966	0.671
$D, -$	1.034	1.329
$\gamma_0, -$	0.001	0.003

Table 5.3: Average fractal parameters for surface profiles 1 and 2.

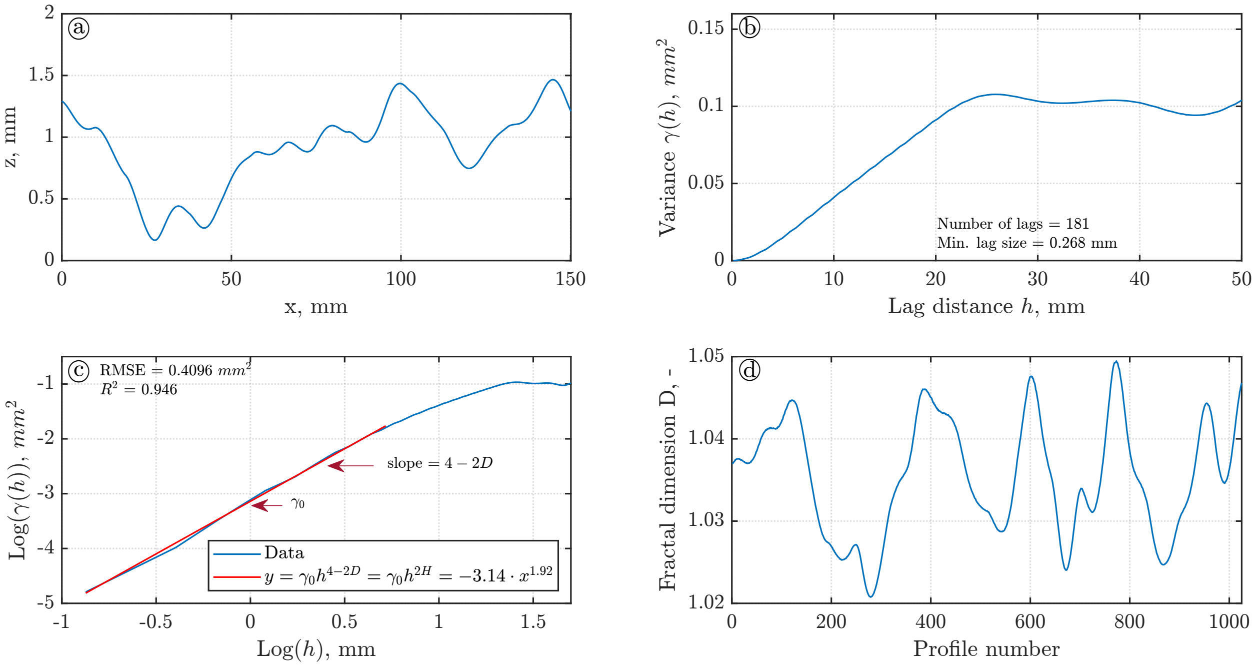

Figure 5.7: Variogram method workflow for type 1 surface: (a) Plot of a one-dimension profile in the x-direction; (b) variogram plot of the entire profile; (c) log-log plot of the variogram with a power law fit of the initial section; (d) fractal dimension of all the surface profiles in the x-direction.

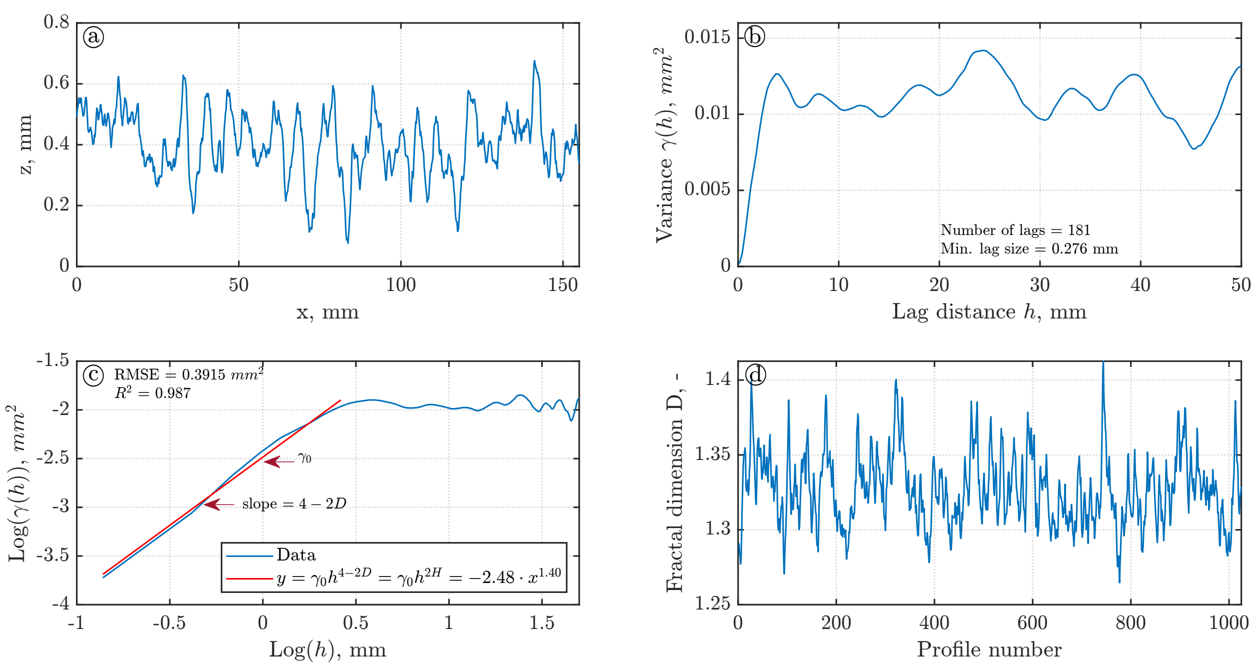

Figure 5.8: Variogram method workflow for type 2 surface: (a) Plot of a one-dimension profile in the x-direction; (b) variogram plot of the entire profile; (c) log-log plot of the variogram with a power law fit of the initial section; (d) fractal dimension of all the surface profiles in the x-direction.

5.4.2 Fracture Aperture and Capillary Number Versus Shear Displacement

For both fracture types, the experimentally observed behavior between the mean mechanical aperture $\bar{b}$ and shear displacement δ_y showed a nearly monotonically increasing trend (Figure 5.9a) which is a result that attempted to replicate the fracture dilation stage under shear loading. The relative aperture increment $\Delta\bar{b}$ from $\delta_y = 0$ mm to $\delta_y = 5$ mm was approximately 33% for the smooth fracture and 44% for the rough fracture. This range of aperture increments aimed to discretely represent the aperture dilation values reported in the literature (Ishibashi et al., 2020). The higher aperture values in the smooth fractures were not attributed to the contact of two surfaces but rather to the use of shims and a greater contrast in surface elevation values, characterized by a higher standard deviation of surface elevations, within the smooth fractures. These factors contributed to a higher pore volume in these samples.

Nevertheless, it is noteworthy that under shear, a smooth fracture —defined by a lower JRC— typically exhibits less dilation compared to a rougher fracture, which would have higher JRC values (Y. Jiang et al., 2004). Consequently, smooth fractures, theoretically, should reach a lower aperture dilation than rough fractures due to a greater number of contact points (Odling, 1994). On their part, fractures with surfaces exhibiting a higher standard deviation of surface elevation values may experience increased dilation (Ishibashi et al., 2020). This prompts speculation that fracture roughness, associated with amplitude properties, controls dilation more than spatial variation parameters. However, this study did not aim to address the factors governing dilation or determine which fracture type presented higher dilation; instead, it was focused on investigating the effects of shear deformation and fracture roughness on two-phase flow through fractures.

On the other hand, for both fracture types, the sequential increase in fracture aperture with respect to shear displacement tended to lower the calculated capillary number (Figure 5.9b). This suggested that as the aperture gradually increased, the dominance of viscous forces over capillary forces tended to decrease, aligning with previous reports (Alturki et al., 2013). This result contradicted the notion that capillary forces play a smaller role in larger fracture apertures. The effects of surface roughness and shear displacement are further analyzed below.

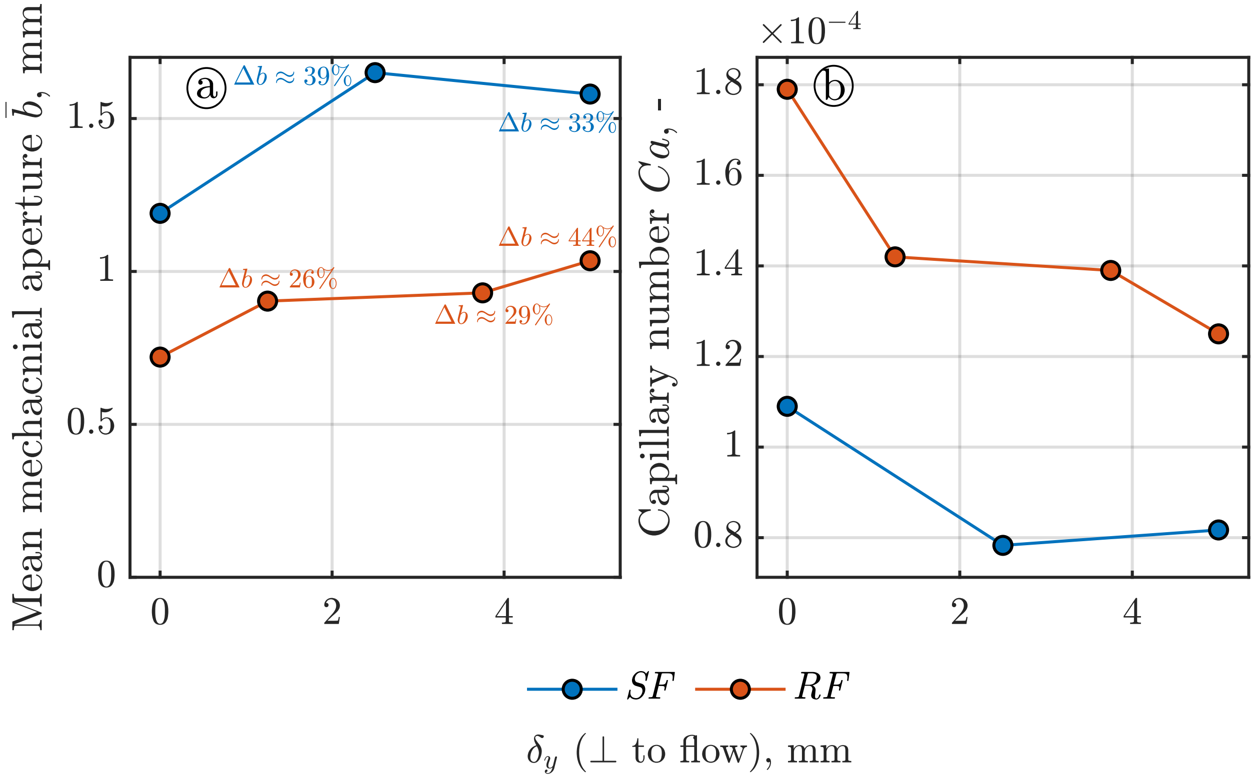

Figure 5.9: Fracture samples mechanical and flow parameters with respect to shear displacement δ_y: (a) mean mechanical apertures; (b) capillary number.

5.4.3 Analysis of Two-Phase Flow Displacements

The saturation binary images of drainage displacements were analyzed at water breakthrough (Figure 5.10a-5.10k). In these images, water was colored in blue and silicone oil was in white. Fractal dimension values from fracture saturation images at water breakthrough have been used to identify flow regimes within fractures (Y.-F. Chen et al., 2017). In this study, the fractal dimension $D_{sat.}$ was calculated using the box-counting method in the software Fiji. This parameter provided a measurement of the complexity of the two-phase flow displacement morphology and served as an indicator of the prevalence of capillary forces.

For a drainage process through the *SF* samples, the fractal dimension did not exhibit a monotonic increase as the mean aperture and shear displacement increased (Figure 5.10a-5.10c). In fact, Figure 5.10a and Figure 5.10c displayed similar $D_{sat.}$ values. Compared to the other two cases, Figure 5.10b showed a lower fractal dimension associated with a more homogeneous displacement. For a drainage process through the rough fractures (Figure 5.10d-5.10g), a shear displacement value higher than zero increased the image fractal dimension. Similar behavior was observed in subsequent drainage through the *RF* samples

(Figure 5.10h-5.10k). Furthermore, these images displayed higher fractal dimension values than those from the initial drainage process. Moreover, Figure 5.10g and Figure 5.10k both exhibited the highest image $D_{sat.}$ values. In summary, the fractal dimension of the images at breakthrough suggested that RF samples presented higher fractal dimension values than the SF models.

At breakthrough, a viscous fingering regime through fractures has been characterized to have fractal dimension values in the range of $D_{sat.}$=1.68±0.04 while a capillary fingering regime values in the range of $D_{sat.}$=1.74±0.05 (Y.-F. Chen et al., 2017). Consequently, the results obtained here indicated that a higher level of surface roughness increased the fractal dimension and that the combined effect of surface roughness, aperture increase, and shear displacements can lead to a flow regime in which capillary effects are more prevalent. These experimental observations coincide with the calculated capillary number, which decreases as shear displacement increases due to an aperture increase. Furthermore, in a phase diagram of flow structure in fractures (Y.-F. Chen et al., 2018), the capillary number and the mobility ratio from the drainage two-phase flow tests conducted here indicated a dominance of capillary fingering. Moreover, for the rough fractures, $D_{sat.}$ tended to increase with respect to a decrease in Ca, similar to other studies (Crandall, 2007).

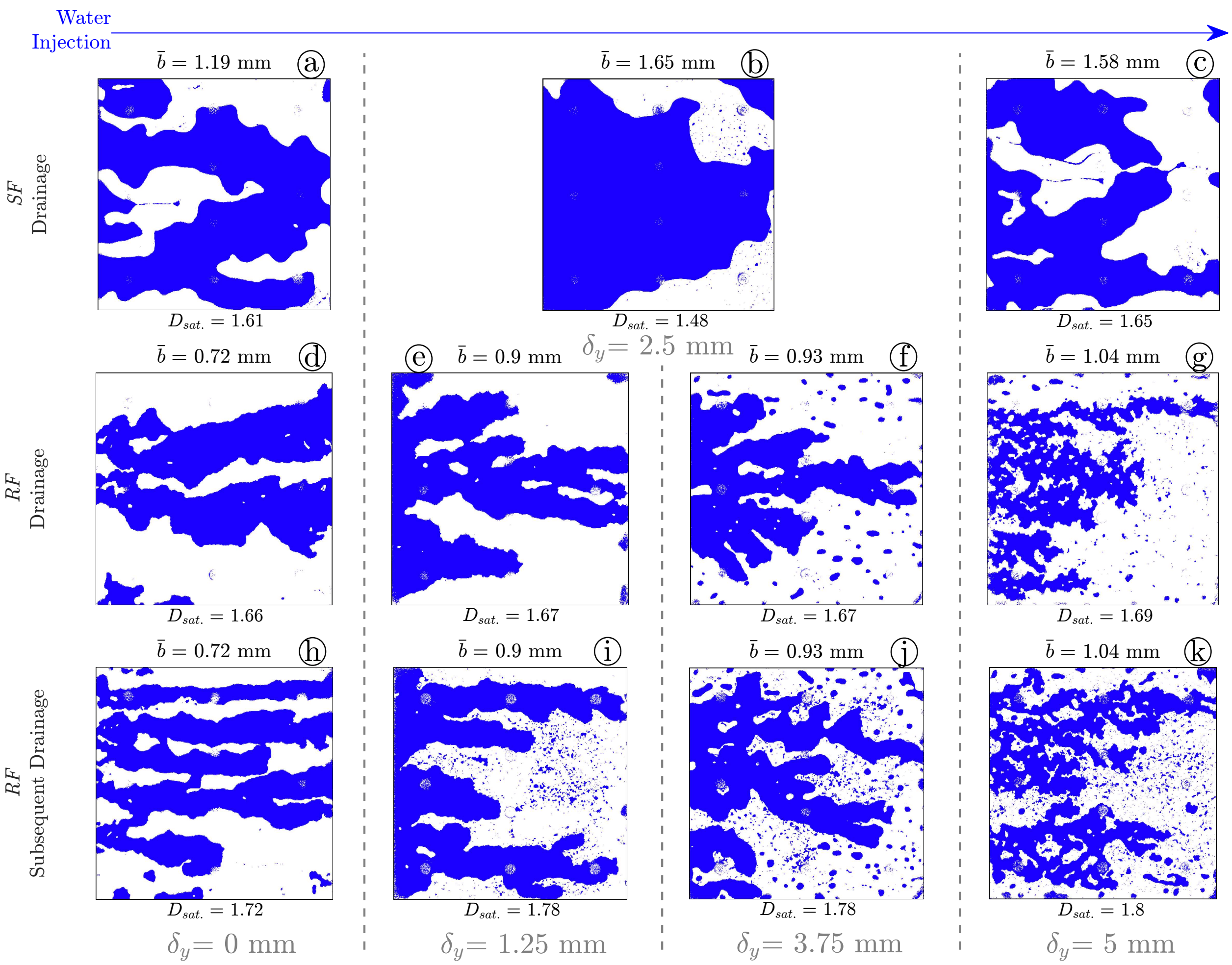

Figure 5.10: Fracture saturation images at water breakthrough. The blue areas correspond to water and the white areas to silicone oil: (a-c) Drainage process across *SF* samples; (d-g) drainage process across *RF* samples; (h-k) subsequent drainage across *RF* samples.

5.4.4 Production Behavior

The differential pressure Δp and the oil production N_{pD}, estimated through image processing, exhibited distinct characteristics during the two-phase flow displacements through the two types of fractures (Figure 5.11a-k). In general, *SF* samples showed an early stagnation in production (Figure 5.11a-c). The final recovery value was highest for the sample with $\delta_y = 2.5mm$ (Figure 5.11b) but slightly decreased for the sample with $\delta_y = 5mm$ (Figure 5.11c). The differential pressure exhibited an initial, brief plateau after water entered the fracture, and the value of this plateau was lower when the mean mechanical aperture was larger. Following this short plateau, the differential pressure decreased and tended to stabilize.

For the *RF* samples (Figure 5.11d-g), the trend observed in the first three samples was a concave production behavior rather than early stagnation. However, in the case of the final sample (Figure 5.11h), fluid production exhibited an early flattening. In contrast to the *SF* samples, the differential pressure did not show an initial plateau but rather a short peak followed by a decline.

In a subsequent drainage process involving *RF* samples (Figure 5.11h-k), a similar production trend was observed, but with an accentuated hysteresis effect evident in the final sample (Figure 5.11k). The differential pressure during this subsequent drainage exhibited lower maximum values and a slightly sharper decline in the initial stage.

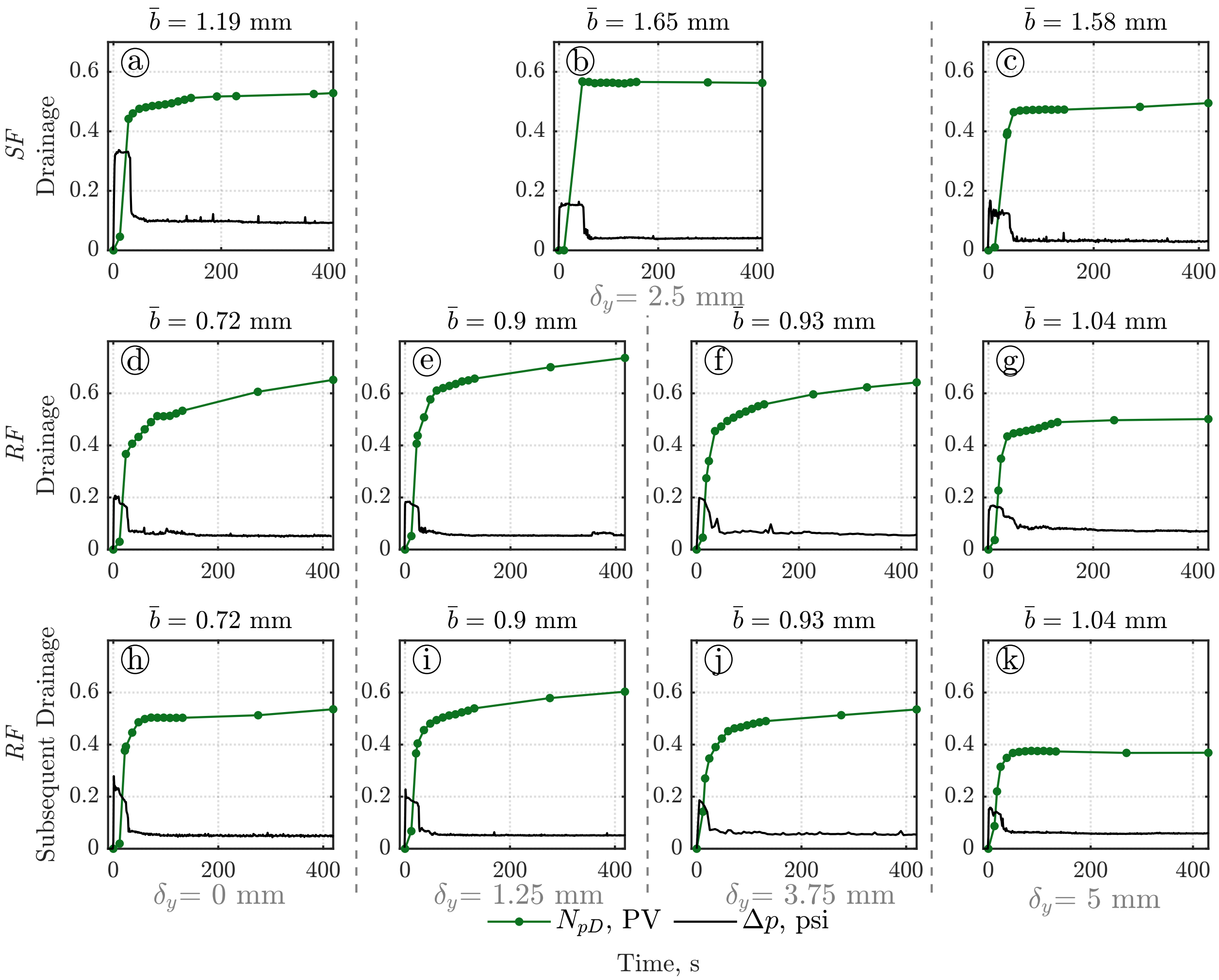

Figure 5.11: Oil production N_{pD} and differential pressure Δp versus time: (a-c) drainage process across *SF* samples; (d-g) drainage process across *RF* samples; (h-k) subsequent drainage across *RF* samples.

5.4.5 Effect of Surface Roughness

The behavior of water saturation at breakthrough S_w^{bt} with respect to the image fractal dimension $D_{sat.}$ (Figure 5.12a) indicated that fracture roughness influenced the behavior of these parameters. Although the *SF* samples had greater aperture values (i.e., larger pore volumes), they exhibited larger S_w^{bt} values than the *RF* samples, suggesting surface roughness resulted in increased flow tortuosity. Moreover, the water saturation values at breakthrough from subsequent drainage through the *RF* samples showed an increase, likely attributable to a hysteresis effect. In any case, the fractal dimension values increased compared to the two other sets of drainage experiments.

The behavior of oil production at breakthrough versus image fractal dimension (Figure 5.12b) suggested that, overall, the *SF* samples tended to have superior oil recovery than the *RF* samples. In addition, the oil recovery data from subsequent drainage through *RF* samples indicated that a hysteresis effect was detrimental to oil recovery. In these latter tests, the fractal dimension values are larger than those in the drainage tests, which suggested that displacement patterns are more complex.

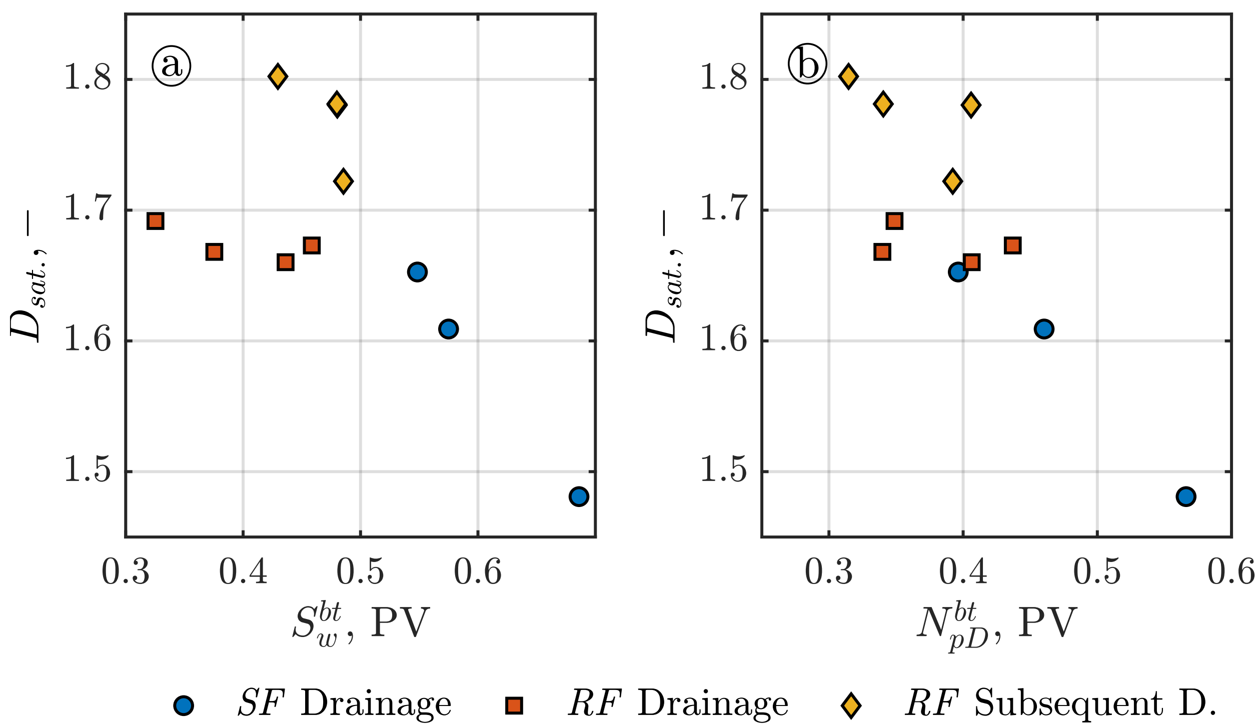

Figure 5.12: Surface roughness and displacement parameters: (a) water saturation at breakthrough S_w^{bt} versus Image fractal dimension $D_{sat.}$; (b) oil production at breakthrough N_{pD}^{bt} versus image fractal dimension $D_{sat.}$.

At water breakthrough, the average oil production from the *SF* samples was higher compared to the *RF* samples (Figure 5.13a). This was attributed to the lower degree of surface roughness, which facilitated an increase in water saturation for these samples (Figure 5.13b). However, at a water injection W_i equal to 7.5 pore volume (PV), the average oil recovery was higher for the *RF* samples. This suggested that the lower degree of surface roughness in the *SF* samples caused the injected water to tend to slip through the open water paths, decreasing the efficiency of the oil recovery. Conversely, the surface asperities in *RF* samples minimized the water slip, increasing water saturation and a more effective oil recovery after breakthrough. The subsequent drainage processes on *RF* samples showed a hysteresis effect, namely lower values, in water saturation and oil production compared to the previous drainage tests.

Water injection W_i, instead of test time, was chosen as the independent variable to compare with oil production and water saturation because it is a parameter associated with the pore volume of each sample, providing a standardized basis. A limit of W_i equal to 7.5 PV was chosen for the comparison since it approximated the highest injected volume into samples with higher pore volume (i.e., the smooth fractures).

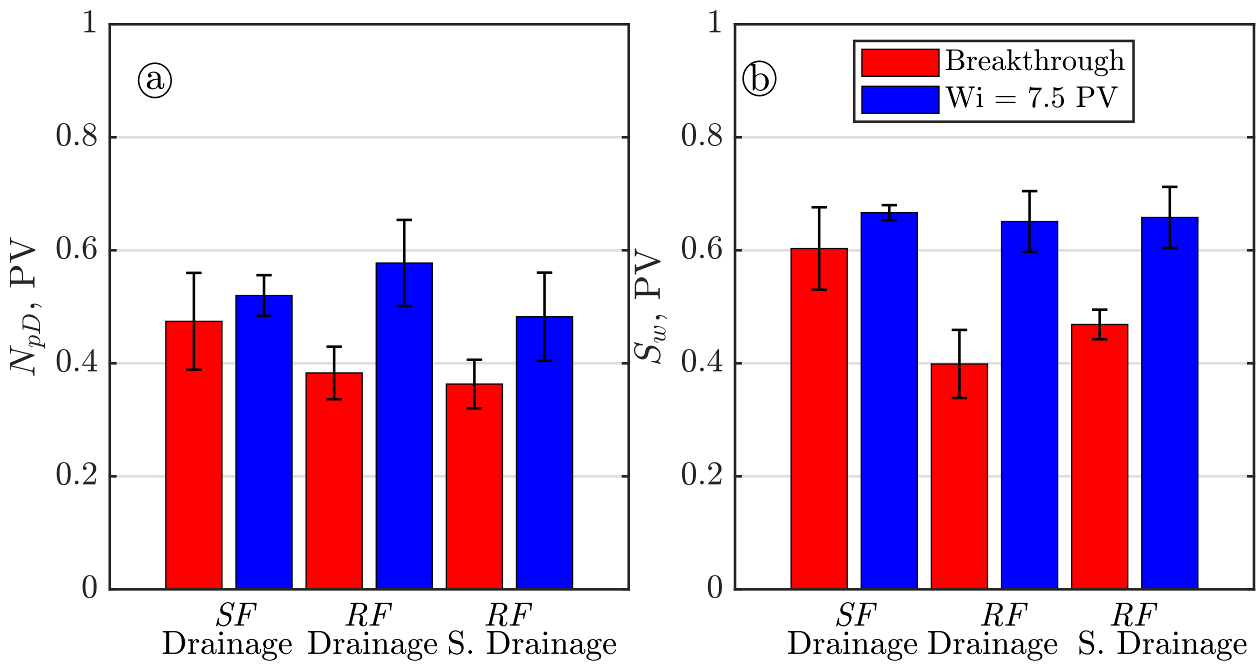

Figure 5.13: Effect of surface roughness at breakthrough and at a water injection of 7.5 PV: (a) surface type versus oil production N_{pD}; (b) surface type versus water saturation S_w.

The pressure measurements from the two-phase flow displacements (Figure 5.14a-c and 5.15 a-k) exhibited an overall similar response; however, specific characteristics suggested a correlation with surface roughness. The initial peak in the differential pressure Δp corresponded to the start of injection. Subsequently, Δp was characterized, in the smooth fractures, by a short plateau, associated to a more homogenous sweep of the silicone oil.

Then, it followed a sharp decline around $W_i = 1$ PV, associated to the water production at the outlet, followed by a relatively quick and smooth stabilization (Figure 5.14a). In contrast, Δp in a drainage process through the RF samples did not tend to show a pressure plateau at early injection but was characterized by a tenuous decline after the maximum pressure. This suggested that fracture roughness tended to cause this gradual decline before the sharp pressure fall, which tended to be followed by a period of continuous pressure reduction. The slope of this reduction was less smooth than the relative stabilization behavior observed in the SF samples during the same period (Figure 5.14b). Such slope reduction is not evident in the Δp response of subsequent drainage processes (Figure 5.14c), which tend to show a relative stabilization, likely associated with less resistance to the water displacement due to higher water saturation prior to injection.

The overall pattern of average local pressure at the inlet p_{in} and at the outlet p_{out} was similar to Δp; however, there are some interesting differences. First, the proximity of p_{in} and p_{out} suggested that the local pressure drop was much lower than the Δp measurement. Although the proximity is more prominent in the smooth fractures (Figure 5.15a-c), it hindered the calculation of the difference between the local pressures for both fracture types. Furthermore, at early injection through the rough fractures, p_{in} showed a short period of values clearly greater than p_{out} (Figure 5.15d-k), a behavior not observed in the SF samples. Consequently, this suggested that surface roughness increaseed the transient local pressure drop prior to water breakthrough.

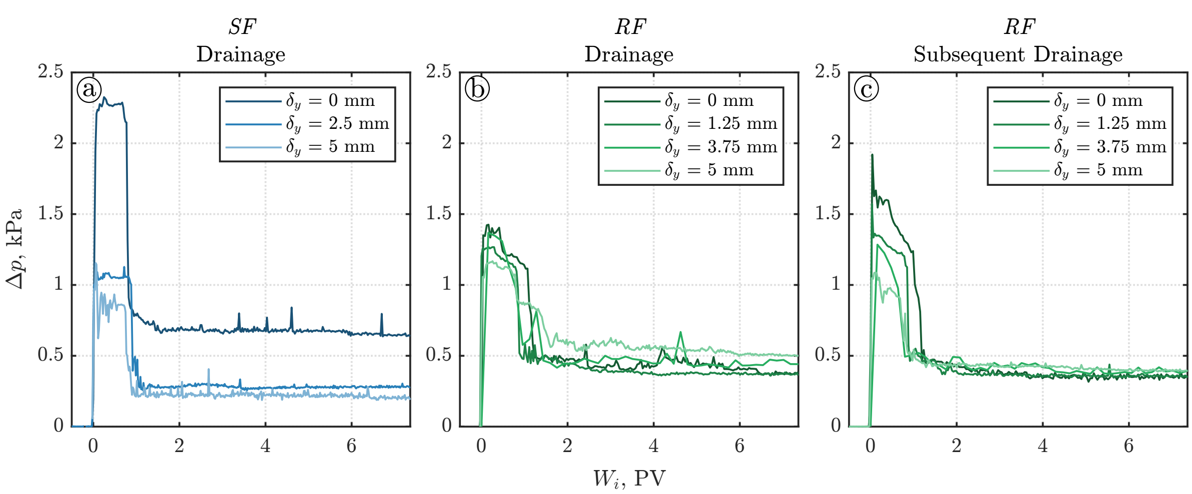

Figure 5.14: Differential pressure Δp versus water injection W_i: (a) drainage process across SF samples; (b) drainage process across RF samples; (c) subsequent drainage across RF samples.

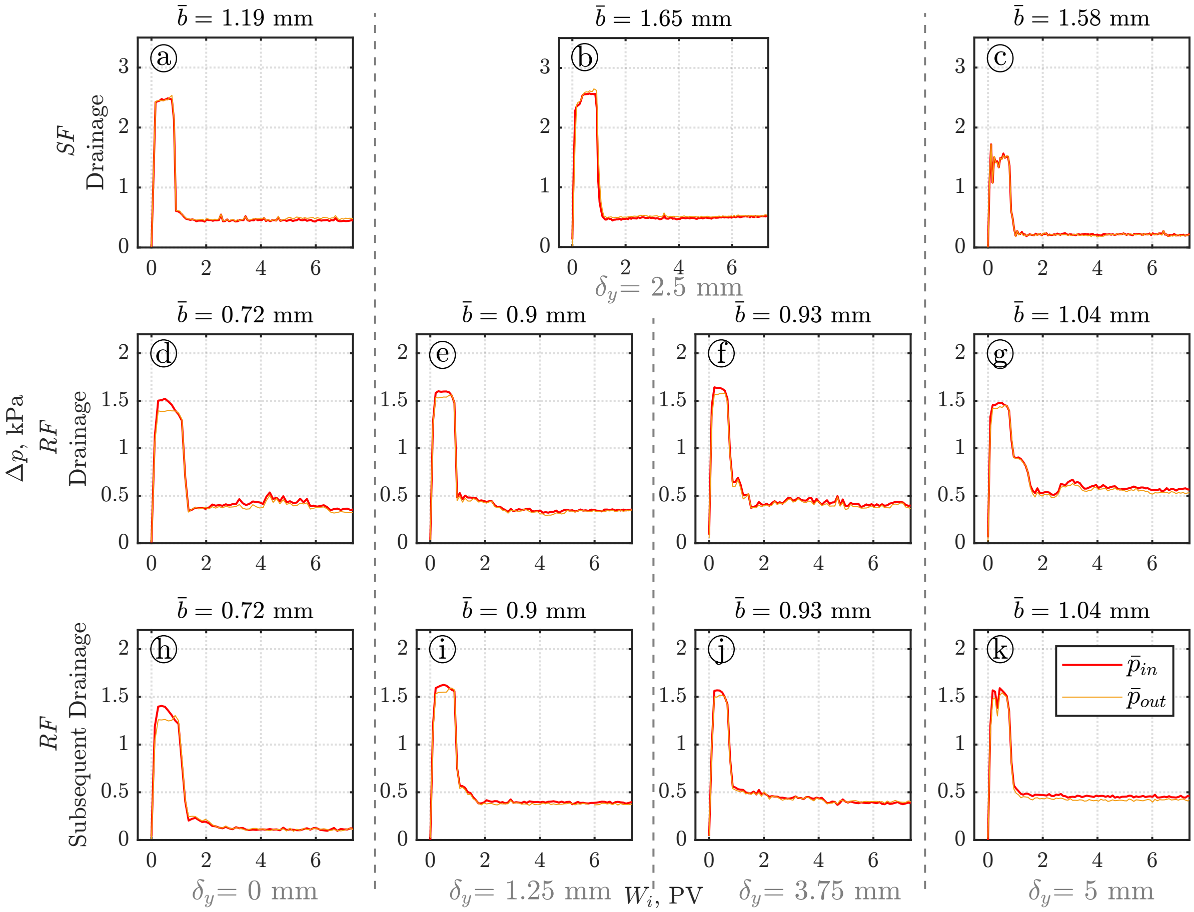

Figure 5.15: Average local inlet pressure p_{in} and average local outlet pressure p_{out} versus water injection W_i: (a-c) drainage process across SF samples; (d-g) drainage process across RF samples; (h-k) subsequent drainage across RF samples.

5.4.6 Effect of Shear Displacements

Shear displacements versus oil production at breakthrough (Figure 5.16a) suggested that, compared to the zero shear displacement, small displacements (i.e., δ_y=1.25 and 2.5 mm) had a positive effect in the oil recovery. However, shear displacements above these values (i.e., δ_y=3.75 and 5 mm) had a detrimental effect regardless of the increased aperture of these samples.

On the other hand, shear displacements versus oil production data at a water injection W_i of 7.5 PV (Figure 5.16b) suggested a concave behavior between these parameters, in which initial shear displacements (i.e., δ_y=1.25 and 2.5 mm) had a positive effect in oil recovery. In contrast, subsequent ones (i.e., δ_y=3.75 and 5 mm) resulted in a decrease in oil recovery.

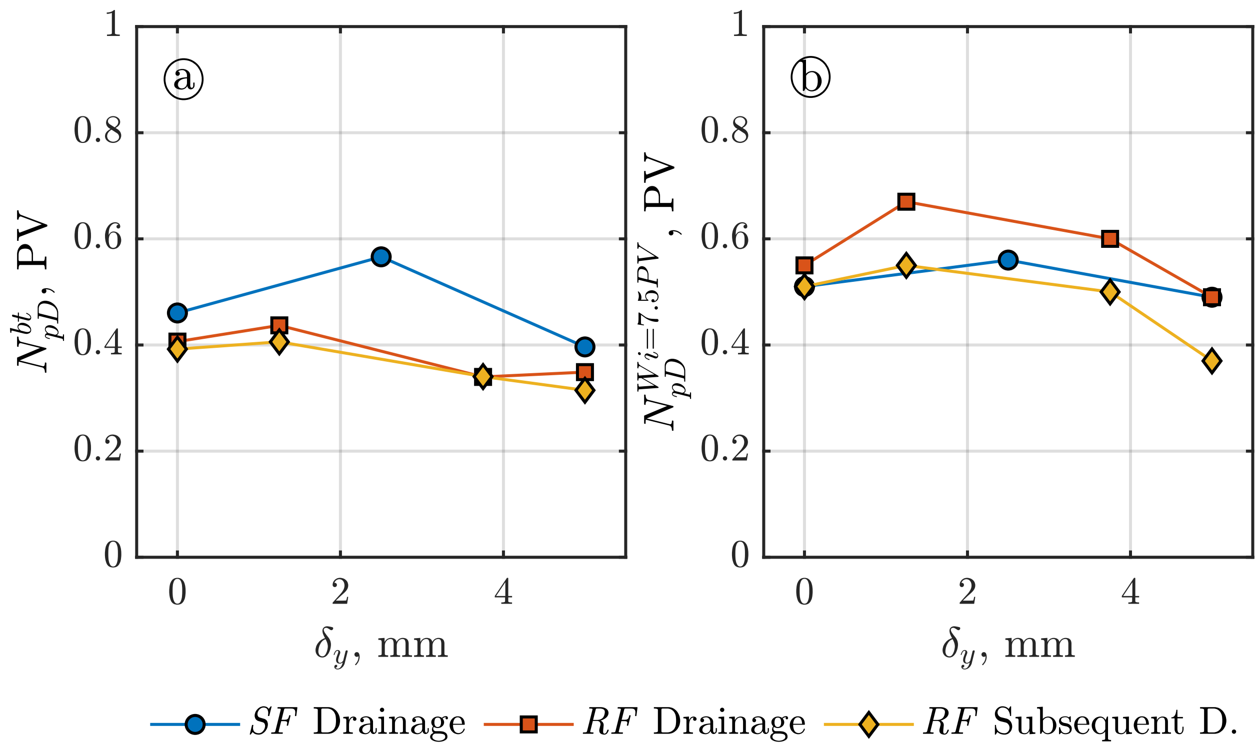

Figure 5.16: Effect of shear displacement δ_y: (a) oil production at breakthrough N_{pD}^{bt}; (b) oil production N_{pD} at a water injection W_i of 7.5 PV.

For the smooth fractures, Δp exhibited an overall reduction associated to an increase in shear displacement, a behavior attributable to an increase in fracture aperture (Figure 5.14a). In the local pressures, such overall reduction was only observed at $\delta_y = 5$ mm (Figure 5.15c). In turn, the differential pressure behavior in the *RF* samples was characterized by two patterns: first, the initial pressure peak appeared to attenuate as the aperture increased linked to a shear displacement increase. Namely, the zero-shear displacement sample tended to show higher peak values compared to the other rough fractures (Figure 5.14b-c). This suggested that before water breakthrough, an increase in shear displacement may have reduced flow resistance in the rough fractures. After water breakthrough, the Δp behavior tended to be non-monotonic; the sample with a shear displacement of $\delta_y = 1.25$ mm had lower pressure values than the sample at zero-shear displacement (Figure 5.14b-c). In comparison, the two remaining samples showed a higher Δp values with respect to the zero-shear displacement sample during this period. This could have indicated that a relatively small shear displacement in the rough fractures could have decreased flow resistance after water breakthrough; however, increasing shear displacement may have induced flow resistance.

5.4.7 Relative Permeability from JBN Method

After analyzing the production and pressure behavior separately and discussing the effects of roughness and shear displacement, the data were evaluated for the applicability of the JBN approach in estimating relative permeability.

One challenge of the JBN approach is that the production data curves should be smooth to minimize numerical noise (Peters & Arabali, 2013). A common practice is to fit the experimental data to smooth functions to calculate relative permeability and thus avoid numerical errors.

In this context, the majority of the production curves presented here exhibited deviations from ideal smoothness and no functions were fitted to the experimental data. Additionally, certain samples displayed short curves with early stabilization of oil production (Figure 5.11a, b, c, h, g, and k). Additionally, smooth fractures often exhibited a brief pressure plateau, rendering the pressure response less suitable for the JBN method. These factors hindered the calculation of consecutive relative permeability points at different saturations for most of the smooth fractures. Thus, with these considerations, the JBN method was exclusively applied to the rough fractures, utilizing the monotonic portion of the production data to avoid numerical errors.

The test experimental parameters (Table 5.4) and the production data (Tables 5.5-5.12), which included oil flow rate Q_o, water injection W_i, differential pressure Δp, cumulative oil production N_{pD}, average water saturation S_{wavg}, oil fractional flow f_o, water saturation at the fracture outlet S_{w2}, reciprocal of the relative injectivity $1/I_r$, slope of the curve of $1/W_i$ plotted versus $1/W_i \times Ir$, relative permeability of oil k_{ro}, and relative permeability of water k_{rw}, were used to produce log—log plots of the reciprocal of water injection $1/W_i$ versus the reciprocal of the term relative injectivity times water injection $1/(W_i \times I_r)$ and model the data with power functions (Figure 5.17).

		RF samples							
		Drainage				S. Drainage			
	Shear displacement, mm	0	1.25	3.75	5	0	1.25	3.75	5
Test parameters	Flow rate absolute permeability, m^3/s	4.5×10^{-7}							
	Absolute permeability, $\times 10^{-8}$ m^2	3.133	3.921	4.217	3.615	Id.	Id.	Id.	Id.
	Flow rate relative permeability, m^3/s	6.6666×10^{-7}							
	Effective permeability, $\times 10^{-9}$ m^2	6.674	1.21	7.550	9.520	Id.	Id.	Id.	Id.
	Pore volume, $\times 10^{-5}$ m^3	1.62	2.043	2.09	2.33	Id.	Id.	Id.	Id.
	Initial water saturation, fraction	0.061	0.039	0.082	0.079	0.077	0.08	0.163	0.166
	Δp_s, $\times 10^{-4}(1/Pa)$	7.208	16.48	10.52	14.83	Id.	Id.	Id.	Id.
JBN	B	1.585	0.963	1.149	0.786	1.6264	0.922	1.048	1.062
	n	0.76	0.747	0.724	0.752	0.7105	0.729	0.637	0.6516

Table 5.4: Test parameters for two-phase flow displacements through rough fractures and coefficients from the power function $Y = Bx^n$ obtained through the JBN method.

Drainage

Q_o, %IOIP	W_i, PV	Δp, Pa	N_{pD}, PV	$S_{w_{avg.}}$, PV	fo, frac	S_{w_2}, PV	$1/I_r$, -	Slope, -	k_{ro}, -	$\frac{k_{ro}}{k_{rww}}$, -	k_{rw}, -
38.1	0.9	1227	0.36	0.42	0.41	0.939	0.884	1.20	0.496	0.14	0.071
48.2	2.5	492	0.45	0.51	0.06	0.635	0.354	1.92	0.116	1.57	0.182
51.0	3.0	443	0.48	0.54	0.05	0.618	0.319	2.06	0.110	1.79	0.197
53.4	3.5	432	0.50	0.56	0.05	0.594	0.311	2.15	0.097	2.13	0.207
55.1	5.4	464	0.52	0.58	0.02	0.535	0.334	2.35	0.049	4.75	0.233
62.5	11.4	397	0.59	0.65	0.01	0.486	0.286	2.92	0.034	8.46	0.291
67.6	17.3	380	0.63	0.70	0.01	0.443	0.274	3.26	0.026	12.54	0.326

Table 5.5: Results for RF $\delta_y = 0$ mm.

Q_o, %IOIP	W_i, PV	Δp, Pa	N_{pD}, PV	$S_{w_{avg.}}$, PV	fo, frac	S_{w_2}, PV	$1/I_r$, -	Slope, -	k_{ro}, -	$\frac{k_{ro}}{k_{rww}}$, -	k_{rw}, -
45.4	0.6	1149	0.44	0.48	0.703	0.96	1.893	0.54	0.381	0.04	0.016
59.9	1.6	476	0.58	0.62	0.177	0.66	0.784	0.86	0.152	0.47	0.071
63.6	2.0	444	0.61	0.65	0.091	0.53	0.731	0.92	0.084	1.01	0.085
64.6	2.3	418	0.62	0.66	0.025	0.40	0.689	0.98	0.024	4.00	0.097
68.3	4.3	372	0.66	0.70	0.014	0.37	0.613	1.18	0.017	6.95	0.117
73.1	9.0	372	0.70	0.74	0.010	0.35	0.612	1.42	0.014	10.18	0.142
76.7	13.7	376	0.74	0.78	0.007	0.33	0.619	1.58	0.012	13.60	0.158

Table 5.6: Results for RF $\delta_y = 1.25$ mm.

Q_o, %IOIP	W_i, PV	Δp, Pa	N_{pD}, PV	$S_{w_{avg.}}$, PV	fo, frac	S_{w_2}, PV	$1/I_r$, -	Slope, -	k_{ro}, -	$\frac{k_{ro}}{k_{rww}}$, -	k_{rw}, -
29.5	0.6	1309	0.27	0.35	0.446	0.92	1.377	0.66	0.296	0.13	0.037
36.3	1.1	577	0.33	0.42	0.117	0.72	0.607	0.99	0.116	0.77	0.088
50.5	1.9	450	0.46	0.55	0.044	0.54	0.473	1.22	0.054	2.20	0.118
53.7	2.7	454	0.49	0.58	0.029	0.50	0.478	1.34	0.039	3.41	0.131
58.0	4.2	478	0.53	0.61	0.023	0.48	0.503	1.50	0.035	4.26	0.148
58.8	7.3	434	0.54	0.62	0.002	0.40	0.457	1.79	0.004	40.54	0.180

Table 5.7: Results for RF $\delta_y = 3.75$ mm.

Q_o, %IOIP	W_i, PV	Δp, Pa	N_{pD}, PV	$S_{w_{avg.}}$, PV	fo, frac	S_{w_2}, PV	$1/I_r$, -	Slope, -	k_{ro}, -	$\frac{k_{ro}}{k_{rww}}$, -	k_{rw}, -
32.5	0.5	1193	0.30	0.38	0.551	0.92	1.764	0.44	0.243	0.08	0.020
45.8	1.0	1091	0.42	0.50	0.251	0.76	1.613	0.53	0.133	0.30	0.040
56.4	1.7	754	0.52	0.60	0.034	0.46	1.114	0.66	0.022	2.87	0.064
56.9	2.1	633	0.52	0.60	0.014	0.43	0.935	0.72	0.010	7.07	0.072
61.9	11.2	511	0.57	0.65	0.002	0.37	0.755	1.15	0.002	56.51	0.116

Table 5.8: Results for RF $\delta_y = 5$ mm.

Subsequent Drainage

Q_o, %IOIP	W_i, PV	Δp, Pa	N_{pD}, PV	$S_{w_{avg.}}$, PV	fo, frac	S_{w_2}, PV	$1/I_r$, -	Slope, -	k_{ro}, -	$\frac{k_{ro}}{k_{rww}}$, -	k_{rw}, -
42.5	0.9	1291	0.39	0.47	0.433	0.92	0.930	0.60	0.497	0.132	0.066
48.3	1.5	474	0.45	0.52	0.093	0.62	0.342	1.25	0.165	0.98	0.162
52.6	2.0	424	0.49	0.56	0.081	0.60	0.305	1.52	0.160	1.153	0.184
54.0	2.5	392	0.50	0.58	0.025	0.49	0.283	1.77	0.054	3.910	0.213
54.6	3.0	374	0.50	0.58	0.011	0.45	0.269	1.98	0.025	9.221	0.231
54.5	5.43	0.053	0.503	0.58	0.001	0.42	0.265	2.768	0.001	310.015	0.28

Table 5.9: Results for RF $\delta_y = 0$ mm.

Q_o, %IOIP	W_i, PV	Δp, Pa	N_{pD}, PV	$S_{w_{avg.}}$, PV	fo, frac	S_{w_2}, PV	$1/I_r$, -	Slope, -	k_{ro}, -	$\frac{k_{ro}}{k_{rww}}$, -	k_{rw}, -
44.1	0.7	1225	0.41	0.49	0.592	0.92	2.018	0.50	0.297	0.07	0.021
52.6	1.6	440	0.48	0.56	0.066	0.54	0.724	0.83	0.054	1.44	0.078
54.0	2.0	388	0.50	0.58	0.033	0.49	0.639	0.91	0.030	2.93	0.089
56.5	3.1	357	0.52	0.60	0.011	0.44	0.588	1.06	0.012	8.76	0.106
63.4	9.0	352	0.58	0.66	0.009	0.41	0.580	1.41	0.012	11.61	0.142
66.1	13.7	354	0.61	0.69	0.005	0.38	0.583	1.58	0.008	19.04	0.159

Table 5.10: Results for $RF\ \delta_y = 1.25$ mm.

Q_o, %IOIP	W_i, PV	Δp, Pa	N_{pD}, PV	$S_{w_{avg.}}$, PV	fo, frac	S_{w_2}, PV	$1/I_r$, -	Slope, -	k_{ro}, -	$\frac{k_{ro}}{k_{rww}}$, -	k_{rw}, -
40.7	0.5	1285	0.34	0.50	0.667	0.84	1.352	0.47	0.313	0.05	0.016
45.8	1.1	493	0.38	0.55	0.067	0.53	0.519	0.89	0.059	1.41	0.084
55.5	3.1	492	0.46	0.63	0.019	0.43	0.518	1.27	0.024	5.24	0.126
57.4	4.2	450	0.48	0.64	0.012	0.41	0.474	1.47	0.017	8.47	0.147
60.0	8.8	439	0.50	0.67	0.005	0.38	0.462	1.94	0.009	20.90	0.195

Table 5.11: Results for $RF\ \delta_y = 3.75$ mm.

Q_o, %IOIP	W_i, PV	Δp, Pa	N_{pD}, PV	$S_{w_{avg.}}$, PV	fo, frac	S_{w_2}, PV	$1/I_r$, -	Slope, -	k_{ro}, -	$\frac{k_{ro}}{k_{rww}}$, -	k_{rw}, -
38.0	0.5	979	0.32	0.48	0.651	0.83	1.448	0.47	0.308	0.05	0.017
42.4	1.0	544	0.35	0.52	0.068	0.55	0.804	0.75	0.051	1.39	0.071
44.9	1.4	471	0.37	0.54	0.060	0.54	0.695	0.88	0.053	1.58	0.083
45.5	1.7	442	0.38	0.55	0.015	0.48	0.653	0.97	0.014	6.75	0.096
45.6	2.1	447	0.38	0.55	0.002	0.47	0.660	1.03	0.002	65.09	0.104
45.8	2.4	432	0.38	0.55	0.005	0.46	0.639	1.10	0.006	19.59	0.110

Table 5.12: Results for $RF\ \delta_y = 5$ mm.

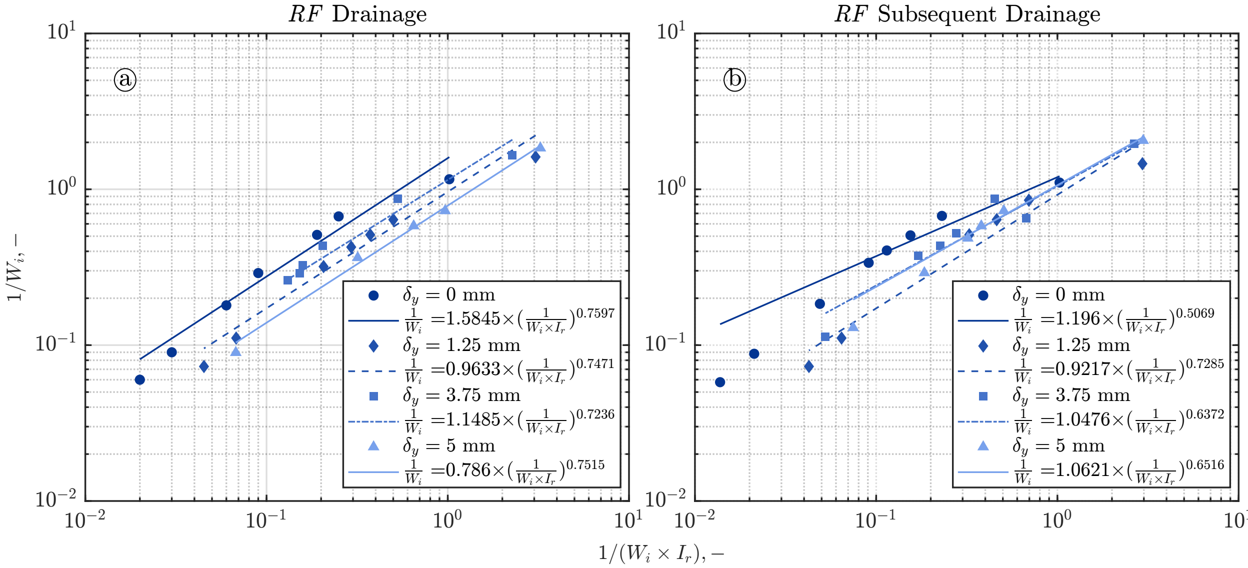

Figure 5.17: Log—log plot of the reciprocal of water injection $1/W_i$ versus the reciprocal of the term relative injectivity times water injection $1/(W_i \times I_r)$ for rough fractures. (a) Drainage tests and (b) subsequent drainage tests.

First, the relative permeability curves estimated through the JBN method indicated that the relative permeability in fractures behaves non-linearly (Figure 5.18). This contrasts with previous experimental results that have reported a linear function between relative permeability and phase saturation for fractures (Pan, 1999; Romm, 1966). This observation is significant because a linear relationship has traditionally been employed in dual-porosity reservoir simulators (Babadagli & Ershaghi, 1992; Saboorian-Jooybari, Hadi, 2016). Thus, these results support the argument (Schiozer & O. Muńoz Mazo, 2013) that the linear approach is inadequate.

Regarding shear displacement, the behavior of the relative permeability curves suggested that, for drainage, any studied level of shear displacement induces phase interference in both phases. This interference is characterized by a reduction in the value of relative permeability (Pruess & Tsang, 1990). Meanwhile, during subsequent drainage, an increase in shear displacement exhibited a rise in phase interference in the relative permeability of water (non-wetting phase) and the oil (wetting phase).

More research is needed to comprehensively characterize the effect of shear deformation on the calculated relative permeability curves, which, by nature, are experimentally non-unique. However, this research demonstrates the potential of 3D printing in this area.

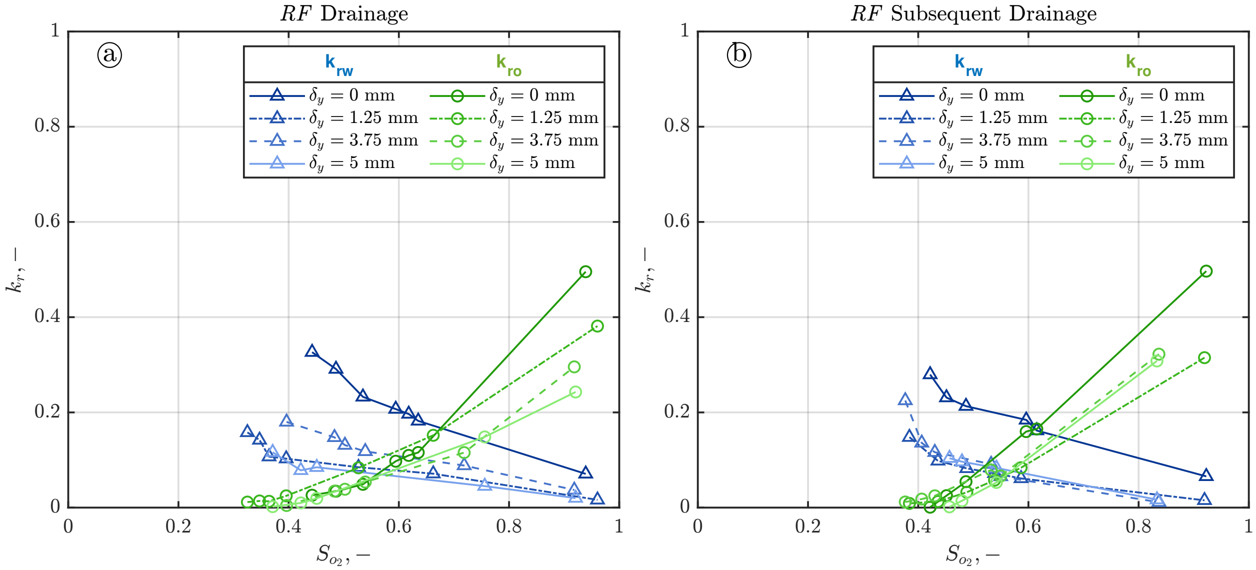

Figure 5.18: Rough fractures relative permeability versus oil saturation at the outlet S_{O_2}. These curves were obtained using differential pressure and image production data. (a) Drainage tests and (b) subsequent drainage tests.

5.5 Conclusions

This study reported on the influence of displacements arising from shear motion on two-phase flow through polyjet 3D-printed fractures, employing two different roughness types to investigate their influence on individual fractures as shear displacements perpendicular to flow and mean apertures increased.

Two fracture surfaces of different roughness were produced digitally. Such topographies were embedded into 3D solids and 3D-printed to create fracture specimens. For each fracture, two-phase flow drainage experiments were conducted to displace silicone oil with dyed distilled water. Experiments were visualized to estimate fluids saturation, oil recovery and analyze displacement patterns.

The fractal-based variogram method provided measurement of the roughness of the used surface types. Employing 3D-printed fractures allowed visualizing fluid flow while controlling the surface roughness level and the samples' shear displacement. Fluid saturations were estimated through image processing, and the displacement patterns were analyzed through the fractal-based box-counting method.

The results presented here suggested that fractal dimension values from fracture saturation images at water breakthrough could be influenced by surface roughness, indicating that a higher level of surface roughness increases the fractal dimension. Furthermore, the combined effect of higher surface roughness with displacements arising from shear motion yielded saturation images with higher fractal dimension values. Consequently, this was an indicator that capillary forces were more dominant under these circumstances.

Surface roughness affected the efficiency of two-phase flow displacements. At water breakthrough, the oil recovery was more efficient in the smooth fractures. However, beyond this point, the efficiency dropped significantly. This demonstrated that roughness affected two-phase flow displacements through fractures.

Oil recovery exhibited a concave behavior with respect to shear displacements, with an increase in oil recovery at zero to mid-shear displacement values (i.e., δ_y = 0,1.25 and 2.5 mm), followed by a subsequent concave decrease in oil recovery at higher shear displacements (i.e., δ_y=3.75 and 5 mm). In turn, pressure measurements from two-phase flow displacements exhibited features that suggest the degree of surface roughness influences their response. Additionally, the displacements resulting from shear motion in combination with a higher degree of roughness, tended to influence the flow behavior differently prior and after water breakthrough: before water breakthrough, an increase in shear displacement may haved reduced flow resistance. However, shear displacement values near the maximum investigated here may have increased flow resistance. Relative permeability for rough fractures was calculated using the JBN method. During drainage, any level of shear displacement led to phase interference in both water and oil phases. In subsequent drainage tests, phase interference was observed only in the water phase. Meanwhile, the oil phase showed an increase in relative permeability with greater shear displacement; it tended to exhibit a single point of less interference with increasing shear displacement, while the remaining calculated points showed similar values.

Although incipient, this research highlights the effects of shear deformation in two-phase flow through fractures and demonstrates the potential of 3D printing in such investigations.

5.6 Data Availability

Experimental data and fracture surface digital files will be available at https://zenodo.org/doi/10.5281/zenodo.10547710. Schematics were created in open-source computer graphics software Blender version 3.2 and Python 3.11.5. Data processing and the figures were made with the licensed software Matlab version R2022a, license number 1088131. The Matlab function variogramfit [Schwanghart (2023) available at https://www.mathworks.com/matlabcentral/fileexchange/25948-variogramfit was used to calculate the variogram.

Chapter 6

Conclusions and Recommendations

6.1 Conclusions

1. This investigation emphasized the importance of examining flow through a single rock fracture in both experimental and numerical investigations. The complexities of real rock fractures, influenced by stress and mechanical factors, require consideration of mechanical parameters and hydraulic conditions for the formulation of suitable models. This investigation addressed some of the relevant topics associated with single-phase and two-phase flow through individual fractures.

2. This study employed PolyJet 3D printing technology to investigate flow through fractures, focusing on taking full advantage of its potential. First, two methodologies for removing support material from 3D-printed samples were evaluated. Effective removal of support material is crucial for using such models in laboratory experiments, and the study explored methods for improving this process and the implications for flow-through fracture investigations.

3. In the context of single-phase flow, the study assessed cubic-law-based models to offer insights for numerical simulation projects. It identified conditions under which cubic-law-based models are most appropriate for estimating the experimental hydraulic conductivity of fractures. The study also approximated an experimental error associated with different methodologies for estimating the hydraulic aperture of fractures. Additionally, the effectiveness of the cubic law in estimating the hydraulic conductivity of fractures was evaluated. The study addressed the criteria for determining the limit of the linear flow regime for fractures. The experimental data indicated that for $Re < 3.4$, a linear correlation existed between pressure and flow rate. This finding was corroborated by empirical equations employed to predict Re_c.

4. In the realm of two-phase immiscible flow, the study explored the impact of surface roughness and mechanical changes, including shear motion, on prevalent flow forces. Given the limited availability of experimental data in this area, the research provided insight on the effect of surface roughness and shear motion on the behavior of pressure and production data from two-phase flow displacements. It further investigated the shape of relative permeability in fractures and examined the effects of fracture roughness and shear displacements.

In summary, this study addressed some of the challenges associated with flow through an individual fracture, aiming to offer practical insights for improving experimental methodologies and contribute valuable findings in the context of single-phase and two-phase flow through fractures.

6.2 Contributions

1. The main contribution of this work is the integrated experimental and numerical workflow, which utilizes 3D printing and fiber optic pressure sensors. This integrated approach may serve for future studies to investigate at a fundamental level multi-phase flow through fractures under varying mechanical apertures or shear conditions, while also facilitating comparison with numerical analyses.

2. This research contributes to the existing body of knowledge by providing visual evidence and flow data regarding the impact of shear displacement perpendicular to flow and the influence of roughness on two-phase flow within fractures.

3. This investigation contributes to the ongoing debate concerning the critical Reynolds number value at which non-linear effects emerge in single-phase flow through fractures. Additionally, it elucidates the conditions under which the cubic law and the local cubic law remain valid for estimating the hydraulic behavior of individual fractures.

4. This work presents a discussion on different roughness methodologies that may contribute to a deeper understanding of available techniques and provide considerations that could be instrumental in achieving scale-independent measurements.

5. This research introduces a limited list of cubic law-based models, categorized by accuracy, to facilitate comparison with other studies aimed at statistically identifying models that offer a more precise description of fracture hydraulic behavior. These

models could be applied in experiments lacking local pressure measurements but with a certain degree of knowledge regarding fracture closure, mechanical aperture, and topographic properties.

6. Furthermore, relative permeability across rock fractures is not typically measured in geoscience laboratories. Nonetheless, this research has the potential to advance the energy industry towards innovative methodologies, such as 3D-printing-based techniques, for studying flow in fractures. Conducting laboratory experiments on identical fracture surfaces could mitigate the influence of sample heterogeneity and fracture morphology on the experimental outcomes.

6.3 Recommendations for future work

Many practical steps can be taken to improve both the incipient experimental and the numerical work presented here. Some of them are the following:

1. With regard to the experimental flow cell, several improvements could be considered for future work. To investigate the effect of a specific level of normal and shear stresses during the injection of immiscible fluids, one of the main challenges is the experimental seal (H. Lee & Cho, 2002; B. Li et al., 2008). One alternative to address this challenge has been to use a cylindrical sample geometry (W. Olsson & Brown, 1993), incorporating an o-ring as the seal or employing a Hassler-type cell (Crandall et al., 2017). In the case of a quadrilateral geometry, gel sheets have been utilized for sealing (Koyama et al., 2008; B. Li et al., 2008). However, the choice of configurations may have implications for the allowed shear direction (i.e., parallel or perpendicular to flow), the type of mechanical boundary condition applied (i.e., normal loading or normal fracture stiffness), control over the measurement of mean mechanical aperture (i.e., the feasibility to measure this parameter with volumetric, imaging or other methods), the range of fracture aperture and surface roughness that can be studied (i.e., narrower fractures with contact points), as well as the seal mechanism of local fiber optic pressure sensors. With respect to the latter, sensor resolution should be carefully chosen based on the selected stress condition and the expected fracture apertures. Additionally, the placement of the fiber optic pressure sensors should be carefully evaluated, aiming to find an optimal separation between measurements that maximizes fracture coverage and avoids measurement similarity.

2. Introducing a stress level to the current static configuration would likely require a more rigorous analysis regarding the loading mechanism, geometry, and seal. This would facilitate studying fracture apertures of smaller values. Nevertheless, it is possible that increasing the thickness of the 3D printed sections would ensure that fixing them to the aluminum cell using screws prevents cracks. Enhancing the thickness of the samples might improve their resistance to normal loading, but it would imply using more 3D printing material. In this regard, the amount and type of polyjet 3D printing material used can be calculated before testing and are other factors to consider when designing the samples and planning the testing program. For example, with the current cell design, maintaining the lower fracture sections static for subsequent tests and only interchanging the upper sections would involve using more 3D printing material due to the design of the top parts.

3. Estimating the local apertures with the current configuration requires minimizing or avoiding any light interference surrounding the fracture sample and at the local pressure ports. Light interference may hinder the accurate implementation of the Beer-Lambert law to estimate local apertures. In this regard, a different approach (e.g., Kishida et al. (2013) and Nowamooz et al. (2009)) could be used rather than the iterative calculation based on the mean mechanical aperture employed here, or a completely different approach could be considered by utilizing computer tomography scanning. An important factor to consider for estimating local apertures is the transparency of the samples (Isakov et al., 2001). In addition, having non-quadrilateral samples would facilitate sanding and polishing the non-textured part of the samples since there would be no corners or sharp edges. Thus, achieving better sample transparency. Another element to improve is the temporary adsorption of the dye by the textured surfaces during the tests, which, along with the geometry of the pressure ports, interferes with the saturation calculation through image processing. Also, when the water displaces the oil out of the cell, a thin film might be left behind (Y.-F. Chen et al., 2018), which, although it frequently does not interfere with image processing calculations (Guerrero Zabala, 2019), should be accounted in the saturation calculation.

4. With respect to the hydraulic design of the flow cell, an improvement could be to have a 1:2 length ratio. This would facilitate investigating greater pressure drops in the longer direction and permit capturing a more heterogeneous local pressure field. On the other hand, placing external pressure ports closer to the fracture sample would

help have realistic measurements of the external pressure. Another enhancement to the current design could involve reducing the volume and redesigning the shape of the inlet and outlet chambers. This adjustment would aid in two-phase flow displacements by minimizing the cell's dead volumes prior to injection, enabling material balance calculations from the two-phase flow displacements, in addition to the saturation and production calculations from image processing. Having less pockets in the cell could also help minimize pressure fluctuations in transient and steady-state two-phase flow experiments, which might occur in the current configuration if the mobility ratio is very disfavorable (i.e., 100). In such cases, the fluids tend to compete to leave the cell, and their interference at the outlet components might cause transient pressure peaks after water breakthrough. This should be considered for both steady and unsteady displacement tests. Finally, the wettability of VeroClear material post-test should be investigated as well as the wettability of VeroClear in an oil-water system.

5. The integration of 3D printing, flow visualization and local fiber optic pressures can help analyze the synchronized two-phase flow data from multiple angles. For example, investigate pressure dynamics along the displacement front.

6. With respect to the fracture surface generation method used and roughness characterization, future studies could focus on replicating fracture surfaces of real rock by coupling computational fracture generation methods with the characteristics obtained from topographic descriptors. Such integration might allow replicating the properties of real rock surfaces. With respect to 3D printing technology, more research is required to find methods to replicate real rock wettability while using 3D-printed samples.

7. Evaluate the steady-state approach to calculate relative permeability in the current experimental configuration and investigate the repeatability of the relative permeability curves and the presence of flow patterns.

8. The effect of saturation history was barely studied here, and further investigation is needed to analyze the pressure response and production behavior, especially during shear deformation.

9. The relationship between parameters of fracture roughness and experiments should be investigated further. Future studies should investigate if flow patterns are correlated

to the local heterogeneities by comparing aperture maps and saturation changes with other calculations.

10. The fracture borders and the geometry of the local pressure ports caused light interferences, which, in turn, led to the removal of these sections from the experimental local aperture maps. To better capture the local aperture maps, such interference should be avoided, allowing the imaged fracture aperture to be exported to numerical simulation meshes without artifacts.

11. 3D printing holds the potential to play a fundamental role in investigating classic models, such as the Kozeny-Carman equation, to an unprecedented level. If this technology were combined with fiber optic sensors and Particle Image Velocimetry (PIV), it could offer a rigorous approach for examining the conditions of validity of classic models, their ranges of application, the effects of pore geometry, and the influence of scale. However, it is essential to rigorously analyze whether PIV is affected by light interference from pressure ports or translucent samples.

12. Besides experimental studies, numerical simulation could be crucial for future studies focusing on predicting the appropriate water pressure needed to remove support material from the samples without altering the samples. While external support material may be removed by convection in water baths and chemical dissolution, complex pore structures may require additional water jetting for faster and better removal of support material.

References

Ahola, M. P., Mohanty, S., & Makurat, A. (1996). Coupled mechanical shear and hydraulic flow behavior of natural rock joints. In O. Stephansson, L. Jing, & C.-F. Tsang (Eds.), *Coupled thermo-hydro-mechanical processes of fractured media* (pp. 393–423, Vol. 79). Elsevier. https://doi.org/https://doi.org/10.1016/S0165-1250(96)80034-4

Alturki, A., Maini, B., & Gates, I. (2013). The effect of fracture aperture and flow rate ratios on two-phase flow in smooth-walled single fracture. *Journal of Petroleum Exploration and Production Technology*, *3*, 119–132. https://doi.org/https://doi.org/10.1007/s13202-012-0047-5

Alvarez, L. W., Alvarez, W., Asaro, F., & Michel, H. V. (1980). Extraterrestrial cause for the cretaceous-tertiary extinction. *Science*, *208*(4448), 1095–1108. https://doi.org/10.1126/science.208.4448.1095

Amadei, B., & Illangasekare, T. (1994). A mathematical model for flow and solute transport in non-homogeneous rock fractures. *International Journal of Rock Mechanics and Mining Sciences and Geomechanics Abstracts*, *31*(6), 719–731. https://doi.org/https://doi.org/10.1016/0148-9062(94)90011-6

Ambusso, W., Satik, C., & Horne, R. A study of relative permeability for steam-water flow in porous media. In: In *Twenty-first workshop on geothermal reservoir engineering*. Stanford, California: Stanford University, 1996, January, 305–311. https://www.osti.gov/biblio/889829

American Society for Testing and Materials. (2014). Standard test methods for compressive strength and elastic moduli of intact rock core specimens under varying states of stress and temperatures [ASTM D7012-14e1]. https://www.astm.org/d7012-14e01.html

American Society for Testing and Materials. (2015). Standard test method for compressive properties of rigid plastics [ASTM D695-15]. https://www.astm.org/d0695-15.html

American Society for Testing and Materials. (2022, March). Additive manufacturing - general principles - fundamentals and vocabulary [ASTM ISO/ASTM52900-21]. https://compass.astm.org/document/?contentCode=ASTM%7CF3177-21%7Cen-US&proxycl=https%3A%2F%2Fsecure.astm.org&fromLogin=true

Archambault, G., Gentier, S., Riss, J., & Flamand, R. (1997). The evolution of void spaces (permeability) in relation with rock joint shear behavior. *International Journal of Rock Mechanics and Mining Sciences*, *34*(3), 14.e1–14.e15. https://doi.org/https://doi.org/10.1016/S1365-1609(97)00046-4

Arshadi, M., Rajaram, H., Detwiler, R. L., & Jones, T. (2015). High-resolution experiments on chemical oxidation of dnapl in variable-aperture fractures. *Water Resources Research*, *51*(4), 2317–2335. https://doi.org/https://doi.org/10.1002/2014WR016159

Auradou, H. (2009). Influence of wall roughness on the geometrical, mechanical and transport properties of single fractures. *Journal of Physics D: Applied Physics*, *42*(21), 214015. https://doi.org/10.1088/0022-3727/42/21/214015

Auradou, H., Drazer, G., Hulin, J. P., & Koplik, J. (2005). Permeability anisotropy induced by the shear displacement of rough fracture walls. *Water Resources Research*, *41*(9). https://doi.org/https://doi.org/10.1029/2005WR003938

Auradou, H., Hulin, J.-P., & Roux, S. (2001). Experimental study of miscible displacement fronts in rough self-affine fractures. *Phys. Rev. E*, *63*, 066306. https://doi.org/10.1103/PhysRevE.63.066306

Babadagli, T. (2020). Unravelling transport in complex natural fractures with fractal geometry: A comprehensive review and new insights. *Journal of Hydrology*, *587*, 124937. https://doi.org/https://doi.org/10.1016/j.jhydrol.2020.124937

Babadagli, T., & Develi, K. (2003). Fractal characteristics of rocks fractured under tension. *Theoretical and Applied Fracture Mechanics*, *39*(1), 73–88. https://doi.org/https://doi.org/10.1016/S0167-8442(02)00139-8

Babadagli, T., Raza, S., Ren, X., & Develi, K. (2015). Effect of surface roughness and lithology on the water–gas and water–oil relative permeability ratios of oil-wet single fractures. *International Journal of Multiphase Flow*, *75*, 68–81. https://doi.org/https://doi.org/10.1016/j.ijmultiphaseflow.2015.05.005

Babadagli, T., & Ershaghi, I. (1992, March). *Imbibition Assisted Two-Phase Flow in Natural Fractures* (Vol. All Days). https://doi.org/10.2118/24044-MS

Bandis, S., Lumsden, A., & Barton, N. (1983). Fundamentals of rock joint deformation. *International Journal of Rock Mechanics and Mining Sciences & Geomechanics Abstracts*, *20*(6), 249–268. https://doi.org/https://doi.org/10.1016/0148-9062(83)90595-8

Barclift, M. W., & Williams, C. B. (2012). Examining variability in the mechanical properties of parts manufactured via polyjet direct 3d printing. *2012 International Solid Freeform Fabrication Symposium*. https://doi.org/http://dx.doi.org/10.26153/tsw/15397

Barton, C. C., & La Pointe, P. R. (1995). *Fractals in the earth sciences*. Plenum Press. https://link.springer.com/book/10.1007/978-1-4899-1397-5

Barton, N., Bandis, S., & Bakhtar, K. (1985). Strength, deformation and conductivity coupling of rock joints. *International Journal of Rock Mechanics and Mining Sciences & Geomechanics Abstracts*, *22*(3), 121–140. https://doi.org/https://doi.org/10.1016/0148-9062(85)93227-9

Barton, N. (1973). Review of a new shear-strength criterion for rock joints. *Engineering Geology*, *7*(4), 287–332. https://doi.org/https://doi.org/10.1016/0013-7952(73)90013-6

Barton, N., & Choubey, V. (1977). The shear strength of rock joints in theory and practice. *Rock mechanics*, *10*, 1–54. https://doi.org/https://doi.org/10.1007/BF01261801

Barton, N. (1972). A model study of rock-joint deformation. *International Journal of Rock Mechanics and Mining Sciences & Geomechanics Abstracts*, *9*(5), 579–582. https://doi.org/https://doi.org/10.1016/0148-9062(72)90010-1

Bear, J. (1972). *Dynamics of fluids in porous media*. American Elsevier Publishing Company.

Bear, J. (1988). *Dynamics of fluids in porous media*. Dover. https://app.knovel.com/hotlink/toc/id:kpDFPM000I/dynamics-fluids-in-porous/dynamics-fluids-in-porous

Bear, J., & Cheng, A. H.-D. (2010). *Modeling groundwater flow and contaminant transport* (Vol. 23). Springer Dordrecht. https://doi.org/https://doi.org/10.1007/978-1-4020-6682-5

Bear, J., Tsang, C.-F., & De Marsily, G. (1993). *Flow and contaminant transport in fractured rock*. Academic Press. https://doi.org/https://doi.org/10.1016/C2009-0-29127-6

Belem, T., Homand-Etienne, F., & Souley, M. (2000). Quantitative parameters for rock joint surface roughness. *Rock mechanics and rock engineering*, *33*(4), 217–242.

Berkowitz, B. (2002). Characterizing flow and transport in fractured geological media: A review. *Advances in Water Resources*, *25*(8), 861–884. https://doi.org/https://doi.org/10.1016/S0309-1708(02)00042-8

Bertels, S. P., DiCarlo, D. A., & Blunt, M. J. (2001). Measurement of aperture distribution, capillary pressure, relative permeability, and in situ saturation in a rock fracture using computed tomography scanning. *Water Resources Research*, *37*(3), 649–662. https://doi.org/https://doi.org/10.1029/2000WR900316

Bhushan, B. (2000). CRC press. https://doi.org/https://doi-org.login.ezproxy.library.ualberta.ca/10.1201/9780849377877

Boulon, M., Armand, G., Hoteit, N., & Divoux, P. (2002). Experimental investigations and modelling of shearing of calcite healed discontinuities of granodiorite under typical stresses [Key Issues in Waste Isolation Research]. *Engineering Geology*, *64*(2), 117–133. https://doi.org/https://doi.org/10.1016/S0013-7952(01)00112-0

Boulon, M., Selvadurai, A., Benjelloun, H., & Feuga, B. (1993). Influence of rock joint degradation on hydraulic conductivity. *International Journal of Rock Mechanics and Mining Sciences and Geomechanics Abstracts*, *30*(7), 1311–1317. https://doi.org/https://doi.org/10.1016/0148-9062(93)90115-T

Brown, S. R. (1987). Fluid flow through rock joints: The effect of surface roughness. *Journal of Geophysical Research: Solid Earth*, *92*(B2), 1337–1347. https://doi.org/https://doi.org/10.1029/JB092iB02p01337

Brown, S. R., & Scholz, C. H. (1985). Broad bandwidth study of the topography of natural rock surfaces. *Journal of Geophysical Research: Solid Earth*, *90*(B14), 12575–12582. https://doi.org/https://doi.org/10.1029/JB090iB14p12575

Brush, D. J., & Thomson, N. R. (2003). Fluid flow in synthetic rough-walled fractures: Navier-stokes, stokes, and local cubic law simulations. *Water Resources Research*, *39*(4). https://doi.org/https://doi.org/10.1029/2002WR001346

Camacho-V., R., Gómez, S., Vásquez-C., M., Fuenleal-M., N., Castillo-R., T., Ramos, G., Minutti M., C., Mesejo, A., & Fuentes-C., G. (2014, September). *Well Testing Characterization of Heavy-Oil Naturally Fractured Vuggy Reservoirs* (Vol. Day 3 Fri, September 26, 2014). https://doi.org/10.2118/171078-MS

Cantú-Chapa, A., & Landeros-Flores, R. (2001, January). The Cretaceous-Paleocene Boundary in the Subsurface Campeche Shelf, Southern Gulf of Mexico. In *The Western Gulf* *of Mexico Basin: Tectonics,Sedimentary Basins, and Petroleum Systems*. American Association of Petroleum Geologists. https://doi.org/10.1306/M75768C17

Cao, C., Xu, Z., Chai, J., & Li, Y. (2019). Radial fluid flow regime in a single fracture under high hydraulic pressure during shear process. *Journal of Hydrology*, *579*, 124142. https://doi.org/https://doi.org/10.1016/j.jhydrol.2019.124142

Charkaluk, E., Bigerelle, M., & Iost, A. (1998). Fractals and fracture. *Engineering Fracture Mechanics*, *61*(1), 119–139. https://doi.org/https://doi.org/10.1016/S0013-7944(98)00035-6

Chen, C.-Y., & Horne, R. N. (2006). Two-phase flow in rough-walled fractures: Experiments and a flow structure model. *Water Resources Research*, *42*(3). https://doi.org/https://doi.org/10.1029/2004WR003837

Chen, C.-Y., Horne, R. N., & Fourar, M. (2004). Experimental study of liquid-gas flow structure effects on relative permeabilities in a fracture. *Water Resources Research*, *40*(8). https://doi.org/https://doi.org/10.1029/2004WR003026

Chen, Y.-F., Fang, S., Wu, D.-S., & Hu, R. (2017). Visualizing and quantifying the crossover from capillary fingering to viscous fingering in a rough fracture. *Water Resources Research*, *53*(9), 7756–7772. https://doi.org/https://doi.org/10.1002/2017WR021051

Chen, Y.-F., Wu, D.-S., Fang, S., & Hu, R. (2018). Experimental study on two-phase flow in rough fracture: Phase diagram and localized flow channel. *International Journal of Heat and Mass Transfer*, *122*, 1298–1307. https://doi.org/https://doi.org/10.1016/j.ijheatmasstransfer.2018.02.031

Chen, Y.-F., Zhou, J.-Q., Hu, S.-H., Hu, R., & Zhou, C.-B. (2015). Evaluation of forchheimer equation coefficients for non-darcy flow in deformable rough-walled fractures. *Journal of Hydrology*, *529*, 993–1006. https://doi.org/https://doi.org/10.1016/j.jhydrol.2015.09.021

Chen, Y., Lian, H., Liang, W., Yang, J., Nguyen, V. P., & Bordas, S. P. (2019). The influence of fracture geometry variation on non-darcy flow in fractures under confining stresses. *International Journal of Rock Mechanics and Mining Sciences*, *113*, 59–71. https://doi.org/https://doi.org/10.1016/j.ijrmms.2018.11.017

Chen, Z., Narayan, S., Yang, Z., & Rahman, S. (2000). An experimental investigation of hydraulic behaviour of fractures and joints in granitic rock. *International Journal of Rock Mechanics and Mining Sciences*, *37*(7), 1061–1071. https://doi.org/https://doi.org/10.1016/S1365-1609(00)00039-3

Chen, Z. (2007). *Reservoir simulation: Mathematical techniques in oil recovery*. Society for Industrial; Applied Mathematics (SIAM). https://app.knovel.com/kn/resources/kpRSMTOR03/toc?b-q=reservoir%20simulation&include_synonyms=no&q=reservoir%20simulation&sort_on=default

Cheng, C., Hale, S., Milsch, H., & Blum, P. (2020). Measuring hydraulic fracture apertures: A comparison of methods. *Solid Earth*, *11*(6), 2411–2423. https://doi.org/10.5194/se-11-2411-2020

Cheng, L., Li, X., Rong, G., & Zhou, C. (2019). The effect of surface wettability and wall roughness on the residual saturation for the drainage process in sinusoidal channels.

Transport in Porous Media, *129*, 203–229. https://doi.org/https://doi.org/10.1007/s11242-019-01284-0

Choi, J.-H., Myshakin, E. M., Lei, L., Kneafsey, T. J., & Seol, Y. (2020). An experimental system and procedure of unsteady-state relative permeability test for gas hydrate-bearing sediments. *Journal of Natural Gas Science and Engineering*, *83*, 103545. https://doi.org/https://doi.org/10.1016/j.jngse.2020.103545

Corey, A. T. (1954). The interrelation between gas and oil relative permeabilities. *Producers monthly*, 38–41.

Crandall, D. (2007). *Two-phase flow in porous media and fractures* [Doctoral dissertation, Clarkson University]. ProQuest. http://proquest.umi.com/pqdweb?did=1390306321&sid=4&Fmt=2&clientId=12445&RQT=309&VName=PQD

Crandall, D., Bromhal, G., & Karpyn, Z. T. (2010). Numerical simulations examining the relationship between wall-roughness and fluid flow in rock fractures. *International Journal of Rock Mechanics and Mining Sciences*, *47*(5), 784–796. https://doi.org/https://doi.org/10.1016/j.ijrmms.2010.03.015

Crandall, D., Moore, J., Gill, M., & Stadelman, M. (2017). Ct scanning and flow measurements of shale fractures after multiple shearing events. *International Journal of Rock Mechanics and Mining Sciences*, *100*, 177–187. https://doi.org/https://doi.org/10.1016/j.ijrmms.2017.10.016

Cunningham, D., Auradou, H., Shojaei-Zadeh, S., & Drazer, G. (2020). The effect of fracture roughness on the onset of nonlinear flow [e2020WR028049 2020WR028049]. *Water Resources Research*, *56*(11), e2020WR028049. https://doi.org/https://doi.org/10.1029/2020WR028049

Dershowitz, W., Redus, K., Wallmann, P., Lapointe, P., & Axelsson, C. (1992). *The implication of fractal dimension in hydrogeology and rock mechanics version 1.1* (tech. rep.). Swedish Nuclear Fuel and Waste Management Co. Stockholm, Sweden.

Detwiler, R. L., Pringle, S. E., & Glass, R. J. (1999). Measurement of fracture aperture fields using transmitted light: An evaluation of measurement errors and their influence on simulations of flow and transport through a single fracture. *Water Resources Research*, *35*(9), 2605–2617. https://doi.org/https://doi.org/10.1029/1999WR900164

Develi, K., & Babadagli, T. (2015). Experimental and visual analysis of single-phase flow through rough fracture replicas. *International Journal of Rock Mechanics and Mining Sciences*, *73*, 139–155. https://doi.org/https://doi.org/10.1016/j.ijrmms.2014.11.002

Di Federico, V., & Neuman, S. P. (1997). Scaling of random fields by means of truncated power variograms and associated spectra. *Water Resources Research*, *33*(5), 1075–1085. https://doi.org/https://doi.org/10.1029/97WR00299

Diomampo, G. P., Chen, C.-Y., Li, K., & Horne, R. N. (2001). *Relative permeability through fractures* [Doctoral dissertation, Stanford University].

Dowd, P. A. (1984). The variogram and kriging: Robust and resistant estimators. In G. Verly, M. David, A. G. Journel, & A. Marechal (Eds.), *Geostatistics for natural resources characterization: Part 1* (pp. 91–106). Springer Netherlands. https://doi.org/10.1007/978-94-009-3699-7_6

Dullien, F. A. (1979). *Porous media: Fluid transport and pore structure*. Academic press. https://doi.org/https://doi.org/10.1016/B978-0-12-223650-1.X5001-3

Durham, W. B., & Bonner, B. P. (1994). Self-propping and fluid flow in slightly offset joints at high effective pressures. *Journal of Geophysical Research: Solid Earth*, *99*(B5), 9391–9399. https://doi.org/https://doi.org/10.1029/94JB00242

Durham, W. B. (1997). Laboratory observations of the hydraulic behavior of a permeable fracture from 3800 m depth in the ktb pilot hole. *Journal of Geophysical Research: Solid Earth*, *102*(B8), 18405–18416. https://doi.org/https://doi.org/10.1029/96JB02813

Dwivedi, P. N., & Upadhyay, S. (1977). Particle-fluid mass transfer in fixed and fluidized beds. *Industrial & Engineering Chemistry Process Design and Development*, *16*(2), 157–165. https://doi.org/https://doi.org/10.1021/i260062a001

Esaki, T., Du, S., Mitani, Y., Ikusada, K., & Jing, L. (1999). Development of a shear-flow test apparatus and determination of coupled properties for a single rock joint. *International Journal of Rock Mechanics and Mining Sciences*, *36*(5), 641–650. https://doi.org/https://doi.org/10.1016/S0148-9062(99)00044-3

Esaki, T., Hojo, H., Kimura, T., & Kameda, N. (1991, September). *Shear-flow Coupling Test On Rock Joints* (Vol. All Days) [ISRM-7CONGRESS-1991-077].

Fang, Y., Elsworth, D., Ishibashi, T., & Zhang, F. (2019, June). *Effects of Roughness on Permeability Evolution and Frictional Behavior of Fractures Under Shear* (Vol. All Days) [ARMA-2019-2109].

Fang, Y., Elsworth, D., Ishibashi, T., & Zhang, F. (2018). Permeability evolution and frictional stability of fabricated fractures with specified roughness. *Journal of Geophysical Research: Solid Earth*, *123*(11), 9355–9375. https://doi.org/https://doi.org/10.1029/2018JB016215

Fardin, N., Stephansson, O., & Jing, L. (2001). The scale dependence of rock joint surface roughness. *International Journal of Rock Mechanics and Mining Sciences*, *38*(5), 659–669. https://doi.org/https://doi.org/10.1016/S1365-1609(01)00028-4

Fourar, M., Bories, S., Lenormand, R., & Persoff, P. (1993). Two-phase flow in smooth and rough fractures: Measurement and correlation by porous-medium and pipe flow models. *Water Resources Research*, *29*(11), 3699–3708. https://doi.org/https://doi.org/10.1029/93WR01529

Gale, J. E., LeMessurier, P., & Seok, E. (2001, July). *Design and application of a biaxial, servo-controlled, test frame to determine the coupled H-M-T properties of discrete fractures* (Vol. All Days) [ARMA-01-0669].

Gallant, J. C., Moore, I. D., Hutchinson, M. F., & Gessler, P. (1994). Estimating fractal dimension of profiles: A comparison of methods. *Mathematical Geology*, *26*(4), 455–481. https://doi.org/https://doi.org/10.1007/BF02083489

Ge, S. (1997). A governing equation for fluid flow in rough fractures. *Water Resources Research*, *33*(1), 53–61. https://doi.org/https://doi.org/10.1029/96WR02588

Ge, Y., Kulatilake, P. H., Tang, H., & Xiong, C. (2014). Investigation of natural rock joint roughness. *Computers and Geotechnics*, *55*, 290–305. https://doi.org/https://doi.org/10.1016/j.compgeo.2013.09.015

Gentier, S., Lamontagne, E., Archambault, G., & Riss, J. (1997). Anisotropy of flow in a fracture undergoing shear and its relationship to the direction of shearing and injection pressure. *International Journal of Rock Mechanics and Mining Sciences*, *34*(3), 94.e1–94.e12. https://doi.org/https://doi.org/10.1016/S1365-1609(97)00085-3

Gibson, I., Rosen, D. W., Stucker, B., & Khorasani, M. (2021). *Additive manufacturing technologies*. Springer Cham. https://doi.org/https://doi.org/10.1007/978-3-030-56127-7

Giger, S., Clennell, M., Harbers, C., Clark, P., Ricchetti, M., Ter Heege, J., Wassing, B., & Orlic, B. (2011). Design, operation and validation of a new fluid-sealed direct shear apparatus capable of monitoring fault-related fluid flow to large displacements. *International Journal of Rock Mechanics and Mining Sciences*, *48*(7), 1160–1172. https://doi.org/https://doi.org/10.1016/j.ijrmms.2011.09.005

Grajales-Nishimura, J. M., Cedillo-Pardo, E., Rosales-Domínguez, C., Morán-Zenteno, D. J., Alvarez, W., Claeys, P., Ruíz-Morales, J., García-Hernández, J., Padilla-Avila, P., & Sánchez-Ríos, A. (2000). Chicxulub impact: The origin of reservoir and seal facies in the southeastern Mexico oil fields. *Geology*, *28*(4), 307–310. https://doi.org/10.1130/0091-7613(2000)28⟨307:CITOOR⟩2.0.CO;2

Graton, L. C., & Fraser, H. J. (1935). Systematic packing of spheres: With particular relation to porosity and permeability. *The Journal of Geology*, *43*(8, Part 1), 785–909. https://doi.org/10.1086/624386

Guerrero Zabala, F. V. (2019). *Experimental study of heavy oil recovery mechanisms in a 2d system* [Doctoral dissertation, Master's thesis, University of Calgary]. http://hdl.handle.net/1880/109490

Gustavson, S. (2005). Simplex noise demystified. *Linköping University, Linköping, Sweden, Research Report*.

Hakami, E., & Larsson, E. (1996). Aperture measurements and flow experiments on a single natural fracture. *International Journal of Rock Mechanics and Mining Sciences and Geomechanics Abstracts*, *33*(4), 395–404. https://doi.org/https://doi.org/10.1016/0148-9062(95)00070-4

Hans, J., & Boulon, M. (2003). A new device for investigating the hydro-mechanical properties of rock joints. *International Journal for Numerical and Analytical Methods in Geomechanics*, *27*(6), 513–548. https://doi.org/https://doi.org/10.1002/nag.285

Hargitai, H., Byrne, P. K., & Korteniemi, J. (2021). Fracture. In *Encyclopedia of planetary landforms* (pp. 1–11). Springer New York. https://doi.org/10.1007/978-1-4614-9213-9_158-1

Hasiuk, F., Ishutov, S., & Pacyga, A. (2018). Validating 3d-printed porous proxies by tomography and porosimetry. *Rapid Prototyping Journal*, *24*(3), 630–636. https://doi.org/https://doi.org/10.1108/RPJ-06-2017-0121

He, X., Sinan, M., Kwak, H., & Hoteit, H. (2021). A corrected cubic law for single-phase laminar flow through rough-walled fractures. *Advances in Water Resources*, *154*, 103984. https://doi.org/https://doi.org/10.1016/j.advwatres.2021.103984

Head, D., & Vanorio, T. (2016). Effects of changes in rock microstructures on permeability: 3-d printing investigation. *Geophysical Research Letters*, *43*(14), 7494–7502. https://doi.org/https://doi.org/10.1002/2016GL069334

Hildebrand, A. R., Penfield, G. T., Kring, D. A., Pilkington, M., Camargo Z., A., Jacobsen, S. B., & Boynton, W. V. (1991). Chicxulub Crater: A possible Cretaceous/Tertiary boundary impact crater on the Yucatán Peninsula, Mexico. *Geology*, *19*(9), 867–871. https://doi.org/10.1130/0091-7613(1991)019⟨0867:CCAPCT⟩2.3.CO;2

Horgue, P., Soulaine, C., Franc, J., Guibert, R., & Debenest, G. (2015). An open-source toolbox for multiphase flow in porous media. *Computer Physics Communications*, *187*, 217–226. https://doi.org/https://doi.org/10.1016/j.cpc.2014.10.005

Huitt, J. L. (1956). Fluid flow in simulated fractures. *AIChE Journal*, *2*(2), 259–264. https://doi.org/https://doi.org/10.1002/aic.690020224

Huo, D., & Benson, S. M. (2016). Experimental investigation of stress-dependency of relative permeability in rock fractures. *Transport in Porous Media*, *113*, 567–590. https://doi.org/https://doi.org/10.1007/s11242-016-0713-z

Indraratna, B., Ranjith, P., & Gale, W. (1999). Single phase water flow through rock fractures. *Geotechnical & Geological Engineering*, *17*, 211–240. https://doi.org/https://doi.org/10.1023/A:1008922417511

International Organization for Standardization. (2021). Geometrical product specifications (gps) — surface texture: Profile - part 2: Terms, definitions and surface texture parameters [ISO 21920-2:2021(E)].

Isaaks, E. H., & Srivastava, R. M. (1989). 4.9 correlation functions, covariance functions, and variograms. In *An introduction to applied geostatistics*. Oxford University Press. https://app.knovel.com/hotlink/khtml/id:kt006QL0W5/an-introduction-applied/correlation-functions

Isakov, E., Ogilvie, S. R., Taylor, C. W., & Glover, P. W. (2001). Fluid flow through rough fractures in rocks i: High resolution aperture determinations. *Earth and Planetary Science Letters*, *191*(3), 267–282. https://doi.org/https://doi.org/10.1016/S0012-821X(01)00424-1

Ishibashi, T., Fang, Y., Elsworth, D., Watanabe, N., & Asanuma, H. (2020). Hydromechanical properties of 3d printed fractures with controlled surface roughness: Insights into shear-permeability coupling processes. *International Journal of Rock Mechanics and Mining Sciences*, *128*, 104271. https://doi.org/https://doi.org/10.1016/j.ijrmms.2020.104271

Ishibashi, T., Watanabe, N., Tamagawa, T., & Tsuchiya, N. (2019). Three-dimensional channeling flow within subsurface rock fracture networks suggested via fluid flow analysis in the yufutsu fractured oil/gas reservoir. *Journal of Petroleum Science and Engineering*, *178*, 838–851. https://doi.org/https://doi.org/10.1016/j.petrol.2019.04.003

Ishutov, S., Hasiuk, F. J., Harding, C., & Gray, J. N. (2015). 3D printing sandstone porosity models. *Interpretation*, *3*(3), SX49–SX61. https://doi.org/10.1190/INT-2014-0266.1

Ishutov, S., Jobe, T. D., Zhang, S., Gonzalez, M., Agar, S. M., Hasiuk, F. J., Watson, F., Geiger, S., Mackay, E., & Chalaturnyk, R. (2018). Three-dimensional printing for geoscience: Fundamental research, education, and applications for the petroleum industry. *AAPG Bulletin*, *102*(1), 1–26. https://doi.org/10.1306/0329171621117056

Iwai, K. (1976). *Fundamental studies of fluid flow through a single fracture* [Doctoral dissertation, University of California, Berkeley].

Javadi, M., Sharifzadeh, M., Shahriar, K., & Mitani, Y. (2014). Critical reynolds number for nonlinear flow through rough-walled fractures: The role of shear processes. *Water Resources Research*, *50*(2), 1789–1804. https://doi.org/https://doi.org/10.1002/2013WR014610

Ji, Y., Wanniarachchi, W., & Wu, W. (2020). Effect of fluid pressure heterogeneity on injection-induced fracture activation. *Computers and Geotechnics*, *123*, 103589. https://doi.org/https://doi.org/10.1016/j.compgeo.2020.103589

Jiang, C., & Zhao, G.-F. (2015). A preliminary study of 3d printing on rock mechanics. *Rock Mechanics and Rock Engineering*, *48*(3), 1041–1050. https://link.springer.com/article/10.1007/s00603-014-0612-y

Jiang, Y., Xiao, J., Tanabashi, Y., & Mizokami, T. (2004). Development of an automated servo-controlled direct shear apparatus applying a constant normal stiffness condition. *International Journal of Rock Mechanics and Mining Sciences*, *41*(2), 275–286. https://doi.org/https://doi.org/10.1016/j.ijrmms.2003.08.004

Johnson, E., Bossler, D., & Bossler, V. N. (1959). Calculation of Relative Permeability from Displacement Experiments. *Transactions of the AIME*, *216*(01), 370–372. https://doi.org/10.2118/1023-G

Ju, Y., Wang, L., Xie, H., Ma, G., Mao, L., Zheng, Z., & Lu, J. (2017). Visualization of the three-dimensional structure and stress field of aggregated concrete materials through 3d printing and frozen-stress techniques. *Construction and Building Materials*, *143*, 121–137. https://doi.org/https://doi.org/10.1016/j.conbuildmat.2017.03.102

Ju, Y., Wang, L., Xie, H., Ma, G., Zheng, Z., & Mao, L. (2017). Visualization and transparentization of the structure and stress field of aggregated geomaterials through 3d printing and photoelastic techniques. *Rock Mechanics and Rock Engineering*, *50*, 1383–1407.

Kaviany, M. (1995). *Principles of heat transfer in porous media*. Springer New York, NY. https://doi.org/https://doi.org/10.1007/978-1-4612-4254-3

Keller, G., Khozyem, H., Adatte, T., Malarkodi, N., Spangenberg, J. E., & Stinnesbeck, W. (2013). Chicxulub impact spherules in the North Atlantic and Caribbean: age constraints and Cretaceous–Tertiary boundary hiatus. *Geological Magazine*, *150*(5), 885–907. https://doi.org/10.1017/S0016756812001069

Kishida, K., Sawada, A., Yasuhara, H., & Hosoda, T. (2013). Estimation of fracture flow considering the inhomogeneous structure of single rock fractures. *Soils and Foundations*, *53*(1), 105–116. https://doi.org/https://doi.org/10.1016/j.sandf.2012.12.007

Klinkenberg, B. (1992). Fractals and morphometric measures: Is there a relationship? [Fractals in Geomorphology]. *Geomorphology*, *5*(1), 5–20. https://doi.org/https://doi.org/10.1016/0169-555X(92)90055-S

Klinkenberg, B. (1994). A review of methods used to determine the fractal dimension of linear features. *Mathematical Geology*, *26*, 23–46. https://doi.org/https://doi.org/10.1007/BF02065874

Kong., L., Ostadhassan., M., Li., C., & Tamimi., N. (2017, June). *Rock Physics and Geomechanics of 3-D Printed Rocks* (Vol. All Days).

Kong, L., Ostadhassan, M., Li, C., & Tamimi, N. (2018). Pore characterization of 3d-printed gypsum rocks: A comprehensive approach. *Journal of materials science*, *53*, 5063–5078.

Konzuk, J. S., & Kueper, B. H. (2004). Evaluation of cubic law based models describing single-phase flow through a rough-walled fracture. *Water Resources Research*, *40*(2). https://doi.org/https://doi.org/10.1029/2003WR002356

Koyama, T., Fardin, N., Jing, L., & Stephansson, O. (2006). Numerical simulation of shear-induced flow anisotropy and scale-dependent aperture and transmissivity evolution of rock fracture replicas. *International Journal of Rock Mechanics and Mining Sciences*, *43*(1), 89–106. https://doi.org/https://doi.org/10.1016/j.ijrmms.2005.04.006

Koyama, T., Li, B., Jiang, Y., & Jing, L. (2008). Coupled shear-flow tests for rock fractures with visualization of the fluid flow and their numerical simulations. *International Journal of Geotechnical Engineering*, *2*(3), 215–227. https://doi.org/10.3328/IJGE.2008.02.03.215-227

Kulatilake, P. H. S. W., Balasingam, P., Park, J., & Morgan, R. (2006). Natural rock joint roughness quantification through fractal techniques. *Geotechnical and Geological Engineering*, *24*(5), 1181–1202. https://link.springer.com/article/10.1007/s10706-005-1219-6

Kulatilake, P., Shou, G., Huang, T., & Morgan, R. (1995). New peak shear strength criteria for anisotropic rock joints. *International Journal of Rock Mechanics and Mining Sciences & Geomechanics Abstracts*, *32*(7), 673–697. https://doi.org/https://doi.org/10.1016/0148-9062(95)00022-9

Kulatilake, P., Um, J., & Pan, G. (1998). Requirements for accurate quantification of self-affine roughness using the variogram method. *International journal of solids and structures*, *35*(31-32), 4167–4189.

Kulatilake, P. H. S. W., Du, S.-G., Ankah, M. L. Y., Yong, R., Sunkpal, D. T., Zhao, X., Liu, G.-J., & Wu, R. (2021). Non-stationarity, heterogeneity, scale effects, and anisotropy investigations on natural rock joint roughness using the variogram method. *Bulletin of Engineering Geology and the Environment: The official journal of the IAEG*, *80*(8), 6121–6143. https://link.springer.com/article/10.1007/s10064-021-02321-3

Kwafniewski, M., & Wang, J. (1997). Surface roughness evolution and mechanical behavior of rock joints under shear. *International Journal of Rock Mechanics and Mining Sciences*, *34*(3), 157.e1–157.e14. https://doi.org/https://doi.org/10.1016/S1365-1609(97)00042-7

Laliberte, G. E., Corey, A. T., & Brooks, R. H. (1966). *Properties of unsaturated porous media* [Doctoral dissertation, Colorado State University. Libraries].

Laura J., P.-N., & David D., N. (2016). Approaching a universal scaling relationship between fracture stiffness and fluid flow. *Nature Communications*, *7*(1), 1–6. https://www.nature.com/articles/ncomms10663

Lee, H., & Cho, T. (2002). Hydraulic characteristics of rough fractures in linear flow under normal and shear load. *Rock mechanics and rock engineering*, *35*(4), 299–318.

Lee, S. H., Lee, K.-K., & Yeo, I. W. (2014). Assessment of the validity of stokes and reynolds equations for fluid flow through a rough-walled fracture with flow imaging. *Geophysical Research Letters*, *41*(13), 4578–4585. https://doi.org/https://doi.org/10.1002/2014GL060481

Li, B., Jiang, Y., Koyama, T., Jing, L., & Tanabashi, Y. (2008). Experimental study of the hydro-mechanical behavior of rock joints using a parallel-plate model containing contact areas and artificial fractures. *International Journal of Rock Mechanics and Mining Sciences*, *45*(3), 362–375. https://doi.org/https://doi.org/10.1016/j.ijrmms.2007.06.004

Li, B., Liu, R., & Jiang, Y. (2016). Influences of hydraulic gradient, surface roughness, intersecting angle, and scale effect on nonlinear flow behavior at single fracture intersections. *Journal of Hydrology*, *538*, 440–453. https://doi.org/https://doi.org/10.1016/j.jhydrol.2016.04.053

Li, J., Cherubini, C., Galindo Torres, S. A., Li, Z., Pastore, N., & Li, L. (2018). Laboratory investigation of flow paths in 3d self-affine fractures with lattice boltzmann simulations. *Energies*, *11*(1). https://doi.org/10.3390/en11010168

Li, Y., & Huang, R. (2015). Relationship between joint roughness coefficient and fractal dimension of rock fracture surfaces. *International Journal of Rock Mechanics and Mining Sciences*, *75*, 15–22. https://doi.org/https://doi.org/10.1016/j.ijrmms.2015.01.007

Li, Y., & Zhang, Y. (2015). Quantitative estimation of joint roughness coefficient using statistical parameters. *International Journal of Rock Mechanics and Mining Sciences*, *77*, 27–35. https://doi.org/https://doi.org/10.1016/j.ijrmms.2015.03.016

Lian, P., & Cheng, L. (2012). The Characteristics of Relative Permeability Curves in Naturally Fractured Carbonate Reservoirs. *Journal of Canadian Petroleum Technology*, *51*(02), 137–142. https://doi.org/10.2118/154814-PA

Liu, P., Ju, Y., Fu, G., & Ren, Z. (2020). Visualization of full-field stress evolution during 3d penetrated crack propagation through 3d printing and frozen stress techniques. *Engineering Fracture Mechanics*, *236*, 107222. https://doi.org/https://doi.org/10.1016/j.engfracmech.2020.107222

Lomize, G. (1951). Water flow through jointed rock. *Gosenergoizdat, Moscow*, *127*.

Loomis, A., & Crowell, D. (1962). *Relative permeability studies: Gas-oil and water-oil systems* (tech. rep.). Bureau of Mines, San Francisco, Calif.(USA). Bulltin 599. https://digital.library.unt.edu/ark:/67531/metadc12753/

Lopez-Saavedra, S., Zambrano-Narvaez, G., Ishutov, S., & Chalaturnyk, R. (2024). The influence of displacements arising from shear motion on two-phase flow through 3d-printed fractures. *Geoenergy Science and Engineering*, 212731. https://doi.org/https://doi.org/10.1016/j.geoen.2024.212731

Louis, C. (1967). *Strömungsvorgänge in klüftigen medien und ihre wirkung auf die standsicherheit von bauwerken und böschungen im fels* (Vol. 30). Universität Fridericiana, Inst. f. Bodenmechanik u. Felsmechanik.

Louis, C. (1969). A study of groundwater flow in jointed rock and its influence on the stability of rock masses. *Rock mechanics research report*, *10*, 1–90.

Macdonald, N. P., Currivan, S. A., Tedone, L., & Paull, B. (2017). Direct production of microstructured surfaces for planar chromatography using 3d printing. *Analytical chemistry*, *89*(4), 2457–2463. https://doi.org/10.1021/acs.analchem.6b04546

Magsipoc, E., Zhao, Q., & Grasselli, G. (2020). 2d and 3d roughness characterization. *Rock Mechanics and Rock Engineering*, *53*, 1495–1519. https://doi.org/https://doi.org/10.1007/s00603-019-01977-4

Mandelbrot, B. B., & Blumen, A. (1989). Fractal geometry: What is it, and what does it do? [and discussion]. *Proceedings of the Royal Society of London. Series A, Mathematical and Physical Sciences*, *423*(1864), 3–16. https://royalsocietypublishing.org/doi/10.1098/rspa.1989.0038

Marchand, S., Mersch, O., Selzer, M., Nitschke, F., Schoenball, M., Schmittbuhl, J., Nestler, B., & Kohl, T. (2019). A Stochastic Study of Flow Anisotropy and Channelling in Open Rough Fractures. *Rock Mechanics and Rock Engineering*. https://doi.org/10.1007/s00603-019-01907-4

Matsuki, K., Kimura, Y., Sakaguchi, K., Kizaki, A., & Giwelli, A. (2010). Effect of shear displacement on the hydraulic conductivity of a fracture. *International Journal of Rock Mechanics and Mining Sciences*, *47*(3), 436–449. https://doi.org/https://doi.org/10.1016/j.ijrmms.2009.10.002

Matsuki, K., Lee, J., Sakaguchi, K., & Hayashi, K. (1999). Size effect in flow conductance of a closed small-scale hydraulic fracture in granite. *Geothermal Science and Technology*, *6*(1-4), 113–138.

McDonald, A. E., Beckner, B. L., Chan, H. M., Jones, T. A., & Wooten, S. O. (1991, April). *Some Important Considerations in the Simulation of Naturally Fractured Reservoirs* (Vol. All Days). https://doi.org/10.2118/21814-MS

McDonald, B. (2023). Surf2stl. https://www.mathworks.com/matlabcentral/fileexchange/4512-surf2stl

Méheust, Y., & Schmittbuhl, J. (2001). Geometrical heterogeneities and permeability anisotropy of rough fractures. *Journal of Geophysical Research: Solid Earth*, *106*(B2), 2089–2102. https://doi.org/https://doi.org/10.1029/2000JB900306

Mofakham, A. A., Stadelman, M., Ahmadi, G., Shanley, K. T., & Crandall, D. (2018). Computational modeling of hydraulic properties of a sheared single rock fracture. *Transport in Porous Media*, *124*(1), 1–30. https://link.springer.com/article/10.1007/s11242-018-1030-5

Mourzenko, V., Thovert, J.-F., & Adler, P. (1995). Permeability of a Single Fracture; Validity of the Reynolds Equation. *Journal de Physique II*, *5*(3), 465–482. https://doi.org/10.1051/jp2:1995133

Mourzenko, V. V., Thovert, J. F., & Adler, P. M. (2018). Conductivity and transmissivity of a single fracture. *Transport in Porous Media*, *123*(2), 235–256. https://link.springer.com/article/10.1007/s11242-018-1037-y

Murata, S., & Saito, T. (1999). The variogram method for a fractal model of a rock joint surface. *Geotechnical and Geological Engineering*, *17*(3-4), 197–210. https://link.springer.com/article/10.1023/A:1008917503259

Myers, N. (1962). Characterization of surface roughness. *Wear*, *5*(3), 182–189. https://doi.org/https://doi.org/10.1016/0043-1648(62)90002-9

National Research Council. (1996). *Rock fractures and fluid flow: Contemporary understanding and applications*. The National Academies Press. https://doi.org/10.17226/2309

Nelson, M. J., Newsom, H. E., Spilde, M. N., & Salge, T. (2012). Petrographic investigation of melt and matrix relationships in chicxulub crater yaxcopoil-1 brecciated melt rock and melt rock-bearing suevite (846–885m, units 4 and 5). *Geochimica et Cosmochimica Acta*, *86*, 1–20. https://doi.org/https://doi.org/10.1016/j.gca.2012.02.022

Nelson, R. A. (2001). *Geologic analysis of naturally fractured reservoirs* (Vol. 1). Gulf Professional Publishing.

Nemoto, K., Watanabe, N., Hirano, N., & Tsuchiya, N. (2009). Direct measurement of contact area and stress dependence of anisotropic flow through rock fracture with heterogeneous aperture distribution. *Earth and Planetary Science Letters*, *281*(1), 81–87. https://doi.org/https://doi.org/10.1016/j.epsl.2009.02.005

Nicholl, M. J., Rajaram, H., Glass, R. J., & Detwiler, R. (1999). Saturated flow in a single fracture: Evaluation of the reynolds equation in measured aperture fields. *Water Resources Research*, *35*(11), 3361–3373. https://doi.org/https://doi.org/10.1029/1999WR900241

Nowamooz, A., Radilla, G., & Fourar, M. (2009). Non-darcian two-phase flow in a transparent replica of a rough-walled rock fracture. *Water Resources Research*, *45*(7). https://doi.org/https://doi.org/10.1029/2008WR007315

Odling, N. E. (1994). Natural fracture profiles, fractal dimension and joint roughness coefficients. *Rock mechanics and rock engineering*, *27*, 135–153. https://doi.org/https://doi.org/10.1007/BF01020307

Olsson, R., & Barton, N. (2001). An improved model for hydromechanical coupling during shearing of rock joints. *International Journal of Rock Mechanics and Mining Sciences*, *38*(3), 317–329. https://doi.org/https://doi.org/10.1016/S1365-1609(00)00079-4

Olsson, W., & Brown, S. (1993). Hydromechanical response of a fracture undergoing compression and shear. *International Journal of Rock Mechanics and Mining Sciences and Geomechanics Abstracts*, *30*(7), 845–851. https://doi.org/https://doi.org/10.1016/0148-9062(93)90034-B

Olsson, W. A. (1992). The effect of slip on the flow of fluid through a fracture. *Geophysical Research Letters*, *19*(6), 541–543. https://doi.org/https://doi.org/10.1029/92GL00197

Oron, A. P., & Berkowitz, B. (1998). Flow in rock fractures: The local cubic law assumption reexamined. *Water Resources Research*, *34*(11), 2811–2825. https://doi.org/https://doi.org/10.1029/98WR02285

Ottemöller, L., Nielsen, H. H., Atakan, K., Braunmiller, J., & Havskov, J. (2005). The 7 may 2001 induced seismic event in the ekofisk oil field, north sea. *Journal of Geophysical Research: Solid Earth*, *110*(B10). https://doi.org/https://doi.org/10.1029/2004JB003374

Pan, X., Wong, R., & Maini, B. (1996, June). *Steady State Two-phase In a Smooth Parallel Fracture* (Vol. All Days) [PETSOC-96-39]. https://doi.org/10.2118/96-39

Pan, X. (1999). *Immiscible two-phase flow in a fracture*. https://doi.org/10.11575/PRISM/18244

Parrish, D. R. (1963, April). *Fluid Flow In Rough Fractures* (Vol. All Days). https://doi.org/10.2118/563-MS

Parsons, R. (1966). Permeability of Idealized Fractured Rock. *Society of Petroleum Engineers Journal*, *6*(02), 126–136. https://doi.org/10.2118/1289-PA

Patir, N., & Cheng, H. S. (1978). An Average Flow Model for Determining Effects of Three-Dimensional Roughness on Partial Hydrodynamic Lubrication. *Journal of Lubrication Technology*, *100*(1), 12–17. https://doi.org/10.1115/1.3453103

Perlin, K. (1985). An image synthesizer. *SIGGRAPH Comput. Graph.*, *19*(3), 287–296. https://doi.org/10.1145/325165.325247

Persoff, P., & Pruess, K. (1995). Two-phase flow visualization and relative permeability measurement in natural rough-walled rock fractures. *Water Resources Research*, *31*(5), 1175–1186. https://doi.org/https://doi.org/10.1029/95WR00171

Peters, F., & Arabali, D. (2013). Interfacial tension between oil and water measured with a modified contour method. *Colloids and Surfaces A: Physicochemical and Engineering Aspects*, *426*, 1–5. https://doi.org/https://doi.org/10.1016/j.colsurfa.2013.03.010

Phillips, T., Bultreys, T., Bisdom, K., Kampman, N., Van Offenwert, S., Mascini, A., Cnudde, V., & Busch, A. (2021). A systematic investigation into the control of roughness on the flow properties of 3d-printed fractures [ewrcr.25233 wrcr.25233]. *Water Resources Research*, *57*(4), ewrcr.25233. https://doi.org/https://doi.org/10.1029/2020WR028671

Pieters, D. A., & Graves, R. M. (1994, October). *Fracture Relative Permeability: Linear or Non-Linear Function of Saturation* (Vol. All Days). https://doi.org/10.2118/28701-MS

Piggott, A. R. (1990). *Analytical and experimental studies of rock fracture hydraulics*. The Pennsylvania State University.

Poon, C. Y., Sayles, R. S., & Jones, T. A. (1992). Surface measurement and fractal characterization of naturally fractured rocks. *Journal of Physics D: Applied Physics*, *25*(8), 1269. https://doi.org/10.1088/0022-3727/25/8/019

Pruess, K., & Tsang, Y. W. (1990). On two-phase relative permeability and capillary pressure of rough-walled rock fractures. *Water Resources Research*, *26*(9), 1915–1926. https://doi.org/https://doi.org/10.1029/WR026i009p01915

Pyrak-Nolte, L. J., Myer, L. R., Cook, N. G., & Witherspoon, P. A. (1987, August). *Hydraulic And Mechanical Properties of Natural Fractures In Low Permeability Rock* (Vol. All Days) [ISRM-6CONGRESS-1987-042].

Quadros, E. F. d., & Cruz, P. T. d. (1982). *Determinação das características do fluxo de água em fraturas de rochas* [Doctoral dissertation, Dept. of Civil Eng., Polytech. School, University of Sgo Paulo].

Quinn, P., Cherry, J., & Parker, B. (2020). Relationship between the critical reynolds number and aperture for flow through single fractures: Evidence from published laboratory studies. *Journal of Hydrology*, *581*, 124384. https://doi.org/https://doi.org/10.1016/j.jhydrol.2019.124384

Radilla, G., Nowamooz, A., & Fourar, M. (2013). Modeling non-darcian single- and two-phase flow in transparent replicas of rough-walled rock fractures. *Transport in Porous Media*, *98*(2), 401–426. https://link.springer.com/article/10.1007/s11242-013-0150-1

Raimbay, A., Babadagli, T., Kuru, E., & Develi, K. (2017). Fractal analysis of single-phase water and polymer solution flow at high rates in open and horizontally displaced rough fractures. *International Journal of Rock Mechanics and Mining Sciences*, *92*, 54–71. https://doi.org/https://doi.org/10.1016/j.ijrmms.2016.12.006

Ranjith, P. G., & Darlington, W. (2007). Nonlinear single-phase flow in real rock joints. *Water Resources Research*, *43*(9). https://doi.org/https://doi.org/10.1029/2006WR005457

Ranjith, P., & Viete, D. (2011). Applicability of the 'cubic law' for non-darcian fracture flow. *Journal of Petroleum Science and Engineering*, *78*(2), 321–327. https://doi.org/https://doi.org/10.1016/j.petrol.2011.07.015

Reitsma, S., & Kueper, B. H. (1994). Laboratory measurement of capillary pressure-saturation relationships in a rock fracture. *Water Resources Research*, *30*(4), 865–878. https://doi.org/https://doi.org/10.1029/93WR03451

Renshaw, C. E. (1995). On the relationship between mechanical and hydraulic apertures in rough-walled fractures. *Journal of Geophysical Research: Solid Earth*, *100*(B12), 24629–24636. https://doi.org/https://doi.org/10.1029/95JB02159

Romm, E. (1966). Flow characteristics of fractured rocks. *Nedra, Moscow*, *283*.

Russ, J. C. (2016). *The image processing handbook*. CRC Press LLC. https://www.taylorfrancis.com/books/mono/10.1201/b18983/image-processing-handbook-john-russ-brent-neal

Rutqvist, J., & Stephansson, O. (2003). The role of hydromechanical coupling in fractured rock engineering. *Hydrogeology Journal*, *11*(1), 7–40. https://link.springer.com/article/10.1007/s10040-002-0241-5

Saavedra, S. L., Ishutov, S., Chalaturnyk, R., & Narvaez, G. Z. (2020). Importance of improving support material removal from polyjet 3d-printed porous models. *ECMOR XVII*, *2020*(1), 1–11. https://doi.org/10.3997/2214-4609.202035210

Saboorian-Jooybari, Hadi. (2016). Analytical estimation of water-oil relative permeabilities through fractures. *Oil Gas Sci. Technol. - Rev. IFP Energies nouvelles*, *71*(3), 31. https://doi.org/10.2516/ogst/2014054

Safka, J., Ackermann, M., & Martis, D. (2016). Chemical resistance of materials used in additive manufacturing. *MM Science Journal*. https://doi.org/10.17973/MMSJ.2016_12_2016185

Salge, T. (2007). *The ejecta blanket of the chicxulub impact crater, yucatán, mexico* [Doctoral dissertation, Humboldt-Universität zu Berlin, Mathematisch-Naturwissenschaftliche Fakultät I]. https://doi.org/http://dx.doi.org/10.18452/15579

Schiozer, D., & O. Mu'noz Mazo, E. (2013). Modeling fracture relative permeability - what is the best option? Article cp-348-00350. https://doi.org/https://doi.org/10.3997/2214-4609.20130867

Schmittbuhl, J., Schmitt, F., & Scholz, C. (1995). Scaling invariance of crack surfaces. *Journal of Geophysical Research: Solid Earth*, *100*(B4), 5953–5973. https://doi.org/https://doi.org/10.1029/94JB02885

Schulte, P., Alegret, L., Arenillas, I., Arz, J. A., Barton, P. J., Bown, P. R., Bralower, T. J., Christeson, G. L., Claeys, P., Cockell, C. S., Collins, G. S., Deutsch, A., Goldin, T. J., Goto, K., Grajales-Nishimura, J. M., Grieve, R. A. F., Gulick, S. P. S., Johnson, K. R., Kiessling, W., . . . Willumsen, P. S. (2010). The chicxulub asteroid impact and mass extinction at the cretaceous-paleogene boundary. *Science*, *327*(5970), 1214–1218. https://doi.org/10.1126/science.1177265

Schwanghart, W. (2023). Experimental (semi-) variogram. https://www.mathworks.com/matlabcentral/fileexchange/20355-experimental-semi-variogram

Seybold, H. J., Carmona, H. A., Filho, F. A. L., Araújo, A. D., Filho, F. N., & Andrade, J. S. (2020). Flow through three-dimensional self-affine fractures. *Phys. Rev. Fluids*, *5*, 104101. https://doi.org/10.1103/PhysRevFluids.5.104101

Sharifzadeh, M., Mehrishal, S., Mitani, Y., & Esaki., T. (2017). Chapter 20 - hydro-mechanical coupling of rock joints during normal and shear loading. In X.-T. Feng (Ed.), *Rock mechanics and engineering* (p. 38, Vol. 5). CRC Press. https://doi.org/https://doi.org/10.4324/9781315708119

Shen, B., Stephansson, O., & Rinne, M. (2020). *Modelling rock fracturing processes: Theories, methods, and applications*. Springer Cham. https://doi.org/https://doi.org/10.1007/978-3-030-35525-8

Skjetne, E., Hansen, A., & Gudmundsson, J. S. (1999). High-velocity flow in a rough fracture. *Journal of Fluid Mechanics*, *383*, 1–28. https://www.cambridge.org/core/journals/journal-of-fluid-mechanics/article/abs/highvelocity-flow-in-a-rough-fracture/9E2AA0CA12C12EC6566B715618091313

Snow, D. T. (1965). *A parallel plate model of fractured permeable media* [Doctoral dissertation, University of California, Berkeley].

Speyer, N., Li, K., & Horne, R. (2007). Experimental measurement of two-phase relative permeability in vertical fractures. *Proceedings of the Thirty-Second Workshop on Geothermal Reservoir Engineering, Stanford University, Stanford, CA, USA*, 22–24.

Stearns, D. W., & Friedman, M. (1972, January). Reservoirs in Fractured Rock. In *Stratigraphic Oil and Gas Fields—Classification, Exploration Methods, and Case Histories.* American Association of Petroleum Geologists. https://doi.org/10.1306/M16371C8

Stratasys. (2015). Polyjet best practice sup707 water-soluble support.

Stratasys. (2016). Guide to basic post-printing processes for polyjet 3d models.

Stratasys. (2017). Application note - veroclear rgd810.

Stratasys. (2020). Veroclear rigid transparent polyjet material. https://www.stratasys.com/siteassets/materials/materials-catalog/polyjet-materials/veroclear/mds_pj_veroclear_0320a.pdf

Streltsova, T. D. (1983). Well Pressure Behavior of a Naturally Fractured Reservoir. *Society of Petroleum Engineers Journal*, *23*(05), 769–780. https://doi.org/10.2118/10782-PA

Sutera, S. P., & Skalak, R. (1993). The history of poiseuille's law. *Annual Review of Fluid Mechanics*, *25*(1), 1–20. https://doi.org/10.1146/annurev.fl.25.010193.000245

Suzuki, A., Minto, J. M., Watanabe, N., Li, K., & Horne, R. N. (2019). Contributions of 3d printed fracture networks to development of flow and transport models. *Transport in Porous Media*, *129*, 485–500.

Suzuki, A., Watanabe, N., Li, K., & Horne, R. N. (2017). Fracture network created by 3-d printer and its validation using ct images. *Water Resources Research*, *53*(7), 6330–6339. https://doi.org/https://doi.org/10.1002/2017WR021032

Swisher, C. C., Grajales-Nishimura, J. M., Montanari, A., Margolis, S. V., Claeys, P., Alvarez, W., Renne, P., Cedillo-Pardoa, E., Maurrasse, F. J.-M. R., Curtis, G. H., Smit, J., & McWilliams, M. O. (1992). Coeval 40ar/39ar ages of 65.0 million years ago from chicxulub crater melt rock and cretaceous-tertiary boundary tektites. *Science*, *257*(5072), 954–958. https://doi.org/10.1126/science.257.5072.954

Tate, N. J. (1998). Estimating the fractal dimension of synthetic topographic surfaces. *Computers & Geosciences*, *24*(4), 325–334. https://doi.org/https://doi.org/10.1016/S0098-3004(97)00119-2

Taufik, M., & Jain, P. K. (2013). Role of build orientation in layered manufacturing: A review [PMID: 58637]. *International Journal of Manufacturing Technology and Management*, *27*(1-3), 47–73. https://doi.org/10.1504/IJMTM.2013.058637

Thomas, T. (1981). Characterization of surface roughness. *Precision Engineering*, *3*(2), 97–104. https://doi.org/https://doi.org/10.1016/0141-6359(81)90043-X

Tiab, D., & Donaldson, E. C. (2015). *Petrophysics: Theory and practice of measuring reservoir rock and fluid transport properties*. Gulf professional publishing. https://doi.org/https://doi.org/10.1016/C2014-0-03707-0

Tsang, Y. W. (1984). The effect of tortuosity on fluid flow through a single fracture. *Water Resources Research*, *20*(9), 1209–1215. https://doi.org/https://doi.org/10.1029/WR020i009p01209

Tsang, Y. W., & Tsang, C. F. (1987). Channel model of flow through fractured media. *Water Resources Research*, *23*(3), 467–479. https://doi.org/https://doi.org/10.1029/WR023i003p00467

Tsang, Y. W., & Witherspoon, P. A. (1981). Hydromechanical behavior of a deformable rock fracture subject to normal stress. *Journal of Geophysical Research: Solid Earth*, *86*(B10), 9287–9298. https://doi.org/https://doi.org/10.1029/JB086iB10p09287

Tse, R., & Cruden, D. (1979). Estimating joint roughness coefficients. *International Journal of Rock Mechanics and Mining Sciences and Geomechanics Abstracts*, *16*(5), 303–307. https://doi.org/https://doi.org/10.1016/0148-9062(79)90241-9

Verhaagen, B., Zanderink, T., & Fernandez Rivas, D. (2016). Ultrasonic cleaning of 3d printed objects and cleaning challenge devices [Ultrasound: A tool of never ending applications]. *Applied Acoustics*, *103*, 172–181. https://doi.org/https://doi.org/10.1016/j.apacoust.2015.06.010

Vilarrasa, V., Koyama, T., Neretnieks, I., & Jing, L. (2011). Shear-induced flow channels in a single rock fracture and their effect on solute transport. *Transport in porous media*, *87*, 503–523. https://doi.org/10.1007/s11242-010-9698-1

Villamor, L. R., Li, B., & Einstein, H. (2019). A methodology to measure fracture aperture using a consumer grade digital camera. *53rd US Rock Mechanics/Geomechanics Symposium*.

Vogler, D., Settgast, R. R., Annavarapu, C., Madonna, C., Bayer, P., & Amann, F. (2018). Experiments and simulations of fully hydro-mechanically coupled response of rough fractures exposed to high-pressure fluid injection. *Journal of Geophysical Research: Solid Earth*, *123*(2), 1186–1200. https://doi.org/https://doi.org/10.1002/2017JB015057

Vogler, D., Walsh, S. D., Bayer, P., & Amann, F. (2017). Comparison of surface properties in natural and artificially generated fractures in a crystalline rock. *Rock Mechanics and Rock Engineering*, *50*, 2891–2909. https://doi.org/10.1007/s00603-017-1281-4

Wang, L., Ju, Y., Xie, H., Ma, G., Mao, L., & He, K. (2017). The mechanical and photoelastic properties of 3d printable stress-visualized materials. *Scientific reports*, *7*(1), 10918. https://doi.org/10.1038/s41598-017-11433-4

Wang, L., & Cardenas, M. B. (2016). Development of an empirical model relating permeability and specific stiffness for rough fractures from numerical deformation experiments. *Journal of Geophysical Research: Solid Earth*, *121*(7), 4977–4989. https://doi.org/https://doi.org/10.1002/2016JB013004

Wang, Z., Xu, C., & Dowd, P. (2018). A modified cubic law for single-phase saturated laminar flow in rough rock fractures. *International Journal of Rock Mechanics and Mining Sciences*, *103*, 107–115. https://doi.org/https://doi.org/10.1016/j.ijrmms.2017.12.002

Watanabe, N., Sakurai, K., Ishibashi, T., Ohsaki, Y., Tamagawa, T., Yagi, M., & Tsuchiya, N. (2015). New ν-type relative permeability curves for two-phase flows through subsurface fractures. *Water Resources Research*, *51*(4), 2807–2824. https://doi.org/https://doi.org/10.1002/2014WR016515

Watson, F., Maes, J., Geiger, S., Mackay, E., Singleton, M., McGravie, T., Anouilh, T., Jobe, T. D., Zhang, S., Agar, S., et al. (2019). Comparison of flow and transport experiments on 3d printed micromodels with direct numerical simulations. *Transport in Porous Media*, *129*, 449–466.

Wen, R., & Sinding-Larsen, R. (1997). Uncertainty in fractal dimension estimated from power spectra and variograms. *Mathematical Geology*, *29*, 727–753. https://doi.org/https://doi.org/10.1007/BF02768900

Witherspoon, P. A., Wang, J. S. Y., Iwai, K., & Gale, J. E. (1980). Validity of cubic law for fluid flow in a deformable rock fracture. *Water Resources Research*, *16*(6), 1016–1024. https://doi.org/https://doi.org/10.1029/WR016i006p01016

Wittmann, A., Kenkmann, T., Schmitt, R. T., Hecht, L., & Stöffler, D. (2004). Impact-related dike breccia lithologies in the icdp drill core yaxcopoil-1, chicxulub impact structure, mexico. *Meteoritics & Planetary Science*, *39*(6), 931–954. https://doi.org/https://doi.org/10.1111/j.1945-5100.2004.tb00938.x

Xie, H., & Wang, J.-a. (1999). Direct fractal measurement of fracture surfaces. *International Journal of Solids and Structures*, *36*(20), 3073–3084. https://doi.org/https://doi.org/10.1016/S0020-7683(98)00141-3

Xie, H., Wang, J.-A., & Xie, W.-H. (1997). Fractal effects of surface roughness on the mechanical behavior of rock joints [Applications of Fractals in Material Science and Engineering]. *Chaos, Solitons and Fractals*, *8*(2), 221–252. https://doi.org/https://doi.org/10.1016/S0960-0779(96)00050-1

Xie, J., Gao, M., Zhang, R., Peng, G., Lu, T., & Wang, F. (2020). Experimental investigation on the anisotropic fractal characteristics of the rock fracture surface and its application on the fluid flow description. *Journal of Petroleum Science and Engineering*, *191*, 107190. https://doi.org/https://doi.org/10.1016/j.petrol.2020.107190

Xie, L. Z., Gao, C., Ren, L., & Li, C. B. (2015). Numerical investigation of geometrical and hydraulic properties in a single rock fracture during shear displacement with the navier-stokes equations. *Environmental Earth Sciences*, *73*(11), 7061–7074. https://link.springer.com/article/10.1007/s12665-015-4256-3

Xiong, X., Li, B., Jiang, Y., Koyama, T., & Zhang, C. (2011). Experimental and numerical study of the geometrical and hydraulic characteristics of a single rock fracture during shear. *International Journal of Rock Mechanics and Mining Sciences*, *48*(8), 1292–1302. https://doi.org/https://doi.org/10.1016/j.ijrmms.2011.09.009

Yang, W., Zhang, D., & Lei, G. (2020). Experimental study on multiphase flow in fracture-vug medium using 3d printing technology and visualization techniques. *Journal of Petroleum Science and Engineering*, *193*, 107394. https://doi.org/https://doi.org/10.1016/j.petrol.2020.107394

Yang, Z. Y., Lo, S. C., & Di, C. C. (2001). Reassessing the joint roughness coefficient (jrc) estimation using Z_2. *Rock Mechanics and Rock Engineering*, *34*, 243–251. https://doi.org/https://doi.org/10.1007/s006030170012

Yeo, I., de Freitas, M., & Zimmerman, R. (1998). Effect of shear displacement on the aperture and permeability of a rock fracture. *International Journal of Rock Mechanics and Mining Sciences*, *35*(8), 1051–1070. https://doi.org/https://doi.org/10.1016/S0148-9062(98)00165-X

Yin, P., Zhao, C., Ma, J., Yan, C., & Huang, L. (2020). Experimental study of non-linear fluid flow though rough fracture based on fractal theory and 3d printing technique. *International Journal of Rock Mechanics and Mining Sciences*, *129*, 104293. https://doi.org/https://doi.org/10.1016/j.ijrmms.2020.104293

Yin, Q., Ma, G., Jing, H., Wang, H., Su, H., Wang, Y., & Liu, R. (2017). Hydraulic properties of 3d rough-walled fractures during shearing: An experimental study. *Journal of Hydrology*, *555*, 169–184. https://doi.org/https://doi.org/10.1016/j.jhydrol.2017.10.019

Yu, X., & Vayssade, B. (1991). Joint profiles and their roughness parameters. *International Journal of Rock Mechanics and Mining Sciences & Geomechanics Abstracts*, *28*(4), 333–336. https://doi.org/https://doi.org/10.1016/0148-9062(91)90598-G

Zelinka, I., Rössler, O. E., Snášel, V., Abraham, A. P., Corchado Rodríguez, E. S., et al. (2013). *Nostradamus: Modern methods of prediction, modeling and analysis of nonlinear systems*. Springer Cham. https://doi.org/https://doi.org/10.1007/978-3-319-07401-6

Zhang, L., Yang, Z., Méheust, Y., Neuweiler, I., Hu, R., & Chen, Y.-F. (2023). Displacement patterns of a newtonian fluid by a shear-thinning fluid in a rough fracture [e2023WR034958 2023WR034958]. *Water Resources Research*, *59*(9), e2023WR034958. https://doi.org/https://doi.org/10.1029/2023WR034958

Zhang, L. (2016). *Engineering properties of rocks*. Butterworth-Heinemann. https://doi.org/https://doi.org/10.1016/C2014-0-02645-7

Zhang, Y., Ye, J., & Li, P. (2022). Flow characteristics in a 3d-printed rough fracture. *Rock Mechanics and Rock Engineering*, 1–21. https://link.springer.com/article/10.1007/s00603-022-02854-3

Zhang, Y., & Chai, J. (2020). Effect of surface morphology on fluid flow in rough fractures: A review. *Journal of Natural Gas Science and Engineering*, *79*, 103343. https://doi.org/https://doi.org/10.1016/j.jngse.2020.103343

Zheng, J., Jin, Y., Liu, X., Wang, C., & Liu, X. (2020). Validity of triple-effect model for fluid flow in mismatched, self-affine fractures. *Advances in Water Resources*, *140*, 103585. https://doi.org/https://doi.org/10.1016/j.advwatres.2020.103585

Zhou, J.-Q., Hu, S.-H., Fang, S., Chen, Y.-F., & Zhou, C.-B. (2015). Nonlinear flow behavior at low reynolds numbers through rough-walled fractures subjected to normal compressive loading. *International Journal of Rock Mechanics and Mining Sciences*, *80*, 202–218. https://doi.org/https://doi.org/10.1016/j.ijrmms.2015.09.027

Zhou, J., Wang, M., Wang, L., Chen, Y., & Zhou, C. (2018). Emergence of nonlinear laminar flow in fractures during shear. *Rock Mechanics and Rock Engineering*, *51*(11), 3635–3643. https://link.springer.com/article/10.1007/s00603-018-1545-7

Zhu, C., Xu, X., Wang, X., Xiong, F., Tao, Z., Lin, Y., & Chen, J. (2019). Experimental investigation on nonlinear flow anisotropy behavior in fracture media. *Geofluids*, *2019*, 1–9. https://doi.org/https://doi.org/10.1155/2019/5874849

Zhu, J., Zhou, T., Liao, Z., Sun, L., Li, X., & Chen, R. (2018). Replication of internal defects and investigation of mechanical and fracture behaviour of rock using 3d printing and 3d numerical methods in combination with x-ray computerized tomography. *International Journal of Rock Mechanics and Mining Sciences*, *106*, 198–212. https://doi.org/https://doi.org/10.1016/j.ijrmms.2018.04.022

Zimmerman, R., & Main, I. (2004). Chapter 7 ▹– hydromechanical behavior of fractured rocks. In Y. Guéguen & M. Boutéca (Eds.), *Mechanics of fluid-saturated rocks* (pp. 363–421, Vol. 89). Academic Press. https://doi.org/https://doi.org/10.1016/S0074-6142(03)80023-2

Zimmerman, R. W., & Bodvarsson, G. S. (1996). Hydraulic conductivity of rock fractures. *Transport in Porous Media*, *23*(1), 1–30. https://link.springer.com/article/10.1007/BF00145263

Zimmerman, R. W., & Yeo, I.-W. (2000). Fluid flow in rock fractures: From the navier-stokes equations to the cubic law. In *Dynamics of fluids in fractured rock* (pp. 213–224). American Geophysical Union (AGU). https://doi.org/https://doi.org/10.1029/GM122p0213

Zou, L., Jing, L., & Cvetkovic, V. (2015). Roughness decomposition and nonlinear fluid flow in a single rock fracture. *International Journal of Rock Mechanics and Mining Sciences*, *75*, 102–118. https://doi.org/https://doi.org/10.1016/j.ijrmms.2015.01.016

Appendix A

Unconfined Compressive Strength of VeroClear & VeroWhite

A.1 Introduction

Unconfined compressive strength (UCS) tests were conducted on 3D-printed VeroWhite and VeroClear samples, using the axial force exerted by a 150 kN INSTRON system. The primary objective of these tests was to evaluate how the orientation of the sample and the choice of material influence UCS. Each sample was subjected to loading until failure, and subsequent to testing, the elastic properties were estimated and the samples were inspected.

A.2 Samples Design

The sample dimensions were approximately 25.2 mm in diameter and around 50.5 mm in length, resulting in an aspect ratio of 2:1. A total of 11 samples were tested. The VeroClear samples were 3D-printed with a matte finish (i.e., a support material coating) and subsequently post-processed in a NaOH for approximately 4 hours at a temperature ranging from 25 to 35°C. Among these, four samples were vertically printed, two samples were printed parallel to the x-axis (HX), and two samples were printed parallel to the y-axis (HY), resulting in the study of three different sample orientations (Figure A.1).

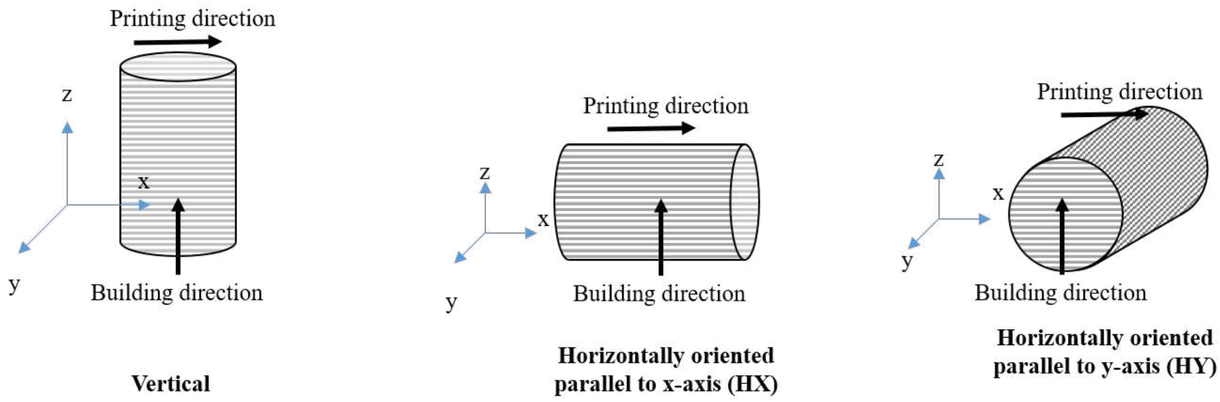

Figure A.1: Samples orientation during 3D printing process.

The three VeroWhite samples were printed with a horizontal orientation parallel to the x-axis (HX). These samples did not require post-processing and were printed with a glossy finish using a material combination of support material 705 and VeroWhite.

A.3 Testing Preparations

To monitor axial and lateral deformation during the UCS tests, two different types of linear variable displacement transducer (LVDT) systems were employed. For measuring axial strain, a LVDT Measurement Specialties MHR 250 ASSY with a range of 12 mm and an accuracy of $\pm 25.4\mu$m was attached parallel to a metallic cylinder. To gauge lateral deformation, an LVDT Measurement Specialties MHR 100 ASSY with a range of 6mm and an accuracy of $\pm 25.4\mu$m was utilized to track changes in chord length. A mathematical formula was applied to estimate the geometric relationship between the alteration in chord length and diameter.

The stresses, strains, and elastic properties were obtained following established standard methods (American Society for Testing and Materials, 2014). Elastic moduli were computed using the tangential approach. The strain rate was maintained at 1.3 mm/minute, within the suggested range for plastic materials (American Society for Testing and Materials, 2015) and lower than the 2 mm/minute rate used in previous studies (Ju, Wang, Xie, Ma, Zheng, & Mao, 2017; L. Wang et al., 2017). However, it is important to note that the influence of strain rate on these 3D-printed specimens is an area that should be further examined.

A.4 Experimental Configuration

In the experimental setup, the samples were placed on a steel platen and a metallic cylinder was placed on top of the samples to ensure they were within the loading frame range (Figure A.2).

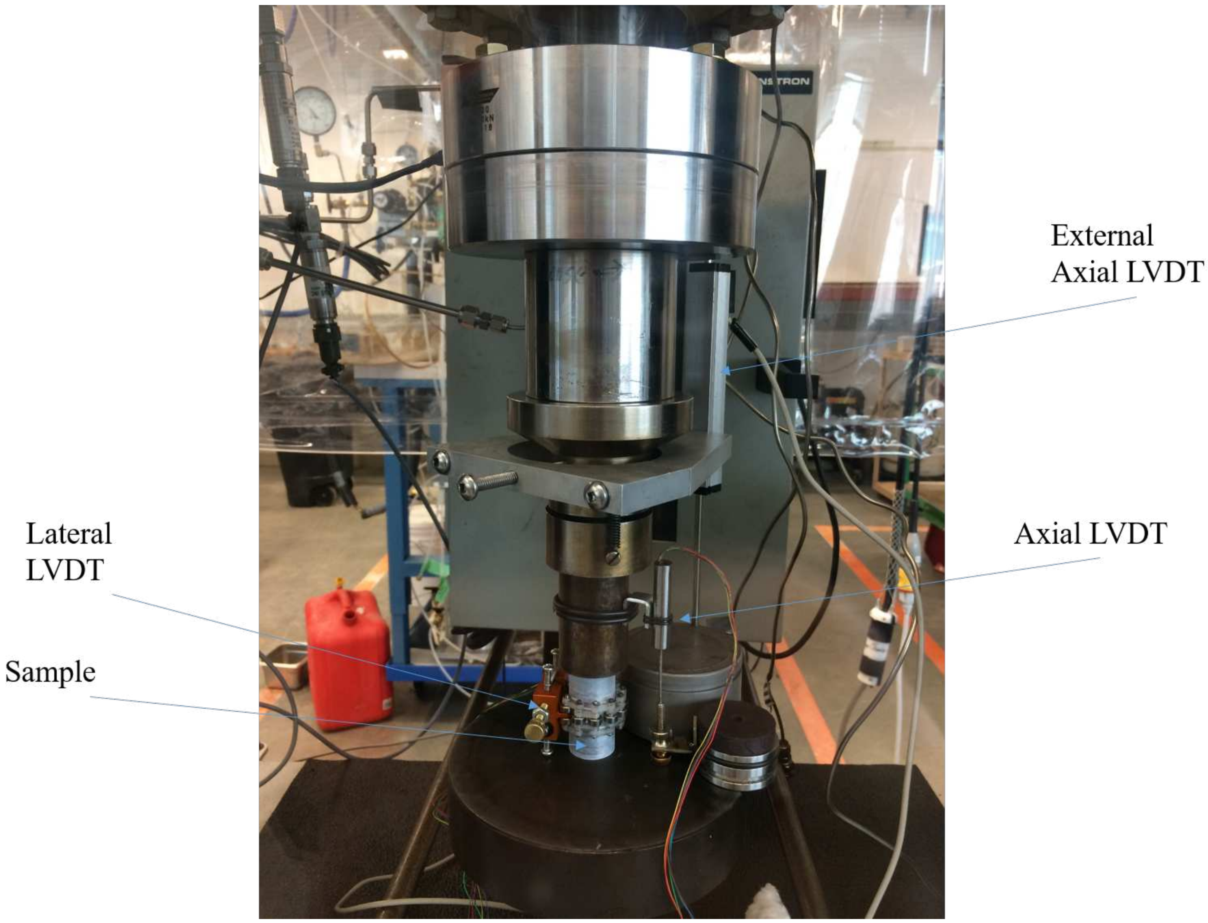

Figure A.2: Experimental configuration for UCS testing.

A.5 Results

The samples exhibited a ductile and homogeneous behavior. The values of UCS remained consistent regardless of the printing orientation (Figure A.3 and Table A.1).

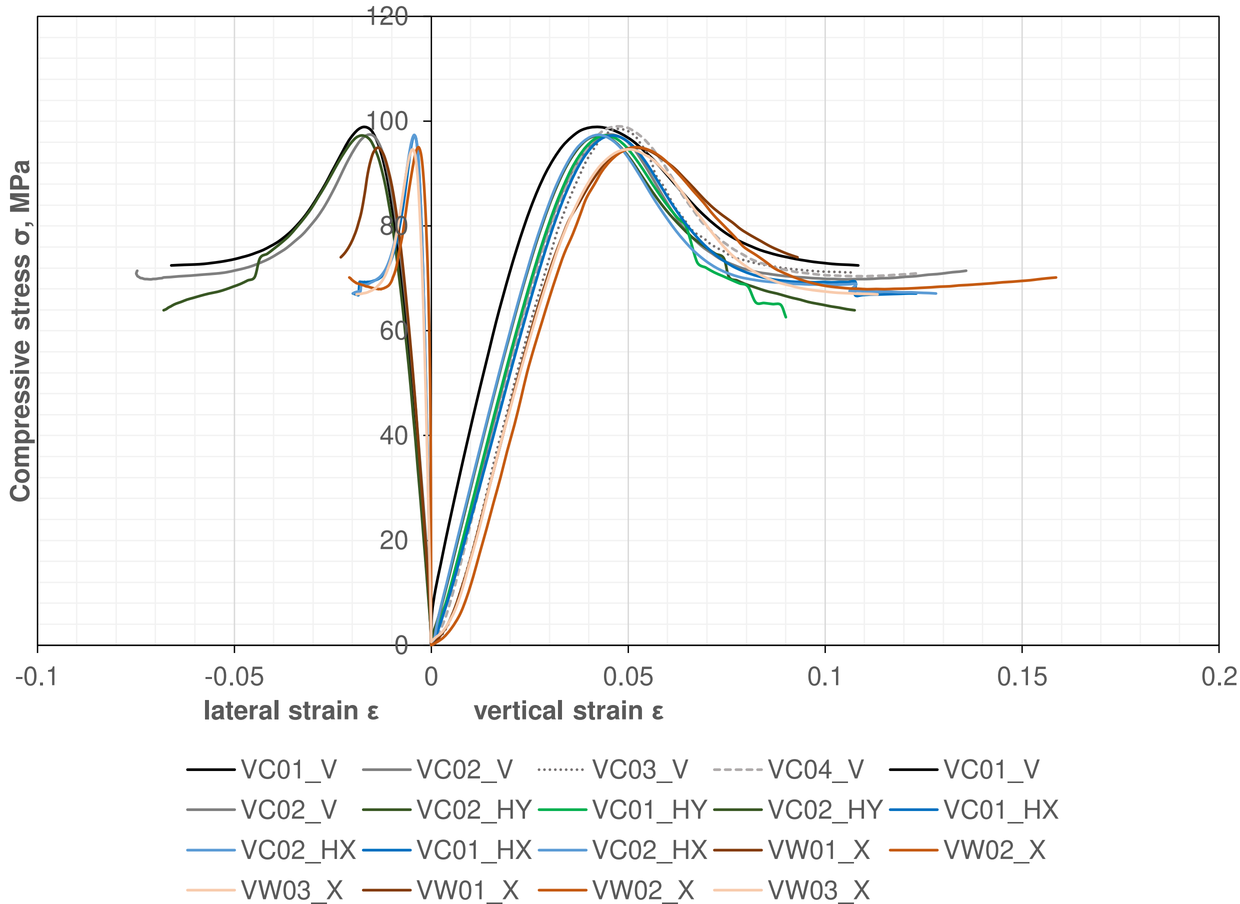

Figure A.3: UCS results on 3D-Printed specimens with different printing orientations.

Sample	Orientation	UCS, MPa	Axial strain at peak,%	Lateral strain at peak,%	Axial Young modulus, MPa	Poisson ratio, -
VC01	Vertical	98.9	4.3	1.7	3741	0.39
VC02	Vertical	97.4	4.6	1.6	2690	0.26
VC03	Vertical	98.5	4.7	-	2676	-
VC04	Vertical	99.1	4.8	-	2889	-
VC01	HY	97.2	4.3	-	2843	-
VC02	HY	97.2	4.3	1.8	2979	0.33
VC01	HX	97.3	4.7	0.4	2649	0.07
VC02	HX	97.4	4.2	0.4	3093.5	0.08
VW01	HX	94.9	5.1	1.3	2748.2	0.27
VW02	HX	95.1	5.2	0.3	2491.3	0.012
VW03	HX	94.6	4.9	0.5	2600.3	0.079

Table A.1: Elastic properties per sample.

The curves of axial stress versus strain exhibited a similar prepeak behavior for most samples (Figure A.3). However, the post-peak response varied in relation to the printing orientation, and this discrepancy was evident upon inspecting the samples after testing.

In general, the stress-strain curves exhibited an elasto-plastic behavior. However, the HY samples showed a strain-softening behavior after reaching peak strength (Figure A.3). This pattern involves continued deformation after the peak strength is reached, without increasing the stress. As a result, the applied energy is dissipated rather than accumulated by the object.

Overall, the standard deviations of the UCS and elastic moduli displayed low values (Table A.2). This indicated homogeneity between the samples, corroborating the repeatability and quality of the 3D printing process. Furthermore, the average value of UCS and the average Young's modulus (Table A.2) aligned with other studies (Ju, Wang, Xie, Ma, Zheng, & Mao, 2017; Stratasys, 2020; L. Wang et al., 2017).

Type	Orientation	Parameter	UCS, MPa	Young Modulus, MPa	Poisson ratio, -
VeroClear	Vertical	μ	98.5	2999	0.33
	Vertical	σ	0.63	437	0.06
VeroClear	HY	μ	97.2	2911	-
	HY	σ	0.01	68	-
VeroClear	HX	μ	97.3	2871	0.08
	HX	σ	0.08	222	0.01
VeroWhite	HX	μ	94.9	2613.3	0.12
	HX	σ	0.22	105.25	0.11

Table A.2: Mean elastic properties and statistical parameters.

A.5.1 VeroClear Samples

In the vertical samples, the post-peak behavior indicated lateral expansion under uniaxial compression. Only one sample (VC02) showed a crack parallel to the printing direction (Figure A.4) after undergoing more than $\sim$10% axial deformation. On the contrary, the HY samples exhibited two cracks on opposite sides of the sample, perpendicular to the printing direction, after $\sim$8% axial deformation. These samples also exhibited less lateral deformation compared to other sample types (Figure A.5). On the contrary, the HX samples showed lateral dilation due to uniaxial compression, with a crack appearing parallel to the building orientation after axial deformation $\sim$ 12% (Figure A.6). It is possible that the cracks observed on the perimeter of the sample were shear fractures associated with compression (Figures A.4-A.6), see Hargitai et al. (2021) for details.

In particular, the sample VC01 oriented in HY direction showed an axial extension crack parallel to the building direction and two shear side cracks that appeared to have propagated in the printing direction (Figure A.5). Similarly, the cracks observed in the HX samples appeared to have grown in the building direction (Figure A.6). The curve of stress versus lateral-strain for the HY samples exhibited a behavior similar to that of the vertical samples and differed from that of the HX samples, which showed less lateral expansion.

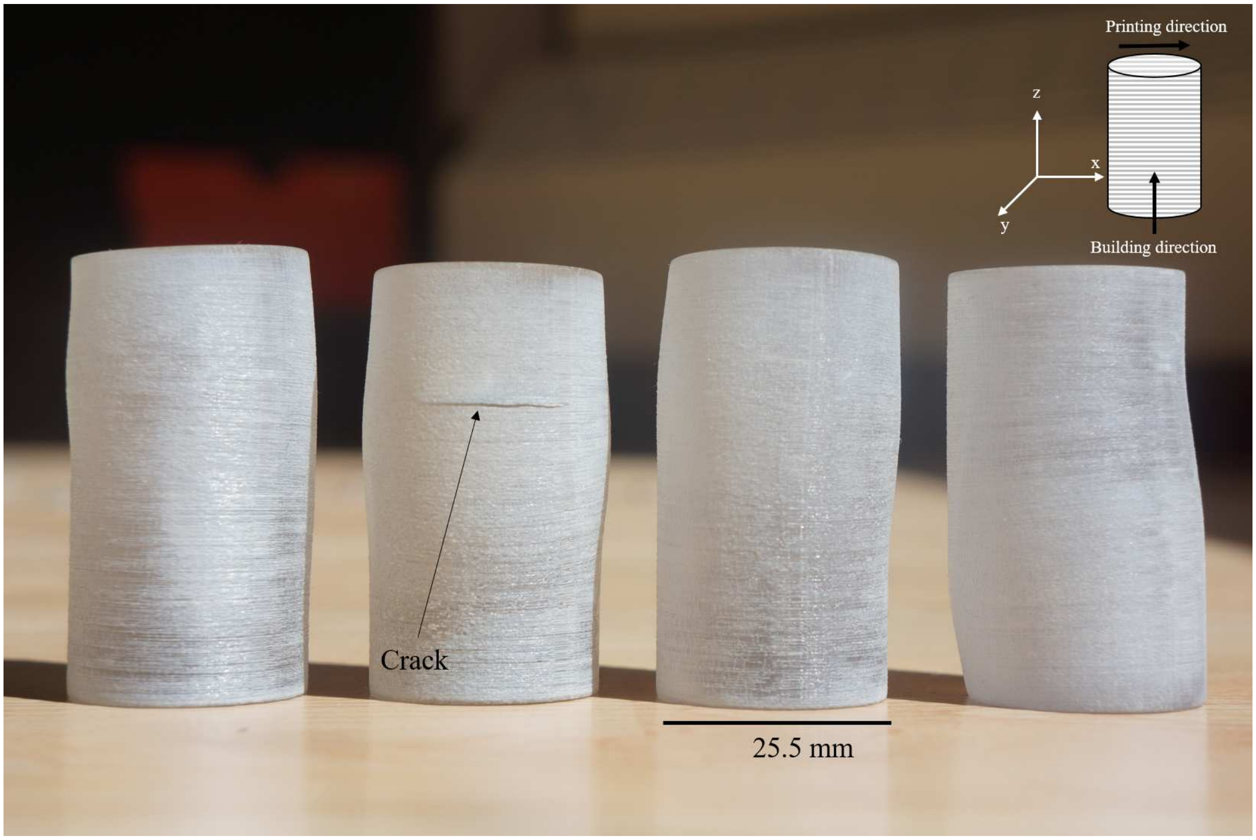

Figure A.4: Vertical samples after UCS tests.

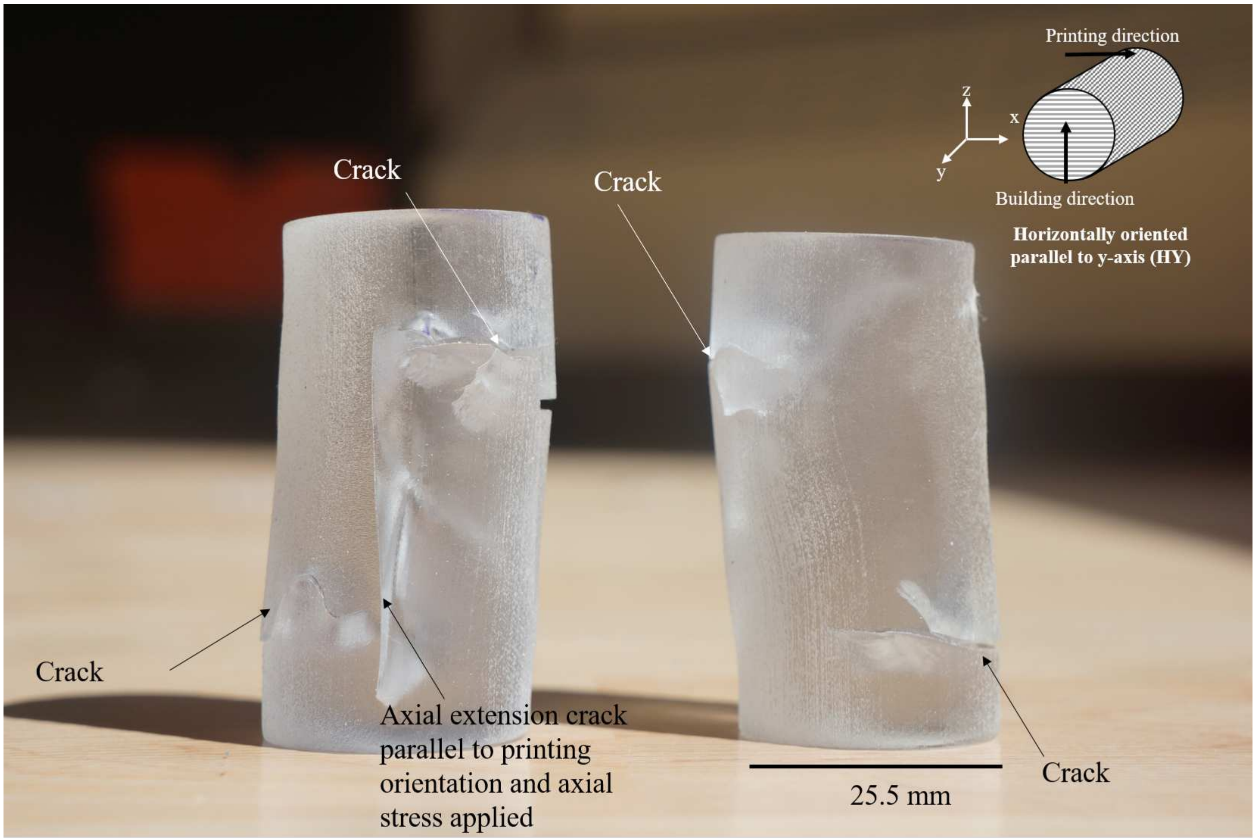

Figure A.5: VeroClear samples oriented parallel to y-axis (HY) after UCS tests.

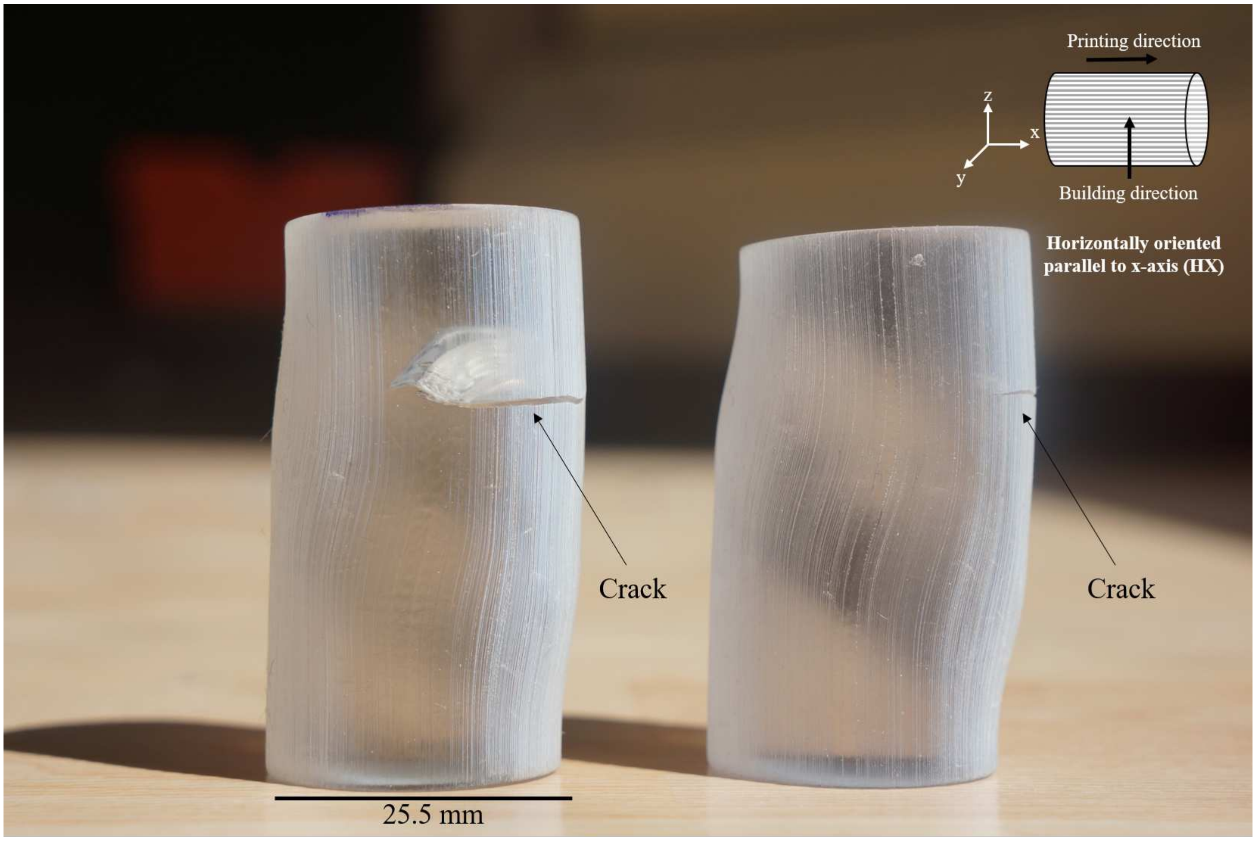

Figure A.6: VeroClear samples oriented parallel to x-axis (HX) after UCS tests.

A.5.2 VeroWhite Samples

These samples exhibited deformation associated with failure; however, there were no external cracks A.7. The behavior of the stress versus axial strain curves showed an elasto-plastic tendency similar to that of the VeroClear samples printed vertically.

Figure A.7: VeroWhite samples oriented parallel to x-axis (HX) after UCS tests.

A.6 Conclusion

Positioning samples parallel to the x-axis does not significantly affect their UCS values; however, it results in shorter printing times, as the print heads travel side-to-side along the x-axis. Additionally, the finish of the printed layers varies based on the 3D printing orientation (Figure A.8).

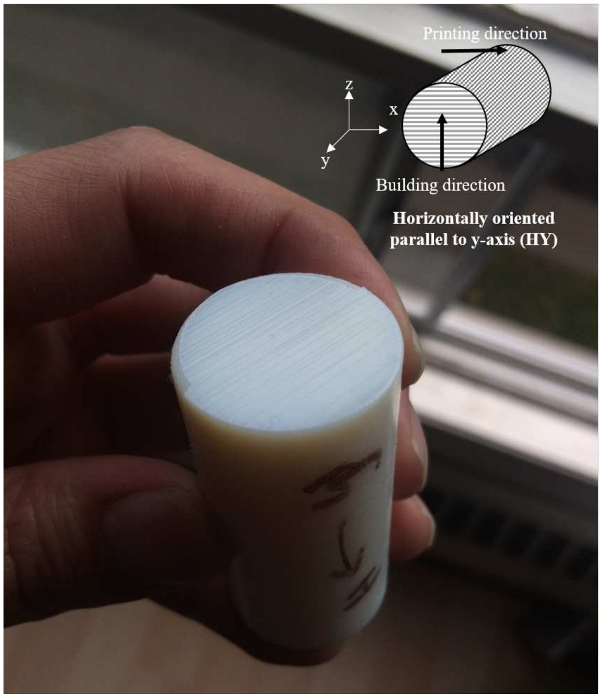

Figure A.8: 3D-Printed layers orientation (different finish depending on the building orientation).

The curves of compressive stress versus vertical-strain for the various types of sample demonstrated reasonably similar behavior, leading to comparable values for elastic properties (Table A.1). However, it is worth noting that in some cases, lateral strain data was not collected.

Furthermore, the use of UV light in the curing of the VeroClear photo-polymer might play a role in the strength of the samples. Exposure to UV light could potentially enhance the strength of the samples (Barclift & Williams, 2012). Therefore, the slightly higher UCS values observed in the vertical samples may be attributed to their increased exposure to UV light due to their specific printing orientation.

Appendix B

Relationship between Rock Surface Topography and Roughness Descriptors from Empirical and Self-Affine-Fractal Character

B.1 Introduction

The description of fracture surface characteristics is essential for better understanding the mechanical and hydraulic behavior of fractures. Numerous experimental and numerical studies have demonstrated the relevance of fracture topography in geomechanical processes through the development of analytic and numerical models based on fracture properties. These models are frequently utilized to predict the mechanical and hydraulic response of individual fractures. For example, a classic formulation used to describe the behavior of peak fracture shear strength in relation to surface roughness and normal stress (N. Barton & Choubey, 1977) and fracture normal stiffness with respect to fracture roughness and aperture (Bandis et al., 1983). On the other hand, fluid flow models have been developed to incorporate geometric properties and fracture roughness (Brush & Thomson, 2003; Lomize, 1951; Romm, 1966; Witherspoon et al., 1980). However, the presence of geologic heterogeneity and multiple scales poses challenges in upscaling single fracture characterization results for large-scale projects. A key preliminary step towards addressing this could be to implement a more homogeneous approach in describing fracture surfaces. This involves analyzing the existing approaches and better understanding the methods employed to characterize fracture topography.

Fracture roughness is usually decomposed into two conceptual scales: primary (large-scale waviness) and secondary (small-scale unevenness) roughness (Zou et al., 2015). However, frequently, studies characterize fracture walls through only one of these aspects, which leads to an incomplete description of all facets of fracture roughness, thereby hindering a comprehensive analysis of results. For example, the empirical parameter of the JRC is regularly estimated through experimental models based on a single statistical property (Y. Li & Zhang, 2015; Z. Y. Yang et al., 2001). However, the application of these models is limited to a short range, and the estimated JRC values might be biased by the selected model, reflecting the statistical property behavior rather than the overall fracture roughness. Additionally, a partial description of fracture texture may not allow for the reconstruction of fracture topography through fracture generation methods, which provide control over various texture properties and could be instrumental in studying scale effects.

Methods used to describe surface characteristics are typically classified into the following groups: roughness (amplitude and frequency or slope variability), statistical distribution, and fractal (Bhushan, 2000). Statistical parameters typically describe the first two categories, while fractal approaches represent the complexity (Zelinka et al., 2013). Fractal techniques, despite being widely used in the scientific community, are not considered standardized surface measurements. For instance, they are not included in recognized standards (International Organization for Standardization, 2021), and some suggest that methodological differences between fractal-based approaches make them inadequate for roughness description (Charkaluk et al., 1998). On the other hand, some indicate that they are quantitatively unreliable (Wen & Sinding-Larsen, 1997) and the values obtained from different fractal methods are not comparable (H. Xie & Wang, 1999) or they are comparable within a narrow range (Gallant et al., 1994). Additionally, implementing them requires several considerations to be resolved beforehand (Magsipoc et al., 2020; Tate, 1998).

The relationship between JRC and fractal parameters obtained from self-similar methods has been investigated (Y. Li & Huang, 2015). However, profiles of fracture surfaces have been suggested to possess a self-affine fractal character (Brown & Scholz, 1985; Poon et al., 1992). Thus, some studies have analyzed the relationship between this type of fractal parameters and the original profiles (N. Barton & Choubey, 1977) used to formulate JRC (Odling, 1994). In this context, some have suggested that fractal-based aperture has a strong correlation with a spatial variation coefficient (Klinkenberg, 1992). However, there are considerations related to existing JRC models and fractal methods that need to be addressed to develop more robust workflows for describing fracture surfaces. Consequently, in this study, we have investigated this subject utilizing real limestone rock samples. The samples were collected from El Guayal outcrop and scanned with a profilometer. Subsequently, different methods were implemented to estimate their surface properties and investigate the relationship between JRC and fractal-based parameters and other roughness descriptors, attempting to clarify the nature of these parameters and contribute to formulating a homogenized approach for characterizing rock surface topography.

B.2 Methods and Analysis

B.2.1 Sampling Rock Surfaces

Rock samples were collected from the El Guayal Cretaceous-Paleocene (K-P) rock outcrop (Figure B.1). This outcrop has been identified to have overwhelming geological similarities with the regional stratigraphy found in the shallow water hydrocarbon fields of the Bay of Campeche Cantú-Chapa and Landeros-Flores (2001), Grajales-Nishimura et al. (2000), and Salge (2007). This stratigraphic column has been correlated with the regional stratigraphy of the Pilar-Akal-Reforma basin and both sequences were found to have the same origin triggered by the impact of the Chicxulub meteorite (Grajales-Nishimura et al., 2000). Furthermore, it has been concluded that the El Guayal section was an analog of the cretaceous-breccia petroleum reservoirs found in this basin (Grajales-Nishimura et al., 2000). This claim was supported by studying the composition of the section and providing a chemical and petrographical analysis of the present lithology (Salge, 2007). Furthermore, some investigations have endorsed the theory that the Chicxulub impact caused the Cretaceous-Paleocene boundary section (Schulte et al., 2010); no conclusive evidence was found supporting the hypothesis that the Chicxulub impact preceded the El Guayal section. Additionally, some have indicated that the evidence supporting the meteorite impact on the Gulf of Mexico caused mass extinction around 65.5 million years ago is substantial (Hildebrand et al., 1991). However, a contrasting posture has theorized that the meteorite impact occurred 300,000 years before the formation of the El Guayal section (Keller et al., 2013). Despite the fact that this continues to be an ongoing discussion, many tend to favor the hypothesis that the K-P boundary section is related to the meteorite crash (Alvarez et al., 1980; Swisher et al., 1992). Additional petrographic data from the core of Yaxcopoil-1 matched well with the stratigraphic sequence previously described (M. J. Nelson et al., 2012; Wittmann et al., 2004). Furthermore, the biostratigraphic description confirmed that the El Guayal section is contemporary (Campanian-Maastrichtian age) to the oil reservoirs in the Bay of Campeche (Cantú-Chapa & Landeros-Flores, 2001).

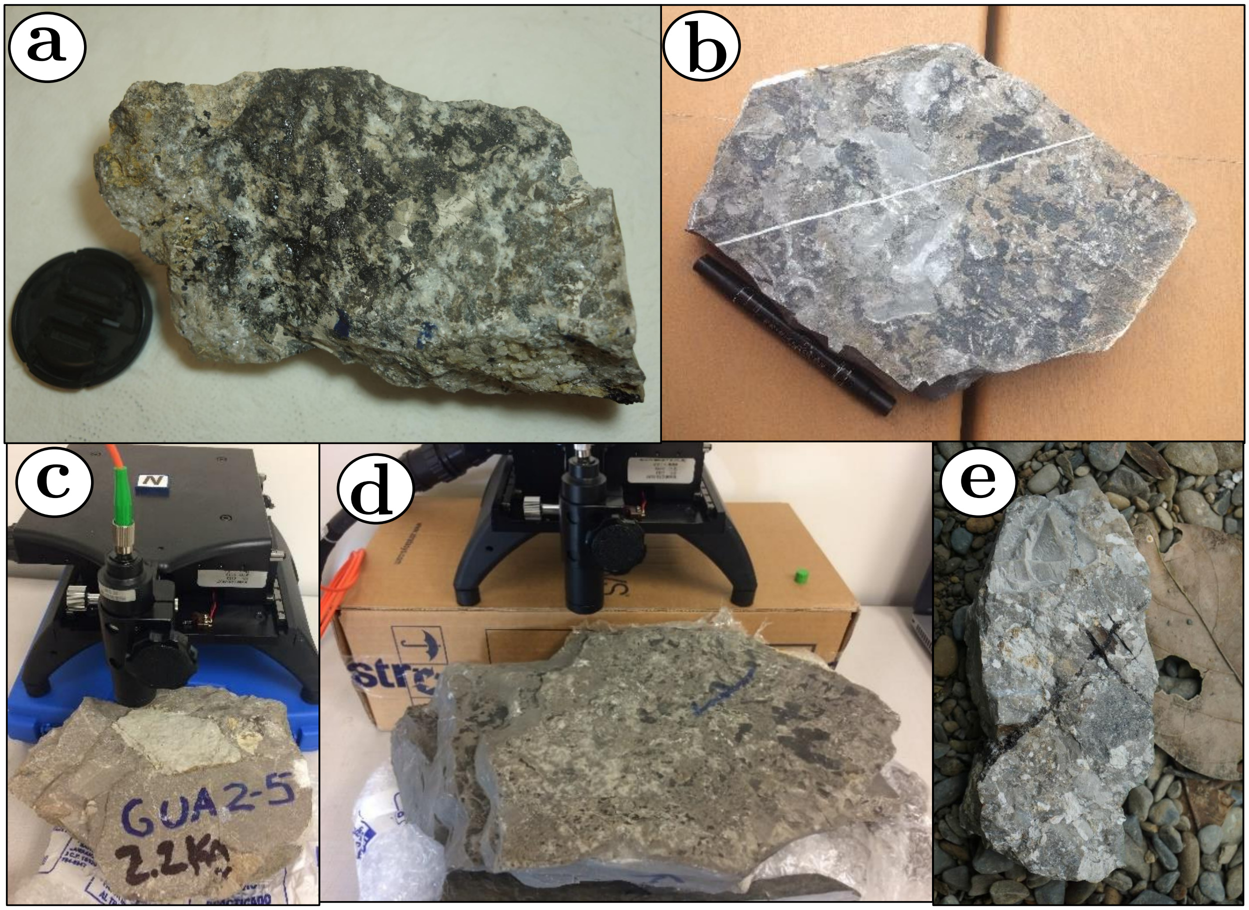

Figure B.1: (a) Sample 1 (Unit 3), (b) Sample 2 (Unit 1), (c) Sample 3 (Unit 2), (d) Sample 4 (Unit 1), (e) Sample 5 (Unit 3). The assignment of units to samples was solely based on field geology observations.

B.2.2 El Guayal Outcrop: A Reservoir Analog

The El Guayal stratigraphic section presents a 60 to 80 m column of Cretaceous rock (Grajales-Nishimura et al., 2000) in which four units (Figure B.2) have been described as follows (Salge, 2007): Unit 1 is estimated to have a thickness of 10 to 14 m of strata of hemipelagic limestone 10 to 30 cm. The limestone is described to have many fossils and to have 20 cm thick breccia intercalations. Unit 2 is described to be 40-m thick with chaotic clastic deposits composed of coarse calcareous breccia (34 m) and the so-called micro-breccia (6 m). The breccia was described to be clast-supported, and fragments are larger than 2 m in diameter at the bottom of the unit. Towards the top, big clasts (>2mm) are embedded in a matrix that has a significant increase in mud and is mud-supported. Unit 3 is presented as an 11-m thick column with a 5-m layer of micro-breccia at the base and overlain by a

6-m loose calcareous sandstone and siltstone beds. Unit 4 consists of calcareous shales or laminated marls of the Palaeocene epoch.

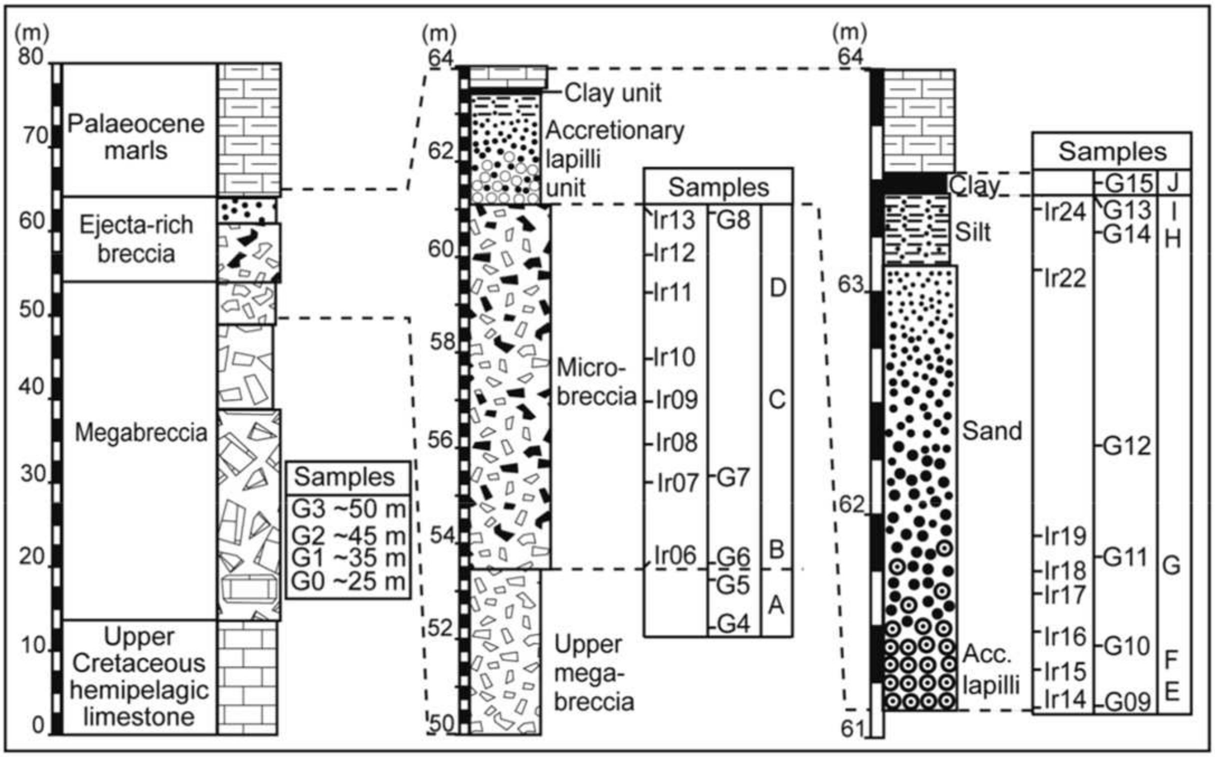

Figure B.2: El Guayal *K-P* Stratigraphic Section (Salge, 2007).

B.2.3 Profilometry

Samples were collected from the El Guayal rock outcrop and five samples (Figure B.1) were scanned using a Nanovea JR 50 profilometer. Each sample was scanned and analyzed in subdomains of 45×45 mm (Figure B.3), examining smaller sections may remove the effects of size dependence (Vogler et al., 2017).

The scanning resolution used was 10 μm in the x and y directions. The optical pen used had a 10 mm tip, which implied less magnification but greater coverage of a larger area and a vertical resolution of 10 mm. The subdomains were scanned at a frequency of 200 Hz, slow enough to minimize non-measured points. The subdomains were processed using Mountains Ultra 7.4 software, which involved first removing outliers and then leveling each section.

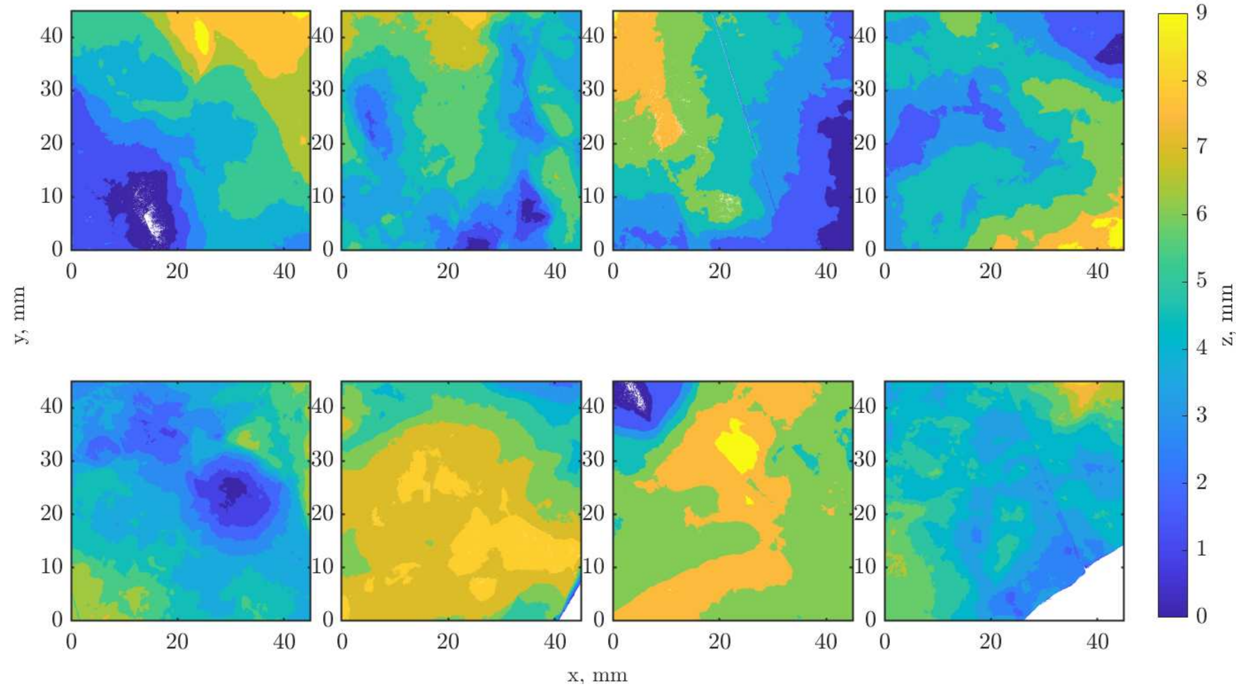

Figure B.3: Sample 2 scanned subdomains.

B.2.4 Profile Analysis

Each profile was analyzed at a constant sampling interval of 10 μm in both directions x and y to minimize the sensitivity of the estimated roughness parameters to scale (Vogler et al., 2017). However, resampling was necessary to yield a practical file size to manage computationally. This involved comparing the estimated surface parameters of analyzing all profiles in a subdomain at 10 μm resolution and analyzing profiles every 150 μm to verify that the topographic properties were accurately captured. The results of this preliminary comparison (Figure B.4 and Figure B.5) indicated that analyzing profiles every 150 μm was sufficient to representively estimate the topographic characteristics.

Different statistical parameters used to describe the surfaces were calculated (Table B.1). These measurements included amplitude parameters (that is, peak asperity height Z, average asperity height R_a, root mean square RMS and standard deviation of surface heights $\sigma_{std.}$), slope or spatial variation parameters (that is, root mean square of the profile's first derivative Z_2, root mean square of the profile's second derivative Z_3, mean angle of inclination θ_p and R_L), and distribution parameters (skewness S_{sk} and kurtosis R_{ku}). On the other hand, the empirical JRC was estimated using expressions based on statistical parameters. Several equations exist and are applicable within specific ranges of values (Y. Li & Zhang, 2015).

In this preliminary assessment, the JRC was calculated using models based on Z_2 and R_a (Table B.2). Priority was given to the equation based on Z_2. If an analyzed profile exhibited Z_2 values outside the valid range, the expression based on R_a was used. On the other hand, fractal-based parameters, fractal dimension D, and the fractal amplitude γ_0 were calculated using the variogram method as described elsewhere (Lopez-Saavedra et al., 2024).

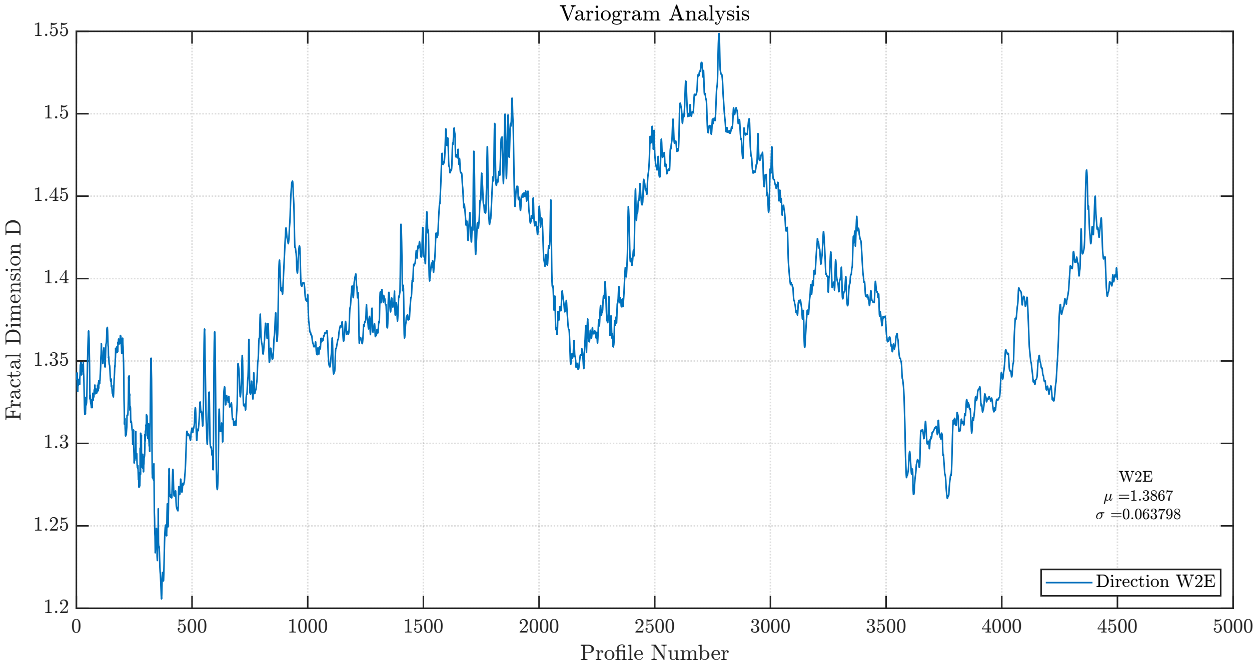

Figure B.4: Fractal dimension from variogram analysis at an analyzed resolution of 10 μm.

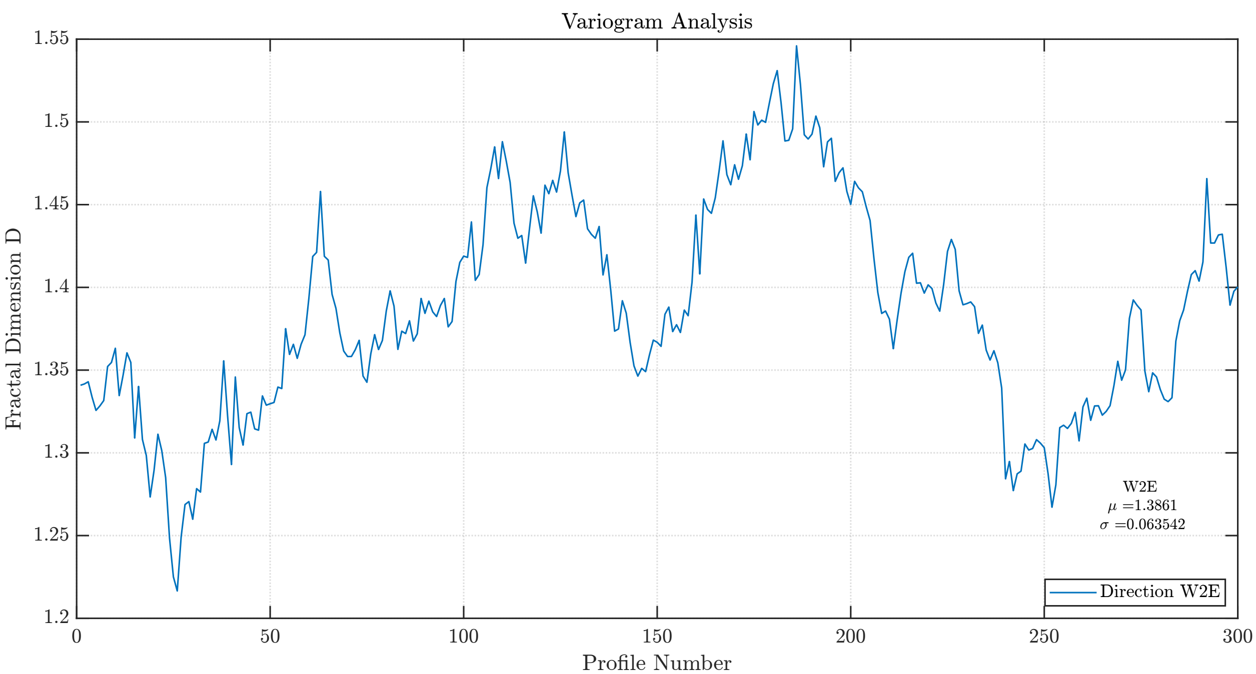

Figure B.5: Fractal dimension from variogram analysis at an analyzed resolution of 150 μm.

Parameter	Definition & Numerical Form	Reference
Z	Peak asperity height $z_{max} - z_{min}$	Y.-F. Chen et al. (2015)
R_a	Average asperity height $\frac{1}{n}\sum_{i=1}^{n}\lvert z_i - z_k\rvert$	Thomas (1981)
RMS	Root mean square $\sqrt{\frac{1}{n\times\Delta x}\left[\sum_{i=1}^{n}\Delta x((z_i - z_k)^2)\right]}$ $= \sqrt{\frac{1}{n}\sum_{i=1}^{n}(z_i - z_k)^2}$	Tse and Cruden (1979)
S_{sk}	Skewness $\frac{1}{n\times RMS^3}\sum_{i=1}^{n}(z_i - z_k)^3$	Thomas (1981)
R_{ku}	Kurtosis (sharpness) $\frac{1}{n\times RMS^4}\sum_{i=1}^{n}(z_i - z_k)^4$	Thomas (1981)
Z_2	Root mean square of the profile's first derivative $\sqrt{\frac{1}{n-1}\sum_{i=1}^{n-1}\left(\frac{z_{i+1}-z_i}{\Delta x}\right)^2}$	Belem et al. (2000)
Z_3	Root mean square of the profile's second derivative $\sqrt{\frac{1}{n-2}\sum_{i=1}^{n-2}\left(\frac{\left(\frac{z_{i+2,j}-z_{i+1,j}}{x_{i+2,j}-x_{i+1,j}}\right)-\left(\frac{z_{i+1,j}-z_{i,j}}{x_{i+1,j}-x_{i,j}}\right)}{\frac{x_{i+2,j}-x_{i,j}}{2}}\right)^2}$	Myers (1962)
θ_p	Mean angle of inclination $\tan^{-1}\left(\frac{1}{n-1}\sum_{i=1}^{n-1}\frac{z_{i+1}-z_i}{\Delta x}\right)$	Modified after Belem et al. (2000)
R_L	Linear roughness coefficient ratio of the actual 2D profile length to the nominal profile length $\frac{1}{n-1}\sum_{i=1}^{n-1}\sqrt{1+\left(\frac{z_{i+1}-z_i}{\Delta x}\right)^2}$	Belem et al. (2000)

[a] z_{max}: maximum elevation, z_{min}: minimum elevation, z_i *ith* elevation, z_k: mean of z_i values, n: total number of measurements and $\Delta x = x_{i+1,j} - x_{i,j}$: $x-$coordinates spacing.

Table B.1: Statistical roughness parameters[a].

JRC	Range	Reference
$98.718 \times Z_2^{1.6833}$	$0 < Z_2 \leq 0.387$	Y. Li and Zhang (2015)
$32.2 + 32.47\log(Z_2)$	$0.387 < Z_2 \leq 0.421$	Tse and Cruden (1979)
$28.10\log(Z_2) + 28.43$	$0.421 < Z_2 \leq 0.5012$	Yu and Vayssade (1991)
$10.5953\log(R_a) + 12.357$	$0.068 \leq R_a \leq 5.265$ & $Z_2 > 0.5012$	Y. Li and Zhang (2015)

Table B.2: Analytic expressions to estimate JRC.

B.3 Results & Discussion

B.3.1 Samples Topographic Properties

The topographic parameters for each profile were determined in both directions x and y, and an overall mean value was calculated for each subdomain and then a mean value was estimated per sample (Figure B.6). In each box, the bottom and top edges of the box indicate the 25th and 75th percentiles, respectively. The circle with the dot denotes the median, and the whiskers extend to the most extreme data points.

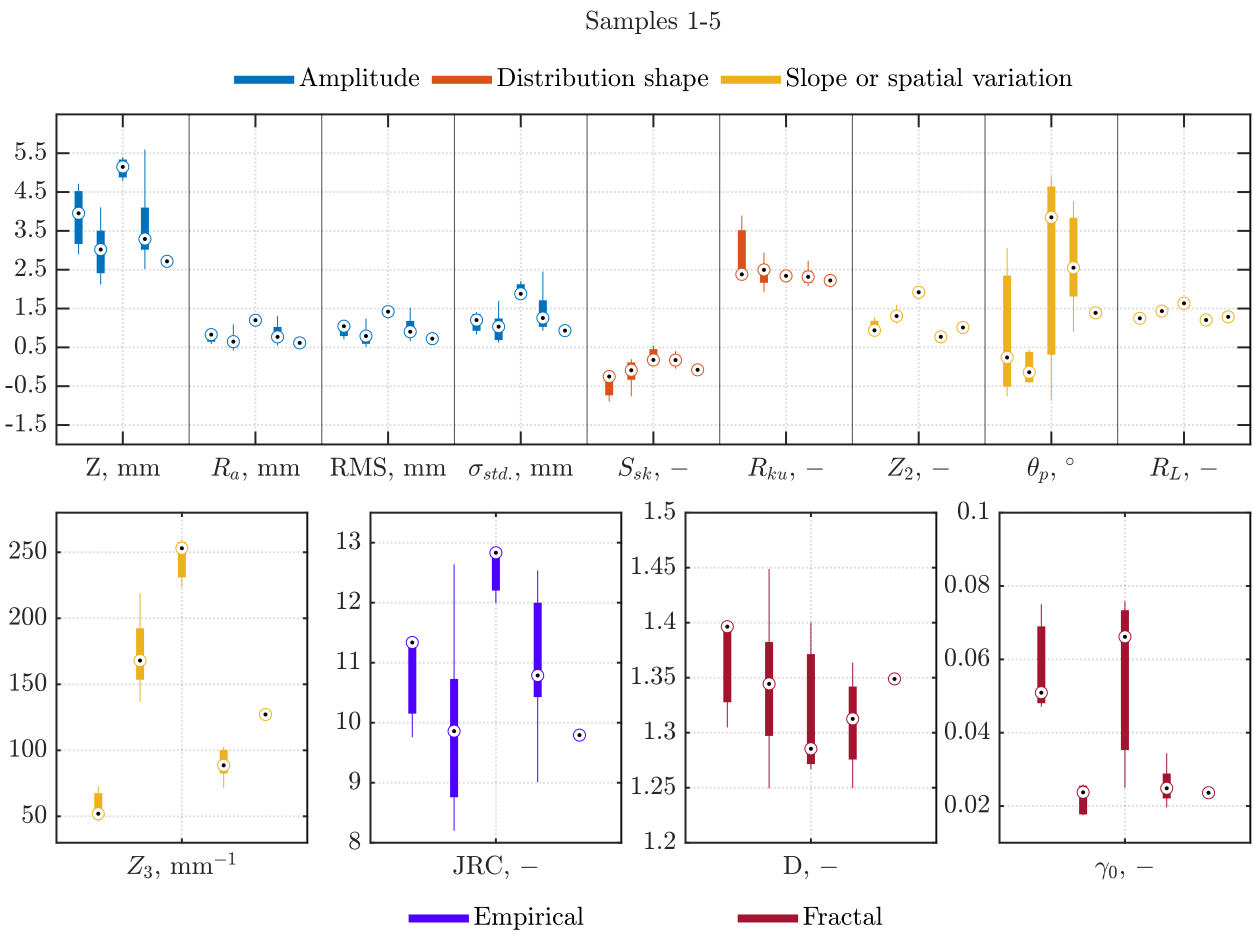

Figure B.6: Topographic parameters for Samples 1-5.

The amplitude parameters reflect the same pattern among them, and the standard deviation exhibited higher values compared to those reported for the surfaces of crystalline rock (Vogler et al., 2017). This might be related to the heterogeneity of the limestone rocks analyzed here. The distribution of profiles varied substantially, while sample 1, 2 and 5 exhibited slightly negative profile skewness S_{sk}, suggesting relatively fewer peaks or less pronounced valleys (Thomas, 1981), samples 3 and 4 displayed slightly positive values. Kurtosis R_{ku} indicated that sample 2 had near-Gausian distribution but most samples had a lack of high peaks and prominent valleys (Thomas, 1981). The slope or spatial variation parameters exhibited a similar pattern between them except for θ_p whose behavior correlated with the amplitude parameters contrary to what was expected (Y. Ge et al., 2014). Similarly, the pattern of JRC correlated with amplitude parameters. This occurred because most of the profiles analyzed were not in the range of the Z_2 equations and consequently, they were calculated with R_a which in turn yielded a correlation to amplitude parameters (Figure B.7a-d).

B.3.2 Behavior of JRC and Fractal Parameters

The correlation between JRC and R_a suggested that when back-calculating JRC from empirical equations it is necessary to verify the correlation with other parameters to identify the roughness type that could be majorly impacting the estimates. On the other hand, the fractal dimension demonstrated a negative correlation with θ_p (from the expression used by Belem et al. (2000), absolute value was not applied to the local slopes (i.e., $\Delta z/\Delta x$)) which supported the argument that non-stationarity of profiles affects results of the variogram method (Figure B.8a). In addition, the fractal dimension showed an unexpected negative correlation with the amplitude parameters (Figure B.8a). This result contrasted with the coarse grains observed in some of the samples, which exhibited high values in amplitude parameters that were expected to reflect a higher fractal-based roughness degree.

On the other hand, the fractal amplitude exhibited a pattern that correlated to amplitude parameters (Figure B.6). This was in line with what has been reported elsewhere (Klinkenberg, 1992) but the response towards Z_2 was not clear a trend (Figure B.8b). Nonetheless, analyzing γ_0 versus Z_2 and $\sigma std.$ appeared to be reasonably useful for clustering the subdomains and differentiating between the rock types analyzed.

These results suggest the existence of a relationship between parameters of different types, and examining these relationships may be beneficial in finding standardized descriptors of roughness. However, it is important to consider that the heterogeneous nature of the limestone rock surface analyzed here, along with the number of evaluated profiles, limits the generalization of these results.

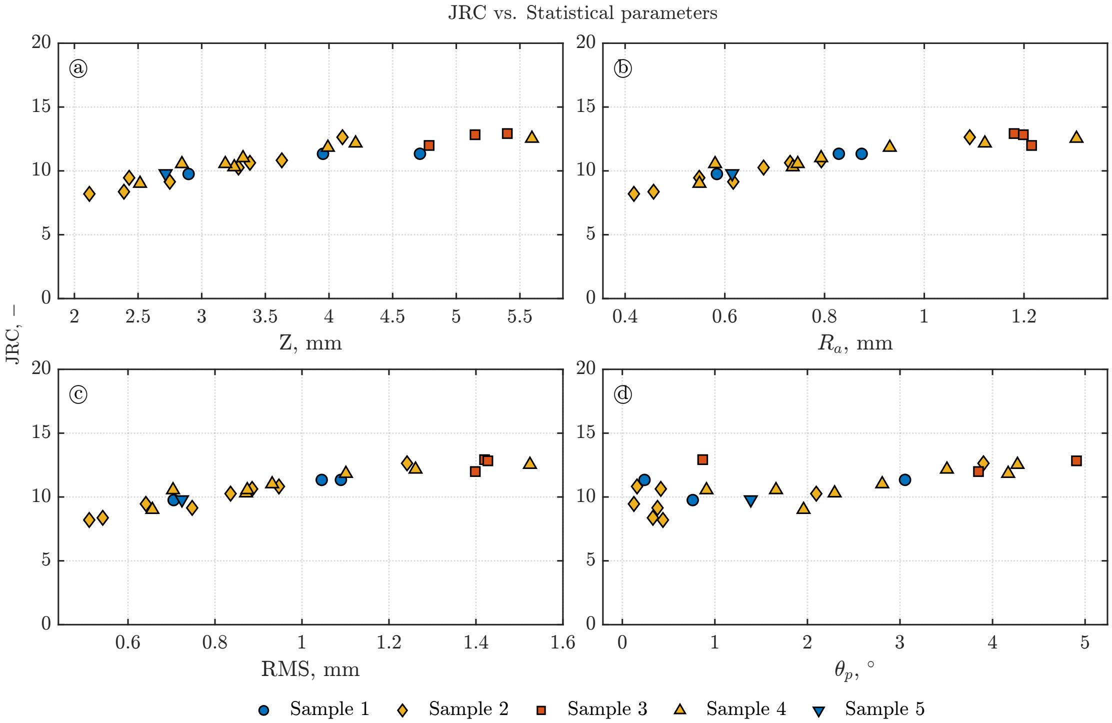

Figure B.7: Correlation between joint roughness coefficient and (a) Z, (b) R_a (c) RMS and (d) θ_p; values averaged per subdomain.

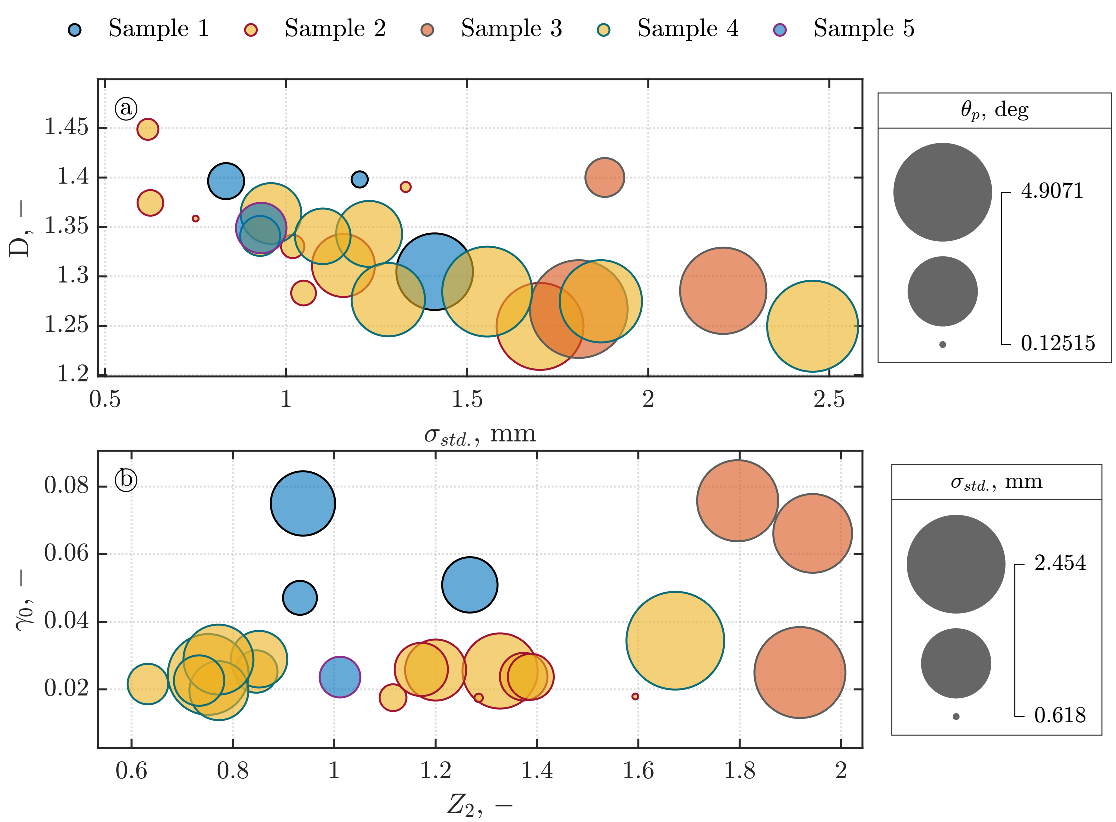

Figure B.8: (a) Standard deviation of surface height versus fractal dimension and θ_p values. (b) Z_2 parameters versus γ_0 estimates and $\sigma_{std.}$ values; values averaged per subdomain.

JRC values of Barton's profiles (N. Barton & Choubey, 1977) have been correlated with fractal parameters (Odling, 1994) estimated with the structure function. This preliminary analysis has found similar results between fractal-based parameters and JRC. First, a poor correlation between D versus γ_0 (Figure B.9a), second, a slightly positive correlation between JRC and γ_0 (Figure B.9b) and stronger correlation between JRC and D (Figure B.9c). These results contradict the relationship found between JRC and self-similar fractal-based parameters (Y. Li & Zhang, 2015) and emphasize the need to investigate which fractal methods, self-similar or self-affine techniques, are suitable for analyzing rock profiles. In this regard, numerous studies indicate that rock profiles can be considered self-affine (C. C. Barton & La Pointe, 1995; Y. Ge et al., 2014; Kwafniewski & Wang, 1997) and their character is not self-similar (Brown & Scholz, 1985).

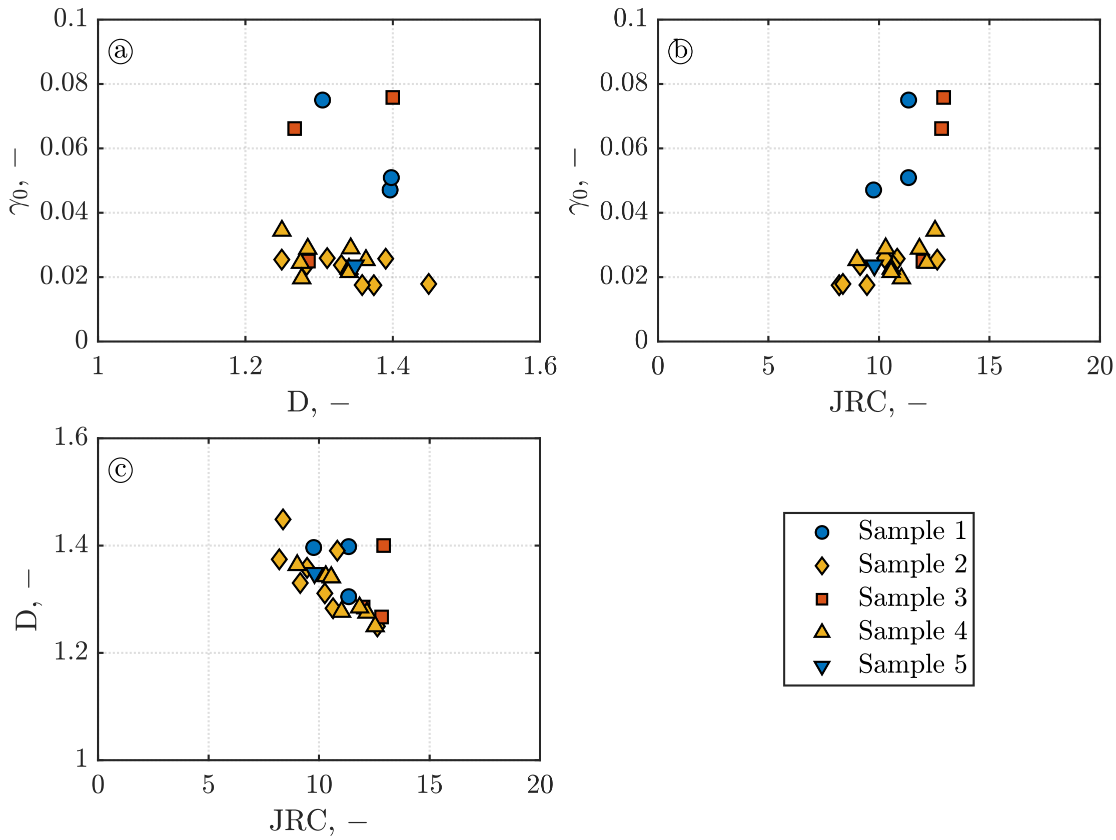

Figure B.9: (a) Amplitude fractal dimension and amplitude, (b) joint roughness coefficient and fractal dimension and (c) joint roughness coefficient and amplitude; values averaged per subdomain.

The measurements from the individual profiles were analyzed to determine if they behaved analogously to the averaged values presented earlier, using some similar plots. First, a plot depicting different parameters against the average asperity height was prepared (Figure

B.10a-c). This indicates that estimating JRC with analytical expressions may introduce bias towards certain types of descriptors, causing the JRC to reflect a single aspect of the overall roughness. Second, a plot identical to that of Odling (1994) was generated (Figure B.11a-c). The fact that both plots were generated from different data sets and exhibited similar behavior supports the existence of such correlations. Finally, a bubble plot involving three parameters was created (Figure B.12), showing a behavior like the one presented above. The trend in this data exhibited a pattern like that of the averaged values.

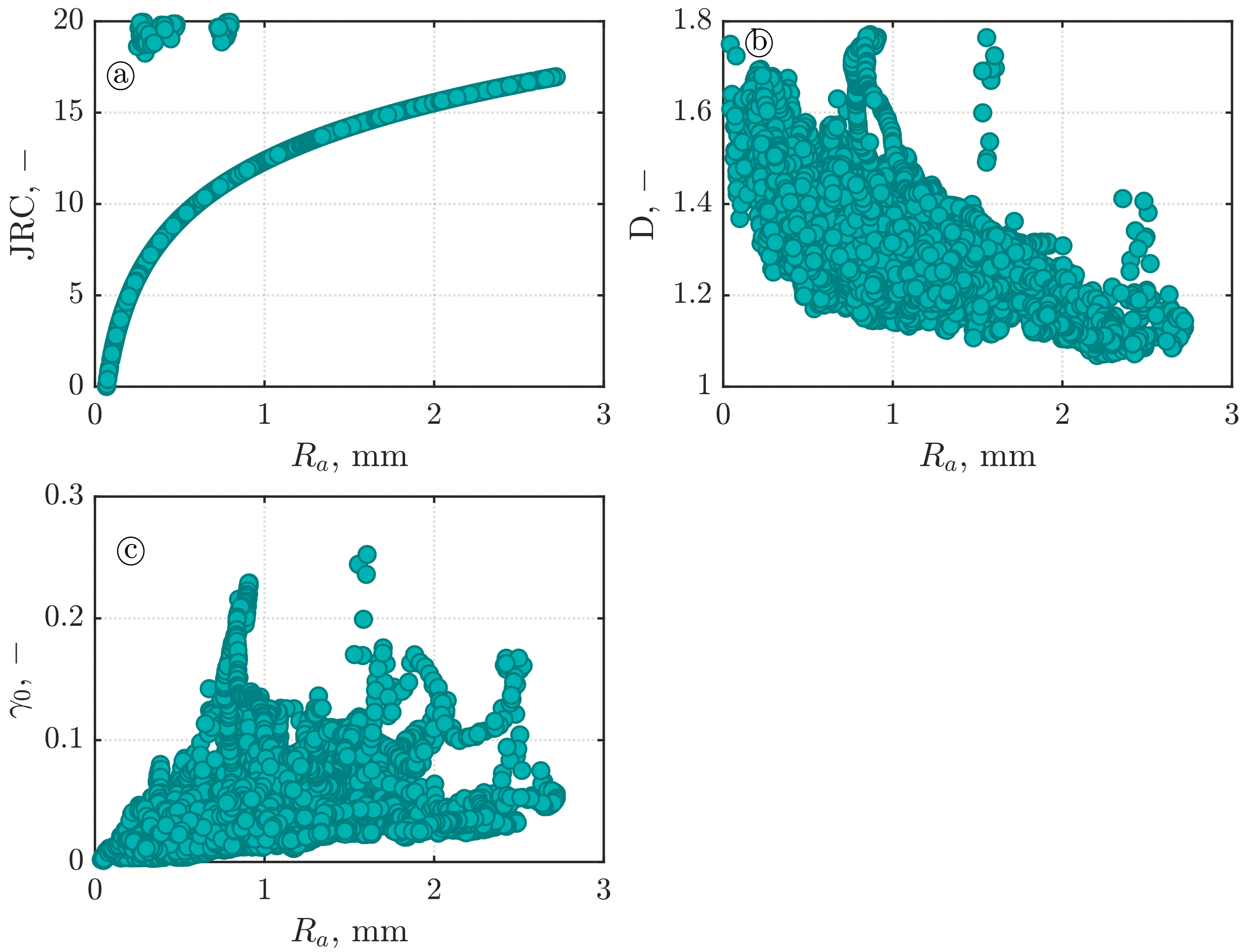

Figure B.10: Correlation between average asperity height and (a) JRC, (b) fractal dimension and (c) amplitude fractal dimension; values plotted for each individual profile in both directions.

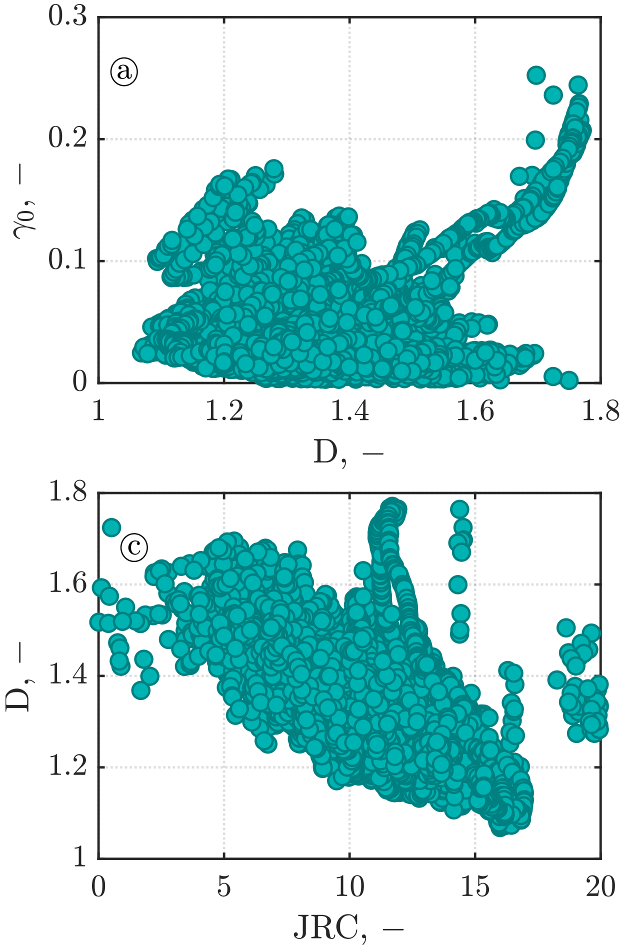

Figure B.11: (a) Fractal dimension and amplitude fractal dimension, (b) joint roughness coefficient and amplitude fractal dimension and (c) joint roughness coefficient and fractal dimension; values plotted for each individual profile in both directions.

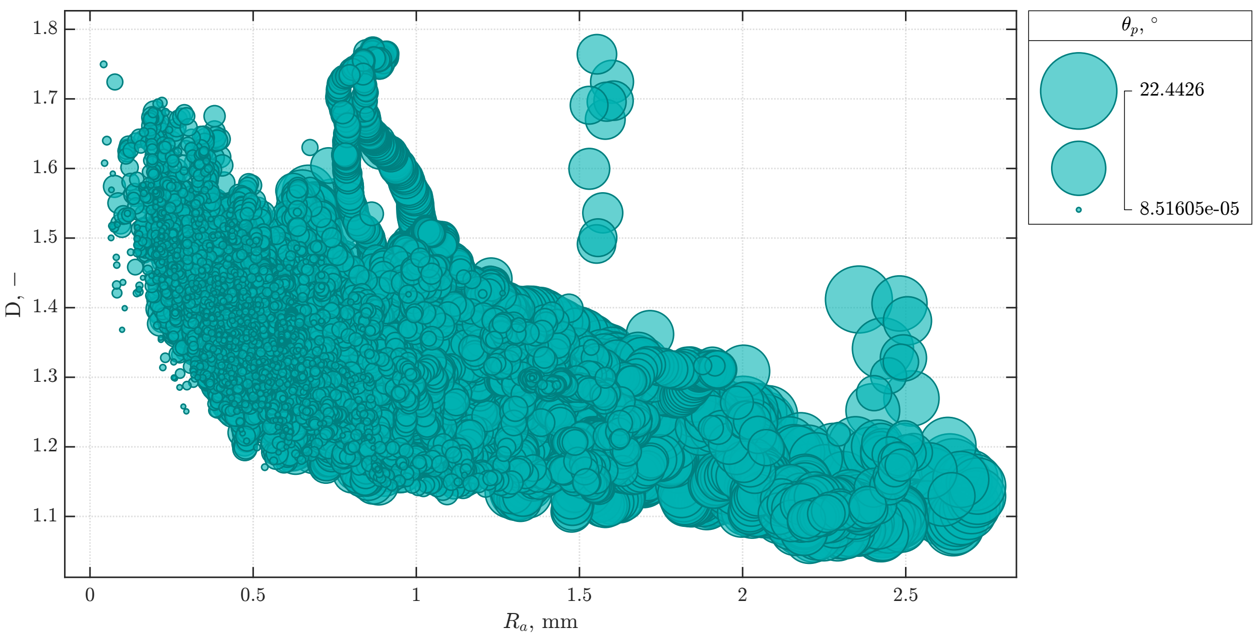

Figure B.12: (a) Average asperity height versus fractal dimension and θ_p values; values plotted for each individual profile in both directions.

B.4 Conclusion

The surface properties of the analyzed limestone samples indicated significant heterogeneity. Employing various surface roughness measurements facilitated a detailed description of the samples. Analyzing the relationship between different types of surface parameters may help in understanding their limitations and assessing the feasibility of having standardized coefficients. Despite previous research exploring the connection between JRC and fractal parameters from self-similar methods, the suggestion that fracture surfaces possess a self-affine fractal character raises concerns about the compatibility of these parameters. Unresolved aspects regarding existing JRC models and fractal methods underscore the necessity for a more robust workflow in characterizing rock surface topography. The collection and profilometer scanning of limestone rock samples from the El Guayal outcrop provided the basis for employing various methods to estimate surface properties. The study aimed to clarify the nature of these parameters and contribute to formulating a homogenized approach for characterizing rock surface topography. The existence of relationships between parameters of different types suggests the potential for attaining standardized roughness descriptors. However, the limited number of evaluated profiles indicates caution when generalizing the results. The results highlight the importance of verifying correlations when back-calculating JRC from empirical equations. Analyzing individual profiles revealed potential biases in estimating JRC with analytical expressions, indicating a tendency to reflect a single aspect of overall roughness. Additionally, the fractal dimension from the variogram method demonstrated a negative correlation with amplitude parameters, while non-stationarity simultaneously diminished the estimates of fractal dimension from the variogram method. The data in this study supported the existence of a correlation between JRC and fractal parameters. These findings highlight the complexity of characterizing rock surface topography and underscore the importance of considering multiple parameters for a comprehensive understanding.

Appendix C

Experimental Configurations

C.1 Preliminary Model

This model, originally created by the RGRG group, was designed so that both fracture sections were fully 3D printed which required substantial amount of 3D printing material. The cell was designed with dimensions of 250 mm $\times$ 150 mm (Figure C.1), and the fracture blocks were intended to be 100 mm $\times$ 172 mm. The sealing mechanism employed a face seal O-ring, and the inlet and outlet manifolds were concave (Figure C.2). Twelve pressure ports were distributed across the lower section (Figure C.3). The cell was assembled using 18-8 1/8-inch bolts, and the inlet and outlet were designed with three 1/4-inch NPT ports (Figure C.4).

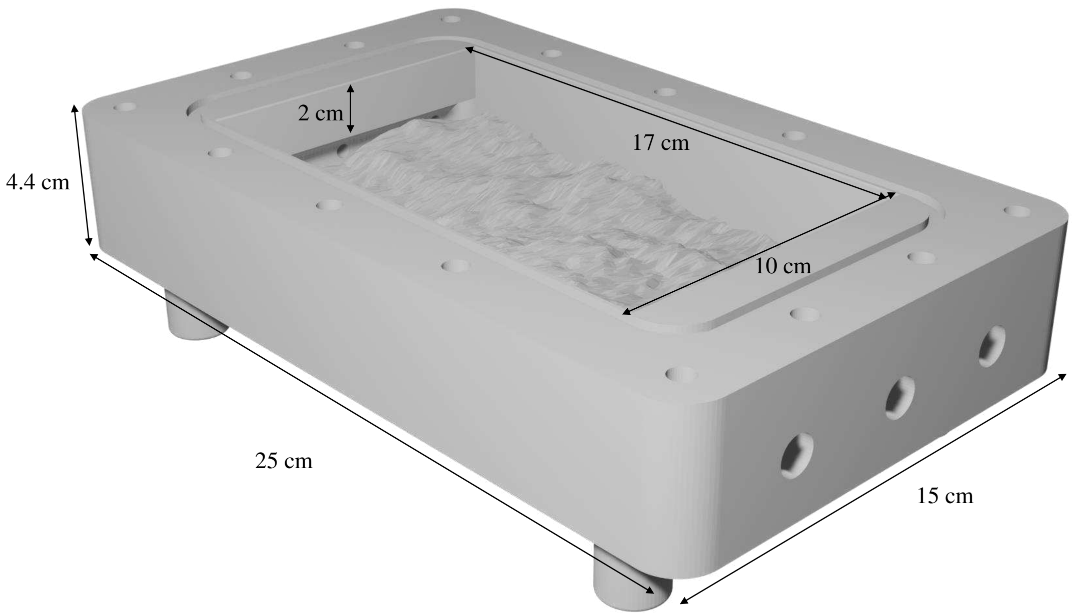

Figure C.1: Lower section with fracture incorporated — preliminary model.

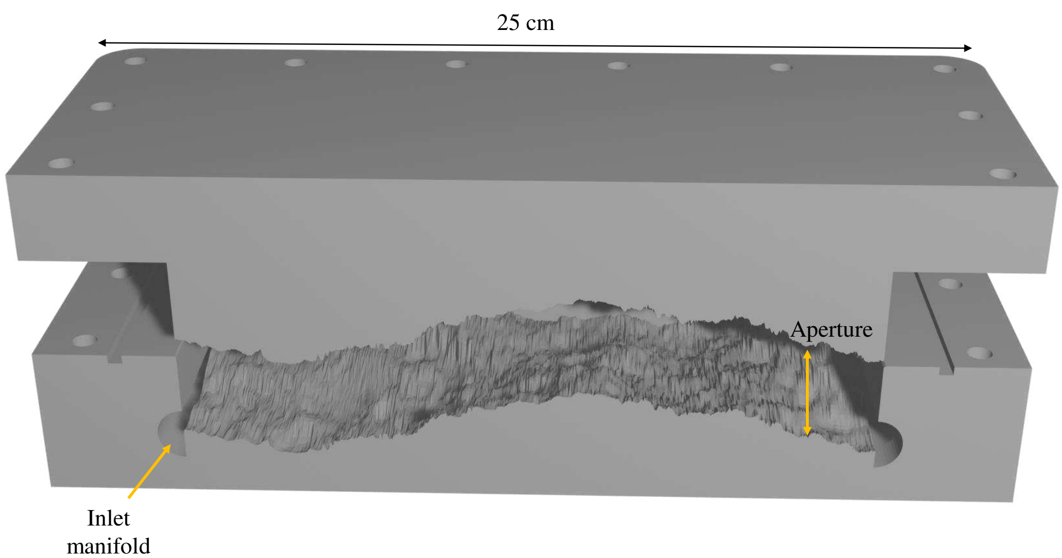

Figure C.2: Cell and fracture cross-section — preliminary model.

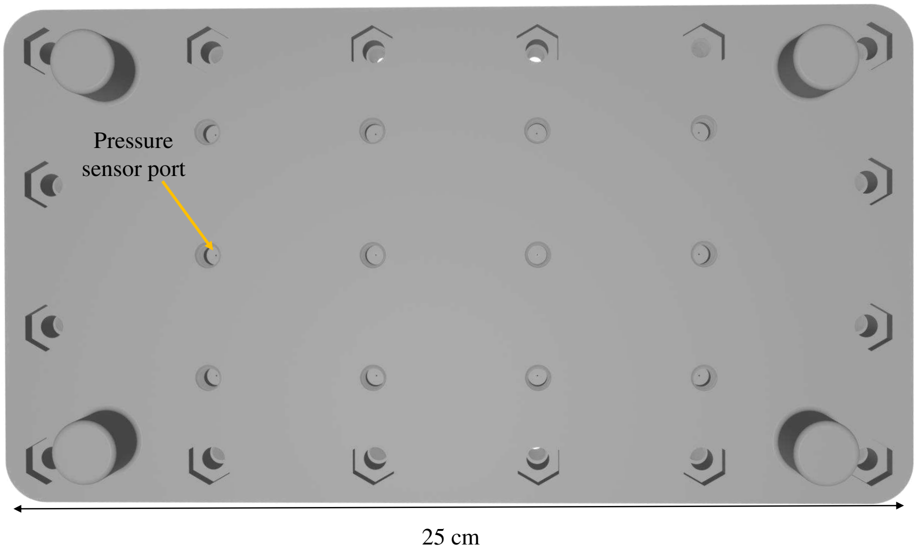

Figure C.3: Integration of local pressure porst — preliminary model.

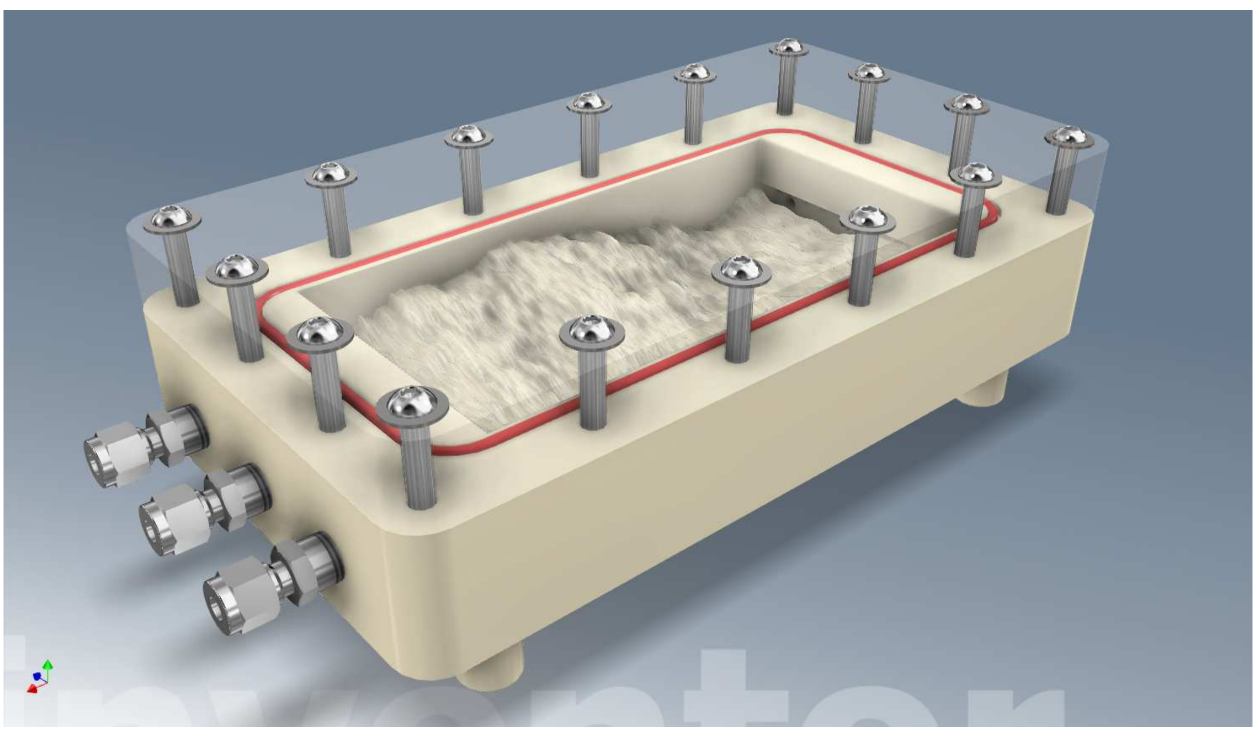

Figure C.4: Cell assembly — preliminary model.

C.2 Final Model

A second model was designed with a quadratic configuration to incorporate the flexibility of investigating how shear displacements perpendicular to flow affect permeability. This couldn't be achieved with a rectangular configuration, leading to the final design adopted in the experimental program.

The cell was manufactured in aluminum, and the 3D-printed fracture parts were mounted onto the cell. It featured conical inlet and outlet manifolds, along with four 1/4-inch ports at both ends (see Figure C.5). The fracture samples measured 150 mm × 150 mm.

The lower fracture part was mounted in the aluminum cell and sealed with silicone. After this process, a 3D-printed face seal (made of TangoBlack FLX973 material) was inserted into the seal slot, and the top fracture part was secured to the cell using 1/4-inch × 1-inch screws to complete the assembly (see Figure C.6). On the other hand, a 3D-printed model was designed and inserted into the inlet and outlet pockets to ensure an even distribution of the injected water and minimize dead volumes in the cell.

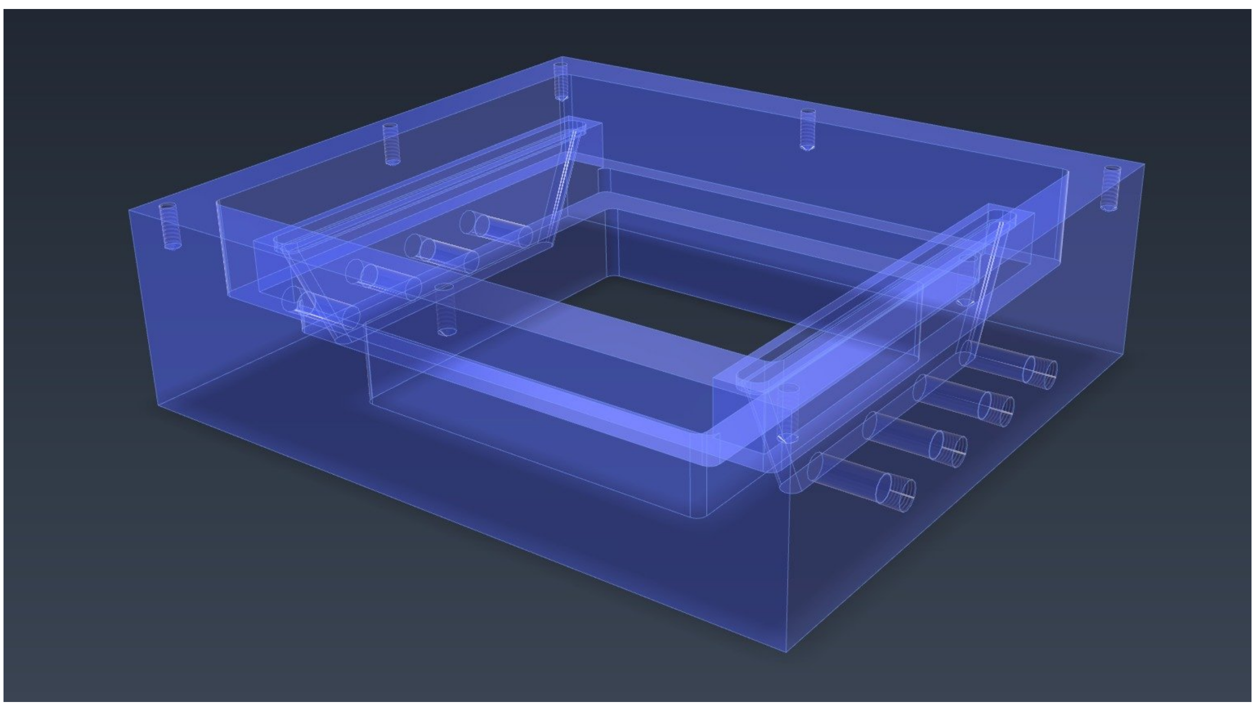

Figure C.5: Aluminum cell — final design.

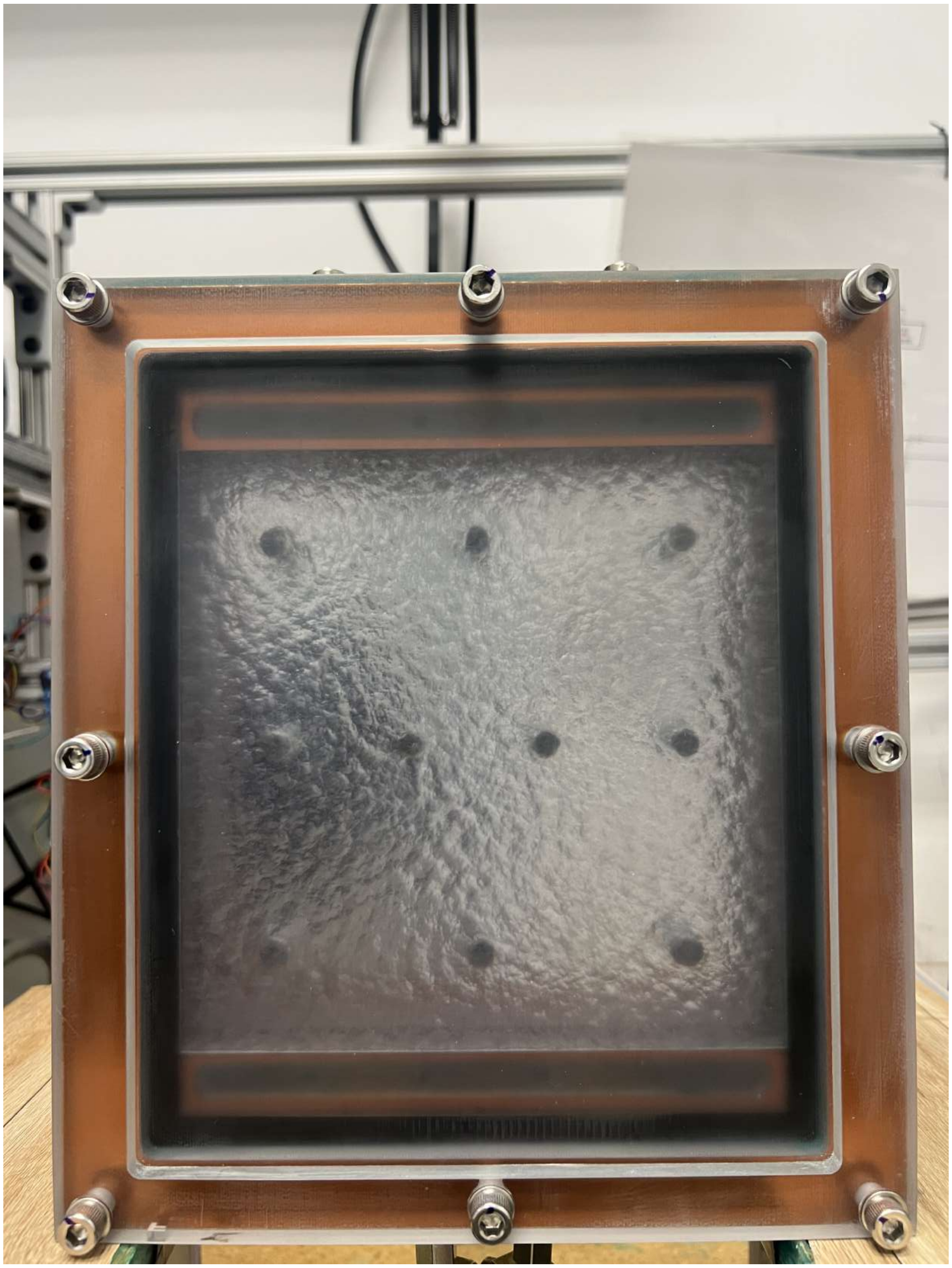

Figure C.6: Cell assembly — final design.

Appendix D

Practical Aspects of Using a Profilometer for Surface Measurements

D.1 Preliminary Scan

The maximum coverage area that can be achieved with a single scan using a Nanovea JR 50 is a 50×50 mm section. Before starting measurements, it is good practice to check that the instrument can cover both the maximum and minimum elevations of the surface and that the entire sample is reasonably leveled. If the surface exceeds the instrument's range (manual range is 3 cm), there will be non-measured points. Therefore, before scanning, ensure that the instrument can reach both the maximum and minimum heights. Ideally, starting with a quick scan at a high frequency (1000-2000 Hz) and a low resolution rate (50-100 μm) may be helpful to ensure comprehensive coverage of the surface by the instrument. In addition, this initial scan will determine the optimal frequency and resolution, focusing on achieving high frequency and sufficient resolution with respect to grain size while minimizing non-measured points.

D.2 Integrating Subodmains to Reproduce a Larger Digital Surface

D.2.1 Sample prepraration

If the surface cannot be covered in a single scan due to height resolution limitations or because the sample is larger, stitching surfaces is an option, but it requires more considerations. To stitch surfaces, it is ideal to plan section scans ahead as much as the sample size permits, namely, marking subdomains, rotating, and moving the sample to evaluate which subareas can be scanned without having to cut it. If possible, using a pen to mark the subsections on the sample will aid the scanning and stitching processes (see Figure D.1). If the sample has to be rotated for scanning due to its size, the orientation of the scanned surfaces can be corrected with Mountains 7.4 or Matlab (Python) software. Also, plan ahead if the sample needs to be cut to scan some areas of the sample.

Figure D.1: Sample preparation prior to surface measurements with a profilometer.

D.2.2 Assembling Subdomains

At least two options exist to stitch surfaces, and both require carefully moving and marking the sample to scan subdomains and documenting any manual vertical displacement applied to the scanning pen. The vertical offset applied to the pen will be used when stitching the subdomains.

One option to stitch subdomains is to use Mountains 7.4 software to join all patches. For this, an overlap portion is recommended so that the software recognizes the overlapping areas. If many subdomains need to be stitched, some computing power may be required. It might be faster to stitch surfaces in one direction first, especially if all subdomains are of the same dimensions, and subsequently in the other direction.

Another option involves manually joining the patches, a process achievable through

Mountains 7.4 or Matlab/Python. For this method, no overlap is needed, but documenting any vertical movements applied to the pen is essential when computationally joining the subdomains.

D.2.3 Processing Data

A basic workflow to process subdomains through Mountains 7.4 is to remove outliers and then fill the non-measured locations with interpolated values, followed by leveling. After these steps, a subdomain can be stitched using any preferred software or used for CAD modeling or exported for numerical simulations.